# The Influence of a Steady Baroclinic Deep Ocean on the Shelf

by

**M. Ross Vennell**

B.E., University of Auckland (1982)

Submitted in partial fulfillment of the
requirements for the degree of

Doctor of Philosophy

at the

MASSACHUSETTS INSTITUTE OF TECHNOLOGY

and the

WOODS HOLE OCEANOGRAPHIC INSTITUTION

June 1988



Signature of Author .....
Joint Program in Physical Oceanography
Massachusetts Institute of Technology
Woods Hole Oceanographic Institution
June 24, 1988

Certified by .....
Paola Malanotte-Rizzoli
Associate Professor, Massachusetts Institute of Technology
Thesis Supervisor

Accepted by .....
Carl Wunsch
Chairman, Joint Committee for Physical Oceanography

# The Influence of a Steady Baroclinic Deep Ocean on the Shelf

by

M. Ross Vennell

Submitted to the Massachusetts Institute of Technology–
Woods Hole Oceanographic Institution
Joint Program in Physical Oceanography
on June 24, 1988, in partial fulfillment of the
requirements for the degree of
Doctor of Philosophy

This Research was carried out with the support of the
National Science Foundation, Grant OCE-85-18487

## Abstract

The degree to which a baroclinic deep ocean could be responsible for the mean flow on the shallow continental shelf is examined using steady, boundary forced models which incorporate bottom friction. One set of models, for a vertically well mixed shelf, includes the horizontal advection of density. The second set of models comprises a three-layer model without and a two-layer model with interfacial friction.

It is found that near bottom flow has a short cross isobath scale due to the steep continental slope and consequently that the deep oceans lower water column could not be responsible for the observed mean flow. The cross isobath scale of flow in the upper deep ocean is predominantly determined by the oceans velocity profile. In a barotropic or near barotropic flow the upper water column follows the near bottom flow and therefore has little influence on the shelf. A surface intensified deep ocean flow is able to cross isobaths until it encounters the bottom. If deep ocean flow is confined to a surface layer thinner than the depth at the shelf break it could be responsible for the observed flow. The depth scale for velocity and density over the slope in the Mid-Atlantic Bight is generally larger than the shelf break depth and consequently it is concluded that the steep continental slope "insulates" this particular shelf from baroclinic deep ocean influence and therefore that the observed shelf flow is not of oceanic origin.

Using oxygen isotope data, Chapman et al. (1986) found that the Scotian shelf is the major source of Mid-Atlantic Bight shelf water. Their barotropic modeling results are extended to show that a baroclinic deep ocean also acts to hold shelf water on the shelf.

Thesis Supervisor: Paola Malanotte-Rizzoli
Title: Associate Professor, Massachusetts Institute of Technology

Contents

## List of Figures

## List of Tables

# Chapter 1

# Background and Introduction

## 1.1 Introduction

It is known that the mean flow over the shelf of the Mid-Atlantic Bight is toward the south west whereas the mean wind stress is eastward (Beardsley, Boicourt and Hanson (1976)). Beardsley and Winant (1979) demonstrated that not all the observed mean shelf flow could be forced by river or estuary outflow, and suggested that the remaining mean flow could be forced by an alongshore pressure gradient of oceanic origin. However Chapman et al. (1986) have shown, using Oxygen isotope data and salinity to distinguish water types, that the water over most of the Mid-Atlantic Bight shelf originates on or north of the Scotian shelf. Their calculations show that, despite mixing with water from over the continental slope and with some river run off, this Scotian shelf water is still discernible over much of the shelf as far south as the Virginian coast. They conclude that the mean shelf flow is an extension of flow over the Scotian shelf and does not originate in the deep ocean. This observation is supported by several models (discussed in detail later) which have shown that a barotropic [1] deep ocean pressure gradient could not drive significant shelf flow and therefore could not be responsible for the observed shelf flow.

This work will examine the question of whether a steady baroclinic [2] deep ocean could be responsible for the observed shelf flow. The shallow shelf is separated from

[1] A "barotropic" flow is defined as one which the velocity profile is independent of depth outside of any frictional boundary layers.

[2] A "baroclinic" velocity profile is defined as one where the velocity varies with depth outside of frictional layers due to horizontal density variation through the thermal wind relation.

the deep ocean by the continental slope. A realistic discussion of the question must consider the effects of bottom topography on the fluid motions above it. Intuitively topography ought to affect near bottom flow. A barotropic flow has a uniform velocity profile and the topography not only influences the near bottom flow but also influences the upper water column. However, the upper water column in a baroclinic flow may not follow the near bottom flow and the effect of topography is therefore more complex. Determining how the topography of the shelf and/or slope affects steady baroclinic flow is central to a discussion of the question addressed here.

In two cases the influence of topography on the flow is, at least intuitively, obvious. In the first case, a barotropic flow, the influence of the topography permeates the entire water column. Near geostrophic flow will not cross topography unless some mechanism, such as bottom friction, breaks the topographic constraint. For typical scales bottom friction permits only weak across topography motion and consequently the rate of cross topography penetration by a barotropic flow will be limited. The second case is that of a layered model where the core of the lower layer is motionless. In this case it is clear that the topography below should have no direct effect on the flow in the layers above the lowest and cross topography motion is not inhibited. However the influence of topography on flows which lie between these two cases and how flow in the upper water column is altered once it encounters the shoaling bottom is not intuitively obvious. The interfacial friction model of section 3.4 is able to smoothly bridge the gap between the two cases of barotropic and surface flows and is also able to obtain solutions for the cases where the surface flow runs into the sloping bottom.

## 1.2 Observations

A good review of observations and models relevant to processes which occur on and between the shelf and slope is given by Johnson and Rockliff (1986). The models presented in this work fall into the steady baroclinic category.

During the Nantucket Shoals Flux Experiment (NSFE79) a line of current meters was deployed across the shelf and upper slope south of New England (Beardsley et

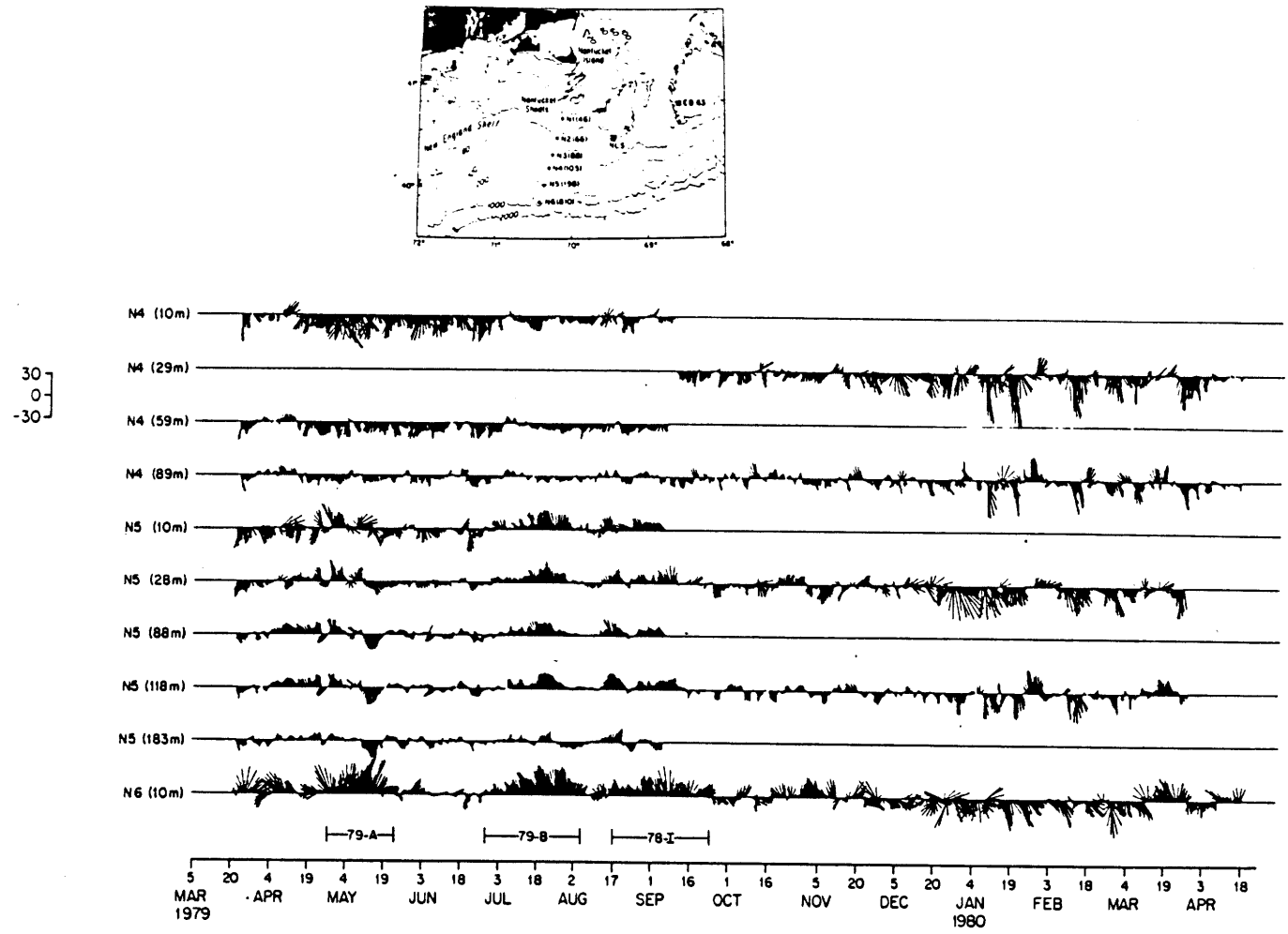


FIG. 8. Composite vector plots of the low-frequency NLS wind stress and currents measured in NSFE79. The positive alongshelf component of wind stress (oriented toward 77°T) and the positive alongshelf component of current (oriented towards 107°T) are both plotted up. All time series have been filtered with a low-pass filter with a half-amplitude period of 33 hours and subsampled every 6 hours.

Figure 1-1: Stick plots of alongshore velocity during Nantucket Shoals Flux Experiment, from Beardsley et al. (1979)

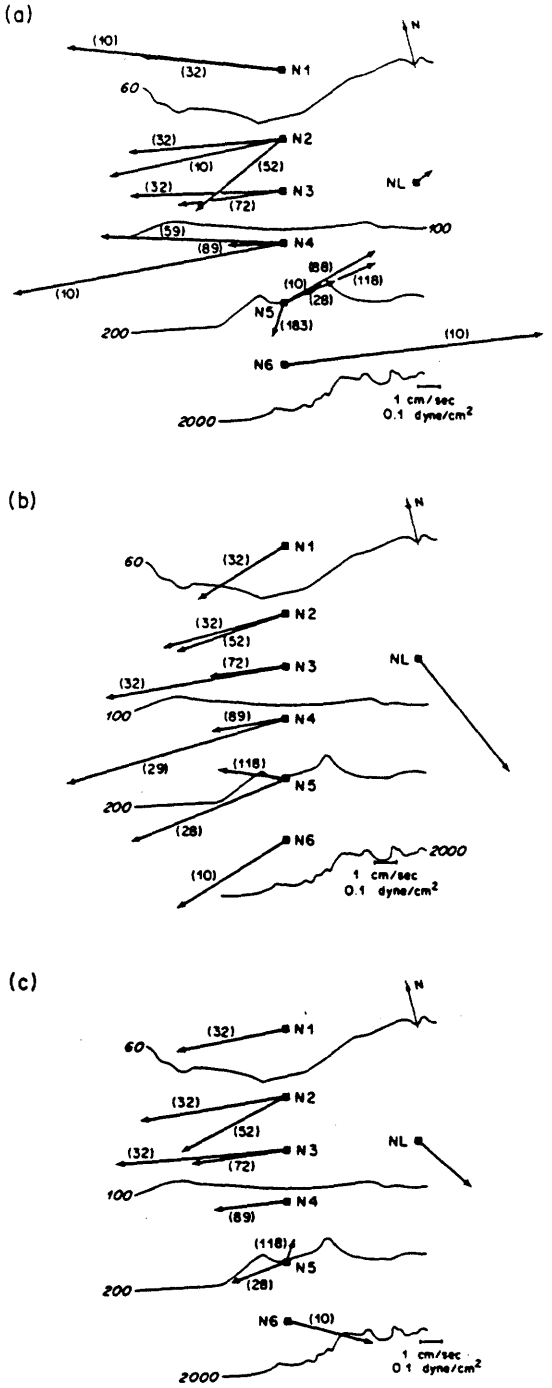


FIG. 10. Mean currents and wind stress computed over the (a) summer, (b) winter and (c) one-year periods. Instrument depth in meters is indicated in parentheses by the corresponding current vector, and the velocity and wind-stress scales are shown in the lower right of each panel. The 60, 100, 200, and 2000 m depth contours are also shown. Mean currents and stresses are tabulated in Table 3.

Figure 1-2: Mean flows during Nantucket Shoals Flux Experiment, from Beardsley et al. (1979)

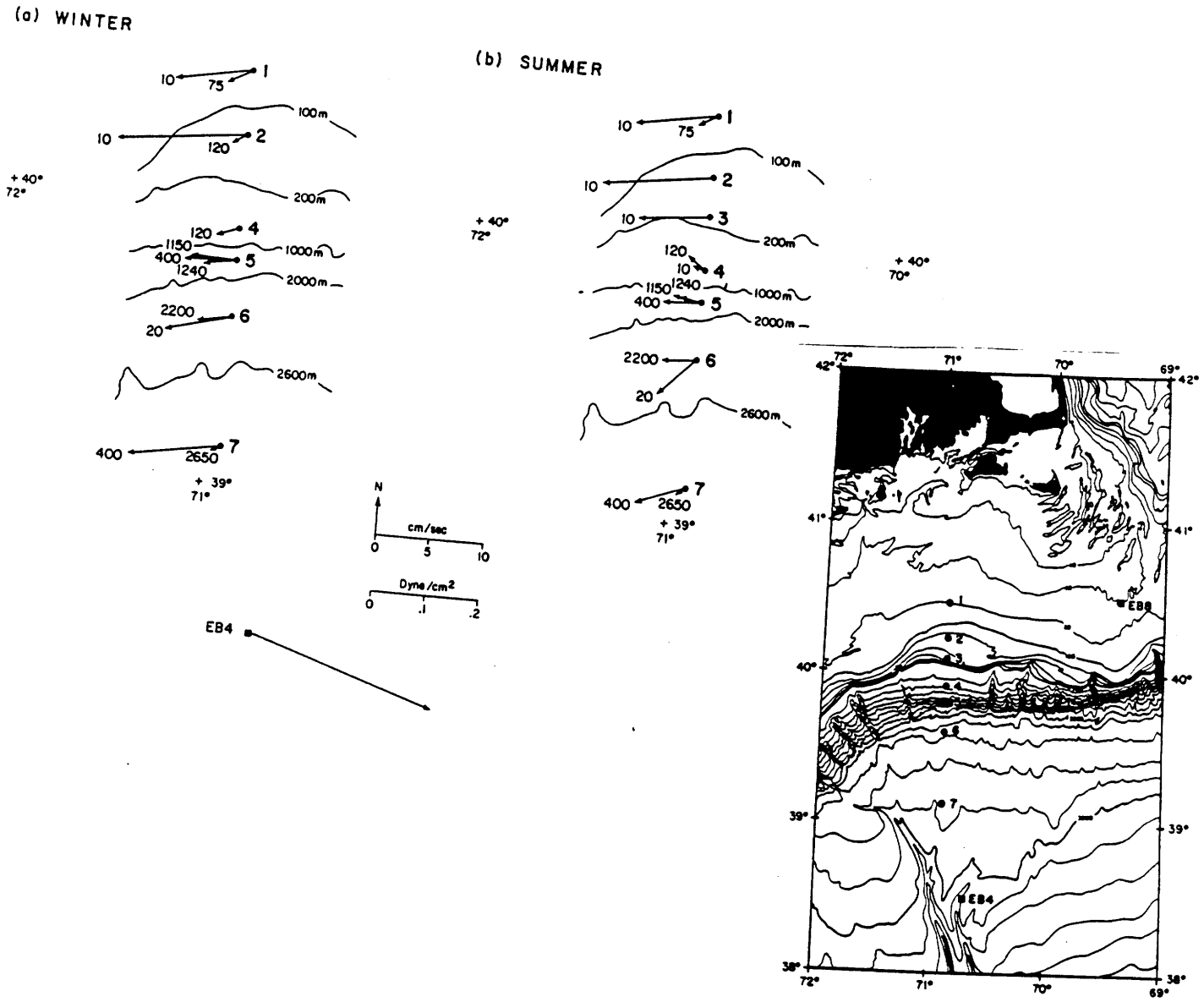


Figure 1-3: Mean flows during Shelf Edge Exchange Processes Experiment, from Aikman et al.(1986)

al. (1979)). Stick plots of the velocity are shown in Figure 1-1. A comparison of the near surface flow (10m) at two moorings which span the shelf break (N4 mooring in 100m of water and N6 situated in 810m of water) shows that the alongshore velocity at these two sites is often in opposite directions. At the intermediate mooring, N5, the alongshore flow direction appears to alternate between that at the moorings either side. The mean currents from NSFE79 in Figure 1-2 also show that alongshore flow over the shelf and slope is in opposite directions, particularly during the summer. Beardsley et al. (1979) noted that motions offshore of the shelf break, which was approximately at the 200m isobath, were dominated by the passage of Warm Core Gulf Stream Rings. Aikman et al.(1986) commented that mean currents observed during the Shelf Edge Exchange Processes experiment (SEEP) which were around $5cms^{-1}$ over the shelf and slope showed a minimum at the shelf break (see Figure 1-3). They also noted that current variability over the shelf was dominated by wind forcing while variability over the slope appeared to be of oceanic origin. These measurements and the calculations of Chapman et al. (1986) lend support to the notion that the shelf is isolated from the deep ocean. However the cause of this isolation is not completely clear.

During both NSFE79 and SEEP mean flows over the shelf and slope were strongly aligned with the topography. The NSFE79 had only a near surface current meter at its deepest mooring on the upper continental slope. However during SEEP three moorings were deployed across the slope. Significant vertical structure can be seen in the mean flows at these moorings (Figure 1-3). The models developed in this work will be used to determine how this vertical structure, i.e. baroclinicity in the deep ocean flow affects the ability of the deep ocean to influence the shelf. It will be shown that the steep continental slope acts as an effective insulator of the shelf from the baroclinic deep ocean influence.

## 1.3 Historical Background

As mentioned earlier several works have sought to determine the degree to which a barotropic deep ocean could be responsible for mean flow over the shelf. Several of

these works are based on the Arrested Topographic Wave model of Csanady (1978) (hereafter ATW). The ATW is a steady model which balances the forces which drive flow against bottom friction on a sloping bottom. By noting that shelves are characteristically narrow compared to their length Csanady was able to develop a relatively simple governing equation in the ATW which has the same form as that governing one-dimensional heat diffusion. He was not the first to notice this simple form (see Pedlosky (1974)), but he has been able to apply it to a variety of forced shelf flows. In the ATW Csanady argued that a steady deep ocean pressure gradient could drive the observed mean flow. Based on observations off the southern coast of Long Island, Scott and Csanady (1976) calculated this alongshore pressure gradient to be of order $10^{-7}$ or $1cm$ per $100km$.

After demonstrating that coastal sources could not explain all the observed mean shelf flow, citing the ATW and after making a detailed examination of the results of the numerical simulations of Semtner and Mintz (1977), Beardsley and Winant (1979) concluded that the southwestward mean shelf flow is driven by the large scale circulation in the western North Atlantic. They did note that the dynamical models used in coming to this conclusion were sufficiently crude that a critical test of the relative importance of run off and large scale forcing would have to wait until more realistic models were developed.

In the ATW Csanady assumed the shelf to be unbounded and of uniform slope. Two subsequent works, Wang (1982) and Csanady and Shaw (1983), incorporated the more realistic topography of a gently sloping shelf and a steep continental slope into the ATW model. They concluded that the continental slope effectively "insulates" the shelf from the influence of a barotropic deep ocean pressure gradient. These two barotropic models support the oxygen isotope data and model of Chapman et al. (1986) in showing that a barotropic deep ocean cannot be responsible for the mean flow over the shelf.

In order to answer from a modeling standpoint the question of whether a baroclinic deep ocean could be responsible for the observed shelf flow an appropriate equation

which governs the advection and/or mixing of density must be incorporated. Such a density equation greatly increases model complexity. Topography further increases this complexity because along-isobath density variations give rise to an extra term in the vorticity balance (Welander (1959)), called JEBAR (Joint Effect of Baroclinicity And Relief) by Sarkisyan and Keonjiyan(1975) and "bottom torque" by Malanotte-Rizzoli and Bergamasco (1983).

Two works (Csanady (1985) and Vennell and Malanotte-Rizzoli (1987)) avoided the difficulty associated with the density equation by assuming that the density field is known everywhere and that it is invariant with time. The steady flow field consistent with the assumed density field was calculated. For a vertically well mixed shelf Vennell and Malanotte-Rizzoli (1987) assumed a density field which is linear in the alongshore coordinate as an idealization of the density pattern produced by deep convection in the northern Adriatic in winter. The model results showed that flow near the Italian coast is of a direction and magnitude consistent with the observed winter mean flow.

In order to find the flow induced by an alongshore pycnocline slope Csanady (1985) used a two-layer model to idealize the alongshore set up of the main pycnocline in the United States Pacific Northwest with a two-layer model. He assumed that the interface had a constant linear slope between two latitudes and was flat outside of this region. Thus he knew a priori where the interface intersected the bottom and was able to calculate the flow pattern consistent with the assumed interface displacement. Both Vennell and Malanotte-Rizzoli (1987) and Csanady (1985) are "diagnostic" solutions because they calculate the flow consistent with an assumed density field and no density equation is included. It is argued that, despite the limitations of this approach, the solutions at least give a sense of the magnitude and direction of flow induced by alongshore density variations. However these models do not give a realistic cross-topography flow distribution and therefore this type of model is of limited use in determining the cross-topography penetration of the deep ocean.

Malanotte-Rizzoli and Bergamasco (1983) addressed the difficulty of combining horizontal density variations with topography using a multi-level hydrodynamic numerical

model for the Northern Adriatic with coupled equations for temperature and salt. This model is forced by observed winds, air/sea fluxes of heat and water vapor, together with sea level, temperature and salinity at the open southern boundary. In the model and observations a mean southward flow on the Italian coastline is evident during winter. It is argued that the alongshore density gradient associated with the dense water mass formed in the central Adriatic during winter is responsible for forcing the mean flow on the Italian coast through the mechanism of bottom torque.

Kelly and Chapman (1987) examined the response of the shelf and slope to a steady baroclinic offshore forcing. Their linear model, an extension of that of McCreary and Chao (1985), includes continuous stratification, bottom friction, vertical and horizontal diffusion of momentum. The density equation used balances mixing of the density perturbation against vertical advection of the assumed background stratification. The model is forced by prescribing the vertical distribution of pressure along the deepest isobath of the continental slope. Their model gave results similar to the low frequency results of Chapman and Brink (1987) and showed that, as it moves into shallower water, near bottom flow turns to follow the topography of the continental slope, and thus does not influence the shelf. The shoreward penetration of the deep ocean's upper water column is governed by the ratio of the cross-topography decay scale of the forcing in the absence of the coastal wall to the slope width. The decay scale is dependent on the internal Rossby radius and the vertical structure of the forcing. If the continental slope is wide compared to the decay scale, the coastal wall has little effect and significant flow is confined to the outer slope. If the slope is narrow, flow can be significant over the upper slope. However in all cases little deep ocean energy was found to penetrate shoreward of the shelf break. Stratification decoupled the upper and lower water column and surface intensified deep ocean flows had a larger cross-topography scale than barotropic deep ocean flows. For a narrow continental slope a surface intensified deep ocean flow is able to move shoreward until it encounters the bottom, at which point it turns to follow the topography.

Chapman and Brink (1987) discussed the circulation over the shelf and slope induced by an unsteady baroclinic deep ocean. This linear model incorporates continuous stratification, bottom friction and is forced by a prescribed pressure distribution along the deepest isobath which is periodic in both the time and alongshore coordinate. Their density equation balances the time rate of change of perturbation density against vertical advection of the mean background stratification. The results showed that for periods less than 10 days the low frequency shelf/slope response is mainly due to near resonances of coastally trapped free waves. At longer periods the cross-topography response to the forcing decays away with a horizontal scale approximately equal to the first baroclinic Rossby radius. If the continental slope lies within the decay scale of the forcing, then the flow forms a bottom trapped alongshore flow maximum offshore of the shelf break. The shelf response is always weak and barotropic, and is not greatly influenced by shelf width. .

## 1.4 Modeling Approach

A complete modeling solution to the question of the influence of the deep ocean on the shelf should include a shelf/slope region coupled to a deep ocean general circulation forced by surface winds and air/sea flows. Due to the computational difficulty few people have developed such models. A common approach, and the one used here, is to assume that the deep ocean is so large that it is unaffected by the dynamics of the narrow shelf/slope region. In other words, the shelf and slope act as a passive boundary layer to an invariant deep ocean general circulation. Thus the shelf/slope model will be forced by prescribing the deep ocean pressure gradient along the offshore edge, the offshore edge being the nearshore boundary of the deep ocean's Sverdrup flow. This approach reduces the problem to the more tractable one of determining the flow pattern over the shelf and slope consistent with the assumed forcing. Some works which have used this approach are Wang (1982), Csanady and Shaw (1983), Chapman and Brink (1987), and Kelly and Chapman (1987). The forcing most often used in this work is a horizontally uniform inflow from the deep ocean. The degree of influence or penetration

of a given deep ocean forcing will be measured by the cross-topography scale of the flow induced over the shelf and/or slope by that forcing. Apart from deep ocean forcing other forms of boundary forcing such as estuarine and forcing by a pressure head over the shelf will be considered here.

In the models used here to determine deep ocean influence, flow is forced by prescribing pressure and density or streamfunction and density on the offshore edge of the model domain. For a deep ocean inflow the density of a fluid parcel will be known at the point where it enters the model domain. However for a deep ocean outflow the density of a fluid parcel is fixed at the point where it exits the domain. In general the density of an outflow to the deep ocean is not determined by the point of exit, but is determined by shelf and/or slope processes upstream of this point. Therefore in the case of an outflow it is shelf/slope processes which determine the density structure of the deep ocean and not vice versa. Since this runs counter to the assumption that the shelf/slope region does not alter the deep ocean, only forcing of the shelf/slope region by deep ocean inflow will, in general, be considered here.

One exception to this rule occurs when considering the shelf/slope flow forced by a Gulf Stream Ring. In this case the deep ocean can be considered to impose an inflow and an outflow condition at the model's offshore edge. If the induced circulation is closed then the density of the outflow is not initially determined at an unknown upstream point over the shelf or slope, but is determined at the point of inflow from the deep ocean. In this case, i.e. that of a closed circulation pattern, a deep ocean outflow can be considered without violating the assumption of an invariant deep ocean.

## 1.5 Outline

To address the question of baroclinic deep ocean influence on the shelf a series of models is developed which are complex enough to contain essential features, e.g. baroclinic flow and shelf/slope topography, while remaining simple enough that the physical mechanisms which influence the flow pattern can be determined. The strategy used is to develop a basic model and then to consider the effects of each additional feature, for

example deep ocean vertical profile or planetary $\beta$, in isolation from other features in order to determine the effects and physical mechanisms associated with each feature.

The first in the series of models is that of Vennell and Malanotte-Rizzoli (1987) reproduced in Appendix C. The second model in this series is that for a vertically well mixed shelf in chapter 2 which incorporates horizontal advection of density. This model is used to examine deep ocean influence and also the flow due to coastal sources. In section 3.3 the third model, a three-layer model extends the depth range of the vertically well mixed model to examine deep ocean influence on the upper continental slope for particular deep ocean velocity profiles. In section 3.4 the fourth model, a two-layer model with interfacial friction, is able to solve cases not covered by the previous model for oceanic influence on the shelf and upper slope. In section 3.4j the fifth model extends the previous model to oceanic depths by including the effects of planetary $\beta$, and is used to examine oceanic influence on the upper and lower continental slope and also on the shelf. In section 3.4k the sixth and final model extends the model results of Chapman et al. (1986) to a baroclinic deep ocean to show how the deep ocean and continental slope act to hold Scotian shelf water on the shelf.

The two-layer model with interfacial friction of section 3.4 is an extension of that of Zang, Janowitz and Pietrafesa (1987) which was used to study estuarine outflow over the shelf. Friction is assumed important in thin boundary layers adjacent to the bottom and interface. In a rotating system these boundary layers are Ekman layers. Interfacial Ekman layers ensure that horizontal velocity is continuous across the interface. The model of Zang, Janowitz and Pietrafesa (1987) is forced at the coast by an estuary. In contrast, the two-layer model used here is forced at its offshore edge by the deep ocean and the effects of planetary $\beta$ are included. Since the forcing is at the offshore edge the density interface intersects the bottom. This intersection moves across the topography as the interface displaces vertically in response to the forcing. A complete solution to the two-layer model consists of the flow pattern in both layers and the position where the interface intersects the bottom. This line of intersection marks the shoreward boundary of the lower layer. A specialized numerical scheme is developed to solve the two layer

model for the layer flow patterns and the position of the intersection. Other differences from the model of Zang et al. are that the topography of the continental slope is also included, that alongshore scales are assumed much larger than cross-topography scales and that the vertical turbulent eddy viscosity away from the bottom boundary layer is permitted to be different from its value in the bottom boundary layer. The reason behind the last difference is that turbulence away from the bottom is expected to be weaker than that near the bottom due to bottom friction.

Zang, Janowitz and Pietrafesa (1987) did not give the details of how they generalized the results of Pedlosky (1979) for an Ekman layer on a sloping bottom to Ekman layers on a sloping interface. In Appendix B these details are given together with detailed velocity profiles for the interfacial Ekman layers and the transports within these layers.

## Chapter 2

## Vertically Well Mixed Shelf Flow

During the winter the Mid Atlantic Bight is vertically well mixed to 100 meters depth by storms. In the northern Adriatic the Bora wind is capable of vertically mixing the water column to 250m (Hendershott and Malanotte-Rizzoli (1976)). In these situations a model which assumes that the shelf waters are vertically well mixed is appropriate. Such a model would be useful in determining the effects of the Atlantic ocean on the Mid-Atlantic Bight and also the coastal flow induced by the alongshore density gradient established by the Bora wind in the Adriatic. The model presented in this chapter is more realistic than the diagnostic one of Vennell and Malanotte-Rizzoli (1987) because it does not assume that the density field is known everywhere apriori.

The aim is to determine how the baroclinic structure of a deep ocean flow affects its ability to penetrate the shelf. Flow penetration is defined as the flow's cross-topographic scale for a given transport. Flow is driven by prescribing the streamfunction and the density at the outer edge of the shelf. Horizontal density gradients cause the flow to have vertical shear in its horizontal velocity.

In Appendix A an analytical solution valid in the near-field for a deep ocean forcing is obtained. The governing equation is similar to that governing heat diffusion in a cylinder. This analogy proves useful in explaining the underlying physical mechanisms which determine the flow pattern.

## 2.1 Derivation of Transport Equations

The transport equations used by Csanady(1979) are derived from the primitive equations. Assumptions are that flow is on an $f$ plane, $x$ is offshore, and $y$ alongshore (see shelf geometry in Figure 2-1). The steady momentum and continuity equations for a shallow hydrostatic Boussinesq fluid are

$$\begin{aligned} u\frac{\partial u}{\partial x} + v\frac{\partial u}{\partial y} + w\frac{\partial u}{\partial z} - fv &= \frac{-1}{\rho_0}\frac{\partial p}{\partial x} + A_V\frac{\partial^2 u}{\partial z^2} + A_H(\frac{\partial^2 u}{\partial x^2} + \frac{\partial^2 u}{\partial y^2}) \\ u\frac{\partial v}{\partial x} + v\frac{\partial v}{\partial y} + w\frac{\partial v}{\partial z} + fu &= \frac{-1}{\rho_0}\frac{\partial p}{\partial y} + A_V\frac{\partial^2 v}{\partial z^2} + A_H(\frac{\partial^2 v}{\partial x^2} + \frac{\partial^2 v}{\partial y^2}) \\ \frac{\partial p}{\partial z} &= -\rho g \\ \frac{\partial u}{\partial x} + \frac{\partial v}{\partial y} + \frac{\partial w}{\partial z} &= 0 \end{aligned} \tag{2.1}$$

where $u$ and $v$ are the cross and alongshore components of velocity, $w$ is the vertical velocity, $\rho$, the density, $\rho_0$, a constant reference density, and $A_V$ and $A_H$ are the vertical and horizontal turbulent diffusivities of momentum. Boundary conditions depend on the particular problem being studied. The non-dimensional scales are defined by

$$\begin{aligned} x = L_x x' \quad y = L_y y' \quad z = h_0 z' \\ u = u_0 u' \quad v = v_0 v' \quad w = w_0 w' \\ p = v_0 f L_x \rho_0 p' \\ \rho = \frac{v_0 f L_x}{g h_0}\rho' \end{aligned} \tag{2.2}$$

where $h_0$ is the depth scale and $L_x$ and $L_y$ are the along and cross shelf horizontal scales. Non-dimensionalized with the above scales (2.1) becomes

$$\begin{aligned} \left(\frac{L_x}{L_y}\right)^2 R_0 \left(u'\frac{\partial u'}{\partial x'} + v'\frac{\partial u'}{\partial y'} + w'\frac{\partial u'}{\partial z'}\right) - v' = \\ -\frac{\partial p'}{\partial x'} + \left(\frac{L_x}{L_y}\right) E_V \frac{\partial^2 u'}{\partial z'^2} + \left(\frac{L_x}{L_y}\right) E_H \left(\frac{\partial^2 u'}{\partial x'^2} + \left(\frac{L_x}{L_y}\right)^2 \frac{\partial^2 u'}{\partial y'^2}\right) \end{aligned} \tag{2.3a}$$

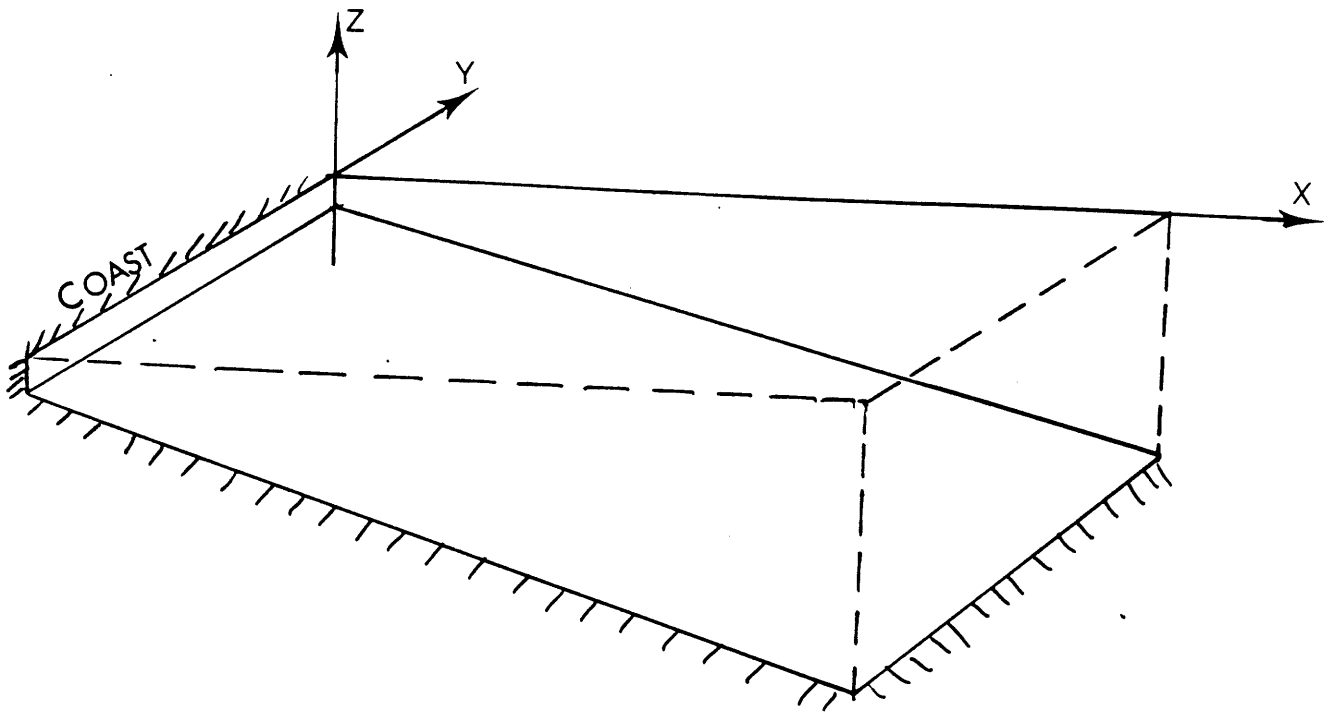


Figure 2-1: Shelf geometry for vertically well mixed model.

$$R_0(u'\frac{\partial v'}{\partial x'} + v'\frac{\partial v'}{\partial y'} + w'\frac{\partial v'}{\partial z'}) + u' =$$
$$-\frac{\partial p'}{\partial y'} + \frac{L_y}{L_x}E_V\frac{\partial^2 v'}{\partial z'^2} + \frac{L_y}{L_x}E_H\left(\frac{\partial^2 v'}{\partial x'^2} + (\frac{L_x}{L_y})^2\frac{\partial^2 v'}{\partial y'^2}\right) \tag{2.3b}$$

$$\frac{\partial p'}{\partial z'} = -\rho' \tag{2.3c}$$

$$\frac{\partial u'}{\partial x'} + \frac{\partial v'}{\partial y'} + \frac{\partial w'}{\partial z'} = 0 \tag{2.3d}$$

where the non-dimensional numbers are defined by

$$\begin{array}{lll} \text{Rossby number:} & R_0 & = \frac{v_0}{fL_x} \\ \text{Vertical Ekman Number:} & E_V & = \frac{A_V}{fh_0^2} \\ \text{Horizontal Ekman Number:} & E_H & = \frac{A_H}{fL_x^2} \end{array} \quad . \tag{2.4}$$

In the continuity equation it is assumed that all terms are of equal importance and hence $\frac{u_0}{L_x} = \frac{v_0}{L_y} = \frac{w_0}{h_0}$. Therefore the Rossby numbers which appear in the non-dimensional equations are equal.

It is assumed that vertical mixing of momentum is stronger than either horizontal mixing or inertial effects i.e.

$$E_H << \frac{L_x}{L_y}R_0 << E_V \quad . \tag{2.5}$$

In addition if the cross-shelf scale is small compared to the alongshelf scale ( i.e. $\frac{L_x}{L_y} << 1$) then the governing equations neglecting small terms are

$$\begin{aligned} -v' &= -\frac{\partial p'}{\partial x'} \\ u' &= -\frac{\partial p'}{\partial y'} + \frac{L_y}{L_x}E_V\frac{\partial^2 v'}{\partial z'^2} \end{aligned} \quad . \tag{2.6}$$

The depth integrals of (2.6) between the surface and bottom, with a rigid lid and in the absence of wind stress, are

$$\begin{aligned} -V' &= -\int_{-h'}^{0} \frac{\partial p'}{\partial x'} dz \\ U' &= -\int_{-h'}^{0} \frac{\partial p'}{\partial y'} dz - \frac{L_y}{L_x} \tau_b^{y'} \\ \frac{\partial U'}{\partial x'} + \frac{\partial V'}{\partial y'} &= 0 \end{aligned} \tag{2.7}$$

where $U'$ and $V'$ are the cross-shelf and alongshore components of transport defined by

$$U' = \int_{-h'}^{0} u' dz' \tag{2.8a}$$

$$V' = \int_{-h'}^{0} v' dz' \quad . \tag{2.8b}$$

The alongshore component of bottom stress per unit mass is defined as

$$\tau_b'^{y} = E_V \frac{\partial v'}{\partial z'}\Big|_{z=-h} \quad . \tag{2.9}$$

Dimensionally the boundary layer thickness is

$$\delta_E = \sqrt{\frac{A_v}{f}}$$

The Ekman number is the square of the ratio of the boundary layer thickness to the depth scale, i.e.

$$E_V = \left(\frac{\delta_E}{h_0}\right)^2$$

With some manipulation the transport equations (2.7) become those used by Csanady (1979). Following his work the pressure in a hydrostatic Boussinesq fluid may be rewrit-

ten dimensionally as

$$\frac{1}{\rho_0}p(x,y,z) \quad = \quad g\eta(x,y) + g\int_z^0 \left(1+\epsilon(x,y,z^*\right)dz^* \tag{2.10}$$

where $\eta$ is the free surface displacement (barotropic pressure) and $\epsilon$ is the density excess defined by $\epsilon = \frac{\rho(x,y,z)-\rho_0}{\rho_0}$. Horizontal gradients of pressure are dynamically important. For example the cross-shelf pressure force per unit mass per unit area is

$$-\frac{1}{\rho_0}\frac{\partial p}{\partial x} \quad = \quad -g\frac{\partial \eta}{\partial x} - g\int_z^0 \frac{\partial \epsilon}{\partial x}dz^* \quad .$$

The depth integral of the horizontal pressure force is

$$-\frac{1}{\rho_0}\int_{-h}^0 \frac{\partial p}{\partial x}dz \quad = \quad -gh\frac{\partial \eta}{\partial x} - g\int_{-h}^0\int_z^0 \frac{\partial \epsilon(x,y,z^*)}{\partial x}dz^*dz \quad .$$

Rewriting this by reversing the order of the double depth integral yields

$$-\frac{1}{\rho_0}\int_{-h}^0 \frac{\partial p}{\partial x}dz \quad = \quad -gh\frac{\partial \eta}{\partial x} - g\int_{-h}^0 (h+z^*)\frac{\partial \epsilon(x,y,z^*)}{\partial x}dz^* \quad .$$

Using this form for the pressure gradient for a water column t hat is vertically well mixed ( $\epsilon(x,y)$) the transport equations (2.7) become dimensionally

$$-fV = -gh\frac{\partial \eta}{\partial x} - \frac{gh^2}{2}\frac{\partial \epsilon}{\partial x} \tag{2.11a}$$

$$fU = -gh\frac{\partial \eta}{\partial y} - \frac{gh^2}{2}\frac{\partial \epsilon}{\partial y} - \tau_b^y \tag{2.11b}$$

$$\frac{\partial U}{\partial x} + \frac{\partial V}{\partial y} = 0 \tag{2.11c}$$

It is assumed that the flow can be considered comprised of two components. One associated with the pressure gradient, the geostrophic component, and one associated with the ageostrophic transport within the bottom frictional layer. Such a decom-

position is sensible if the frictional layer does not occupy the entire water column. Conceptually the bottom stress in (2.11b) is assumed to be proportional to the velocity just above the bottom frictional layer where the flow is in geostrophic balance. The geostrophic component of velocity varies in the vertical due to thermal wind. The depth scale of this variation is assumed to be of order the shelf break depth, i.e. $100m$. The bottom boundary layer is of order $10m$ thick. Consequently the variation in geostrophic velocity over the thickness of the boundary layer is small and the geostrophic velocity evaluated at the bottom is a good approximation of that $\delta_E$ above the bottom. When this is the case the bottom stress may be taken proportional to the geostrophic velocity at the bottom (Csanady (1979)) i.e.

$$\tau_b^y = r v_b \tag{2.12}$$

where $r$ is a constant drag coefficient and has the dimensions of velocity. The components of bottom geostrophic velocity for a vertically well mixed flow are

$$f u_b = -g\left(\frac{\partial \eta}{\partial y} + h\frac{\partial \epsilon}{\partial y}\right) \tag{2.13a}$$

$$f v_b = g\left(\frac{\partial \eta}{\partial x} + h\frac{\partial \epsilon}{\partial x}\right) \quad . \tag{2.13b}$$

The stream function for total transport (geostrophic plus frictional) is defined by

$$\begin{aligned} \frac{\partial \psi}{\partial x} &= V \\ \frac{\partial \psi}{\partial y} &= -U \quad . \end{aligned} \tag{2.14}$$

Assuming depth is a function of x only, dividing (2.11a and 2.11b) by depth, cross differentiating to eliminate the free surface displacement and using (2.14), yields

$$r\frac{\partial}{\partial x}\left(\frac{1}{h^2}\frac{\partial \psi}{\partial x}\right) + \frac{f h_x}{h^2}\frac{\partial \psi}{\partial y} = -\frac{gr}{2f}\frac{\partial^2 \epsilon}{\partial x^2} - h_x\frac{g}{2}\frac{\partial \epsilon}{\partial y} \quad . \tag{2.15}$$

Using the momentum equations to eliminate $\eta$ from the definitions of near bottom geostrophic velocity the bottom velocities can be rewritten as

$$u_b = -\frac{1}{h}\frac{\partial \psi}{\partial y} + \frac{gh}{2f}\frac{\partial \epsilon}{\partial y} + \frac{r}{fh}v_b \tag{2.16a}$$

$$v_b = \frac{1}{h}\frac{\partial \psi}{\partial x} + \frac{gh}{2f}\frac{\partial \epsilon}{\partial x} \quad . \tag{2.16b}$$

Flow will be forced by prescribing $\psi$, $\epsilon$ or their derivatives on all lateral boundaries.

## 2.2 Advective Density Equation for Vertically Well Mixed Flow

The density equation is difficult to solve because of the non-linearity due to advection. However a simple form can be obtained if it is assumed that vertical mixing is strong compared to advection. For turbulent flow it is assumed that the diffusivities for momentum and density can be taken to be the same (i.e. $A_H = K_H$ and $A_V = K_V$) in which case the steady density equation may be written

$$u\frac{\partial \epsilon}{\partial x} + v\frac{\partial \epsilon}{\partial y} + w\frac{\partial \epsilon}{\partial z} = A_V\frac{\partial^2 \epsilon}{\partial z^2} + A_H\frac{\partial^2 \epsilon}{\partial x^2} + A_H\frac{\partial^2 \epsilon}{\partial y^2} \quad . \tag{2.17}$$

The bottom boundary condition for density for a small bottom slope and $\frac{E_H}{E_V} << 1$ is no heat or salt flux through the bottom, i.e. $\frac{\partial \epsilon}{\partial z} = 0$ at $z = -h$. The surface boundary condition requires more careful consideration. During winter the Mid-Atlantic Bight is well mixed by storms and it is assumed that the wind, thermal and vertical boundary forcings can be viewed as acting in isolation from each other. The aim is to develop a model for vertical boundary forcing acting alone. In this case the surface boundary condition for the density is no heat or salt flux through the surface. Therefore the boundary conditions for density are

$$\frac{\partial \epsilon}{\partial z} = 0 \qquad at \quad z = 0, -h \quad . \tag{2.18}$$

Equation (2.17) can be non-dimensionalized using the scales (2.2) to yield

$$\left(\frac{L_x}{L_y}\right) R_0 \left(u' \frac{\partial \epsilon'}{\partial x'} + v' \frac{\partial \epsilon'}{\partial y'} + w' \frac{\partial \epsilon'}{\partial z'}\right) = E_V \frac{\partial^2 \epsilon'}{\partial z'^2} + E_H \left(\frac{\partial^2 \epsilon'}{\partial x'^2} + \left(\frac{L_x}{L_y}\right)^2 \frac{\partial^2 \epsilon'}{\partial y'^2}\right) \tag{2.19}$$

subject to

$$\frac{\partial \epsilon'}{\partial z'} = 0 \qquad at \quad z' = 0, -h' \quad . \tag{2.20}$$

Since it is assumed that vertical mixing dominates advection and that horizontal mixing is unimportant, the non-dimensional numbers have the relative sizes given by (2.5). Expanding the density in terms of the vertical Peclet number defined by

$$P_e = \frac{R_0}{E_V} \tag{2.21}$$

$$\begin{aligned} \epsilon' &= \epsilon^{(0)} + P_e \epsilon^{(1)} + ... \\ u' &= u^{(0)} + P_e u^{(1)} + ... \\ v' &= v^{(0)} + P_e v^{(1)} + ... \\ w' &= w^{(0)} + P_e w^{(1)} + ... \end{aligned}$$

yields to zeroth order

$$\frac{\partial^2 \epsilon^{(0)}}{\partial z'^2} = 0 \quad . \tag{2.22}$$

Integrating this and applying the boundary conditions (2.20) yields

$$\frac{\partial \epsilon^{(0)}}{\partial z'} = 0 \tag{2.23}$$

which shows to zeroth order that density varies only in the horizontal i.e. that density is vertically well mixed, $\epsilon^{(0)}(x', y')$.

At first order in the Peclet number (2.21) is

$$u^{(0)}\frac{\partial \epsilon}{\partial x'}^{(0)} + v^{(0)}\frac{\partial \epsilon}{\partial y'}^{(0)} = \frac{\partial^2 \epsilon}{\partial z'^2}^{(1)} \quad . \tag{2.24}$$

$u^{(0)}$ and $v^{(0)}$, the dominant horizontal velocities are the same as the velocities $u'$ and $v'$ which occurred in the development of the ATW model in (2.6). Depth integration of (2.24) together with the boundary conditions (2.20) and the definitions for transport (2.8a) and (2.8b) yields

$$U'\frac{\partial \epsilon}{\partial x'}^{(0)} + V'\frac{\partial \epsilon}{\partial y'}^{(0)} = 0 \quad . \tag{2.25}$$

Thus contours of total transport and density are parallel for this vertically well mixed flow. Using (2.14) the advective density equation (2.25) can be rewritten dimensionally as the Jacobian

$$J(\psi, \epsilon) = 0 \quad . \tag{2.26}$$

This illustrates a very important point; namely that, in the vertically well mixed flow described above, density is conserved as it is advected along streamlines. This conservation can be exploited by noting that the Jacobian (2.26) implies that density must be a function of the streamfunction, i.e.

$$\epsilon = \mathcal{F}(\psi) \quad . \tag{2.27}$$

If the values of $\psi$ and $\epsilon$ are known along some line, then their functional relation may be determined. Because of (2.26) this functional relation is the same in all regions of the domain containing streamlines which cross the line on which $\psi$ and $\epsilon$ are prescribed.

## 2.2a Streamfunction Flow Equation

Combining the dynamical equation (2.15) and the density equation (2.27) yields an equation in one variable

$$\frac{r}{f}\frac{\partial}{\partial x}\left(\left(\frac{1}{h^2}+\frac{g}{2f}\frac{\mathrm{d}\mathcal{F}}{\mathrm{d}\psi}\right)\frac{\partial\psi}{\partial x}\right)+h_x\left(\frac{1}{h^2}+\frac{g}{2f}\frac{\mathrm{d}\mathcal{F}}{\mathrm{d}\psi}\right)\frac{\partial\psi}{\partial y}=0 \tag{2.28}$$

where $\mathcal{F}$ is determined from the boundary conditions appropriate to the particular problem being studied. This equation is in general non-linear, however for simplicity attention will be restricted to problems where the boundary conditions are such that density is linearly proportional to streamfunction, i.e.

$$\frac{\mathrm{d}\mathcal{F}}{\mathrm{d}\psi}=K \tag{2.29}$$

where $K$ is a constant. Then (2.28) becomes

$$\frac{r}{f}\frac{\partial}{\partial x}\left(\left(\frac{1}{h^2}+\frac{gK}{2f}\right)\frac{\partial\psi}{\partial x}\right)+h_x\left(\frac{1}{h^2}+\frac{gK}{2f}\right)\frac{\partial\psi}{\partial y}=0 \quad . \tag{2.30}$$

$K$ is determined by the values of density and streamfunction given on the boundaries. Prescribing $\psi$ on the boundary fixes the sum of the geostrophic and frictional ageostrophic transports across the boundary.

To understand what $K$ physically represents, the flow's surface and bottom geostrophic velocities must be examined. The surface geostrophic velocities are

$$\begin{aligned} u_s=-\frac{g}{f}\eta_y &= \tfrac{-1}{h}\tfrac{\partial\psi}{\partial y}+\tfrac{r}{fh^2}\left(1+\tfrac{gh^2K}{2f}\right)\tfrac{\partial\psi}{\partial x} \\ v_s=\frac{g}{f}\eta_x &= \tfrac{1}{h}\left(1-\tfrac{gh^2K}{2f}\right)\tfrac{\partial\psi}{\partial x} \end{aligned}$$

Taking the difference between surface and bottom geostrophic velocities ((2.16a) and (2.16b) and dividing by the depth averaged velocity yields the same ratio for each component

$$\frac{u_s-u_b}{-\frac{1}{h}\frac{\partial\psi}{\partial y}}=\frac{v_s-v_b}{\frac{1}{h}\frac{\partial\psi}{\partial x}}=-\frac{gh^2K}{f} \quad . \tag{2.31}$$

Inspection of this ratio shows that $K$ is positive for bottom intensified flow and negative for surface intensified flow. Hence $K$ is a measure of the vertical shear in geostrophic component of flow relative to the average velocity.

### 2.2b Non-Dimensional Equation

The non-dimensional scaling appropriate for (2.31) is

$$\begin{aligned} y &= L_y y' \\ x &= L_x x' \\ h &= h_0 h' \\ K &= \frac{2f}{g h_0^2} K' \\ \ell &= L_x \ell' \\ \psi &= \psi_0 \psi' \\ \eta &= \frac{f \psi_0}{g h_0} \eta' \end{aligned} \tag{2.32}$$

where $\ell$ is the shelf width, $s$ is the bottom slope, and $h_0 = h_c + s\ell$, $h_c$ being the depth at the coastal boundary. The two terms in (2.31) balance if $L_x$ and $L_y$ are related by the ATW scale relationship

$$L_x = \sqrt{\frac{r}{fs} L_y} \quad . \tag{2.33}$$

Equation (2.31) in non-dimensional form is

$$\frac{\partial}{\partial x'}\left(\left(\frac{1}{h'^2} + K'\right)\frac{\partial \psi'}{\partial x'}\right) + \left(\frac{1}{h'^2} + K'\right)\frac{\partial \psi'}{\partial y'} = 0 \tag{2.34}$$

where the shelf edge is at $x' = \ell'$. The depth profile used has linear topography and a finite depth at the coast $h_c$, i.e. $h = h_c + sx$. The non-dimensional depth profile is

$$h' = h'_c + ax' \tag{2.35}$$

where $a = \frac{sL_x}{h_0}$. The solution depends on three non-dimensional numbers: $K'$ (the shear), $\ell'$ and $a$. The latter two depend on the drag coefficient, latitude and shelf geometry. $\ell'$ may be rewritten

$$\ell' = \frac{\ell}{L_x} = \frac{\ell}{\sqrt{\frac{rL_y}{fs}}} \tag{2.36}$$

and measures the importance of friction, rotation and shelf geometry. $\ell'$ is the width of the shelf in non-dimensional units. Shelves with the same physical width may have different non-dimensional widths and therefore may appear wide or narrow to an oceanic intrusion depending on their bottom slope, drag coefficient and latitude. Hence $\ell'$ is a measure of the shelf "stiffness" to intrusions of flow from the deep ocean. Hence it will be seen that if $\ell'$ is small, as it is for a weak bottom slope or strong frictional drag, then the shelf is very compliant and flow may easily cross topography. Conversely if $\ell'$ is large the shelf is very stiff and resists any attempt of flow to cross topography. For the typical scales in Table 2.1 , $\ell'$ is around 5 and therefore such a shelf is stiff.

Equation (2.35) is a parabolic equation and hence may be solved by "time stepping" towards negative y. To improve computational speed and numerical stability an implicit finite difference scheme is used where a tri-diagonal matrix is inverted to find the solution at each "time" step. In all cases in this section a unit of alongshore distance, $y'$, is equivalent to $50km$ and a unit of cross-shelf distance, $x'$, is equivalent to $15km$ as shown in Table 2.1. The surface displacement and bottom pressure will be calculated numerically for selected examples .

### 2.2c Pressure Calculation

In order to calculate the pressure from the streamfunction the transport equation (2.12b) must be integrated to give the surface displacement which is proportional to surface pressure

$$\eta = -\frac{f}{gh}\left(1 - \frac{gh^2K}{2f}\right)\left(\psi|_{y=0} - \psi\right) + \frac{r}{gh^2}\left(1 + \frac{gh^2K}{2f}\right)\int_y^0 \frac{\partial\psi}{\partial x}dy + \eta|_{y=0} \quad . \tag{2.37}$$

From (2.12a) the surface displacement along $y = 0$ relative to the origin (i.e. assuming $\eta(0,0) = 0$) is

$$\eta|_{y=0} = f \int_0^x \left(1 - \frac{gh^2K}{2f}\right) \frac{1}{gh} \quad \frac{\partial \psi}{\partial x}|_{y=0} \quad dx \quad . \tag{2.38}$$

Using the scales (2.33) the non-dimensional displacement becomes

$$\eta' = -\frac{1}{h'}\left(1 - h'^2K'\right)\left(\psi'|_{y'=0} - \psi'\right)$$

$$+\frac{1}{h'^2}\left(1 + h'^2K'\right)\int_{y'}^0 \frac{\partial \psi'}{\partial x'} dy'$$

$$+\int_0^{x'}\left(1 - h'^2K'\right)\frac{1}{h'}\frac{\partial \psi'}{\partial x'}|_{y'=0} dx' \quad . \tag{2.39}$$

With the hydrostatic relation (2.1) and (2.30) the non-dimensional bottom pressure is

$$p'_b = \eta' + 2h'K'\psi' \quad . \tag{2.40}$$

## 2.3 Deep Ocean Forcing

Three types of shelf forcing by the deep ocean are considered here: a wide inflow, a narrow inflow and forcing by a Gulf Stream Ring.

### 2.3a Wide Inflow

A wide inflow ($1000km$) is assumed to impinge on the edge of the shelf. In order for the Rossby number to remain small compared to the Ekman number as assumed in (2.6) the flow speed must be of order $10cms^{-1}$ or less (see Table 2.1). Boundary conditions for this flow are

$$\psi' = \begin{cases} 0, & 0 < y' \\ y', & y' \leq 0 \end{cases} \qquad \text{at} \quad x' = \ell' \quad .$$

The "initial" condition is that there is no flow across $y = 0$ and no transport through the coast, i.e. that $\psi' = 0$ at $x = 0$. The density boundary conditions are

$$\epsilon' = \begin{cases} 0, & 0 < y' \\ K'y', & y' \leq 0 \end{cases} \qquad \text{at} \quad x' = l' \quad .$$

From these boundary conditions the functional relationship between density and streamfunction required by the advective density equation (2.30) is $\epsilon' = K'\psi'$.

The solution for the wide inflow is shown in Figure 2-2. The shelf region shown is $1000km$ long and $100km$ wide. The interval between solid contours is 0.2. These diagrams show the streamfunction and also the density when scaled by $K'$. In Figures 2-2a and 2-2b $K'$ is negative and hence flow is surface intensified. Figure 2-2c shows the flow pattern for barotropic flow and in Figures 2-2d and 2-2e the flow is bottom intensified. For typical scales given in Table 2.1 the maximum surface displacement is $5cm$ over the $1000km$ width of the inflow, and $K' = 1$ is equivalent to a maximum density anomaly of 0.5 parts per thousand. This series of Figures illustrates that surface intensified flows penetrate the shelf less strongly than bottom intensified flows.

As $K' \to -1$ the cross-shelf scale narrows. As the cross-shelf scale shrinks effects such as horizontal mixing of momentum and density, and flow inertia become important. The first of these neglected process to become order one in its governing equation is the horizontal mixing of density. Its importance is proportional to the square of the actual cross-shelf scale divided by the assumed cross-shelf scale $L_x$ and is order one when the cross-shelf scale is 0.15 of the assumed scale. In Figure 2-5 cross shelf scale as measured by the the 0.2 contour at $y' = -1$, relative to its barotropic value, is plotted against shear. From this it can be seen that the cross-shelf width is not a strong function of shear except when $K'$ approaches $-1$, at which point bottom velocities are zero.

As has been shown, neglected effects are important when the relative cross-shelf scale corresponds to 0.15, but may be neglected when the relative scale is 1. The relative cross-shelf scale of $\frac{2}{3}$ is arbitrarily selected to be the lower limit for applicability of this wide inflow model. Thus, from Figure 2-5, $K' = -0.9$ is the lowest value of shear to which this model may be applied.

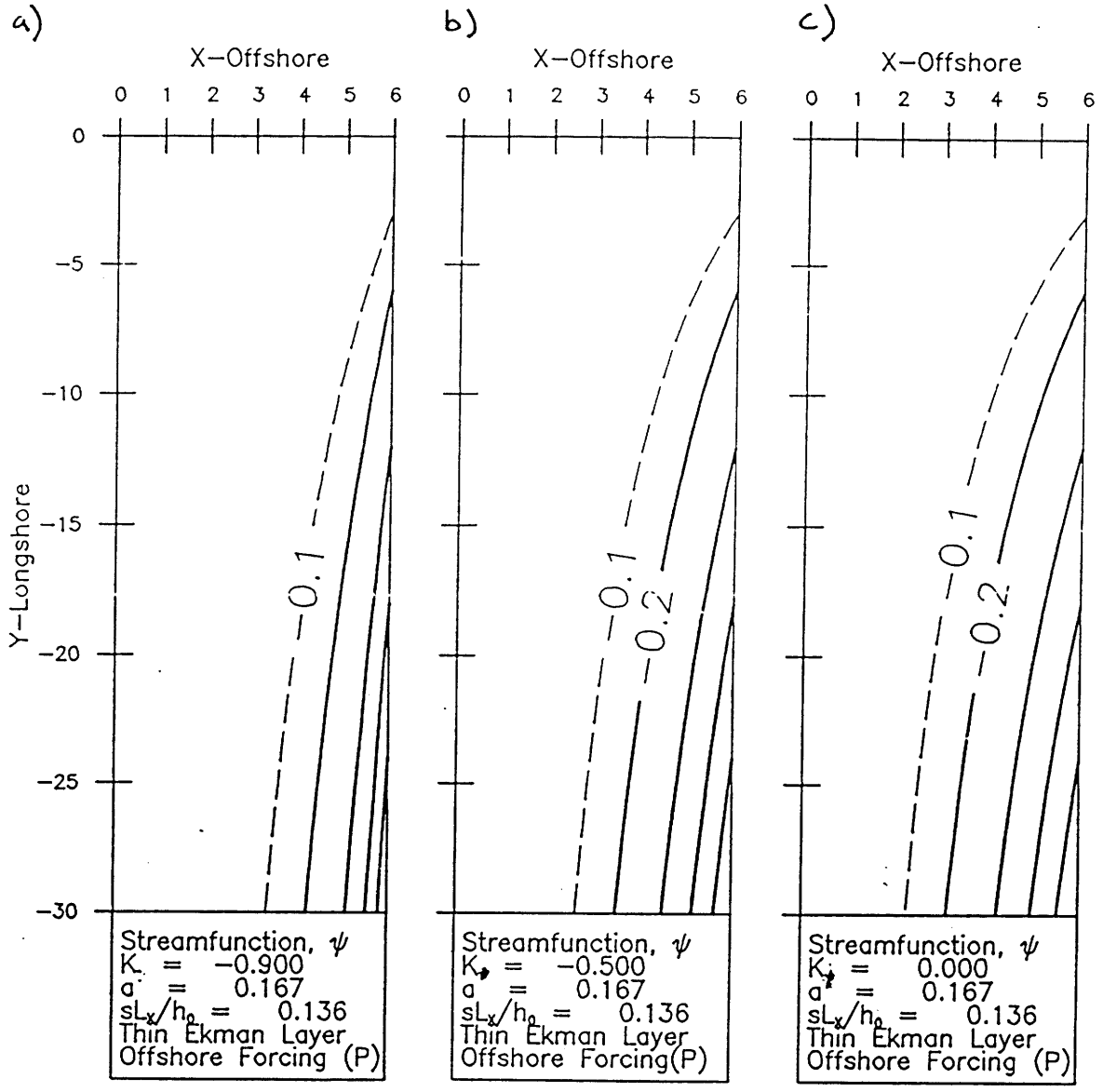


Figure 2-2: Full field solutions for a wide inflow of unit transport onto the shelf. This figure shows total transport streamlines for various degrees of vertical shear. Note that contours also represent the density distribution since $\epsilon = K\psi$. The solid contours are 0.2 apart. For our typical scales the region shown corresponds to a $90km$ wide shelf $1000km$ long. a) $K' = -0.9$. A surface intensified flow penetrates the shelf poorly. b) $K' = -0.5$. c) $K' = 0$. A barotropic flow.

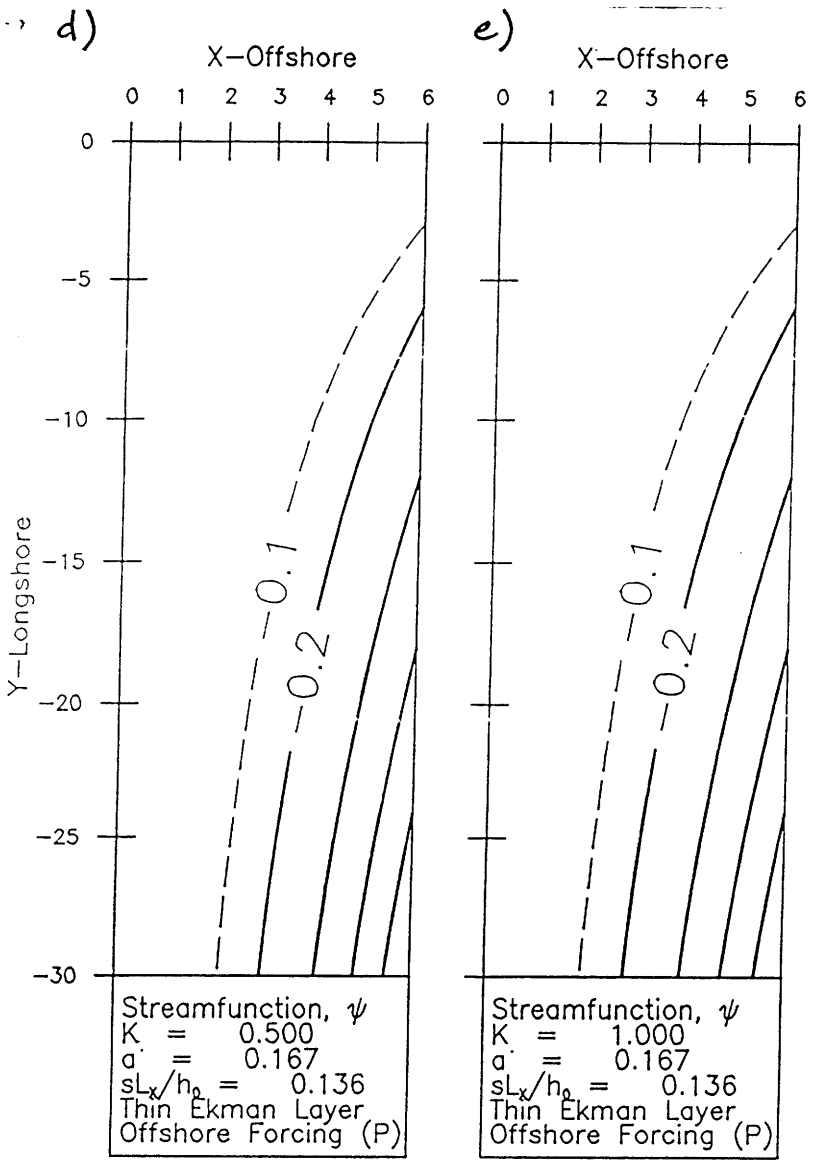


Figure 2-3: Figure 2-2 continued d) $K' = 0.5$. e) $K' = 1$. This series of figures shows that the cross-shelf penetration of flow is enhanced by increasing bottom intensification.

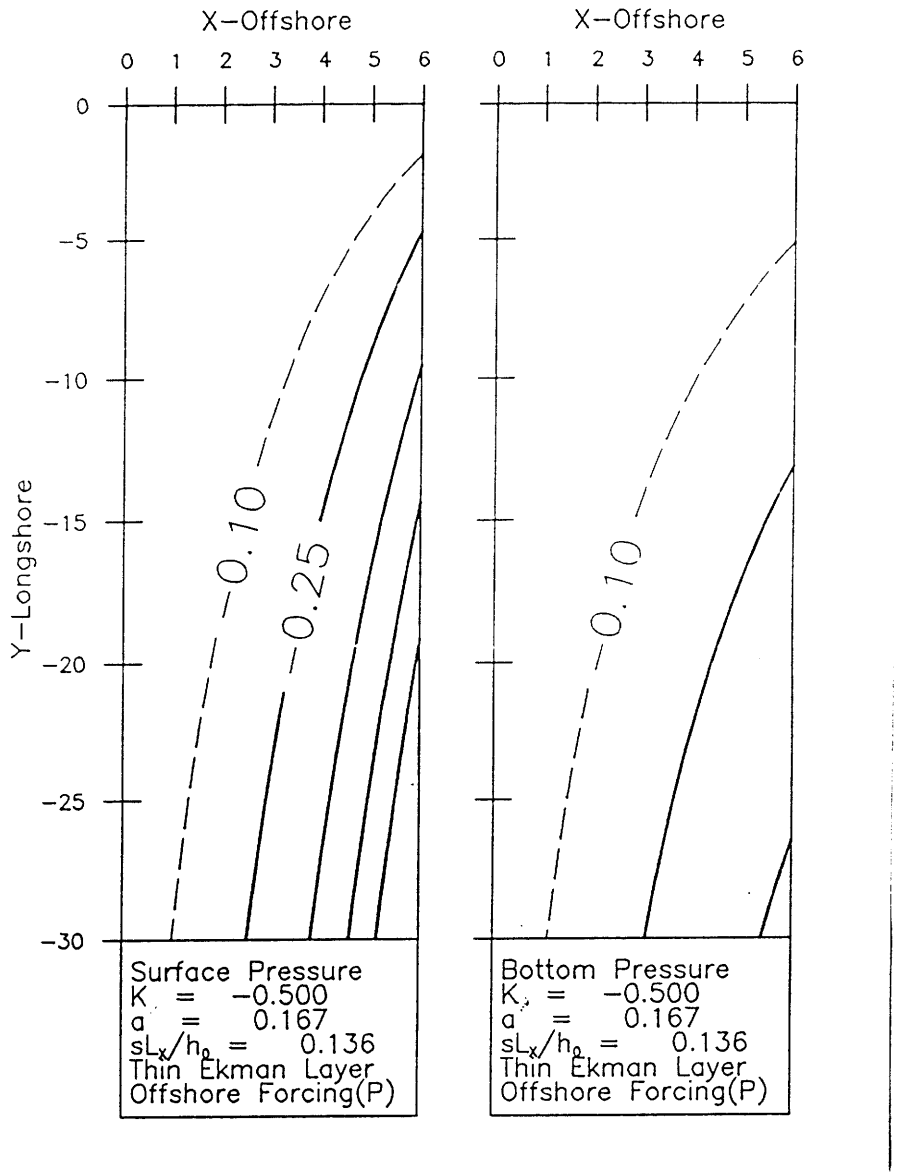


Figure 2-4: Pressures for $K' = -0.5$ corresponding to the streamfunction shown in Figure 2-2b. Solid contour spacing is 0.25. a) Surface displacement /surface pressure. b) Pressure at the bottom ($z = -h$).

As $K'$ gets very large the flow becomes strongly bottom intensified, however, even if the surface velocity is zero, bottom velocities become too large for the Rossby number to remain small compared to the Ekman number and (2.6) is violated. This can be avoided by setting an upper limit for $K'$ of 1.

Surface and bottom pressures for a surface intensified flow ($K' = -0.5$) are shown in Figure 2-4. As the flow is surface intensified the surface pressure signature penetrates farther across the topography than the bottom pressure signature.

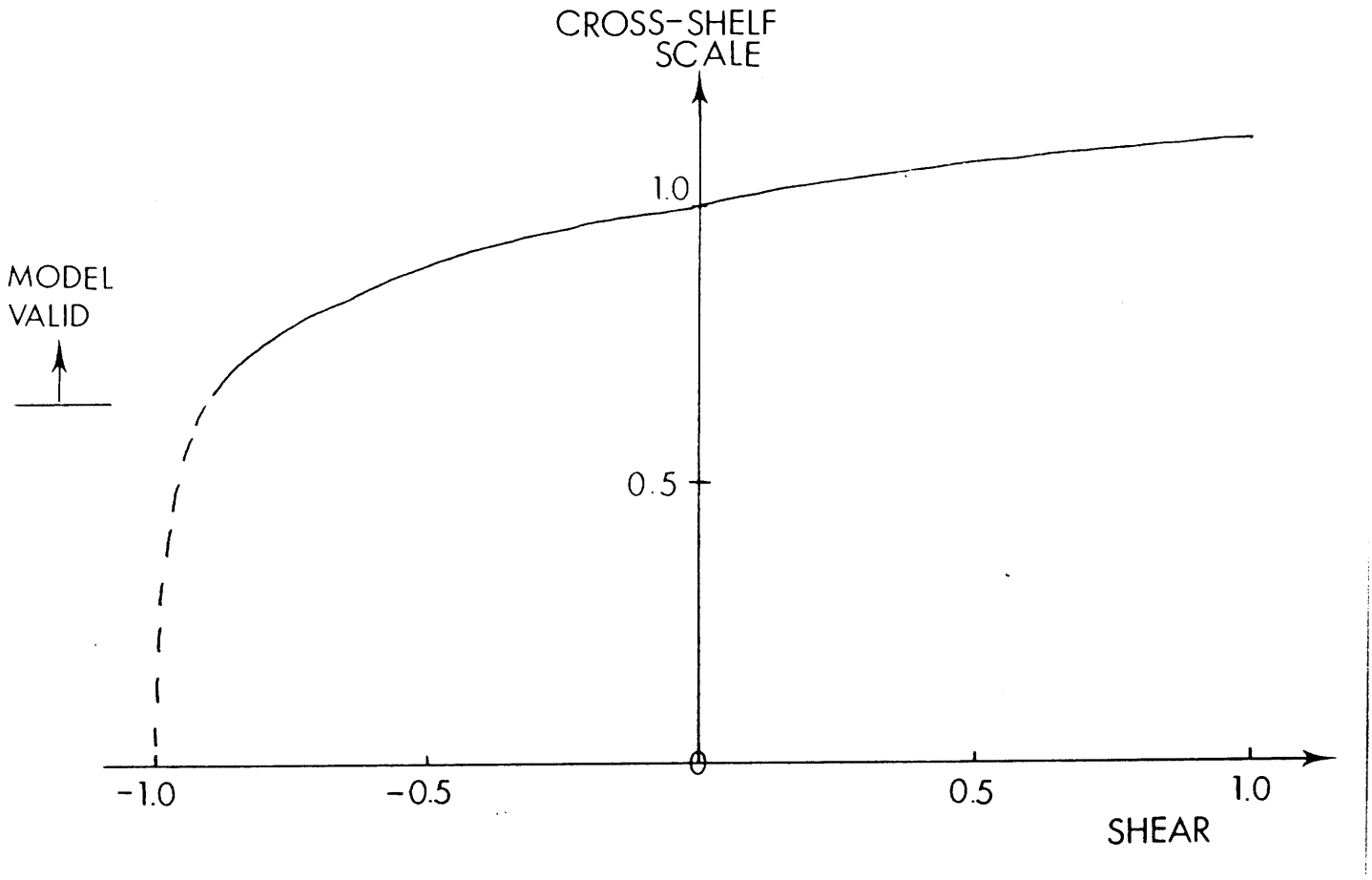


Figure 2-5: Cross-shelf scale as a function of shear. The scale is defined by the point at which the 0.2 contour crosses $y = -20$ $(1000km)$, relative to the cross-shelf scale of a barotropic flow ($K = 0$). Cross-shelf scale is not a strong function of shear except near the point where bottom velocities are zero ($K = 0$). Model is only valid for cross-shelf scales which are large enough that all neglected effects remain small (see text).

### 2.3b Ring Forcing

An extension of this deep ocean inflow model can be used to illustrate the effect on the shelf of a glancing blow by the outer edge of a Gulf Stream Ring. Warm Core Gulf Stream Rings formed offshore are known to propagate westward until they collide with the Gulf Stream or the continental shelf. This Ring forcing model will be used to demonstrate that rings have little effect on the shelf. Rings are vertically homogeneous to at least $100m$ (Joyce (1984)). Assuming that the time scale of frictional decay is short compared to the rate of ring propagation, so that shelf flow induced by a ring might be considered quasi-steady, then this model may be appropriate. An idealistic representation of a ring glancing against the shelf is a linear peak in streamfunction and density imposed at the shelf edge. The boundary conditions used are as follows

$$\psi = \begin{cases} 0 & 0 < y' \\ y', & -1 < y' \leq 0 \\ -(2+y) & -2 < y' \leq -1 \\ 0 & y' \leq -2 \end{cases} \qquad at \quad x' = \ell'$$

and

$$\epsilon = \begin{cases} 0 & 0 < y' \\ K'y', & -1 < y' \leq 0 \\ -K'(2+y) & -2 < y' \leq -1 \\ 0 & y' \leq -2 \end{cases} \qquad at \quad x' = \ell'$$

For an anti-cyclonic flow $K' < 0$ corresponds to a Warm Core Ring. Cold Core Rings which occur to the south of the Gulf Stream are cyclonic and also correspond to $K' < 0$. Flow patterns for a warm, an isothermal and a cold core cyclonic ring are shown in Figure 2-6. Warm Core Rings have a weaker influence on the shelf than isothermal rings because they are surface intensified and experience a weaker bottom drag. Figure 2-7 shows that for surface intensified flows the surface pressure has a wider cross-topography scale than the bottom pressure.

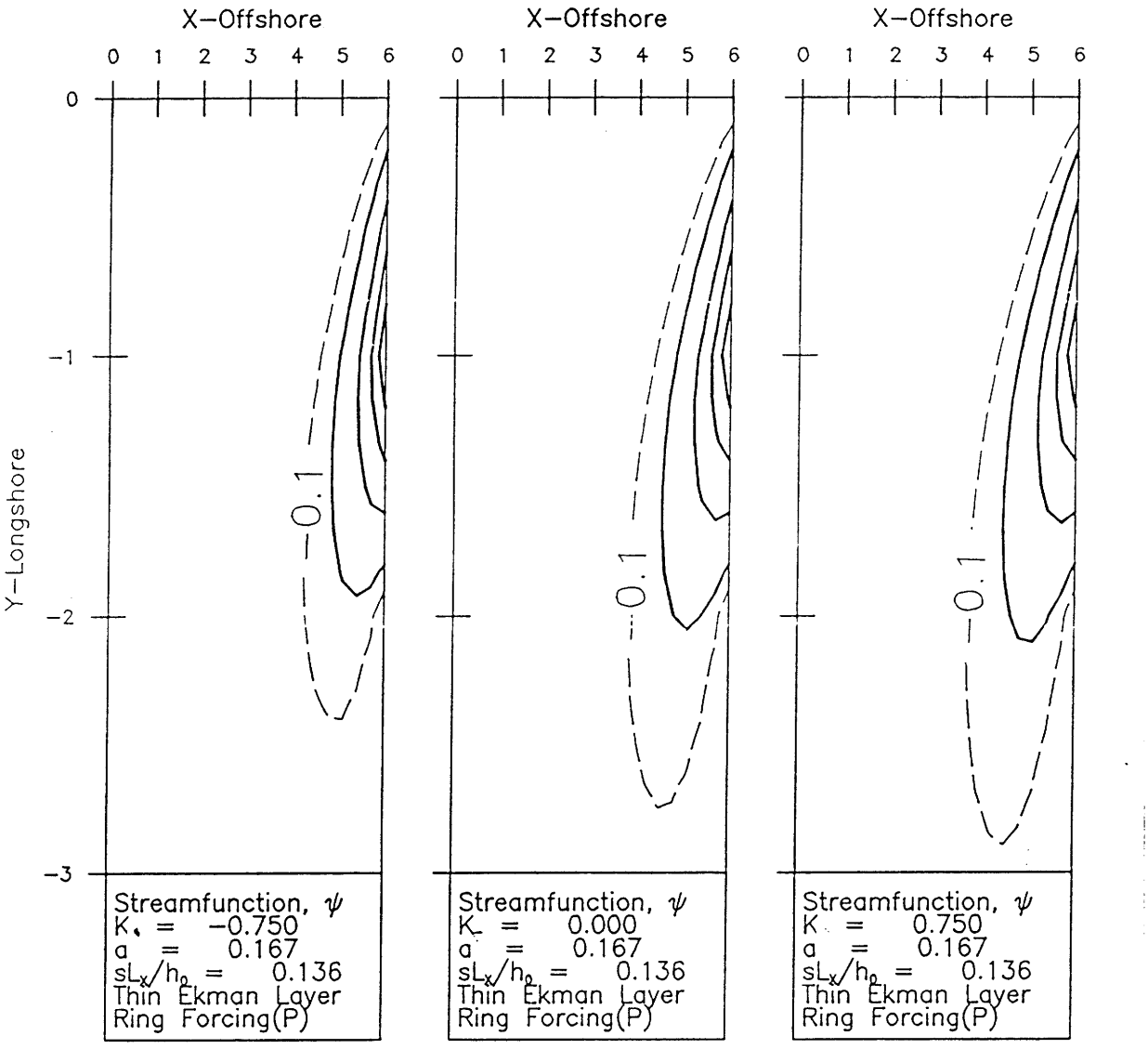


Figure 2-6: Transport streamlines for varying degrees of vertical shear in the flow which enters the shelf between $y' = -1$ and $y' = 0$ and leaves the shelf between $y' = -2$ and $y' = -1$. This example is intended to show the effect on the shelf of the outer edge of a $100km$ diameter Gulf Stream Ring. Solid contour spacing is 0.2. The contours also give the density. The alongshore extent of these figures is $150km$ for typical scales. a) $K' = -0.75$. A surface intensified flow penetrates the shelf poorly. b) $K' = 0$. A barotropic flow. c) $K' = 0.75$.

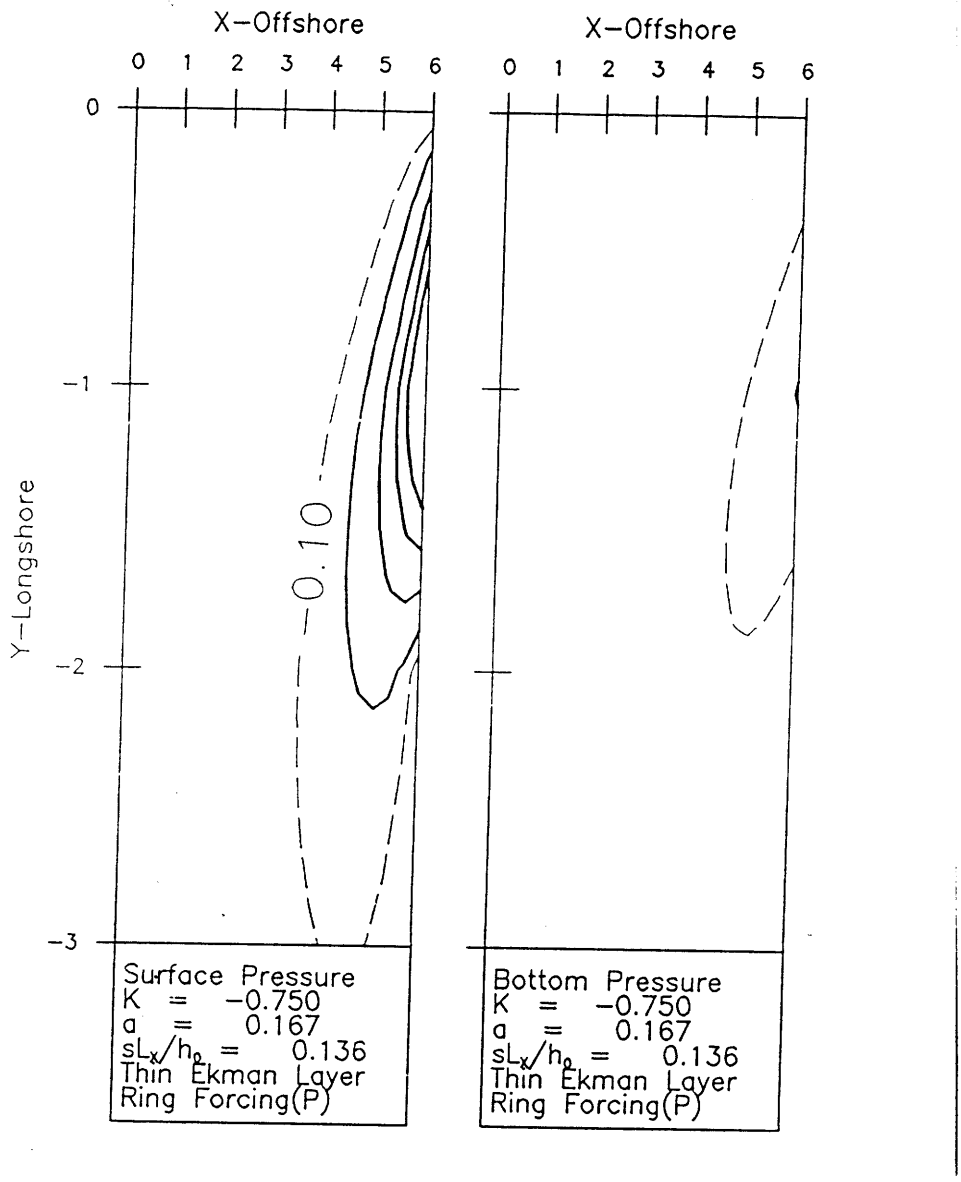


Figure 2-7: Pressures for $K' = -0.75$ for the Gulf Stream Ring streamfunction solution shown in Figure 2-6. Solid contour spacing is 0.25. a) Surface displacement and surface pressure. b) Pressure at the bottom ($z = -h$). As the flow is surface intensified ($K' < 0$) surface pressures are larger than bottom pressures.

### 2.3c Narrow Deep Ocean Inflow

This example illustrates the effects of different offshore boundary conditions on the cross-shelf penetration of flow from the deep ocean.

At forced latitudes flow is forced onto the shelf across $x' = \ell'$ between $y = 0$ and $y = -1$. Thus the offshore boundary conditions are

$$\psi' = \begin{cases} 0, & 0 < y' \\ y', & -1 < y' \leq 0 \end{cases} \qquad at \quad x' = \ell' \tag{2.41}$$

and $\psi' = 0$ at the coast. Since the inflow from the deep ocean has finite width, the choice of boundary conditions at the offshore edge at unforced latitudes has a significant effect on the flow pattern. Three different boundary conditions are considered.

The first boundary condition applied to the unforced latitudes is that for channel flow, i.e.

$$\psi' = -1 \qquad for \quad y' < -1 \qquad at \quad x' = \ell' \quad .$$

This boundary condition constrains the flow to remain on the shelf and ultimately motion will be parallel to the shelf edge. The solution is shown in Figure 2-8a.

The second boundary condition requires that there be no geostrophic transport across the shelf edge. If the deep ocean has no surface displacement and has a weak alongshore gradient of density at the shelf edge then, through the thermal wind relation, geostrophic transport is fixed onto the shelf. From the alongshore transport equation (2.12b) and using (2.30) this boundary condition may be stated

$$\frac{\partial \psi}{\partial y} = \frac{r}{f}\left(\frac{1}{h} + \frac{ghK}{2f}\right)\frac{\partial \psi}{\partial x} \qquad at \quad x = \ell \qquad and \quad y < -1 \quad . \tag{2.42}$$

The solution for this second boundary condition is shown in Figure 2-8b and is very similar to the channel solution in Figure 2-8a. This is understandable because frictional transports are weak in deep water so that fixing the total transport to be zero is almost equivalent to fixing the geostrophic transport to be zero.

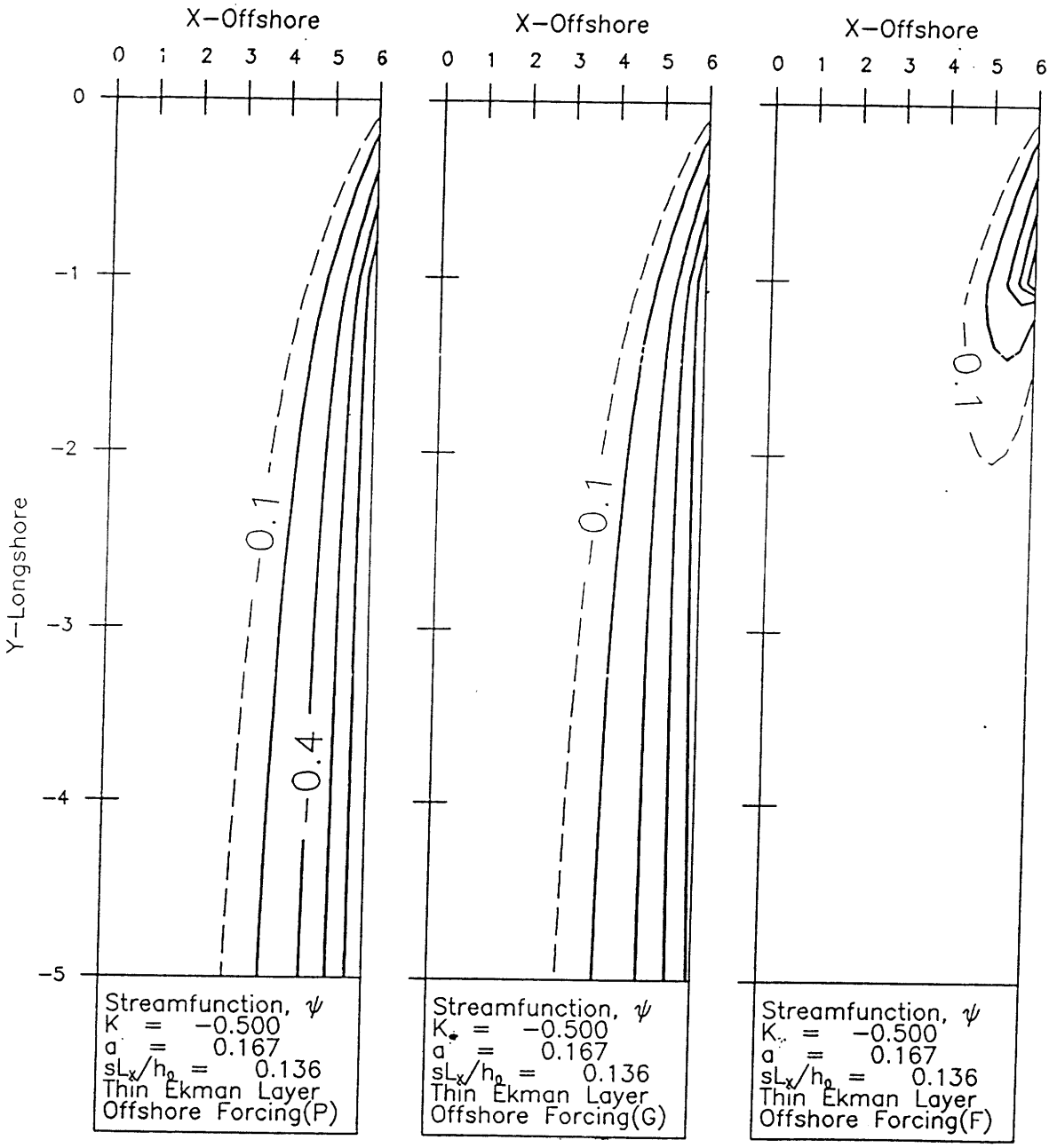


Figure 2-8: Comparison of three boundary conditions for an inflow from the deep ocean. Flow enters the shelf between $y = -1$ and 0 where, in each case, the streamfunction is prescribed to be a linear function of $y$. In the region $y < -1$ a different boundary condition is applied to the offshore edge for each Figure. Solid contour spacing is 0.2. a) Prescribed boundary condition, $\psi = -1$. b) Zero geostrophic flow across shelf edge. c) Flux boundary condition, $\left(\frac{1}{h'^2} + K'\right) \frac{\partial \psi'}{\partial x'} = \psi'$.

The third boundary condition used is to apply the open boundary condition (2.44) developed in Section 2.4 to unforced latitudes along $x' = \ell'$. The solution shown in Figure 2-8c is quite different to that for the previous two boundary conditions because inflow can return rapidly to the deep ocean. The flow rapidly leaves the shelf indicating that, unless fluid is forced to remain on the shelf, it will rapidly return offshore.

## 2.4 Nearshore Forcing

Although the primary focus here has been on the forcing of the shelf by the deep ocean this model is also applicable to flow forced from boundaries other than the offshore, for example that entering the shelf as a river at the coast. Before examining forcing by a river outflow and an alongshore jet, an appropriate boundary condition for the outer edge of the shelf which is now open to the deep ocean is developed.

### 2.4a Open Shelf Edge Boundary Condition

For a flow that enters the shelf near to shore the appropriate offshore boundary condition is $\psi' \to 0$ as $x' \to \infty$. The domain of the numerical solution is finite, therefore a boundary condition at the open boundary, $x' = \ell'$ should be developed which mimics the effect of an infinitely wide shelf. Equation (2.35) is similar to that governing heat conduction in a wide bar of thickness $(\frac{1}{h'^2} + K')$. The $\frac{1}{h'^2}$ term is large near the coast so that the bar does not necessarily have the same temperature across its thickness. This diffusion across the thickness of the bar should be included. Although not a perfect analogy the solutions to (2.35) can be assumed to have at least some of the character of a heat conduction problem. In the heated bar problem the region far from $x = 0$ acts as a sink for heat which enters the bar at $x = 0$ where the temperature, $\psi'$, is prescribed. One way to mimic this sink in a bar of finite length is to take the end boundary condition to be radiation of heat into a medium at a temperature of zero, i.e. to take the flux out of the end proportional to the temperature at the end (see Carslaw and Jaeger (1959)). The flux crossing $x' = \ell'$ is the product of the temperature gradient and bar thickness at that point, thus the open boundary condition may be stated

$$\left(\frac{1}{h'^2} + K'\right)\frac{\partial \psi'}{\partial x'} \qquad \propto \qquad \psi' \qquad at \qquad x' = \ell' \quad . \tag{2.43}$$

For simplicity the constant of proportionality is arbitrarily assumed to be unity. It will be shown such an assumption gives reasonable results . This boundary condition

behaves in the correct sense for changes in flow density. Bottom intensified flow, $K' > 0$, crosses the topography more easily than barotropic flow. In this case the area of the end of the bar is larger than when $K' = 0$ and hence heat may leave the end of the bar more easily. This is consistent with the ease with which bottom intensified flows cross topography.

When $K' < 0$ the above open boundary condition tends to impede heat (and by analogy, flow) from leaving the domain, which is consistent with the increased difficulty which surface intensified flows have in crossing topography. When $K' = -1$ the boundary condition becomes $\psi' = 0$ at the offshore edge and hence acts like a channel. For offshore forcing, at the limit $K' = -1$, no flow may enter the shelf because the bottom velocities of the flow are zero. The converse of this non-penetration is that flow on the shelf cannot cross the line where bottom velocities are zero. The above boundary condition correctly blocks flow from leaving the shelf when $K' = -1$. In conclusion, this boundary condition has a behavior which is completely consistent with the nature of the solutions to our density driven flow model and therefore should not greatly affect the nature of the solutions obtained for the shelf region.

The sensitivity of the solutions to the open boundary condition (2.44) can be tested by comparing a solution to that obtained with twice the shelf width. If this boundary condition has only a weak effect then the two solutions should be very similar. The solution to the river inflow problem for $K' = 0.75$ is shown in Figure 2-9a for a shelf 6 units wide and in Figure 2-9b for a shelf 12 units wide. The details of the solution will be given later. Note by comparing Figures 2-9a and 2-9b that doubling the shelf width has little effect on the point where the 0.1 and 0.2 contours cross $x = 6$ and that the 0.4 contour has moved only 1 unit across the shelf at $y' = -10$. From this demonstration it can be seen that the open boundary condition influences the interior only weakly for distances of up to 10 units of $y'$ along the coast (equivalent to $500km$) when the offshore edge is at $x' = 6$. The influence of the offshore boundary increases for larger distances along the shelf. If the shelf were infinitely wide then as $y$ goes to negative infinity, i.e. in the far field, the streamfunction in the nearshore region would tend to

its value at the coast. In the examples for nearshore forcing this value is unity. The far field solution of (2.31) when the "heat radiation" boundary condition is applied at the edge of a finite width shelf is the rather complicated expression

$$\psi'(x') = 1 \quad + \quad \frac{1}{1 - \int_0^{l'} \frac{h'^2}{1+K'h'^2}} \quad \int_0^{x'} \frac{h'^2}{1+K'h'^2} dx'$$

which is not unity. Therefore (2.44) is a reasonable mimic of an open boundary condition only for moderate distances from the flow's source because it cannot give the correct far field behavior.

Real shelves are not infinitely wide. The steep continental slope has a tendency to block flow from leaving the shelf. This can be seen in the relationship between horizontal scales (2.34). When the bottom slope is large the cross-shelf scale is reduced and the flow follows the isobaths more closely. Therefore fluid crossing from a gently sloping shelf to the steep continental slope will turn to follow the topography. This effect will not be included in the offshore boundary condition used here but it should be kept in mind that a more realistic boundary condition might have a proportionality constant in (2.44) greater than unity.

### 2.4b Coastal Outflow

River deltas and estuaries inject a plume of fresh water onto the shelf. These coastal outflows are idealized as a band of transport entering the shelf at the coast between $y' = 0$ and $-1$ with a density extremum at $y' = -b$. In order that horizontal advection of density remain small compared to vertical mixing flow speed in this outflow model is restricted to be of order $2cms^{-1}$ or less. The boundary conditions for an outflow are

$$\psi = \begin{cases} 0 & 0 < y' \\ -y', & -1 < y' \leq 0 \\ 1, & y' \leq -1 \end{cases} \qquad \text{at } x' = 0 \quad . \tag{2.44}$$

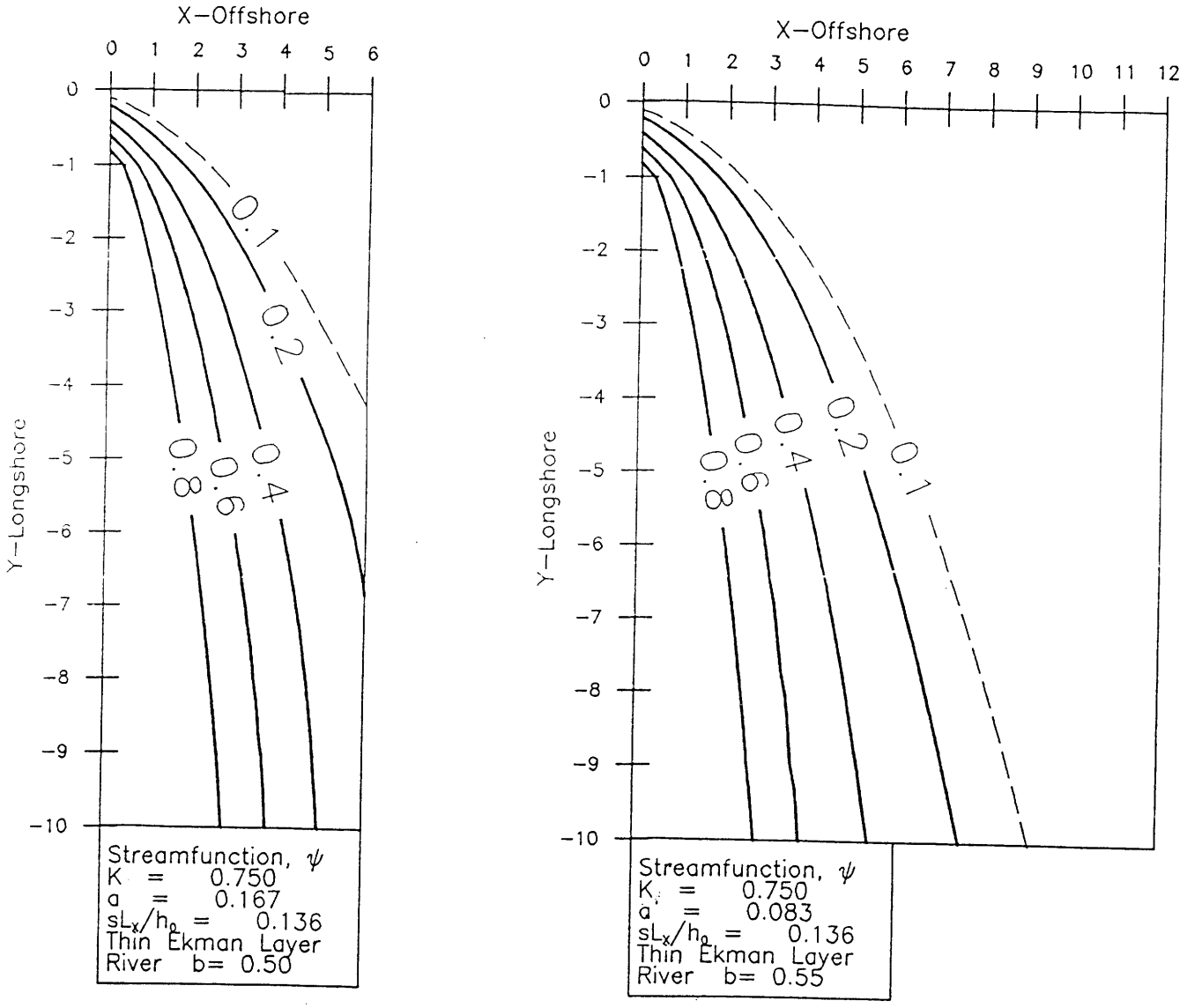


**Figure 2-9:** Test of the open boundary condition $\left(\frac{1}{h'^2} + K'\right) \frac{\partial \psi'}{\partial x'} = \psi'$. a) Solution for 6 unit wide shelf. b) Solution for 12 unit wide shelf differs only slightly for narrower shelf for moderate alongshore distances, (up to 10 units / $500km$).

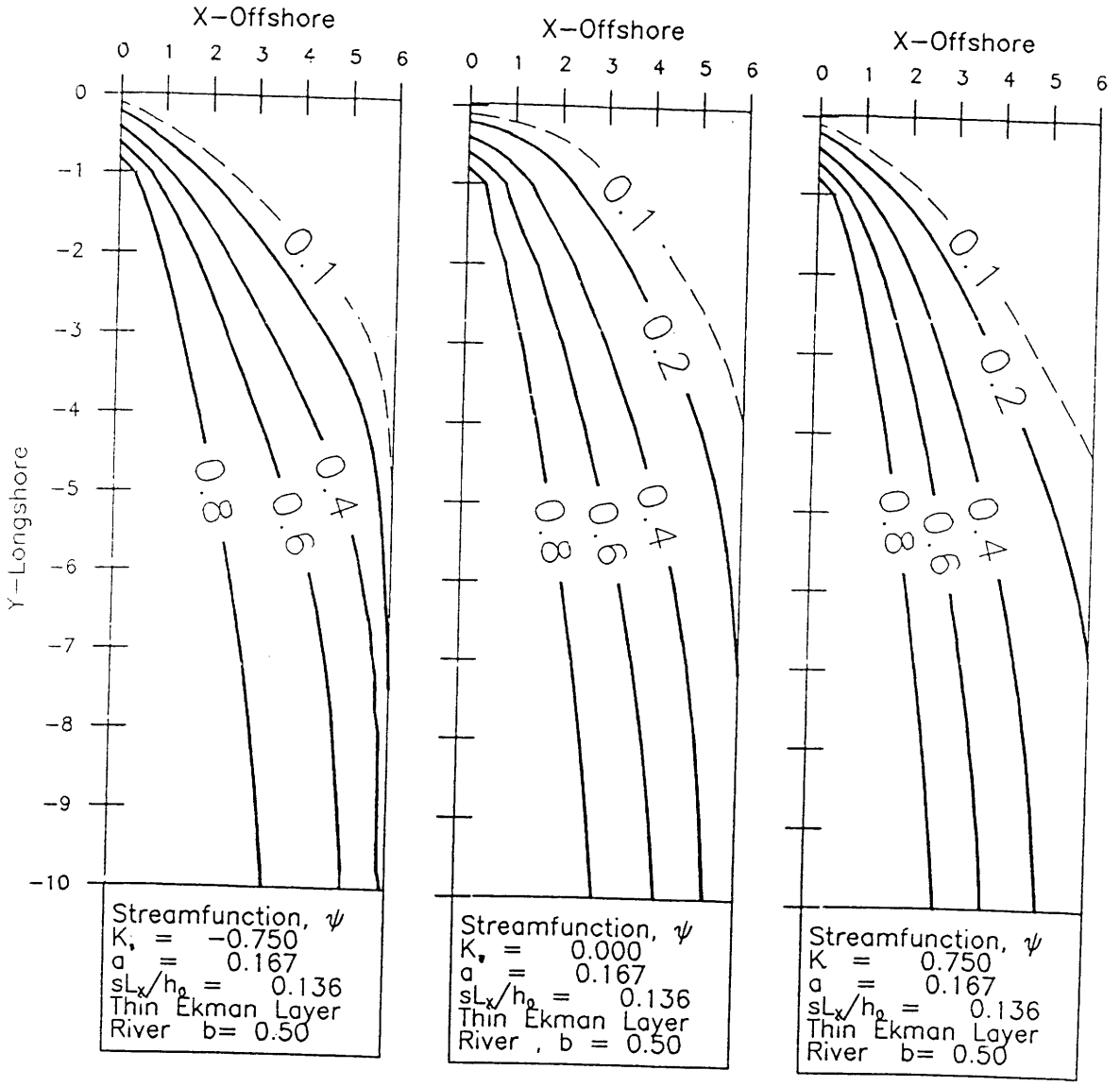


Figure 2-10: Flow induced by coastal river source. Transport streamlines for varying degrees of vertical shear in the flow which enters the shelf between $y' = -1$ and $y' = 0$ at the coast. Density has a extremum at the center of the inflow and along the streamline $\psi = \frac{1}{2}$ . The alongshore extent of these figures is $500km$ for typical scales. a) A river with a light water core, $K' = -0.75$ , surface intensified. b) A constant density river, barotropic flow. c) A river with a heavy core, $K' = 0.75$. A fresh water river, ($K' < 0$), will cross topography less strongly than a barotropic or heavy river outflow.

The density boundary condition is

$$\epsilon = \begin{cases} 0 & 0 < y' \\ -\frac{y'}{2b}K', & -b < y' \leq 0 \qquad \text{at } x' = 0 \\ \frac{1}{2}(1 + \frac{y'+b}{1-b})K', & -1 < y' \leq -b \\ 0, & y' \leq -1 \end{cases} \tag{2.45}$$

chosen so that the maximum density anomaly, $\frac{K'}{2}$, is independent of its position. The density field has its extremum along the streamline $\psi = b$. If $K' < 0$, then the outflow has a core of light water, if $K' > 0$, then the core is heavy relative to shelf water.

The value of $\frac{d\mathcal{F}}{d\psi'}$ on a particular streamline depends on where that streamline originated. Hence the function $\frac{d\mathcal{F}}{d\psi'}$ is discontinuous

$$\frac{d\mathcal{F}}{d\psi'} = \begin{cases} 0 & \psi' = 0 \\ \frac{1}{2b}K' & 0 < \psi' \leq b \\ -\frac{1}{2(1-b)}K' & b < \psi' < 1 \\ 0, & \psi' = 1 \end{cases} . \tag{2.46}$$

If the flow is bottom intensified on one side of the density extremum it will be surface intensified on the other and vice versa. In calculating the solution numerically it is necessary to ascertain whether the value of $\psi'$ is greater or less than $b$ in order to determine whether to replace $K'$ with $\frac{1}{2b}K'$ or $-\frac{1}{2(1-b)}K'$ in equation (2.35) and in the boundary condition (2.44).

This example for $K < 0$ is intended as an idealization of the fresh water outflow of the river Po into a Northern Adriatic which has been vertically well mixed by winter winds.

Solutions for various values of $K'$ are shown in Figure 2-10 for a flow with its density extremum at the middle of the inflow ($b = \frac{1}{2}$). This figure shows that the 0.8 contour moves slightly offshore as the density is changed from a light water to heavy water outflow while a large variation is seen in the 0.1 and 0.2 contours which are much farther offshore in the heavy outflow than in the light outflow. Equation (2.32) shows that the shear depends on both $K'$ and the water depth, because forces on a flow due

to horizontal density variation increase with the depth of the water for the same shear. Therefore the overall response of the outflow depends on whether the flow is surface or bottom intensified in the deep water region offshore of the density extremum. For the heavy water outflow in Figure 2-10c the flow is bottom intensified offshore of the extremum and therefore the outflow ought to be more widely distributed across the shelf than the light water outflow of 2-10a.

The blocking of flow from leaving the region due to small bottom velocities at $x = \ell'$ is evident in Figure 2-10a.

The solutions for the same shear but different positions of the density maximum are shown in Figure 2-11. In Figure 2-11a the maximum is on the left, facing downstream, ($b = 0.25$), and in Figure 2-11b, it is on the right ($b = 0.75$). Even though the density anomaly is the same for both cases the outflow with the density maximum on the left expands across the topography slightly slower than the outflow with the maximum on the right. The flow in the region offshore of the density maximum is bottom intensified and hence any increase in its size will tend to enhance the expansion of the flow across the shelf. The converse is true for a light outflow. Moving the density maximum from the left to the right side increases the proportion of shelf area where the flow is bottom intensified, and thus will cause flow to expand more rapidly across the shelf.

Therefore the rate at which an outflow expands across the shelf depends on both the magnitude of its density anomaly and, to a lesser extent, on the position of the maximum anomaly in the outflow. It is the shear and the size of the region offshore of the density extremum which determine the overall responses of the outflow to the topography.

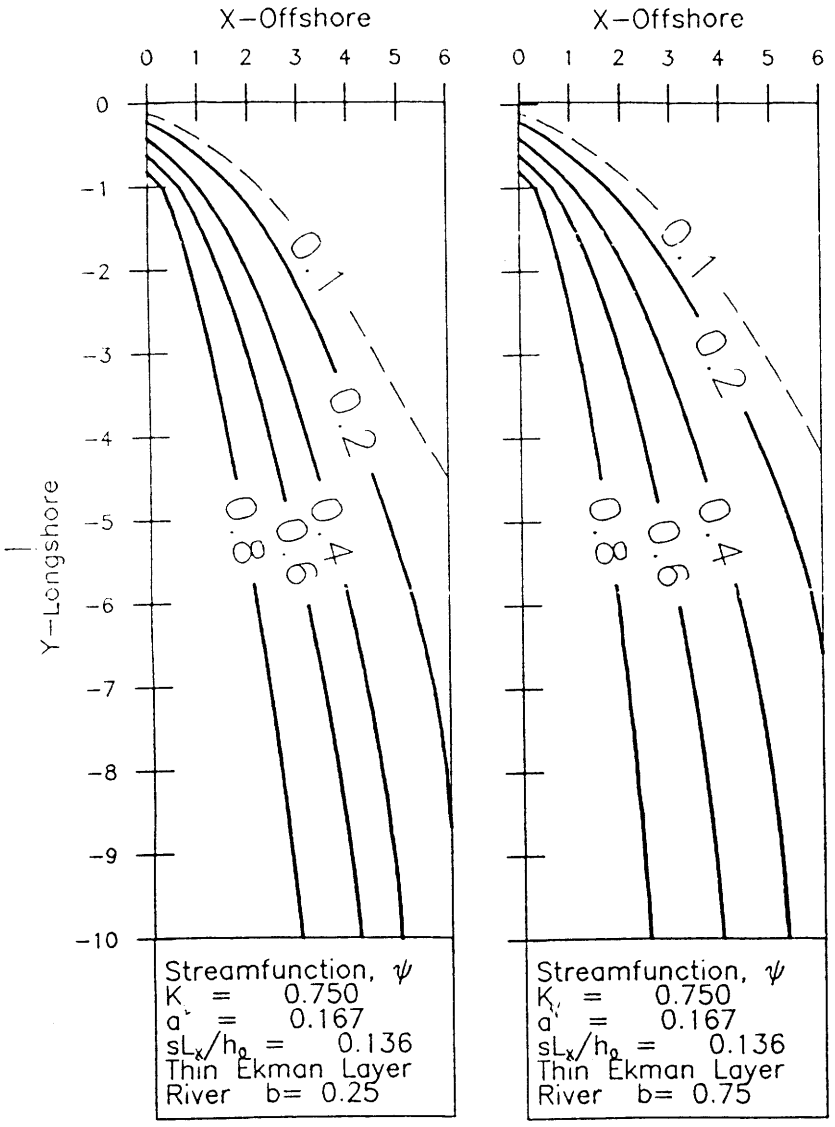


Figure 2-11: Variation in flow pattern due to changes in position of the density extremum in the river inflow. a) Density maximum along 0.25 streamline. b) Maximum along 0.75 streamline. The flow for a density maximum at the middle of the inflow is shown in Figure 2-10c.

### 2.4c Alongshore Jet

A coastal jet may have a density different from the waters immediately offshore of it. This example is intended to suggest how density may alter the flow pattern of a frictionally controlled jet. In order for the scaling (2.6) to be valid flow speeds in the jet must be of order $20cms^{-1}$ or less.

This idealized jet flows across $y = 0$ where density is assumed to vary linearly across the inflow with a density extremum at the coast. The boundary conditions for streamfunction are

$$\psi = \begin{cases} 1 - x & 0 < x' \leq 1 \\ 0, & 1 < x' \qquad \text{at } y' = 0 \end{cases} . \tag{2.47}$$

$\psi = 1$ at $x' = 0$ and the flux boundary condition (2.44) is applied at $x' = 6$. The density boundary at the inflow is

$$\epsilon = \begin{cases} K'(1 - x) & 0 < x' \leq 1 \\ 0, & 1 < x' \qquad \text{at } y' = 0 \end{cases} . \tag{2.48}$$

Solutions plotted in Figure 2-12 are quite similar to those for a coastal outflow (Figure 2-10). Although there is a slight shoreward movement of the 0.8 contour with increasing shear the major variation is in the offshore movement of the 0.1 and 0.2 contours. An alongshore jet which is light relative to its surroundings ($K' < 0$, Figure 2-12a) is surface intensified and hence expands across the shelf more slowly than a barotropic jet. A heavy jet expands across the shelf more quickly than a barotropic flow due to enhanced bottom friction (Figure 2-12 ).

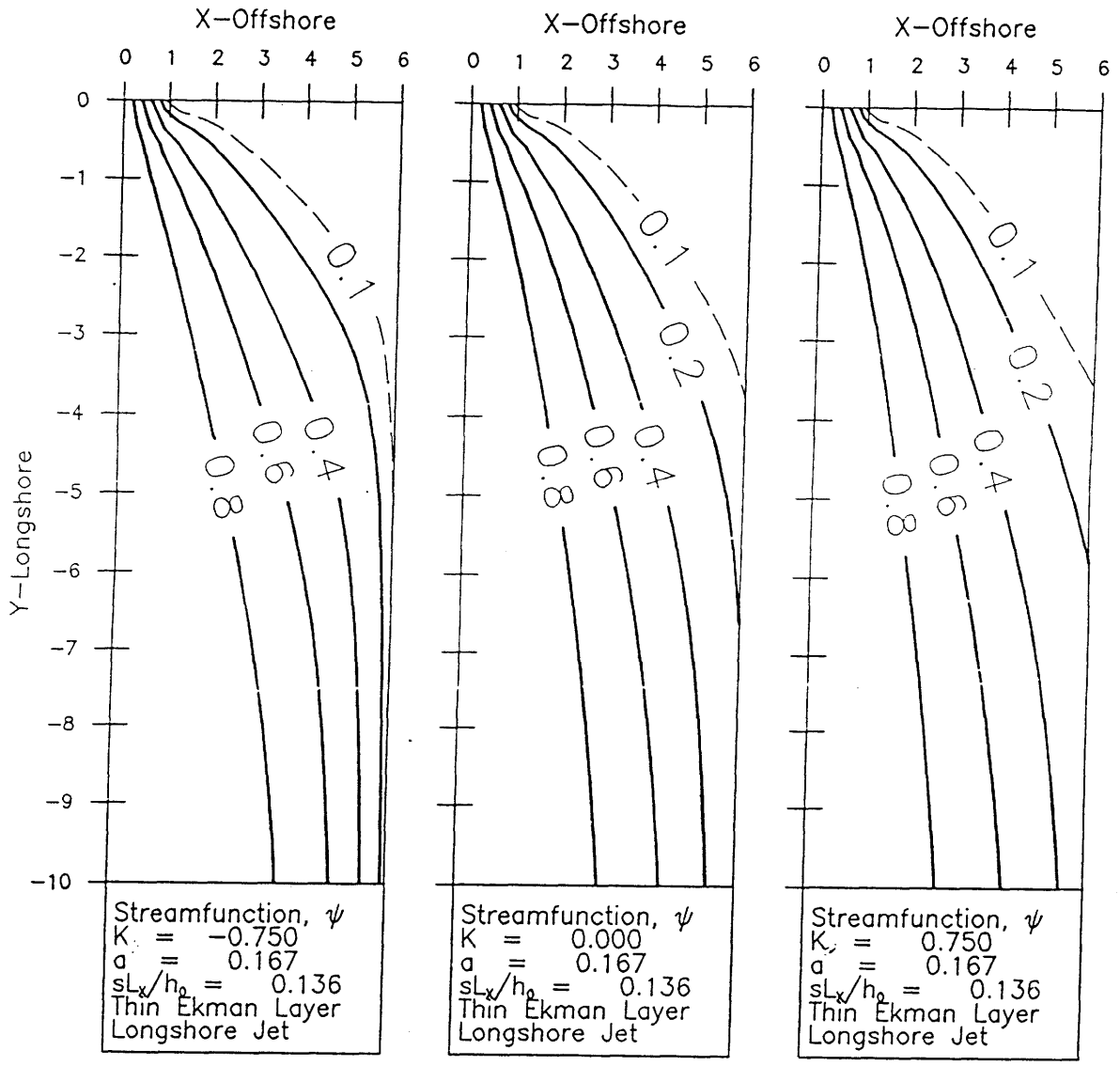


Figure 2-12: Flow induced by a coastal alongshore jet. Transport streamlines and density when scaled by $K$ for varying degrees of vertical shear for a flow which enters the region between $x' = 0$ and $x' = 1$ across $y' = 0$. Density has an extremum at the coast. The alongshore extent of these figures is $500km$ for typical scales. a) A light jet, $K' = -0.75$, surface intensified. b) A constant density jet. c) A heavy jet, $K' = 0.75$, bottom intensified.

## 2.5 Discussion of Well Mixed Advective Flow

In all the examples studied the mechanism by which flow was able to cross topography was bottom friction. The solutions demonstrate that the tendency for flow to follow isobaths is much stronger than the degree to which bottom friction allows cross-isobath motions. For typical scales the deep ocean flow must travel $1000km$ along the shelf in order to penetrate $50km$ across it. The deep ocean inflow forms a horizontal boundary layer against the shelf edge of approximate width given by

$$\delta^x \approx \sqrt{\frac{r\,|y|}{fs}} \quad . \tag{2.49}$$

This is the same result obtained by Wang (1982) for a barotropic deep ocean inflow. The width of this boundary layer, and therefore shelf penetration, is larger if the drag coefficient is higher, the latitude lower or the bottom slope weaker. Vertical shear in horizontal velocity has an effect on the degree of shelf penetration which can be explained by examining the bottom friction felt by the flow.

It has been demonstrated that the deep ocean inflows across-shelf penetration varies with shear in the geostrophic component of flow. To determine the mechanisms behind this variation consider the ATW model which can be derived from (2.12a), (2.12b) and (2.12c) . It can be written using (2.14a) and (2.14b) in the form

$$h_x u_b = \frac{-1}{f}\frac{\partial \tau_b^y}{\partial x} \quad . \tag{2.50}$$

In this equation there is balance between the cross-shelf motion of the geostrophic component of flow and the divergence of the bottom stress. As bottom stress is assumed proportional to the along shelf bottom geostrophic velocity it would appear that the balance (2.51) is independent of magnitude of the velocity. Thus a doubling of the alongshore geostrophic velocity would lead to an exact doubling of the across-shelf geostrophic and consequently no change in the angle the horizontal flow makes with the topography. Such a scenario would suggest that a deep ocean's inflow cross-shelf penetration is independent of the deep ocean's velocity. Closer examination of (2.51)

shows that this conclusion is incorrect if there is shear in the geostrophic velocity. Consider a flow which is spatially uniform and the geostophic component is independent of depth. By assumption the alongshore geostrophic velocity is the same everywhere and therefore the bottom stress will be non-divergent and the right hand side of (2.51) is zero. Consequently there can be no cross-shelf geostrophic velocity. Consider a second flow which is also horizontally uniform but has a constant uniform shear in the geostrophic component of flow. In this case the spatial variation of bottom stress will not be uniform if the bottom slopes because of the vertical shear. For example if the geostrophic flow were surface intensified, flow in shallow water would experience a larger bottom stress than that in deeper water simply because of the depth difference. The bottom stress in (2.51) will be divergent and there will be some cross-shelf geostrophic motion. Thus there is a component of the divergence which results from the spatial variation in bottom stress due to the the depth change in the presence of a vertical shear in geostrophic velocity. It is this component of the divergence which is responsible for the variation in cross topography scale with shear. Mathematically it arises because the divergence is found by evaluating the stress at the bottom then taking the horizontal derivative an not by differentiation followed by evaluation at the bottom. The importance of the spatial variation of stress due to shear is determined by the ratio of the depth change over the flows horizontal scale to the depth sacle of the vertical shear. This ratio is assumed to be order 1 in this model.

In this vertically well mixed model the density of a fluid column traveling with the mean flow is determined initially at the point on the boundary where it enters the domain of interest. During its subsequent motion the column's density does not change because horizontal mixing is neglected and surface density fluxes due to air sea exchange are not considered. This leads to a model which emphasizes where a fluid column began its motion. In a more complete model horizontal mixing and/or surface fluxes would alter a column's density as it moved over the shelf thus reducing the emphasis on the columns origin. With these additional mechanisms included, density would no longer be conserved as the column was advected by the flow field and consequently density

contours and streamlines will not necessarily be aligned. This misalignment will in turn alter the forces acting on the water column and therefore the overall flow pattern. The dynamic consequences of non-conservation of density are difficult to gauge with this model.

The main conclusion for the deep ocean inflow is that although density variations may change the ability of flow to cross isobaths this effect is limited and the ATW scaling of small cross-shelf movement for a large alongshore movement still holds for vertically well mixed flow.

The density structure of Warm Core Gulf Stream Rings is such that they are surface intensified, hence they will have less effect on the shelf than an isothermal ring.

The application of the open boundary condition to the unforced latitudes of a narrow deep ocean inflow shows that, unless flow is being forced onto the shelf or is prevented from leaving by the application of channel-like boundary conditions, it will rapidly leave the shelf.

The two examples of flow entering the shelf region near to shore, a coastal outflow and a coastal jet, both show that it is the vertical shear which determines the overall flow pattern. Because of friction, a light alongshore jet or a low density river outflow expands across the topography more slowly than a barotropic flow while a heavy jet or outflow expands more rapidly than barotropic flow.

| | | | | |
|---|---|---|---|---|
| Coriolis, $f$ | $10^{-4}\ \ s^{-1}$ | | | |
| Bottom slope, $s$ | 0.001 | | | |
| Shelf width, $\ell$ | $100km$ | | | |
| Bottom friction, $r$ | $4 \times 10^{-4} ms^{-1}$ | | | |
| Minimum water depth, $h_c$ | $20m$ | | | |
| "Thermal Diffusivity", $\frac{r}{fs}$ | $4km$ | | | |
| Turbulent Eddy viscosity, $A_V$ | $100cm^2s^{-1}$ | | | |
| Ekman Layer Thickness, $\sqrt{\frac{A_V}{f}}$ | $10m$ | | | |
| | **Deep ocean Inflow** | | **Nearshore Forcing** | |
| Depth scale | 100m | | 50m | |
| | Wide | Narrow | River | Alongshore Jet |
| Alongshore scale, $L_y$ | $1000km$ | $50km$ | $50km$ | $50km$ |
| Cross-shelf scale, $L_x = \sqrt{\frac{rL_y}{fs}}$ | $63km$ | $14km$ | $14km$ | $14km$ |
| Velocity scale, $\|v\|$ | $10cms^{-1}$ | $1cms^{-1}$ | $2cms^{-1}$ | $20cms^{-1}$ |

Table 2.1: Scales for the Well Mixed Model

# Chapter 3

# Layered Models

## 3.1 Introduction

The vertically well mixed model of the previous chapter is limited to depths of order $100m$ and consequently, in addressing the question of deep ocean influence on the shelf, assumes that the deep ocean inflow is able to cross the continental slope and impinge directly on the shelf. Two steady layered models which include the topography of the continental slope will be used to determine the degree to which a baroclinic deep ocean can influence the shallow continental shelf. This will be done by assuming that the vertical structure of the deep ocean flow across the models' deepest isobaths is known and is unaffected by the response of the continental shelf and slope. The degree of influence of various flows, as measured by their cross-topography scale, will be compared to determine which deep ocean flows produce a significant flow over the shelf.

Both models include bottom Ekman layers but they differ in that one includes frictional boundary layers at the interface between the fluid layers while the other does not. Although the dynamics of the model without interfacial friction could be derived as a special case of the one with interfacial friction it will be derived separately after demonstrating several properties common to both. It will be shown that interfacial friction ( or some other mechanism which breaks strict geostrophy) must be included because the model without interfacial friction cannot accommodate all possible deep ocean velocity profiles.

The two models with and without interfacial friction can both in principle be extended to any number of layers which would sensibly fit within the maximum water depth permitted by the approximations used. The model without interfacial friction will be developed as a three-layer model, this being the minimum number to demonstrate the various cases of deep ocean flow. The model with interfacial friction will be developed as a two-layer model because to solve for a larger number of layers would significantly increase its complexity and the computational effort required in its solution.

## 3.2 Common Properties

Assumptions common to both models are that they are in steady state, hydrostatic balance, the surface is a rigid lid with no wind stress applied and the fractional density difference between layers is small $O(10^{-3})$. In both models flow in the core of any constant density layer is in geostrophic balance. The geostrophic core is that part of the density layer outside any Ekman layers which may be present adjacent to the interfaces and/or bottom. It is assumed that the stratification is strong enough that there is no exchange of mass between layers despite the turbulence introduced by any interfacial frictional layers which may be present. Such an assumption makes the models presented here more applicable to laboratory situations than to a continuously stratified ocean.

The geometry of the two models can be seen in Figures (3-1) and (3-4). In both figures $x$ is offshore, $y$, alongshore and $z$, the vertical coordinate, is zero at the surface. The free surface displacement is $\eta$ and the uppermost density interface displacement is $\varsigma$. Subscript 1 refers to the uppermost density layer and subscript 2, to the next to uppermost density layer. In the three-layer model subscript 3 refers to the lowest density layer and $\xi$ is the displacement of the lower density interface.

The total depth, $h$, will depend only on the offshore coordinate, i.e. $h(x)$. The depth of the deepest isobath included in the models is $h_{max}$. The nominal thickness of the $i$th layer, i.e. its thickness when all displacements are zero, is $d_i$.

Flow will be forced by prescribing the vertical distribution of pressure along the deepest isobath in the models. Because flow within the layers is mainly geostrophic, prescribing pressure is equivalent to prescribing the vertical distribution of geostrophic velocity normal to the deepest isobath.

It is found that solutions to the layered models exhibit short cross-topography scales and therefore it is necessary to determine the conditions under which flow inertia may be neglected. Planetary $\beta$ is included only in the interfacial friction model.

The equations governing steady hydrostatic flow on a $\beta$-plane in the core of the $i$th density layer when mixing is unimportant are (see Pedlosky (1979))

$$u_i\frac{\partial u_i}{\partial x} + v_i\frac{\partial u_i}{\partial y} + w_i\frac{\partial u_i}{\partial z} - (f_0 + \beta y)v_i = -\frac{1}{\rho_i}\frac{\partial p_i}{\partial x} \tag{3.1}$$

$$u_i\frac{\partial v_i}{\partial x} + v_i\frac{\partial v_i}{\partial y} + w_i\frac{\partial v_i}{\partial z} + (f_0 + \beta y)u_i = -\frac{1}{\rho_i}\frac{\partial p_i}{\partial y} \tag{3.2}$$

$$\frac{\partial p_i}{\partial z} = -g\rho_i \tag{3.3}$$

$$\frac{\partial u_i}{\partial x} + \frac{\partial v_i}{\partial y} + \frac{\partial w_i}{\partial z} = 0 \quad . \tag{3.4}$$

$u_i$ and $v_i$ are the horizontal velocities and $w_i$ is the vertical velocity. $f_0$ is the Coriolis parameter at a reference latitude, $p_i$ is the pressure in the $i$th layer and $\rho_i$ is the layer density. It is assumed that $|\frac{\beta y}{f_0}|$ is small but not necessarily negligible. Such an assumption restricts the applicability of these layered models to mid or high latitudes. Differentiating (3.3) with respect to both horizontal coordinates shows that $\frac{\partial}{\partial z}\frac{\partial p_i}{\partial x} = \frac{\partial}{\partial z}\frac{\partial p_i}{\partial y} = 0$, i.e. that the horizontal pressure gradient is independent of depth within a layer. A consequence of this is that the forcing for the horizontal momentum equations (3.1) and (3.2) is depth-independent and therefore horizontal velocities are also depth-

independent, i.e.

$$\frac{\partial u_i}{\partial z} = \frac{\partial v_i}{\partial z} = 0 \quad . \tag{3.5}$$

Flow within the core of each layer is barotropic.

Solutions to both models exhibit a cross-topography scale short compared to their along-topography scale. If the cross- and along-topography scales are $L_x$ and $L_y$ then, from continuity (3.4), the magnitudes of the cross- and along-topography velocities $u_0$ and $v_0$ are related by

$$\frac{u_0}{L_x} = \frac{v_0}{L_y} \quad . \tag{3.6}$$

If $\frac{L_x}{L_y} << 1$, then $\frac{u_0}{v_0}$ is also small.

Inertia may be neglected in (3.1) and (3.2) only if

$$\frac{v_0}{f_0 L_x} << 1 \tag{3.7}$$

i.e. if the Rossby number based on the stronger velocity and the shorter horizontal scale is small. Csanady (1985) requires only that the Rossby numbers $\frac{u_0}{fL_x}$ and $\frac{v_0}{fL_y}$ be small in order to neglect inertia. In fact the more restrictive condition (3.7) must be met. The shortest cross-topography scale exhibited by solutions of either model is of order $12km$. For (3.7) to be true flow speeds in both models must be small compared to $120cms^{-1}$.

Cross-differentiating (3.1) and (3.2) substituting into (3.4) and neglecting small terms yields

$$\underbrace{\frac{\partial w_i}{\partial z}}_{A} = \frac{1}{f_0}\Big( \underbrace{\beta v_i}_{B} + \underbrace{(u_i \frac{\partial}{\partial x} + v_i \frac{\partial}{\partial y})(\frac{\partial v_i}{\partial x} - \frac{\partial u_i}{\partial y})}_{C} \Big) \quad . \tag{3.8}$$

The three terms in this equation are A, the stretching due to vertical velocity, B the change in planetary vorticity and C the advection of relative vorticity. In both the

layered models presented here the magnitude of the vertical velocity in the layers above the lowest is given by that of a parcel following the topography of the interface

$$w_0|_{interface} = \frac{u_0 \zeta_0}{L_x} \tag{3.9}$$

where $\zeta_0$ is the magnitude of the interface displacement. In the lowest layer the vertical velocity scale is given by a parcel following the bottom

$$w_0|_{bottom} = s u_0 \tag{3.10}$$

where $s$ is the bottom slope. The relative magnitudes of the terms A,B and C in (3.8) in the upper layers are

$$1 \quad : \quad \frac{d_0}{\zeta_0} \frac{\beta L_y}{f_0} \quad : \quad \frac{d_0}{\zeta_0} \frac{v_0}{f_0 L_x} \tag{3.11}$$

and in the lowest layer

$$1 \quad : \quad \frac{h_0}{s L_x} \frac{\beta L_y}{f_0} \quad : \quad \frac{h_0}{s L_x} \frac{v_0}{f_0 L_x} \tag{3.12}$$

where $d_0$ is a representative layer thickness and $h_0$ a representative water depth.

On an $f-$plane it is assumed that the right hand side of (3.8) is negligible. This is so if the second and third non-dimensional numbers in both (3.11) and (3.12) are small. For the scales given in tables 3.1 and 3.2 this is generally so. However the neglect of relative vorticity is marginal for a $5 cms^{-1}$ velocity scale when the flow is barotropic or near barotropic because, as will be seen, the cross-topography scale is at a minimum. It should be noted that as the vertical velocity due to the $\beta$ effect increases with the models latitudinal extent and its maximum water depth the size of both these dimensions is restricted on an $f-$plane.

To neglect relative vorticity on a $\beta-$plane the third term in both (3.11) and (3.12) must be small compared to the other two terms. This is the case if

$$\frac{v_0}{\beta L_x L_y} << 1 \tag{3.13}$$

Again this condition is generally satisfied for $5cms^{-1}$ currents ( see Table 3.2) but is marginally satisfied for the short scales exhibited by near barotropic flows.

When relative vorticity is negligible (3.8) becomes

$$\frac{\partial w_i}{\partial z} = \frac{\beta}{f_0} v_i \quad . \tag{3.14}$$

In both models integrating the hydrostatic relation gives the pressure at any depth. For example, the pressure in the second layer is

$$p_2 = g\rho_1(\eta + d_1 - \varsigma) + g\rho_2(\varsigma - d_1 - z) \quad . \tag{3.15}$$

The dynamically significant pressure in any layer is the component of pressure which varies in the horizontal. Expressed as an equivalent head of water, these pressures, for up to three layers, are

$$\begin{aligned} \chi_1 &= \eta \\ \chi_2 &= \eta + \epsilon_1 \varsigma \\ \chi_3 &= \eta + \epsilon_1 \varsigma + \epsilon_2 \xi \end{aligned} \tag{3.16}$$

where $\epsilon_1 = \frac{\rho_2 - \rho_1}{\rho_2}$ $(O(10^{-3}))$ is the non-dimensional density deficit of layer 1 over layer 2, and $\epsilon_2 = \frac{\rho_3 - \rho_2}{\rho_3}$ is the density excess of layer 2 over layer 3.

Dropping small terms from (3.1) and (3.2) the components of geostrophic velocity in the $i$th layer may be expressed

$$\begin{aligned} f_0 u_i &= -g\frac{\partial \chi_i}{\partial y} \\ f_0 v_i &= g\frac{\partial \chi_i}{\partial x} \quad . \end{aligned} \tag{3.17}$$

These definitions show that isobars of $\chi_i$ are also flow lines for geostrophic flow in the $i$th layer. Rewriting (3.16) the displacements are related to the pressures by

$$\begin{aligned} \eta &= \chi_1 \\ \varsigma &= \frac{1}{\epsilon_1}(\chi_2 - \chi_1) \\ \xi &= \frac{1}{\epsilon_2}(\chi_3 - \chi_2) \end{aligned} \tag{3.18}$$

Both layered models will be derived by matching the vertical velocity within the geostrophic core of any given layer to the vertical velocities which exist at or near the top and bottom of that layer due to the bottom topography, the "topography" of the interfaces and any Ekman layers which may be present. The vertical velocities in both interfacial and bottom Ekman layers will be calculated from the bulk properties of the frictional layers and expressed in terms of the geostrophic velocities in the adjacent layer core or cores.

## 3.3 Development of Three-Layer Model

Consider the three density layer model shown in Figure 3-1. The upper two layers are in geostrophic balance throughout their thickness. The bottom layer is in geostrophic balance over most of its thickness except in a thin bottom Ekman layer. The topography is linear with slope, $s$ and is intended to be an idealization of the continental slope of an east coast in the northern hemisphere. Other model assumptions are an $f$-plane, that flow does not cross the interfaces, that interfaces do not outcrop at the surface nor intersect each other, and that the intersection of the lowest interface with the bottom is far enough away so as not to affect the flow.

On an $f$-plane (3.14) becomes

$$\frac{\partial w}{\partial z} = 0 \tag{3.19}$$

i.e. vertical velocity is depth independent where the layers are in geostrophic balance. Integrating (3.19) between the surface and the upper interface with a rigid lid yields

$$u_1 \frac{\partial \varsigma}{\partial x} + v_1 \frac{\partial \varsigma}{\partial y} = 0 \tag{3.20}$$

i.e. upper layer flow is along contours of interface displacement.

Using the definitions of geostrophic velocity, (3.17), equation (3.20) may be written as the Jacobian

$$J(\chi_1, \varsigma) = 0 \tag{3.21}$$

where $J(A,B) = \frac{\partial A}{\partial x}\frac{\partial B}{\partial y} - \frac{\partial A}{\partial y}\frac{\partial B}{\partial x}$. Mathematically if the Jacobian of two functions is zero, then neither varies along contours of the other. Consequently isobars of upper layer pressure must be parallel to contours of upper interface displacement.

After multiplying by $\epsilon_1$, noting that the Jacobian of a quantity with itself is zero, (i.e. $J(A,A) = 0$), and incorporating the definition of pressure (3.16), (3.21) can be

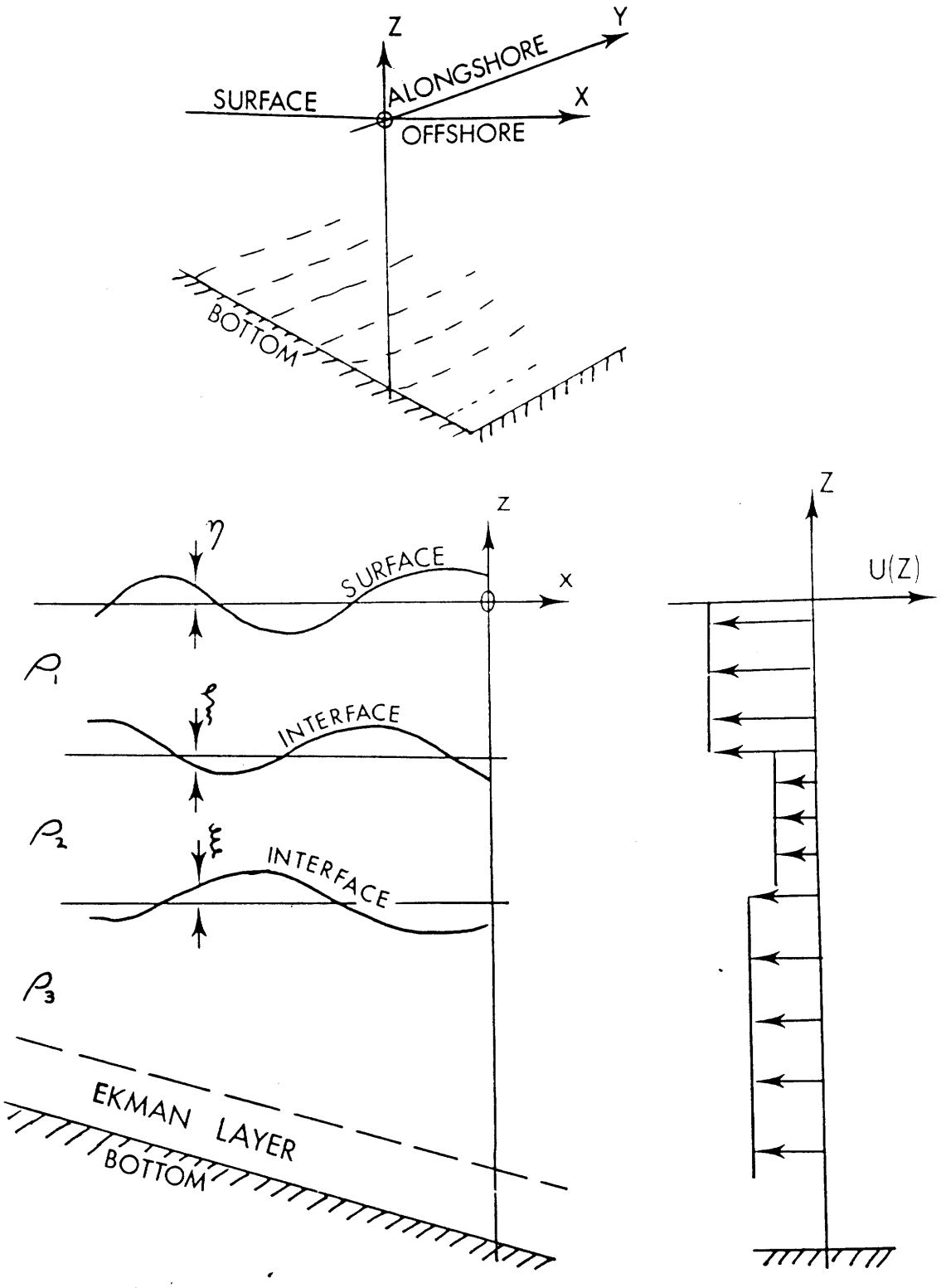


Figure 3-1: a) Geometry for layered model. b) Schematic velocity profile of deep ocean inflow.

shown to be exactly equivalent to

$$J(\chi_1, \chi_2) = 0 \tag{3.22}$$

i.e. pressure contours in the middle layer are parallel to pressure contours in the upper layer. Because flow in these layers is in geostrophic balance, flow in the middle layer must be parallel or anti-parallel to upper layer flow. Equation (3.22) in conjunction with (3.21) implies that middle layer flow is also along contours of upper interface displacement, i.e.

$$J(\chi_2, \varsigma) = 0 \quad . \tag{3.23}$$

Equation (3.23) implies that the vertical velocity on the lower side of the upper interface is zero, and by (3.19) it must be zero throughout the middle layer, i.e. $w_2 = 0$. Because vertical velocity is zero, middle layer flow must also be parallel to contours of lower interface displacement, which is the case when

$$J(\chi_2, \xi) = 0 \quad . \tag{3.24}$$

When the middle layer is in motion, i.e. $\chi_2 \neq 0$, (3.23) and (3.24) can be simultaneously true only if contours of upper interface displacement are parallel to contours of lower interface displacement, i.e.

$$J(\varsigma, \xi) = 0 \qquad if \qquad \chi_2 \neq 0 \quad . \tag{3.25}$$

Multiplying by $\epsilon_2$ and noting that $J(\chi_2, \chi_2) = 0$, (3.24) is exactly equivalent to

$$J(\chi_2, \chi_3) = 0 \quad . \tag{3.26}$$

Consequently flow in the middle layer must be parallel or anti-parallel to flow in the lowest density layer. By (3.24) lower layer flow must also be along contours of lower

interface displacement, i.e.

$$J(\chi_3, \xi) = 0 \quad . \tag{3.27}$$

This equation together with (3.19) implies that $w_3$ is also zero in the core of the bottom density layer.

Clearly this derivation can be extended downward to any number of geostrophic layers which would sensibly fit within the maximum depth permitted by the model assumptions (i.e. that the flow is geostrophic and on an $f$-plane). The generalized results are that vertical velocity is zero in any geostrophic layer, that geostrophic flow must be along the displacement contours of any density interfaces surrounding the layer, and that geostrophic flow in any two adjacent moving layers must be parallel or anti-parallel.

The dynamics of the lowest density layer differ slightly from those above because it contains a thin Ekman layer at the bottom. From Pedlosky (1979) the vertical velocity just above an Ekman layer on a linearly sloping bottom, and expressed in terms of the geostrophic velocities just above the bottom, is

$$w|_{z=-h} = -su_3 + w_E \quad . \tag{3.28}$$

$w_E$ is the vertical velocity due to Ekman pumping within the bottom frictional layer and, as has been demonstrated, $w|_{z=-h} = w_3 = 0$.

The Ekman pumping velocity expressed in terms of the geostrophic velocities just above the Ekman layer is, (Pedlosky (1979))

$$w_E = \frac{\delta_E}{2}\left(\frac{\partial v_3}{\partial x} - \frac{\partial u_3}{\partial y}\right) \tag{3.29}$$

where $\delta_E$ is the thickness of the bottom Ekman layer equal to $\sqrt{\frac{2A_V}{f_0}}$, and $A_V$ is the vertical turbulent eddy viscosity in the frictional boundary layer. Vertical velocity is zero in the core of the lowest layer, therefore, using (3.29) and the definitions of

geostrophic velocity (3.17), (3.28) can be written

$$\frac{\delta_E}{2}\left(\frac{\partial^2 \chi_3}{\partial x^2}+\frac{\partial^2 \chi_3}{\partial y^2}\right)+s\frac{\partial \chi_3}{\partial y}=0 \quad . \tag{3.30}$$

Boundary conditions will be developed later for the particular problems under discussion.

In the absence of bottom friction (3.30) becomes $s\frac{\partial \chi_3}{\partial y}=0$, i.e. flow in the lowest layer will follow isobaths. The length scale, $\frac{\delta_E}{2s}$, determines the rate at which lower layer flow will diffuse or spread across the topography. A more turbulent bottom boundary layer, low latitude or weak bottom slope will all increase a flow's ability to cross isobaths. The physical mechanism implicit in (3.30) will also be discussed later.

Although this discussion centers on the cross-isobath movement of the geostrophic flow, it should be kept in mind that there will also be an Ekman transport which flows parallel to and down the pressure gradient in the lowest density layer. The Ekman pumping velocity from (3.28) and (3.17) is

$$\dot{w}_E=\frac{-g}{f_0}s\frac{\partial \chi_3}{\partial y} \quad . \tag{3.31}$$

Equations (3.22), (3.26) and (3.30) are three independent equations in the three unknown pressures. With appropriate boundary conditions (3.30) can be solved for bottom pressure. The remaining two equations can then be solved for upper and middle layer pressure, and using (3.18) the displacements can be calculated.

It is shown later that for particular boundary conditions certain layers will be motionless and, in these cases, the solution scheme outlined above breaks down. For example if the bottom layer is motionless, i.e. $\chi_3 = 0$, then (3.26) and (3.30) are trivially satisfied. The remaining equation (3.22) contains two unknowns and thus has an infinite number of solutions. This degeneracy results from the assumption that flow in the upper layers is purely geostrophic and on an $f$-plane (see Pedlosky (1979)).

Similarly, when the middle layer is motionless, i.e. $\chi_2 = 0$, equation (3.30) together with appropriate boundary conditions can be solved for bottom pressure. However (3.22) and (3.26) are trivially satisfied and there is no equation remaining with which

to determine the upper layer pressure from the infinite number of possible solutions. In this case flow in the top layer is also geostrophically degenerate.

It should be noted that the solution scheme does work when the top layer is motionless, i.e. $\chi_1 = 0$. (3.26) and (3.30) are two independent equations in the unknown middle and bottom layer pressures and, with appropriate boundary conditions, they can be solved for a unique and non-trivial solution.

These examples are demonstrations of a general rule: that this model can only give a unique solution if the bottom layer is moving, i.e. if $\chi_3 \neq 0$, in which case the flow pattern in all layers above the lowest, but below the first motionless layer, will be parallel or anti-parallel to the flow in the lowest layer.

### 3.3a Point Source Solution

Before proceeding to solve the specific problem of a deep oceanic flow impinging on the continental slope the "steady point source" solution to (3.30), i.e. the Green's function of (3.30), is sought. A point source entering the lowest layer will raise the lower interface above the source, reducing the depth averaged temperature at that point. Thus a source in the lowest layer acts as a point cooling. Conversely, withdrawing fluid from the lower layer acts as a point warming. The physical interpretation for fluid being injected into other layers is discussed later.

Equation (3.30) is analogous to that governing the steady state diffusion in a two-dimensional medium which is moving parallel to the $y$ axis. The fluid sink is equivalent to a point sink of heat; $\frac{\delta_E}{2}$ is analogous to the thermal diffusivity and $-s$ to the speed at which the medium is moving. From Carslaw and Jaeger (1959) the solution for a point sink at the origin valid for all $x$ and $y$ is

$$\chi_3 = q \frac{1}{2\pi f_0(\frac{\delta_E}{2s})} \; exp\Big(\frac{-y}{2\frac{\delta_E}{2s}}\Big) K_0 \left(\frac{1}{2(\frac{\delta_E}{2s})}\sqrt{x^2+y^2}\right) \tag{3.32}$$

where $K_0$ is the zeroth order modified Bessel function of the second kind, and $q$ is proportional to the rate at which fluid is being withdrawn per unit area of the sink.

The isobars of the non-dimensional solution (3.32) are plotted in Figure 3-2a. Horizontal lengths are non-dimensionalized by $\frac{\delta_E}{2s}$, which for the typical scales given in Table 3.1 is $0.4km$. The region shown is 40 by 100 non-dimensional units, which corresponds to a section of continental slope $16km$ wide and $40km$ long.

The isobars in Figure 3-2a are also flow lines for geostrophic flow in the lowest layer. Geostrophic flow is along closed paths around the sink, but the pattern is strongly elongated along the topography with a much shorter "upstream" scale, positive $y$, than the "downstream" negative $y$ scale. In the heat analogy it is clear that on scales large compared to $\frac{\delta_E}{2s}$ the advection of heat is much stronger than the cross-current diffusion of heat. The oceanographic conclusion is that on these scales the tendency for geostrophic flow to follow isobaths is much stronger than the rate at which friction allows the flow to cross isobaths.

The sink draws down the lowest interface but will not induce flow in the layer above because middle layer velocities are independent of the lower interface displacement (see (3.16),(3.17)). In short, the flow pattern induced by the sink in the lowest geostrophic layer is confined to that layer.

A sink in the middle layer would draw down the upper interface, inducing mid-level flow, however the upper layer would remain motionless. Such a sink would also draw up the lower interface reducing pressure gradients in the lower layer. If the opposing displacement of the two interfaces is such that pressure in the lower layer is exactly compensated then the lower layer will not move and middle layer flow cannot be determined with this model. If the lower interface does not exactly compensate for the upper interface, then the flow pattern of the lower layer and the middle layer will be as in Figure 3-2a. However, it is not clear how to determine the degree of pressure compensation in the bottom layer.

There is an Ekman transport down the bottom pressure gradient associated with motion in the lowest geostrophic layer. From (3.31) and (3.32) the Ekman pumping

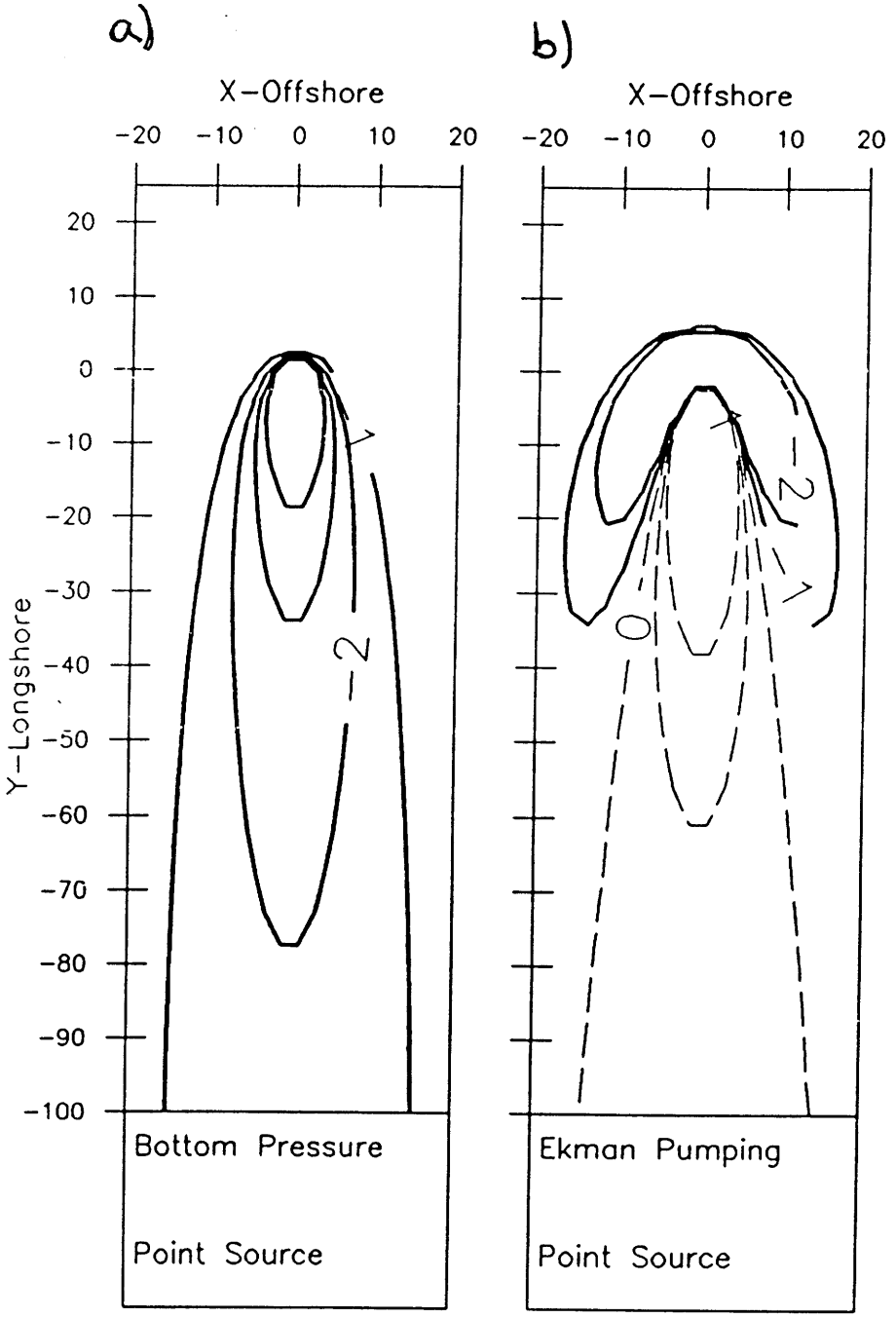


Figure 3-2: Isobars of bottom pressure for a point source in the lowest geostrophic layer (the Green's function solution to (3.30)). a) Solid contour spacing is 1 and pressure decreases monotonically towards the origin. Isobars are also flow lines for geostrophic flow in the lowest layer. b) Contours of Ekman pumping velocity. Contour spacing is 1. Solid contours are negative values, dashed contours, positive values. Ekman pumping velocity for the point source is downward in regions of upslope geostrophic flow and upward in regions of downslope flow. Contours near the origin are omitted because the solution is singular there.

velocity for the point source is

$$w_E = q\frac{gs}{4\pi f_0^2(\frac{\delta_E}{2s})^2}\ exp\left(\frac{-y}{2(\frac{\delta_E}{2s})}\right)\left(K_0\left(\frac{1}{2\frac{\delta_E}{2s}}\sqrt{x^2+y^2}\right)\right.$$

$$\left.+\frac{y}{\sqrt{x^2+y^2}}K_1\left(\frac{1}{2\frac{\delta_E}{2s}}\sqrt{x^2+y^2}\right)\right) \quad . \tag{3.33}$$

$K_1$ is the first order modified Bessel function of the second kind. Contours of the Ekman pumping velocity are shown in Figure 3-2b. The Ekman transport across any closed isobar in Figure 3-2a is balanced by fluid being withdrawn by the sink.

The Green's function (3.32) is useful because it shows that, for typical oceanographic scales, the inherent character of solutions to (3.30) is a very short influence towards positive $y$, a large region of influence towards negative $y$, and a small degree of cross-isobath influence. In principle by superimposing point source solutions the solutions to many more complex problems could be obtained. The superposition would retain the general elongated character of the individual point solutions.

### 3.3b Deep Ocean Inflow

In this section the flow pattern of a deep ocean flow impinging on the continental slope will be found.

It is possible to simplify (3.30) further by exploiting the elongation exhibited by Green's function solution. The alongshore diffusion is of order one in (3.30) when the horizontal length scales are isotropic and equal to $\frac{\delta_E}{2s}$. For the scales in Table (3.1) $\frac{\delta_E}{2s}$ is $0.4km$ while the alongshore scale is $250km$. Therefore alongshore diffusion may be neglected in (3.30) reducing it to a balance between cross-topography frictional diffusion and topographic steering

$$\frac{\delta_E}{2}\frac{\partial^2 \chi_3}{\partial x^2} + s\frac{\partial \chi_3}{\partial y} = 0 \quad . \tag{3.34}$$

The long and cross-slope scales are related by

$$L_x = \sqrt{\frac{\delta_E}{2s} L_y} \quad . \tag{3.35}$$

For scales in Table (3.1) $L_x$ is much smaller than $L_y$, i.e.

$$\frac{L_x}{L_y} << 1 \quad . \tag{3.36}$$

This is often referred to as the longwave approximation. This term will be used here though, strictly speaking, there are no waves in this steady model. Continuity, (3.36) implies that

$$\frac{u_0}{v_0} << 1 \quad . \tag{3.37}$$

which shows that the geostrophic velocities along isobaths are much stronger than velocities across isobaths. The scale relationship (3.35) is similar to that derived by Csanady(1978) for frictionally controlled barotropic flow, since his drag coefficient, $r$, is related to the Ekman layer thickness by $r = \frac{f\delta_E}{2}$. Equation (3.34) is the same as Csanady's except that in this layered model the bottom pressure replaces his surface pressure. As in Csanady's equation pressure information propagates only in one alongshore direction in (3.34) given by the sign of $-\frac{\delta_E}{2s}$.

### 3.3c Boundary Conditions

Equation (3.34) is parabolic and also governs one-dimensional heat diffusion where $-y$ is the "time-like" coordinate. Thus it requires two cross-topography boundary conditions and an "initial condition". Flow is forced by prescribing the three displacements on $x = 0$. As an "initial condition" it is assumed that no flow enters the domain of interest across $y = 0$ from farther up the shelf. This can be ensured by prescribing all the pressures to be zero on $y = 0$. This boundary condition allows the flow induced by forcing at the offshore boundary to be considered in isolation from flow which may be forced at other lateral boundaries.

Boundary conditions could be developed for the flow at the lines where the interface intersects the bottom. However solutions to (3.34) are error functions which decay rapidly with cross-slope distance. For the scales in Table 3.1 the cross-slope scale of a $250km$ wide inflow is only $10km$ whereas the lowest interface intersects the bottom $30km$ shoreward of $x = 0$. Thus the flow where the lowest interface intersects the bottom is negligible and the shoreward boundary condition for the displacements is that they vanish as $x \to -\infty$. Therefore no special boundary conditions need be developed for any of the interface/bottom intersections. The boundary conditions for this deep ocean inflow model are

(i) $\chi_1$, $\chi_2$ and $\chi_3$ given on $x = 0$

(ii) $\chi_1$, $\chi_2$ and $\chi_3$ zero on $y = 0$

(iii) $\chi_1$, $\chi_2$ and $\chi_3 \to 0$ as $x \to -\infty$.

For simplicity the pressures are prescribed to slope linearly along $x = 0$ i.e.

$$\left.\begin{aligned} \chi_1 &= ay \\ \chi_2 &= by \\ \chi_3 &= cy \end{aligned}\right\} \quad at \quad x = 0 \tag{3.38}$$

where $a, b$ and $c$ are arbitrary constants.

For particular boundary conditions some layers will be motionless. The upper layer is motionless if $a = 0$, the middle layer, if $b = 0$ and the lowest layer, when $c = 0$.

### 3.3d Solution

The example we will consider consists of a surface mixed layer of $100m$, a $100m$ thick middle layer and a $300m$ thick bottom layer. Equation (3.34) is analogous to that for heat diffusion in an infinite bar with thermal diffusivity $\frac{\delta_E}{2s}$. The bar has zero initial temperature and a prescribed temperature at $x = 0$ which changes linearly with time. The solution from Carslaw and Jaeger (1959) (page 63) is

$$\chi_3 = cy\Big\{\Big(1+\frac{x^2}{2\frac{\delta_E}{2s}(-y)}\Big)\Big(1-erf(\frac{x}{2\sqrt{\frac{\delta_E}{2s}(-y)}})\Big)$$

$$-\frac{x}{\sqrt{\pi\frac{\delta_E}{2s}(-y)}}\exp\Big(\frac{x^2}{4\frac{\delta_E}{2s}(-y)}\Big)\Big\} \tag{3.39}$$

where $erf$ is the error function.

Contours for non-dimensional bottom pressure are plotted in Figure 3-3. The solution was non-dimensionalized with the following scales

$$\chi_3 = cL_y\ \chi_3'$$

$$\chi_1 = cL_y\ \chi_1'$$

$$\chi_2 = cL_y\ \chi_2'$$

$$y = L_y y'$$

$$x = \sqrt{\frac{\delta_E L_y}{2s}}\ x' \quad .$$

The region plotted in Figure 3-3 corresponds to an area of continental slope $250km$ long and $20km$ wide. The narrow region of cross-slope influence of the deep ocean's lower layer is clearly evident here.

The remaining governing equations (3.22) and (3.26) need not be laboriously solved in order to determine the surface and middle layer pressures. Equation (3.26) shows that contours of middle layer pressure must be parallel to contours of lower layer pressure if both layers are moving. Furthermore (3.22) shows that contours of upper layer pressure are parallel to contours of middle layer pressure if both layers are moving.

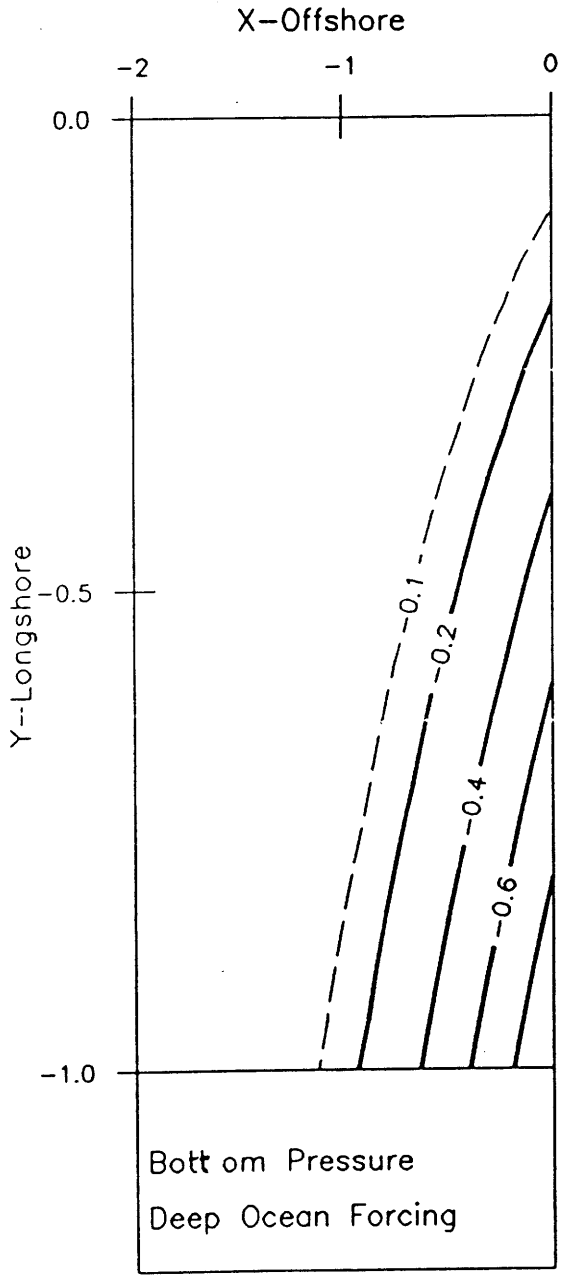


Figure 3-3: Isobars of bottom pressure for the inflow solution (3.39).The pressure increases linearly along $x = 0$. This non-dimensional domain corresponds to a portion of continental shelf $20km$ wide and $250km$ long. Solid contours are spaced at 0.2 and pressure has a minimum of $-1$ at $y = -1$, $x = 0$. This solution demonstrates that the influence of a deep ocean pressure gradient is limited by the steep continental slope. The interface displacements are parallel to the isobars of bottom pressure and geostrophic flow is along the isobars in all layers between the bottom and the first motionless layer.

Therefore the contours of any pressure will be parallel to the contours of any other pressure if the middle layer is in motion. Consequently both upper and middle layer pressures must be functionally related to bottom pressure, i.e.

$$\begin{aligned} \chi_1 &= F(\chi_3) \\ \chi_2 &= G(\chi_3) \quad . \end{aligned} \tag{3.40}$$

These functional relationships can be determined from the boundary conditions. Given $\chi_1$, $\chi_2$ and $\chi_3$ along some line then $F$, and $G$ can be determined on that line. The relationships will also hold in all regions containing contours of $\chi_1$, $\chi_2$ and $\chi_3$ which cross the line. For the boundary conditions (3.38) the functional relations for this inflow where $\chi_1$, $\chi_2$ and $\chi_3$ are prescribed independently on $x = 0$ are

$$\begin{aligned} \chi_1 &= \frac{a}{c}\chi_3 \\ \chi_2 &= \frac{b}{c}\chi_3 \quad . \end{aligned} \tag{3.41}$$

For more general boundary conditions the other pressures will not necessarily be linearly related to the bottom pressure.

Substituting for $\chi_3$ in (3.41) from (3.39) gives the solutions for the middle and upper layer pressures. Thus if the middle layer is moving its non-dimensional pressure, and therefore flow pattern, is given by Figure 3-3 after contour values are scaled by the factor $\frac{b}{c}$. If the upper layer is also moving, its flow pattern is also given by Figure 3-3 when contours are scaled by $\frac{a}{c}$. When the middle layer is motionless only the lower layer flow is as in Figure 3-3. The upper layer flow cannot be determined from this model.

The solutions for surface and interface displacements from (3.18) are

$$\begin{aligned} \eta &= \frac{a}{c}\,\chi_3 \\ \zeta &= \frac{1}{\epsilon_1 c}(b-a)\,\chi_3 \\ \xi &= \frac{1}{\epsilon_2 c}(c-b)\,\chi_3 \end{aligned}$$

where $\chi_3$ is given by (3.39).

| | |
|---|---|
| Alongshore scale, $L_y$ | $250km$ |
| Maximum water depth, $h_{max}$ | $500m$ |
| Bottom slope, s | 0.01 |
| Ekman layer thickness, $\delta_E$ | $10m$ |
| Coriolis, f | $10^{-4}s^{-1}$ |
| Layer thicknesses, $d_1$,$d_2$ | $100m$ |
| Bottom layer thickness, $d_3$ | $300m$ |
| Free surface displacement, $\eta_0$ | $0.025m$ |
| Interface displacements, $\zeta_0$, $\xi_0$ | $20m$ |
| Density excess, $\epsilon_1$, $\epsilon_2$ | 0.001 |
| **Calculated Scales** | |
| Cross-shelf scale, $L_x = \sqrt{\frac{\delta_E}{2s} L_y}$ | $12km$ |
| "Thermal diffusivity", $\frac{\delta_E}{2f}$ | $0.4km$ |
| Alongshore velocity,$v_0$ | $5cms^{-1}$ |

Table 3.1: Scales for the Three-Layer Model

### 3.3e Summary of Three-Layer Model

The three-layer model shows that:

1. the cross-topography penetration of bottom layer flow is severely restricted by the continental slope;

2. flow in layers above a moving bottom layer but below the lowest motionless layer is parallel or anti-parallel to the flow in the bottom layer and therefore cross-topography penetration in these layers is also very limited;

3. this model cannot determine the flow in layers above the lowest motionless layer because of geostrophic degeneracy and therefore cannot determine the cross-topography penetration of all possible deep ocean velocity profiles.

## 3.4 Interfacial Friction Model Development

As discussed earlier the three-layer model cannot be used to find the flow in a density layer which overlies a motionless layer because of geostrophic degeneracy. However by including higher order dynamics such as internal friction into the layers above the bottom layer this degeneracy can be eliminated.

Consider the two-layer model shown in figure (3-4). Internal friction resulting from the relative motion of the two density layers will cause frictional Ekman boundary layers to form at the interface. There are two Ekman layers associated with the interface, one above and one below. There is also a third Ekman layer at the bottom which results from the frictional drag of the sloping bottom. Both constant density layers are comprised of a core where the flow is in geostrophic balance, and of thin Ekman layers adjacent to the interface and bottom. Since turbulence away from the rigid bottom is expected to be weaker than that at the bottom the turbulent eddy viscosity near the interface will be smaller than in the bottom boundary layer. Consequently the interfacial Ekman layers will be thinner than the bottom Ekman layers.

The use of interfacial Ekman layers an idealization which has been used in layered models for the general wind driven circulation (Huang (1987)). its use in these models is to provide a mechanism by which momentum may be transferred downward in a manner similar to mesoscale eddies in the real ocean. In the models presented here it provides a mechanism, although an idealized one, for inter-layer momentum transfer.

The geometry of the two-layer model is shown in Figure 3-4. The topography is intended to be an idealization of the continental shelf and slope of a northern hemisphere east coast. The gently linearly sloping shelf with depth zero at the coast intersects the steeper linear gradient of the slope at the shelf break ($x = x_s$) i.e.

$$h = \begin{cases} s_s x & 0 \leq x < x_s \\ s_s x_s + s(x - x_s) & x_s < x < x_{max} \end{cases} . \tag{3.42}$$

$s_s$ is the bottom slope of the shelf and $s$, the bottom slope of the continental slope. $x_{max}$ is the seaward extent of the model where flow is forced by prescribing the pressure, and hence also the geostrophic flow, onto the topography. The single interface intersects the bottom along the line $x_I(y)$. As the interface moves up or down this intersection with the topography will move on or offshore. The position of the intersection must be determined as part of the solution. The geostrophic velocities in the core of each layer are given by (3.17).

An interface is not necessarily flat and may be warped in both the $x$ and $y$ directions. Thus the "topography" of the interface and the relative motion of the two density layers must be taken into consideration. In the three-layer model without interfacial friction horizontal velocities were discontinuous across the interface. Ekman layers allow the velocities in the two density layers to be smoothly joined without this discontinuity. In addition, because the stress exerted by the upper layer on the lower layer must be equal and opposite to the stress exerted by the lower layer on the upper, there must be continuity of stress across the interface.

In Appendix B the equations governing Ekman layers on a sloping interface are derived and the detailed velocity solutions which join the geostrophic flow in one layer to the other while ensuring continuity of velocity and stress at the interface are given. The final, and most useful result obtained is that the vertical velocity just outside the interfacial Ekman layers is the sum of two components: one due to the Ekman pumping which results from convergences and divergences of interfacial Ekman transport, and another component due to the "topography" of the interface. This result is very similar to that obtained by Pedlosky (1979) for an Ekman layer on a rigid sloping bottom where the vertical velocity outside the bottom Ekman layer is also the sum of components due to topography and Ekman pumping. The main difference is that Ekman pumping at the interface depends on the difference between the geostrophic velocities in the density layers on either side of the interface, rather than on the absolute geostrophic velocity as it does in a bottom Ekman layer.

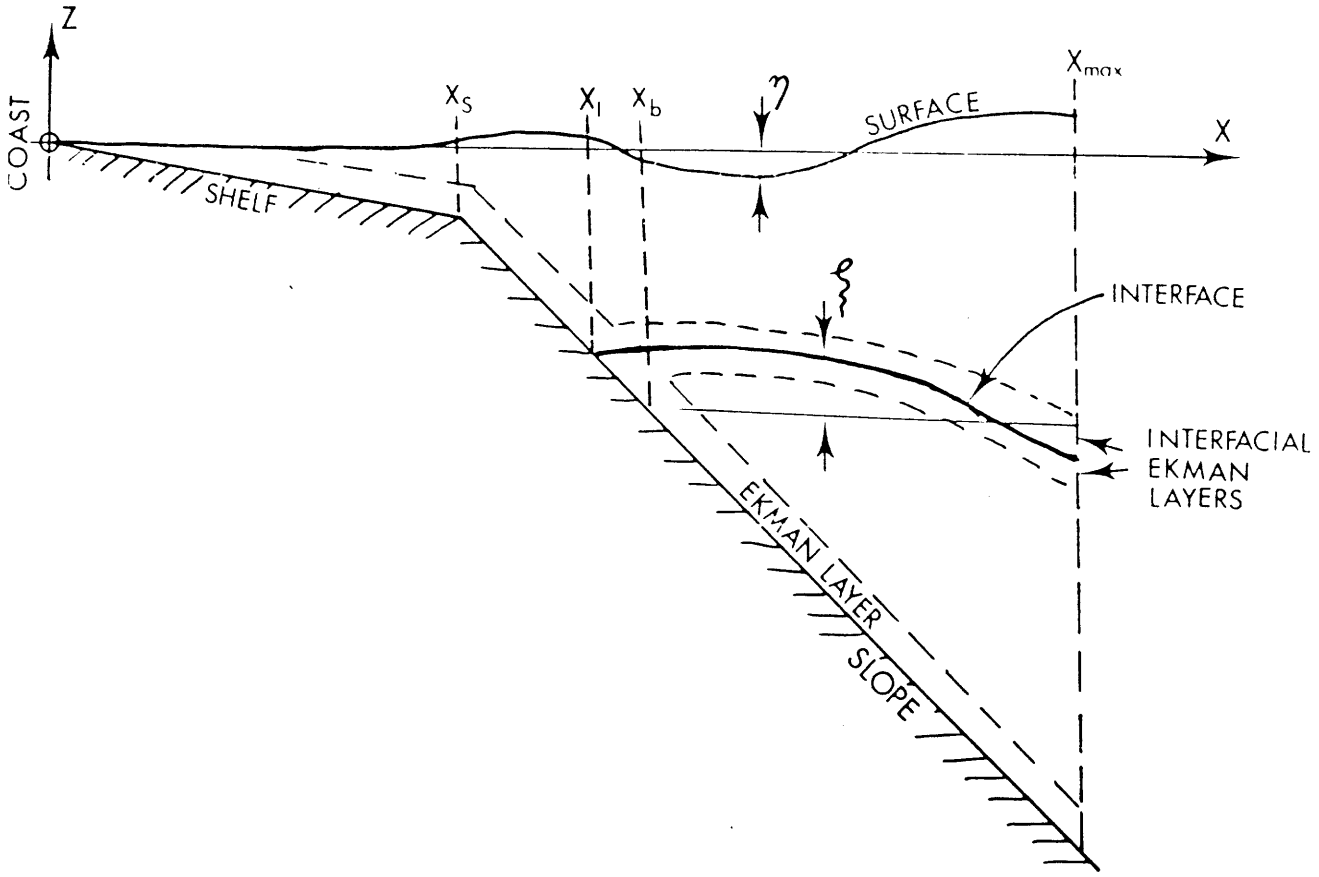


Figure 3-4: Geometry for the two-layer interfacial friction model is an idealization of the shelf and slope of a northern hemisphere east coast. $x$ is offshore. $y$ is northward. a) The shelf break is at $x_s$, the single interface intersects the topography along $x_I(y)$, the interface would intersect the bottom at $x_b$ if it were flat. There are thin Ekman layers at the bottom and adjacent to the interface in both density layers.

The model equations can be developed by matching the vertical velocity in the geostrophic core of each layer to the vertical velocity just outside the Ekman layers at the interface and at the bottom. In dimensional terms the vertical velocity in the geostrophic core of the upper layer just outside the thin upper interfacial Ekman layer from Appendix B ((B.24)) is

$$w_1|_{z=-d_1} = \vec{u_1} \bullet \nabla_H \zeta + \frac{\delta_E^I}{4}[\frac{\partial}{\partial x}(v_1 - v_2) - \frac{\partial}{\partial y}(u_1 - u_2)] \quad . \tag{3.43}$$

$\vec{u_1}$ is the horizontal geostrophic velocity vector and $\nabla_H$ is the vector $(\frac{\partial}{\partial x}, \frac{\partial}{\partial y})$. $\delta_E^I$ is the thickness of the interfacial Ekman layer equal to $\sqrt{\frac{2A_V^I}{f}}$, $A_V^I$ being the turbulent eddy viscosity away from the bottom boundary layer which is expected to be smaller than the eddy viscosity at the bottom. Similarly in dimensional form the vertical velocity just below the thin lower interfacial Ekman layer from (B.25) is

$$w_2|_{z=-d_1} = \vec{u_2} \bullet \nabla_H \zeta + \frac{\delta_E^I}{4}[\frac{\partial}{\partial x}(v_1 - v_2) - \frac{\partial}{\partial y}(u_1 - u_2)] \quad . \tag{3.44}$$

In making the $\beta$-plane approximation it has already been assumed that the variation in $f$ is small. Consequently the variation in interfacial (and bottom) Ekman layer thickness due to latitude need not be considered, so that

$$\delta_E^I = \sqrt{\frac{A_V^I}{2f_0}} \quad . \tag{3.45}$$

The first term on the right hand side of both (3.43) and (3.44) is the vertical motion due to the "topography" created by the displacement of the interface, and the remaining terms are due to the Ekman pumping resulting from the relative motion in the two geostrophic cores.

Taking the difference of (3.43) and (3.44) gives

$$w_1|_{z=-d_1} - w_2|_{z=-d_1} = (\vec{u_1} - \vec{u_2}) \bullet \nabla_H \zeta \tag{3.46}$$

The velocity shear $\vec{u_1} - \vec{u_2}$ is perpendicular to the gradient of interface slope, $\nabla_H \zeta$, (see (3.17) and (3.18)), therefore the right hand side of (3.46) is zero and thus

$$w_1|_{z=-d_1} = w_2|_{z=-d_1} \tag{3.47}$$

i.e. the vertical velocity is continuous across the interfacial Ekman layers, though is was assumed that no flow crosses the interface. Thus (3.46) is an identity.

Depth integrating (3.14) for a thin Ekman layer, a small interface displacement and with a rigid lid gives

$$w_1|_{z=-d_1} = -\frac{\beta}{f_0} d_1 v_1 \quad . \tag{3.48}$$

Expressing (3.43) in terms of pressure and combining it with (3.17) yields

$$\frac{\delta_E^I}{4} \nabla_H^2 (\chi_1 - \chi_2) + J(\chi_1, \zeta) = -\frac{\beta}{f_0} d_1 \frac{\partial \chi_1}{\partial x} \quad . \tag{3.49}$$

Noting that the Jacobian of a variable with itself is zero, and that

$$\zeta = \frac{1}{\epsilon} ( \chi_2 - \chi_1) \tag{3.50}$$

where $\epsilon = \frac{\rho_2 - \rho_1}{\rho_2}$, (3.49) can be rewritten

$$\frac{\epsilon \delta_E^I}{4} \nabla_H^2 (\chi_1 - \chi_2) + J(\chi_1, \chi_2) = -\frac{\epsilon \beta}{f_0} d_1 \frac{\partial \chi_1}{\partial x} \quad . \tag{3.51}$$

Except for the additional term due to planetary $\beta$, this equation is the dimensional form of the equation derived by Zang, Janowitz and Pietrafesa (1987). The coupling of flow between the layers is clearly evident here. If interfacial friction were zero, i.e. $\delta_E^I = 0$, and planetary $\beta$ were negligible, then (3.51) would reduce to a condition that geostrophic flow be parallel or anti-parallel in the two layers (cf. (3.22)). This tendency for the upper layer flow to parallel that in the lower layer can be envisaged as the steering of the upper layer by the lower through displacements of the interface. The first term in (3.51) represents a frictional drag on the upper layer by the lower

layer due to their relative motion. This frictional term reduces the ability of the lower layer to steer the upper, tends to spread upper layer flow in all directions and adds a new degree of freedom when compared to the three-layer model. Comparing (3.51) to that governing two-dimensional heat diffusion shows that the planetary $\beta$ term acts in such a way as to "advect" the upper layer pressure westward. Thus the dynamics of the upper layer, where it overlies the lower layer, can be envisaged as a combination of steering and drag due to the lower layer, and westward "advection" by planetary $\beta$. An alternative physical explanation of (3.51) in terms of potential vorticity would balance the vorticity loss due to friction plus the change in vorticity due to stretching of upper layer fluid columns against the advection of planetary vorticity.

Integrating (3.14) between the surface and bottom gives the vertical velocity just above the thin bottom Ekman layer as

$$w_2|_{z=-d_1} = -\frac{\beta}{f_0}(d_1 v_1 + (h-d_1)v_2) \quad . \tag{3.52}$$

Combining this with Pedlosky's result for an Ekman layer on a sloping bottom, (3.28) the equations governing motion where layers are in contact with the bottom are

$$\begin{aligned} \tfrac{\delta_E}{2}\nabla_H^2\,\chi_1 + \tfrac{\partial h}{\partial x}\tfrac{\partial\,\chi_1}{\partial y} &= -\tfrac{\beta}{f_0}h\tfrac{\partial\,\chi_1}{\partial x} && x \le x_I \\ \tfrac{\delta_E}{2}\nabla_H^2\,\chi_2 + \tfrac{\partial h}{\partial x}\tfrac{\partial\,\chi_2}{\partial y} &= -\tfrac{\beta}{f_0}(d_1\tfrac{\partial\,\chi_1}{\partial x} + (h-d_1)\tfrac{\partial\,\chi_2}{\partial x}) && x > x_I \end{aligned} \quad . \tag{3.53}$$

The right hand sides of the second equation is in fact one of the terms in the Sverdrup balance for a two-layer model.

Under the long wave approximation (3.36) alongshore derivatives are small compared to cross-topography derivatives so that the Laplacians $\nabla_H^2$ in (3.51) and (3.53) may be approximated by $\frac{\partial^2}{\partial x^2}$ to an accuracy of order $(\frac{L_x}{L_y})^2$. Using this approximation the equations which must be solved become

$$\frac{\delta_E}{2}\frac{\partial^2\,\chi_1}{\partial x^2} + \frac{\partial h}{\partial x}\frac{\partial\,\chi_1}{\partial y} = -\frac{\beta}{f_0}\frac{\partial\,\chi_1}{\partial x}, \quad x \le x_I \tag{3.54}$$

$$\left.\begin{aligned} \epsilon\tfrac{\delta_E^I}{4}\tfrac{\partial^2}{\partial x^2}(\chi_1-\chi_2)+J(\chi_1,\chi_2) &= -\tfrac{\beta}{f_0}\epsilon d_1\tfrac{\partial\chi_1}{\partial x} \\ \tfrac{\delta_E}{2}\tfrac{\partial^2\chi_2}{\partial x^2}+\tfrac{\partial h}{\partial x}\tfrac{\partial\chi_2}{\partial y} &= -\tfrac{\beta}{f_0}(d_1\tfrac{\partial\chi_1}{\partial x}+(h-d_1)\tfrac{\partial\chi_2}{\partial x}) \end{aligned}\right\} x > x_I \qquad (3.55)$$

### 3.4a Boundary and Matching Conditions

Boundary conditions and matching conditions at the coast, the shelf break and along the line where the topography intersects the bottom all involve constraints on the transport within the layers at those points. It is useful to state the transports before proceeding to derive the specific matching and boundary conditions.

The total transport in a layer is the sum of a geostrophic transport plus one or more Ekman transports. The components of transport due to geostrophic flow within the density layers can be written

$$\begin{aligned} U_1^g &= \begin{cases} hu_1 & x \le x_I \\ (d_1-\zeta)u_1 & x > x_I \end{cases} \\ V_1^g &= \begin{cases} hv_1 & x \le x_I \\ (d_1-\zeta)v_1 & x > x_I \end{cases} \end{aligned} \qquad (3.56a)$$

$$\left.\begin{aligned} U_2^g &= (d_2+\zeta)u_2 \\ V_2^g &= (d_2+\zeta)v_2 \end{aligned}\right\} x \ge x_I \quad . \qquad (3.56b)$$

From Appendix B the interfacial Ekman transports in the upper and lower density layers in dimensional form are

$$\left.\begin{aligned} U_1^I &= -\tfrac{\delta_E^I}{4}[(u_1-u_2)+(v_1-v_2)] \\ V_1^I &= \tfrac{\delta_E^I}{4}[(u_1-u_2)-(v_1-v_2)] \\ U_2^I &= \tfrac{\delta_E^I}{4}[(u_1-u_2)+(v_1-v_2)] \\ V_2^I &= -\tfrac{\delta_E^I}{4}[(u_1-u_2)-(v_1-v_2)] \end{aligned}\right\} x \ge x_I \quad . \qquad (3.57)$$

Note that the interfacial Ekman transports on either side of the interface are equal in magnitude but are opposite in direction. From Pedlosky (1979) the components of transport due to friction in the bottom Ekman layers where the upper and lower density layers are in contact with the bottom are

$$\left.\begin{aligned} U_1^b &= -\tfrac{\delta_E}{2}[u_1 + v_1] \\ V_1^b &= \tfrac{\delta_E}{2}[u_1 - v_1] \end{aligned}\right\} x \le x_I \tag{3.58a}$$

$$\left.\begin{aligned} U_2^b &= -\tfrac{\delta_E}{2}[u_2 + v_2] \\ V_2^b &= \tfrac{\delta_E}{2}[u_2 - v_2] \end{aligned}\right\} x \ge x_I \quad . \tag{3.58b}$$

Boundary and matching conditions must be applied along the line where the interface intersects the bottom, $x_I(y)$. Due to the topography this intersection moves on and offshore as the interface moves up and down, and its position must be determined as part of the solution. The position of the intersection for our idealized slope topography is related to the interface displacement by

$$x_I(y) = \begin{cases} x_b - \frac{1}{s_e}\zeta|_{x_I} & x_I \le x_s \quad x_b \le x_s \\ x_s + \frac{s}{s_e}(x_b - x_s) - \frac{1}{s_e}\zeta|_{x_I} & x_I \le x_s \quad x_b > x_s \\ x_s + \frac{s}{s_e}(x_b - x_s) - \frac{1}{s}\zeta|_{x_I} & x_I > x_s \quad x_b \le x_s \\ x_b - \frac{1}{s}\zeta|_{x_I} & x_I > x_s \quad x_b > x_s \end{cases} \tag{3.59}$$

$x_b$ is where the interface would intersect the bottom if it were flat, (see Figure 3-4). Of the four cases above the middle two are complicated by the fact that $x_b$ and $x_I$ span the shelf break.

Flow is forced by prescribing the surface and interface displacement, and thus the vertical pressure distribution, along the deepest isobath $x = x_{max}$. This establishes a geostrophic flow into the domain from the deep ocean. For simplicity this offshore forcing of the shelf and slope will be forced by imposing linear pressure gradients along

the deepest isobath i.e.

$$\left.\begin{aligned} \chi_1 &= \Gamma_1 y \\ \chi_2 &= \Gamma_2 y \end{aligned}\right\} x = x_{max} \quad . \tag{3.60}$$

The coastal boundary condition is that the sum of geostrophic and Ekman transports across the coast, $x = 0$, be zero. Since the depth at the coast is also zero there is no geostrophic transport there (see (3.56a)). Thus the coastal boundary condition for total transport is that the cross-shelf bottom Ekman transport vanishes. From (3.58a), noting that alongshore velocities are assumed to be much stronger than cross-shelf velocities, this can stated approximately

$$v_1 = 0 \qquad at \qquad x = 0 \quad . \tag{3.61}$$

In the lower layer there can be no geostrophic transport across the line where the interface intersects the bottom since the layer has no thickness there. Thus the boundary condition that there is no total transport in the lower layer across this line can be satisfied if the sum of interfacial and bottom Ekman transports normal to the line of intersection is zero. In order to conserve mass the interfacial Ekman transport must be converted to Ekman transport in the bottom boundary layer. The vanishing lower layer thickness blocks any interfacial Ekman transport from crossing the line of intersection. The boundary condition developed for this situation is very similar to the boundary condition for the blocking of wind driven Ekman transport at a coast used by Csanady (1978) and examined in detail by Mitchum and Clarke (1986). If $\alpha_I$ is the angle which the line of intersection of the interface with the bottom makes with the topography defined by $\tan \alpha_I = \frac{\partial x_I}{\partial y}$,then, due to the assumption about horizontal scales (3.36), $\alpha_I$ is a small angle. In addition it was assumed that cross-shore velocities are weak compared to alongshore velocities. Therefore the boundary condition, from (3.57) and (3.58b), may be approximated to order $(\frac{L_x}{L_y})$ as

$$\frac{\delta_E^I}{2}(v_1 - v_2) - \delta_E v_2 = 0 \qquad at \qquad y = 0 \quad . \tag{3.62}$$

Both (3.54) and (3.55) are parabolic and have the form of the equation governing one-dimensional heat diffusion where $-y$ is the "time-like" coordinate. Both equations must have an "initial" condition along $y = 0$. It will be assumed that no flow enters the domain of interest across $y = 0$, so that the pressure along this line can be taken to be zero, i.e.

$$\chi_1 = \chi_2 = 0 \qquad at \qquad y = 0 \quad . \tag{3.63}$$

### 3.4b Matching Conditions

Flow in either layer which crosses the shelf break, and flow in the upper layer which crosses the line where the interface and topography intersect must conserve mass, and therefore the transport across these lines must be continuous. In addition the pressure across both of these lines must also be continuous. This can be stated

$$\begin{aligned} [\chi_1]_{x_s^-} &= [\chi_1]_{x_s^+} \quad x_I \geq x_s \\ [\chi_2]_{x_s^-} &= [\chi_2]_{x_s^+} \quad x_I < x_s \end{aligned} \tag{3.64}$$

where $x_s^-$ is a small distance shoreward of the shelf break and $x_s^+$, a small distance offshore of the shelf break, and

$$[\chi_1]_{x_I^-} = [\chi_1]_{x_I^+} \tag{3.65}$$

where $x_I^-$ is a small distance shoreward of the line where topography and interface intersect and $x_I^+$ is a small distance offshore of this line.

Continuity of pressure across any given line in the upper layer implies that the pressure gradient along the line must also be continuous across that line. The geostrophic transport in a density layer at right angles to any line is the product of the layer thickness and the pressure gradient along the line (3.56a) . Provided that the layer thickness is continuous across a line then pressure continuity implies that geostrophic transport normal to the line must also be continuous. Thus at the shelf break and at the topography/interface intersection pressure continuity ensures that geostrophic

transport is also continuous. To ensure continuity of total mass transport across these lines the Ekman transport must also be continuous across them.

Transport will be continuous across the shelf break if the bottom Ekman layer transport normal to the shelf break is continuous. There are two cases depending on which layer is in contact with the bottom at the shelf break. From (3.58a) and (3.58b) assuming that alongshore velocities are much larger than cross-shelf velocities, this matching condition is approximatly

$$\begin{aligned} [v_1]_{x_s^-} &= [v_1]_{x_s^+} \quad x_I \geq x_s \\ [v_2]_{x_s^-} &= [v_2]_{x_s^+} \quad x_I < x_s \quad . \end{aligned} \tag{3.66}$$

In order for upper layer flow crossing the line where the interface intersects the bottom to conserve mass, the Ekman transport normal to this line must be continuous. Therefore the component of upper layer bottom Ekman transport normal to and just shoreward of the interface/topography intersection must equal the component of upper layer interfacial Ekman transport normal to and just offshore of this intersection. Assuming that alongshore flows are strong compared to cross-shore flows and that alongshore scales are large compared to cross-shore scales, so that $\alpha_I$ is a small angle, the above may be approximated by

$$\delta_E [v_1]_{x_I^-} = \frac{\delta_E^I}{2} [(v_1 - v_2)]_{x_I^+} \tag{3.67}$$

It should be noted that all the boundary and matching conditions are either independent of the Ekman layer thickness (e.g. ((3.61),(3.66)) or dependent on the ratio of interfacial to bottom Ekman layer thickness equal to $\sqrt{\frac{A_V^I}{A_V}}$ (e.g. (3.62), (3.67)). This ratio is independent of the value of $f$ and consequently the boundary or matching conditions are exactly the same whether on an $f$ or a $\beta$-plane.

### 3.4c Non-Dimensional Equations

The governing equations and boundary conditions can be shown to be dependent on a small group of non-dimensional numbers. Dimensionless variables can be defined by

$$\begin{aligned} y &= L_y y' \\ x &= \sqrt{\tfrac{\delta_E}{2s}} L_y x' \\ \chi_1, \chi_2 &= \eta_0(\chi_1', \chi_2') \\ \varsigma &= \varsigma_0 \eta' \\ \beta' &= \tfrac{\beta L_y}{f_0} \\ h &= h_0 h' \\ d_1 &= h_0 d_1' \end{aligned} \quad . \tag{3.68}$$

$\eta_0$ is the magnitude of the surface displacement and also gives the magnitude of the pressure expressed in meters of water. The non-dimensional interface displacement from (3.18) is

$$\varsigma' = \chi_2' - \chi_1' \quad . \tag{3.69}$$

Horizontal scales in equation (3.54) are related by (3.35). With the scales (3.68) the non-dimensional governing equations are

$$\frac{\partial^2 \chi_1'}{\partial x'^2} + s' \frac{\partial \chi_1'}{\partial y'} = -\frac{\beta' h'}{\Delta h'} \frac{\partial \chi_1'}{\partial x'} \qquad x \le x_I \tag{3.70a}$$

$$R \frac{\partial^2}{\partial x'^2}(\chi_1' - \chi_2') + J(\chi_1', \chi_2') = -\frac{\beta'}{\frac{\varsigma_0}{h_0}} d_1' \frac{\partial \chi_1'}{\partial x'} \qquad x > x_I \tag{3.70b}$$

$$\frac{\partial^2 \chi_2'}{\partial x'^2} + s' \frac{\partial \chi_2'}{\partial y'} = -\frac{\beta'}{\Delta h'}\left(d_1' \frac{\partial \chi_1'}{\partial x'} + (h' - d_1') \frac{\partial \chi_2'}{\partial x'}\right) \qquad x > x_I \quad . \tag{3.70c}$$

The non-dimensional bottom slope for the idealized topography is

$$s' = \begin{cases} s_{rel} & x \leq x_s \\ 1 & x > x_s \end{cases} \quad . \tag{3.71}$$

$s_{rel}$ is the ratio of the linear shelf slope to the slope of the continental slope, i.e. $s_{rel} = \frac{s_s}{s}$.

The non-dimensional number $R$ is

$$R = \frac{\epsilon \delta_E^I}{4\eta_0} \sqrt{\frac{2sL_y}{\delta_E}} \tag{3.72}$$

and measures the importance of such effects as stratification and the size of the interfacial and bottom Ekman layers. For the scales in Table 3.2 $R$ is of order 1, thus interfacial friction in the upper density layer is as important as the steering by the lower density layer.

$\Delta h' = \frac{sL_x}{h_0}$ is the depth change over the flow's horizontal scale relative to the total depth. $\frac{\beta'}{\Delta h'}$ measures the importance of planetary $\beta$ relative to topographic $\beta$. In (3.70b) $\frac{\eta_0}{\epsilon h_0}$ is equal to $\frac{\zeta_0}{h_0}$ which is the magnitude of the interface displacement relative to the total depth. The ratio $\frac{\beta' d_1'}{\frac{\zeta_0}{h_0}}$ measures the importance of planetary $\beta$ relative to the "topographic" $\beta$ which is due to the warping of the interface.

For shoreward flow the forcing along the deepest isobath (3.60) is

$$\left.\begin{aligned} \chi_1' &= -y' \\ \chi_2' &= -\Gamma' y' \end{aligned}\right\} x' = x'_{max} \quad . \tag{3.73}$$

$\Gamma'$ is the strength of the lower layer flow relative to the strength of the upper layer flow. The initial conditions are

$$\chi_1' = \chi_2' = 0 \qquad at \qquad y = 0 \quad . \tag{3.74}$$

The coastal boundary condition (3.61) expressed in terms of pressure is

$$\frac{\partial \chi_1'}{\partial x'} = 0 \qquad at \qquad x = 0 \quad . \tag{3.75}$$

| | | |
|---|---|---|
| Depth at shelf break, $h_s$ | $100m$ | |
| Bottom slope: shelf, $s_s$ | 0.001 | |
| Shelf width, $x_s$ | $100km$ | |
| Coriolis, $f_0$ | $10^{-4}s^{-1}$ | |
| Planetary $\beta$ | $10^{-11}m^{-1}s^{-1}$ | |
| Density excess, $\epsilon = \frac{\rho_2 - \rho_1}{\rho_2}$ | 0.001 | |
| Bottom turbulent eddy viscosity, $A_V$ | $10^{-2}m^2s^{-1}$ | |
| Interior turbulent eddy viscosity, $A_V^I$ | $10^{-3}m^2s^{-1}$ | |
| Bottom Ekman layer thickness, $\delta_E = \sqrt{\frac{2A_V}{f}}$ | $10m$ | |
| Interfacial Ekman layer thickness, $\delta_E^I = \sqrt{\frac{2A_V^I}{f}}$ | $3m$ | |
| Relative Ekman layer thickness, $\frac{\delta_E^I}{\delta_E}$ | 0.3 | |
| Unit of cross-shelf distance (i.e. $x'$ units) | $10km$ | |
| | $f-plane$ | $\beta-plane$ |
| Alongshore scale, $L_y$ | $250km$ | $1000km$ |
| Cross-shelf scale, $L_x$ | $\geq 12km$ | $\geq 20km$ |
| Maximum water depth, $h_{max}$ | $500m$ | $3100m$ |
| Bottom slope: slope, $s$ | 0.01 | 0.05 |
| Slope width, $x_{max} - x_s$ | $40km$ | $60km$ |
| Upper layer thicknesses, $d_1$ | $100 - 250m$ | $100 - 1000m$ |
| Lower layer thicknesses, $d_2$ | $250 - 400m$ | $2100 - 3000m$ |
| Free surface displacement, $\eta_0$ | $1cm$ | $10cm$ |
| Interface displacement, $\zeta_0$ | $20m$ | $100m$ |
| **Calculated Scales** | | |
| Alongshore velocity, $v_0$ | $5cms^{-1}$ | $5cms^{-1}$ |
| Cross isobath interfacial movement, shelf= $\frac{\zeta_0}{s_s}$ | $10km$ | $10km$ |
| Cross isobath interfacial movement, slope= $\frac{\zeta_0}{s}$ | $2km$ | $0.4km$ |
| Non-dimensional interface movement over slope , $\Delta_s = \frac{\zeta_0}{sL_x}$ | 0.1 | 0.2 |
| Non-dimensional interfacial friction,$R$ | 1.8 | 0.83 |

Table 3.2: Scales for Two-Layer Model with Interfacial Friction

The boundary condition for the lower layer where the interface intersects the bottom (3.62) in terms of pressure is

$$\frac{\delta_E^{rel}}{2}\left(\frac{\partial \chi_1'}{\partial x'} - \frac{\partial \chi_2'}{\partial x'}\right) - \frac{\partial \chi_2'}{\partial x'} = 0 \quad at \quad x' = x_I' \quad . \tag{3.76}$$

$\delta_E^{rel}$ is the thickness of the interfacial Ekman layer relative to the thickness of the bottom Ekman layer, i.e. $\delta_E^{rel} = \frac{\delta_E^I}{\delta_E}$. Continuity of surface pressure at the shelf break, (3.64), and that at the interface/bottom intersection, (3.65) are, in terms of pressure

$$\begin{aligned} [\,\chi_1']_{x_s^{-\prime}} &= [\,\chi_1']_{x_s^{+\prime}} \quad x_I' \geq x_s' \\ [\,\chi_2']_{x_s^{-\prime}} &= [\,\chi_2']_{x_s^{+\prime}} \quad x_I' < x_s' \quad . \\ [\,\chi_1']_{x_I^{-\prime}} &= [\,\chi_1']_{x_I^{+\prime}} \quad x_I' < x_s' \end{aligned} \tag{3.77}$$

The match of Ekman transport across the shelf break (3.66) is

$$\left[\frac{\partial\, \chi_1'}{\partial x'}\right]_{x_s^{-\prime}} = \left[\frac{\partial\, \chi_1'}{\partial x'}\right]_{x_s^{+\prime}} \qquad x_I' \geq x_s'$$

$$\left[\frac{\partial\, \chi_2'}{\partial x'}\right]_{x_s^{-\prime}} = \left[\frac{\partial\, \chi_2'}{\partial x'}\right]_{x_s^{+\prime}} \qquad x_I' < x_s' \quad . \tag{3.78}$$

The match of Ekman transport across the interface/bottom intersection (3.67) in terms of pressure is

$$\left[\frac{\partial\, \chi_1'}{\partial x'}\right]_{x_I^{-\prime}} = \frac{\delta_E^{rel}}{2}\left[\frac{\partial}{\partial x'}(\,\chi_1' - \,\chi_2')\right]_{x_I^{+\prime}} \quad . \tag{3.79}$$

In non-dimensional coordinates the position of the interface/bottom intersection (3.59) is

$$x_I' = \begin{cases} x_b' - \frac{\Delta_s}{s_{rel}}\zeta' & x_I' \le x_s' \quad x_b' \le x_s' \\ x_s' + \frac{1}{s_{rel}}(x_b' - x_s') - \frac{\Delta_s}{s_{rel}}\zeta' & x_I' \le x_s' \quad x_b' > x_s' \\ x_s' + \frac{1}{s_{rel}}(x_b' - x_s') - \Delta_s\zeta' & x_I' > x_s' \quad x_b' \le x_s' \\ x_b' - \Delta_s\zeta' & x_I' > x_s' \quad x_b' > x_s' \end{cases} . \tag{3.80}$$

$\Delta_s = \frac{\zeta_0}{L_x s}$ is the size of the cross-slope movement of the interface/bottom intersection over the continental slope. For the values in Table 3.2 $\Delta_s$ is 0.1 non-dimensional units or $1km$. Such a small movement implies that the continental slope is steep enough that cross-slope movement of the intersection need not be considered. However the shelf has a much gentler slope and consequently the scale of the cross-shelf movement, $\frac{\Delta_s}{s_{rel}}$, is 1 non-dimensional unit or $10km$ for the values in Table 3.2. Such movement over the shelf is significant and must be included in the solution.

### 3.4d Solution Scheme

Solving the governing equations is complicated by the fact that they are coupled. Equation (3.70b) contains both the upper and lower layer pressure and therefore cannot be solved independently of (3.70c). Equation (3.70c) is dependent on the upper layer pressure and is also coupled to the upper layer through the boundary condition at the interface/bottom intersection (3.76). The following is a development of a scheme which allows the coupled equations to be solved.

The governing equations are related to equations governing unsteady one-dimensional heat diffusion. The "time-like" coordinate is $-y$. Equations (3.70a) and (3.70c) are the same as that governing heat diffusion in a solid bar with thermal diffusivity, $s'$. The upper layer equation (3.70b) is the same as that governing one-dimensional heat diffusion in a medium which is moving parallel to the x-axis. The strength of the advection of heat is given by

$$\frac{\frac{\partial \chi_2'}{\partial y'}}{\frac{\partial \chi_2'}{\partial x'}} \tag{3.81}$$

and the thermal diffusivity is

$$\frac{R}{\frac{\partial \chi_2'}{\partial x'}} \quad . \tag{3.82}$$

Exploiting the parabolic nature of the governing equations a numerical solution would use the pressures at one "time step", $y_1$, to find the pressures at the next time step, $y_2$ (lower latitude for an east coast). Given both pressures at $y_1$ (3.70c) cannot be solved first for lower layer pressure at $y_2$ because the cross-shore derivative of the as yet unknown upper layer pressure at $y_2$ is required for both (3.70c) and the boundary condition (3.76). Similarly (3.70b) cannot be solved first for upper layer pressure at $y_2$ because lower layer pressure at $y_2$ is needed to calculate the advection (3.81) and the matching condition (3.79).

The position of the interface/bottom intersection at the new time step $x_I(y_2)$ must be known in order to determine where to apply the boundary condition (3.76) and the

matching condition (3.79). This position is related to interface displacement which is proportional to the pressure difference between the layers. Consequently $x_I(y_2)$ cannot be calculated without knowing both pressures at $y_2$ but these pressures cannot be determined without knowing $x_I(y_2)$. This difficulty can be resolved if the position of the interface/bottom intersection at the current time step, $y_1$, is used as an estimate for the position at the new time step, $y_2$. i.e. assume

$$x_I|_{y_2} \approx x_I|_{y_1} \quad . \tag{3.83}$$

In the solutions given later it is found that the intersection moves only a small distance across the topography, thus the intersection's position at $y_1$ is such a good estimate of its position at $y_2$ that it need not be revised once a complete solution at $y_2$ is obtained.

The cross-shore derivative of the as yet undetermined upper layer pressure at the next time step, $y_2$, is required for (3.70c) and the boundary condition (3.76). This can also be estimated by its value at the current time step, $y_1$, i.e. assume

$$\frac{\partial \chi_1'}{\partial x'}|_{(x,y_2)} \approx \frac{\partial \chi_1'}{\partial x'}|_{(x,y_1)} \quad . \tag{3.84}$$

The difference between the derivative and its estimate was found to be less than 5% for the 80 by 100 grid point numerical domain used to solve the governing equations. Thus the error in the estimate (3.84) is also so small that it need not be revised.

The solution scheme proceeds as follows: given the upper and lower layer pressures $\chi_1'$ and $\chi_2'$ at $y_1$, then (3.70c), together with the offshore boundary condition (3.73), the estimated position of the interface/bottom intersection, (3.83), and the estimated value for the cross-slope derivative of upper layer pressure (3.84) can all be solved numerically to give the lower layer pressure at the next time step, $y_2$. To ensure numerical stability upstream differences for the $\beta'$ term and an implicit finite difference scheme are used. The lower layer pressure at $y_2$ is then used to calculate the advection speed (3.81), the thermal diffusivity, (3.82), and the derivative of lower layer pressure in the matching condition (3.79). Equations (3.70a) and (3.70b) are then solved for upper layer pressure at the new time step, $y_2$. Again an implicit finite difference scheme is used

employing centered differences for the diffusive term $\frac{\partial^2 \chi_1'}{\partial x'^2}$ and upstream differences for the "advective" term $\frac{\partial \chi_1'}{\partial x'}$ to ensure numerical stability. The interface displacement at $y_2$ is calculated by taking the difference in pressures and is used in (3.69) to calculate a position for the interface bottom intersection at $y_2$. To reduce the complexity of the numerical scheme the intersection is assumed to be at the nearest cross-shore grid point to its calculated position. With a complete solution at the new time step , $y_2$, the above procedure can be repeated successively until the latitudinal extent of the numerical domain is covered.

### 3.4e Results and Discussion

Using the method outlined in the previous section the governing equations together with the boundary and matching conditions can be solved. Solutions will be presented in the form of contours of upper and lower layer pressure as well as contours of interface displacement. Contours of pressure in the upper or lower layer are also flow lines for geostrophic motion in each layer's core. Though calculated, the solution for the inner shelf will not be plotted when the solutions show no significant flow there. Thus all plots show only the outer shelf and the continental slope. In each plot the labeled dashed line marks the straight shelf break and the chain dashed line is where the interface intersects the bottom. This line may curve due to the vertical movement of the interface. In all cases the upper layer is forced by a prescribed pressure which increases linearly along the offshore isobath to a maximum value of unity. The lower layer is forced by a prescribed pressure which increases linearly to a maximum value, $\Gamma'$, along the deepest isobath.

Unless specifically stated solutions of this interfacial friction model are for an $f$-plane. Table 3.2 gives typical scales for an $f$-plane flow with a $250km$ wide inflow impinging on the upper continental slope. The maximum water depth is $500m$, the bottom slope is 0.001 for the shelf and 0.01 for the continental slope. The upper layer thickness varies between $80m$ and $200m$ depending on the case being studied.

For a larger alongshore scale and greater water depths the effects of planetary $\beta$ must be included. This is done in section 3.4j. Typical scales in these cases, also given in Table 3.2, are a $1000km$ wide inflow, comparable to the large scale general circulation of the deep ocean, a maximum water depth of $3100m$, a bottom slope of 0.001 for the shelf and 0.05 for the continental slope.

### 3.4f Baroclinicity

Variations due to the baroclinicity of the deep ocean forcing can be studied by varying the relative strength of the upper and lower layer forcing, $\Gamma'$. In this $f$ plane series of solutions an upper layer is chosen which is twice as thick as the water depth at the shelf break, and various cases of deep ocean flow ranging from a barotropic flow to a flow with a motionless lower layer are considered.

Figure 3-5 shows the solution when the deep ocean inflow is barotropic ($\Gamma' = 1$). Both the upper and lower layer pressures, Figures 3-5a and 3-5b, have the same pattern. The response of the shelf/slope is a barotropic flow confined near the deep ocean forcing as in the barotropic solutions of Wang (1982). Friction, which allows cross-topography flow, is not strong enough to allow significant motion across the steep continental slope. The flow pattern in both layers is approximately 1 unit wide at its widest point, verifying that the ATW scaling (3.35) in this case is appropriate to both layers. The interface displacement is not shown since the interface is flat for this barotropic flow.

In Figure 3-6 the strength of the deep ocean forcing in the lower layer is half that in the upper layer ($\Gamma' = 0.5$). The lower layer flow pattern in Figure 3-6a is similar to that for barotropic flow and to that obtained in the model without interfacial friction in Figure 3-3. The upper layer flow in Figure 3-6c has a slightly wider cross-slope width than the barotropic flow in Figure 3-5c. The interface displacement is shown in Figure 3-6b.

In Figure 3-7 the deep ocean forcing in the lower layer is one tenth ($\Gamma' = 0.1$) of the upper layer forcing. The lower layer flows are weak and there are two distinct regions of flow: one adjacent to the forcing and another adjacent to the interface/bottom inter-

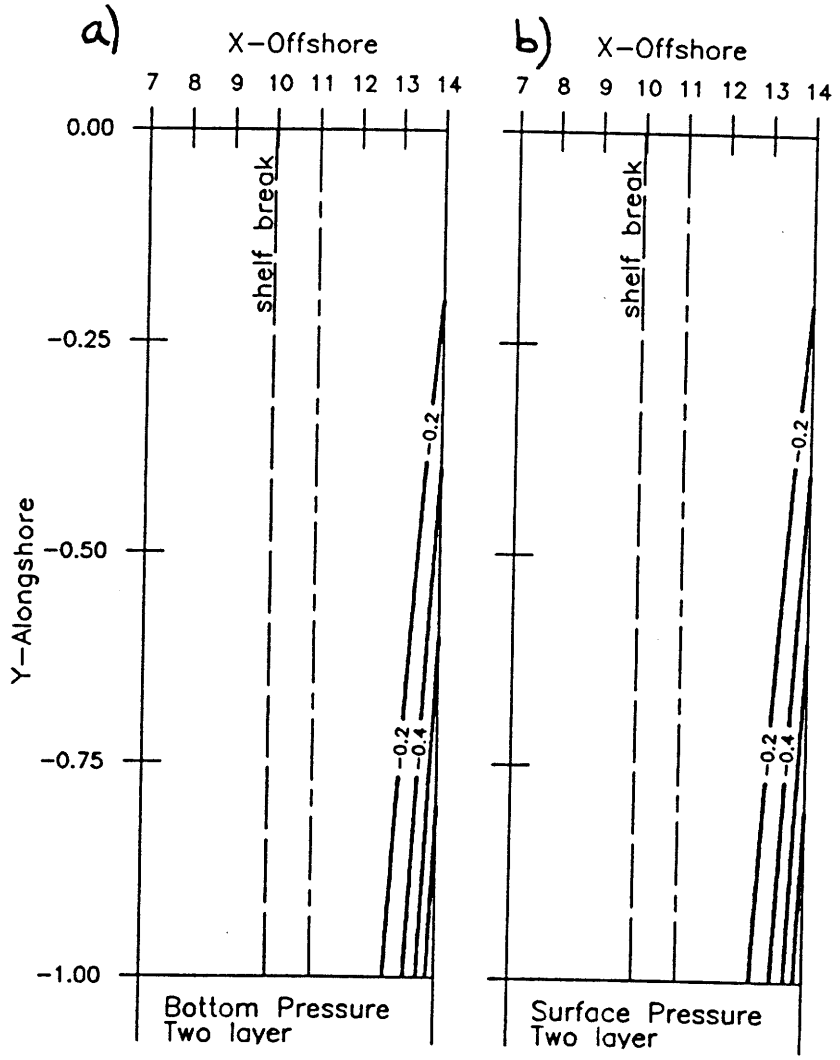


Figure 3-5: Pressure pattern in two-layer model due to barotropic deep ocean forcing of the shelf/slope ($R = 1.8, \delta_E^{rel} = 0.3, \Delta_s = 0.1, s_{rel} = 0.1, \Gamma' = 1$). Contour spacing is 0.2, minimum value is $-1$. Pressure contours are also flow lines for geostrophic flow in the layer cores. The labeled dashed line is the shelf break and the unlabeled chain dashed line is where the single interface intersects the bottom. a) Lower layer isobars. b) Upper layer isobars. The interface displacement is not plotted as it is zero for this barotropic flow.

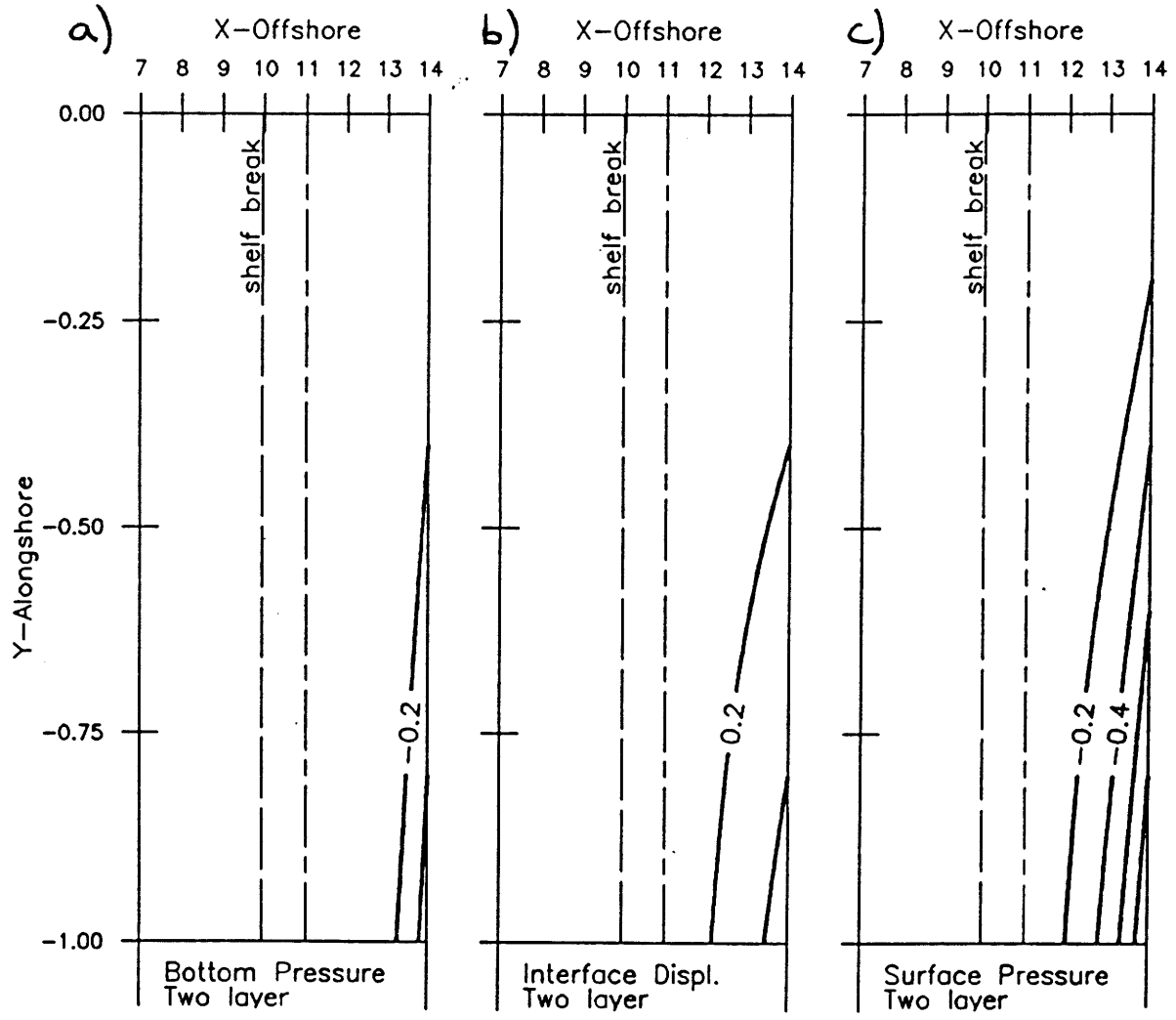


Figure 3-6: Flow induced by a baroclinic deep ocean when lower layer forcing is one half the strength of upper layer forcing ($R = 1.8, \Delta_s = 0.1, s_{rel} = 10, \delta_E^{rel} = 0.3, \Gamma' = 0.5$). Contour spacing is 0.2. a) Bottom layer pressure, minimum value $-0.5$. b) Interface displacement. c) Upper layer pressure, minimum value $-1.0$.

section. The latter results from the blocking of lower layer interfacial Ekman transport at the intersection. The upper layer flow pattern is wider than in the previous two cases but still does not penetrate onto the shelf. The upward interface displacements shown in Figure 3-7b mirror the upper layer pressure in Figure 3-7c.

In Figure 3-8 there is no lower layer flow in the deep ocean ($\Gamma' = 0$), a case not covered by the previous three layer model. Significant flow in the upper layer is confined to the region between the deep ocean forcing and the interface/bottom intersection. There is a weak lower layer flow in Figure 3-8a due to the blocking of lower layer interfacial Ekman transport.

Figure 3-9 shows the solution when the bottom flow is stronger than the surface flow, $\Gamma' = 1.25$. The flow pattern in this case is confined near the forcing and is very similar to that for a barotropic flow (Figure 3-5).

The last figure of this series, Figure 3-10, shows the solution when the deep ocean upper layer is motionless ($\Gamma' = \infty$) and when the lower layer inflow onto the slope is forced by a pressure which varies linearly from 0 to $-1$ along the deepest isobath. As in previous cases where the lower layer was moving, lower layer flow forms a narrow band adjacent to the deep ocean forcing. In Figure 3-10c there is significant upper layer flow induced by the moving lower layer despite the lack of direct forcing by the deep ocean. This flow is northward near the intersection but southward near the deep ocean. At the turning point $\frac{L_x}{L_y}$ is not small and consequently the details of the solution in the vicinity of this point are not reliable.

This series of figures shows that lower layer geostrophic flow is comprised of two components, one due directly to the forcing at the offshore boundary and another induced by the blocking of interfacial Ekman transport along the line where the interface intersects the bottom. The directly forced component of flow is confined to the outer continental slope and does not give rise to significant flow at the interface/bottom intersection. Consequently the shoreward boundary condition for this component is that flow vanishes far from the forcing. This boundary condition and the governing equation (3.70c) are exactly the same as those developed in the previous three layer model in

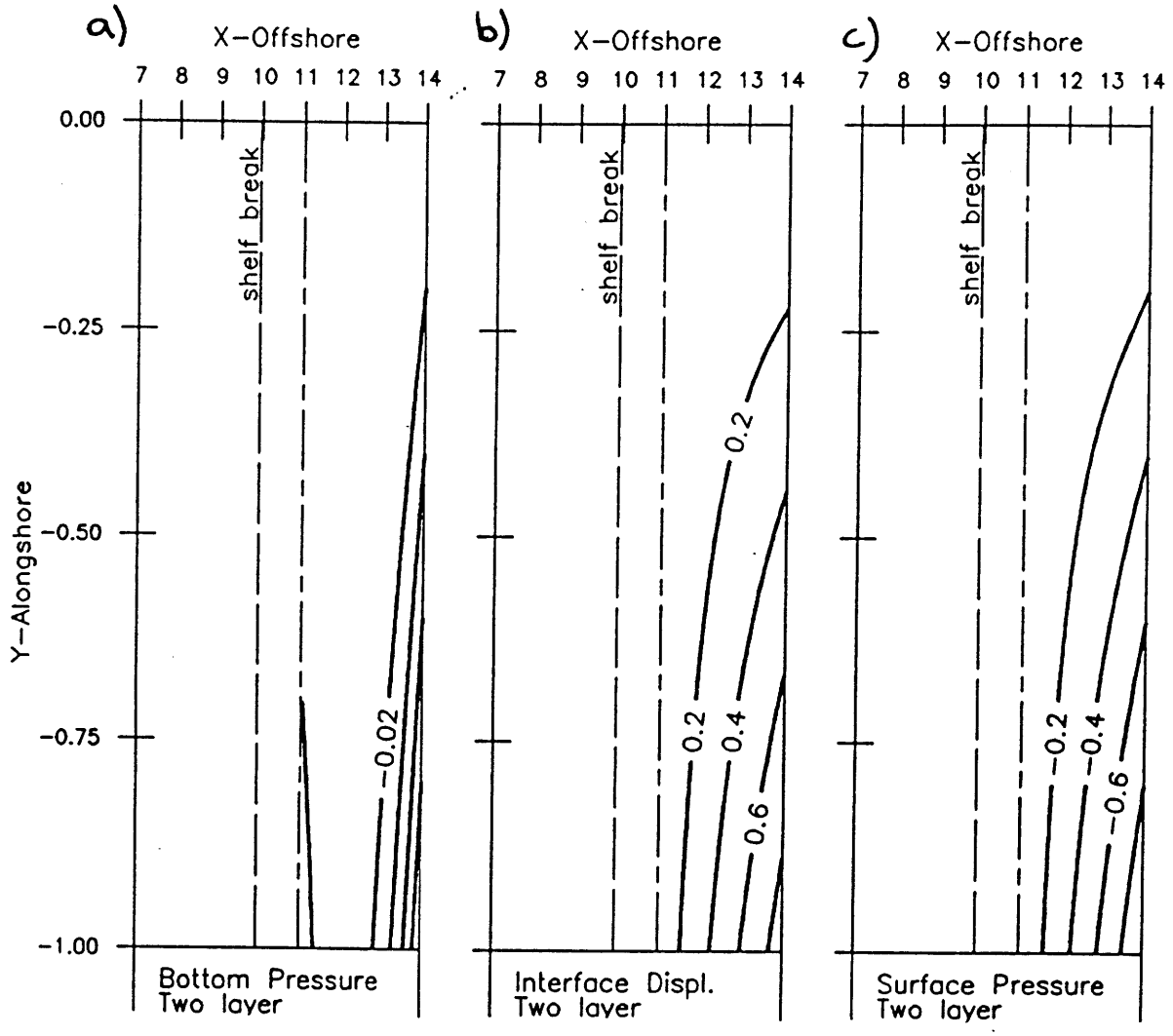


Figure 3-7: Flow induced when lower layer forcing is one tenth of that in the upper layer ($R = 1.8, \delta_E^{rel} = 0.2, \Delta_s = 0.1, s_{rel} = 0.1, \Gamma' = 0.1$). a) Lower layer pressure, minimum value $-0.1$, contour spacing 0.02. Note the weak ($= 0.02$) southward flow induced by the blocking of interfacial Ekman transport where the interface intersects the bottom. b) Interface displacement. c) Upper layer flow, minimum value $-1$.

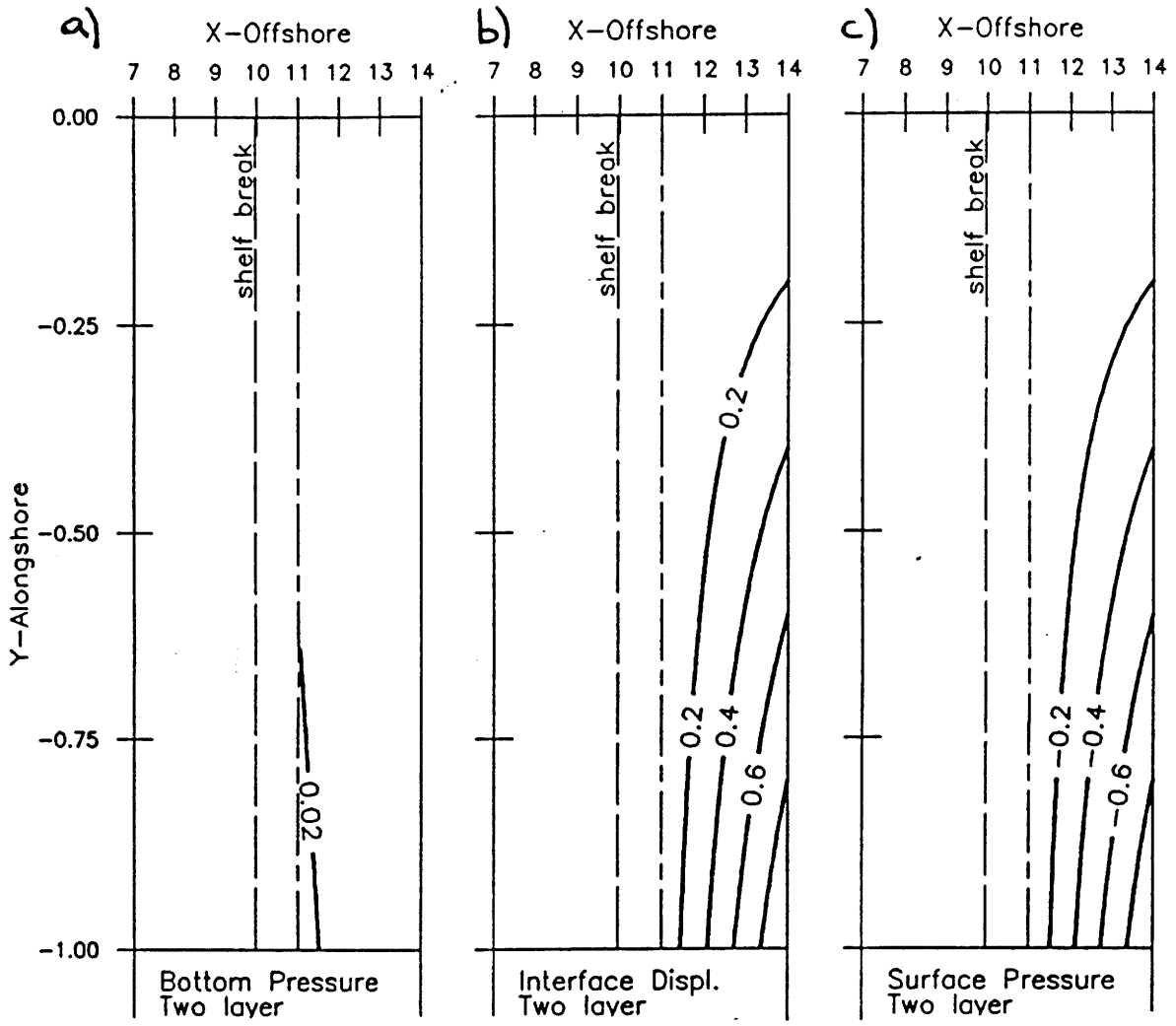


Figure 3-8: Flow induced by deep ocean forcing with a motionless bottom layer. ($R = 1.8, \delta_E^{rel} = 0.3, \Delta_s = 0.1, s_{rel} = 0.1, \Gamma' = 0$). a) Lower flow pressure is weak (0.02) and consists of a weak southward flow due to blocking of interfacial Ekman transport at the intersection of the interface and bottom. b) Interface displacement is upward. c) Surface pressure, minimum value $-1.0$.

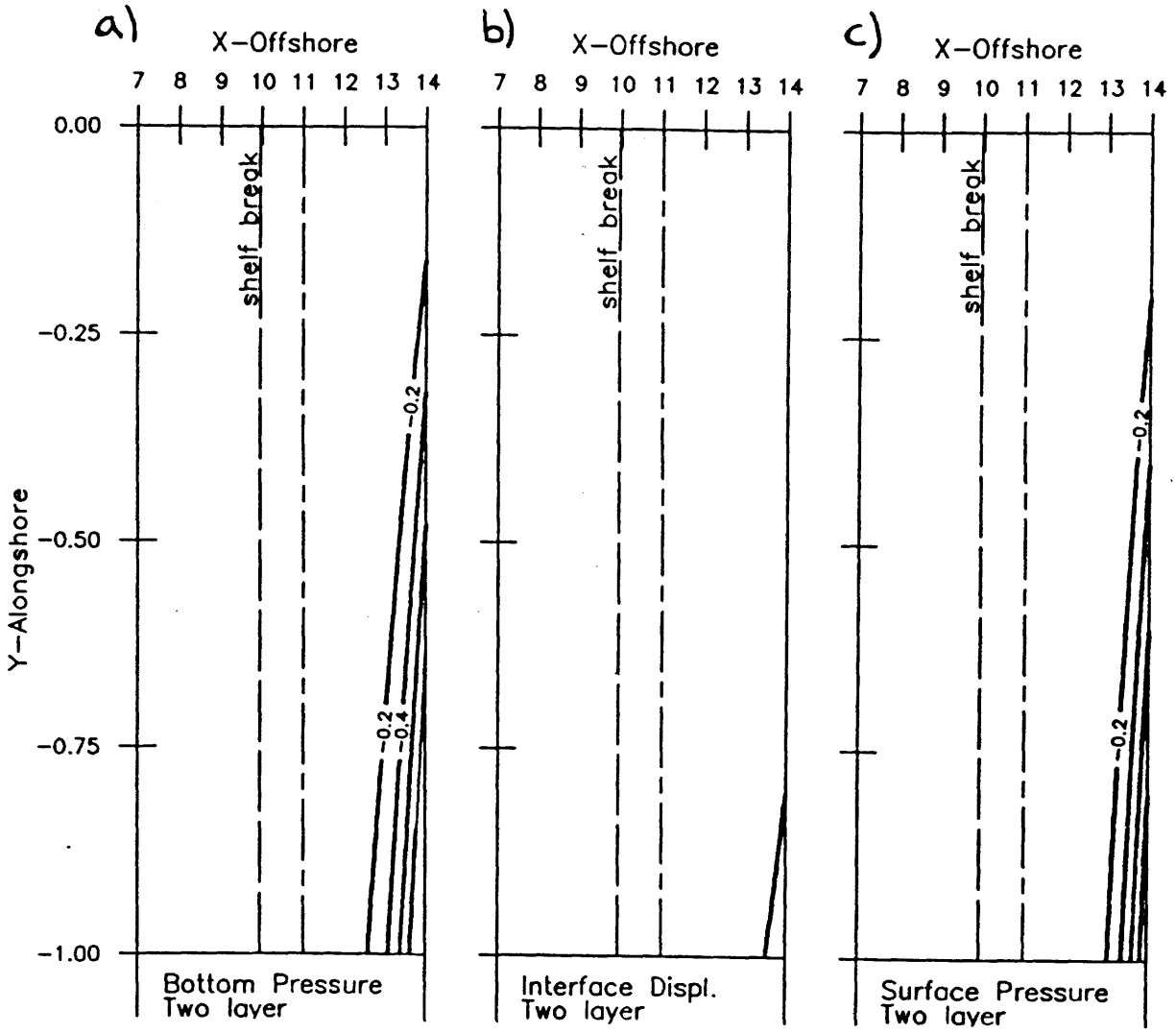


Figure 3-9: Flow pattern for a bottom intensified flow ($R = 1.8, \delta_E^{rel} = 0.3, \Delta_s = 0.1, s_{rel} = 0.1, \Gamma' = 1.25$). a) Lower layer pressure. b) Interface displacement. c) Upper layer pressure.

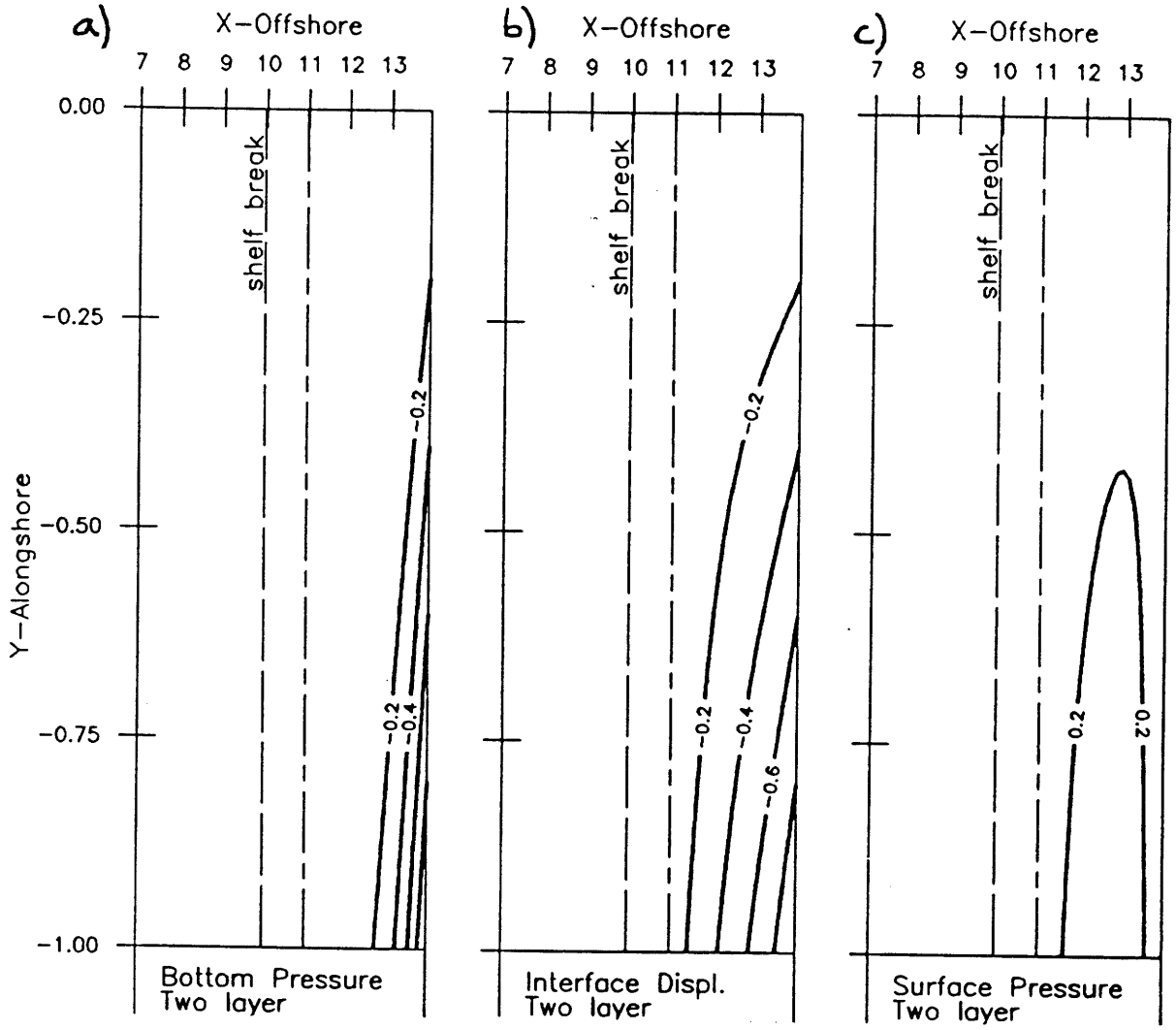


Figure 3-10: Solution for motionless deep ocean upper layer ($R = 1.8, \delta_E^{rel} = 0.3, \Delta_s = 0.1, s_{rel} = 0.1, \Gamma' = \infty$). a) Bottom layer pressure, minimum value $-1.0$. b) Interface displacement. c) Upper layer pressure.

section 3.3c. Flow within this component will be strongly influenced by topography, its cross-slope scale being determined by the ATW scaling (3.35). For typical scales (see Table 3.2) the cross-slope scale is $10km$ for an alongshore scale of $250km$. Thus bottom deep ocean flow can have little influence on the shelf as it is confined by topography to the outer slope.

The second component of lower layer geostrophic flow is not directly forced by the deep ocean, but is induced by motion in the upper layer through the boundary condition (3.76). The induced lower layer flow moves down the slope and equatorward (on an east coast) with a narrow cross-topography scale. Like the first component, its dynamics are governed by the bottom pressure equation (3.70c), and thus its horizontal scales will also be related by the ATW scaling (3.35). This induced flow is very similar to that due to the blocking of wind-driven Ekman transport by the coast, examined by Csanady (1978). The induced flow is weak being at most $\frac{1}{5}$ as strong as the upper layer flow. It is maximum when upper layer flow extends farthest shoreward, because near the interface/bottom intersection there will be a greater interfacial Ekman transport resulting from lower layer drag on the upper layer.

Significant upper layer flow is confined to the region between the forcing and the interface/bottom intersection. Flow shoreward of the intersection is weak, 0.02 or less, (see Figure 3-8c), and the reasons for this will be examined later. The cross-topography scale in the upper layer where it overlies the lower is determined by a combination of steering by the lower layer and interfacial drag which tends to spread the flow in all directions (see (3.51)). If the lower layer flow is strong, (Figures 3-5 and 3-6), steering dominates and the upper layer's cross-slope scale is almost the same as that in the lower layer (cf. the previous three-layer model). The region of cross-slope influence for these two flows is small, being limited by the steep continental slope. When lower layer flow is weak (Figures 3-7 and 3-8), interfacial frictional drag dominates and upper layer flow spreads to fill the region between the forcing and the interface/bottom intersection. The cross-slope scale is much wider in this case.

Any upper layer flow which does cross the intersection of the interface with the bottom (see Figure 3-8c) has a short cross-topography scale because its dynamics are governed by the ATW equation (3.70a) and therefore the scale relationship (3.35) applies. Thus further cross-topography motion is severely limited.

In a strongly bottom intensified deep ocean flow (Figure 3-10) lower layer motion induces upper layer motion in the same direction. The induced southward flow in Figure 3-10c cannot originate in the motionless upper deep ocean and by assumption cannot have crossed $y = 0$. Consequently upper layer fluid moving southward near the deep ocean must originate shoreward and southward of the forcing. Thus continuity is responsible for the northward flow near the interface/bottom intersection in Figure 3-10c.

This series of solutions demonstrates that near bottom deep ocean flow has a small cross-topography influence and that the upper deep ocean has its largest cross-topography influence when the lower layer is motionless, i.e. when the deep ocean is most strongly surface intensified, and its smallest influence when it is barotropic or near-barotropic. The maximum region of influence extends form the deep ocean to just shoreward of the interface/bottom intersection.

The conclusions for near bottom flow appear to contradict those of Chapter 2 where surface intensified flows had smaller cross-topography scales than bottom intensified flows. Unlike the vertically well mixed model the cross-topography scale of near bottom flow in this layered model is independent of the vertical shear in geostrophic velocity. In both models the bottom friction is assumed proportional to the near bottom geostrophic velocity. In the vertically well mixed model it was noted that the near bottom geostrophic velocity had vertical shear due to thermal wind. This vertical structure gave rise to a variation in bottom stress due to depth change alone and hence to a dependence of cross-topography scale on shear. Though there is clearly vertical structure in geostrophic flow in the layered models the near bottom geostrophic velocity is independent of depth because flow within the lowest layer is barotropic. Therefore bottom stress will not be affected by the vertical structure higher in the water column

and there ought to be no direct influence of shear on the cross topography scale of the near bottom flow.

### 3.4g Upper Layer Thickness

In the previous section significant upper layer flow was confined to the region between the deep ocean forcing and the line where the interface intersects the bottom. As the upper layer thins the intersection moves shoreward. In this section the consequent variation in flow pattern will be considered. It was found in the previous section that flows which were close to barotropic had small cross-slope scales, and thus were not greatly influenced by the intersection. Therefore attention here is restricted to deep ocean flows where the lower layer is motionless and the effect of the intersection is most pronounced.

The flow pattern for an upper layer with a thickness equal to the depth at the shelf break is shown in Figure 3-11. The flow patterns when the upper layer is $\frac{9}{10}$ and $\frac{8}{10}$ of the depth at the shelf break are shown in Figures 3-12 and 3-13. The most notable feature of these three solutions is that the thinning upper layer allows upper layer flow to spread proportionately further across the topography, although significant flow is still confined between the forcing and the interface/bottom intersection.

In the latter two figures the interface intersects the shelf rather than the slope. The intersection moves slightly shoreward due to upward movement of the interface (Figures 3-12b and 3-13b).

In all three cases, Figures 3-11a, 3-12a and 3-13a, the weak lower layer flow is forced by upper layer motion and is confined to the narrow band adjacent to the interface/bottom intersection. The flow is stronger and has a wider cross-topography scale when the interface intersects the shelf rather than the slope. Using the ATW scaling (3.35) which applies to lower layer flow, this wider scale is due to the weaker bottom slope of the shelf.

This series of figures demonstrates that the thinner the upper layer, i.e. the closer the interface/bottom intersection is to the coast, the wider the cross-topography influence of the deep ocean flow.

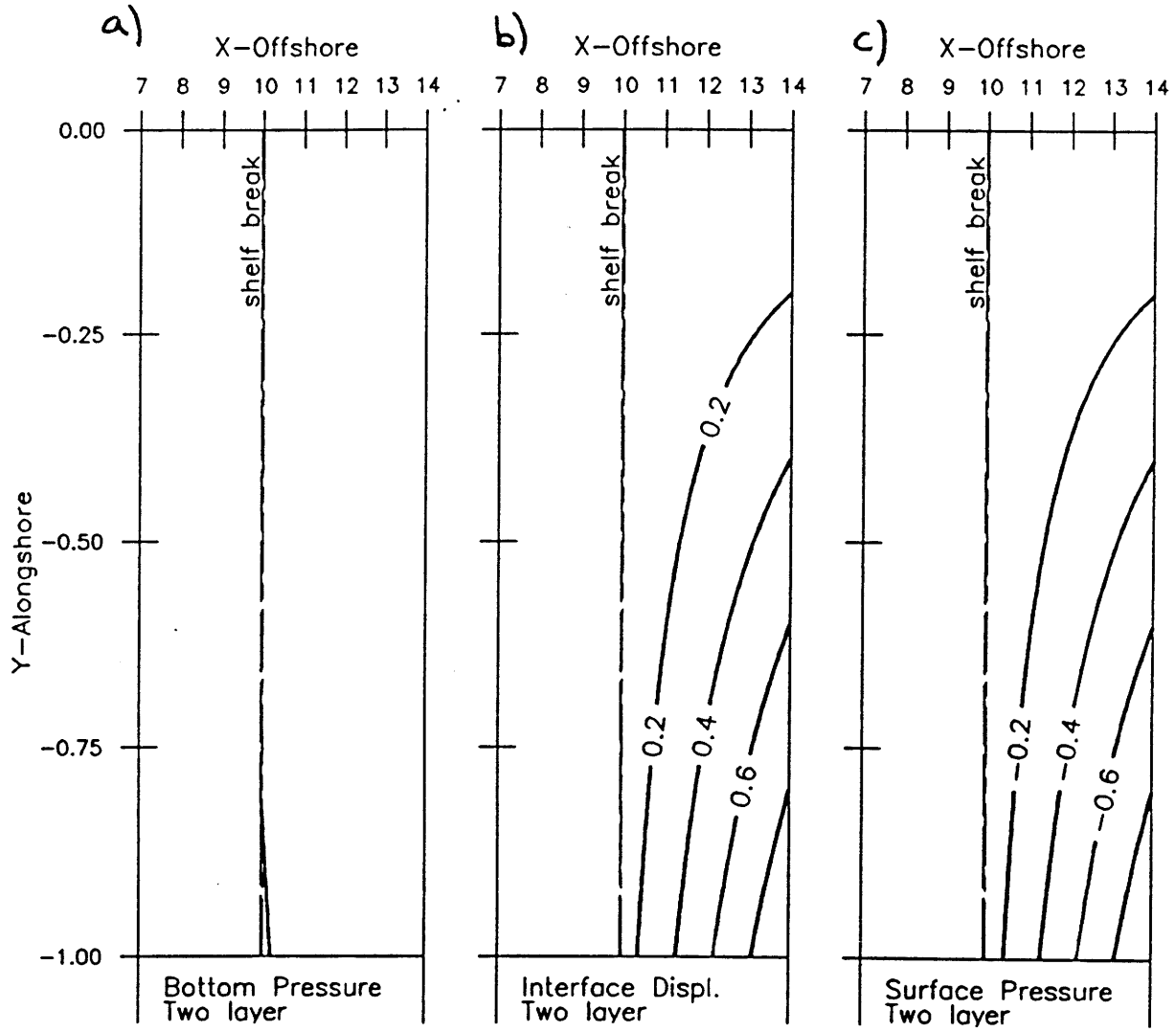


Figure 3-11: Solution when upper layer has a thickness equal to depth at shelf break and there is no deep ocean forcing of lower layer. ($R = 1.8, \delta_E^{rel} = 0.3, \Delta_s = 0.1, s_{rel} = 0.1, \Gamma' = 0$). The line where the interface intersects the bottom is coincident with the shelf break. a) Weak bottom flow, 0.02 contour is shown. b) Interface displacement. c) Isobars of upper layer pressure.

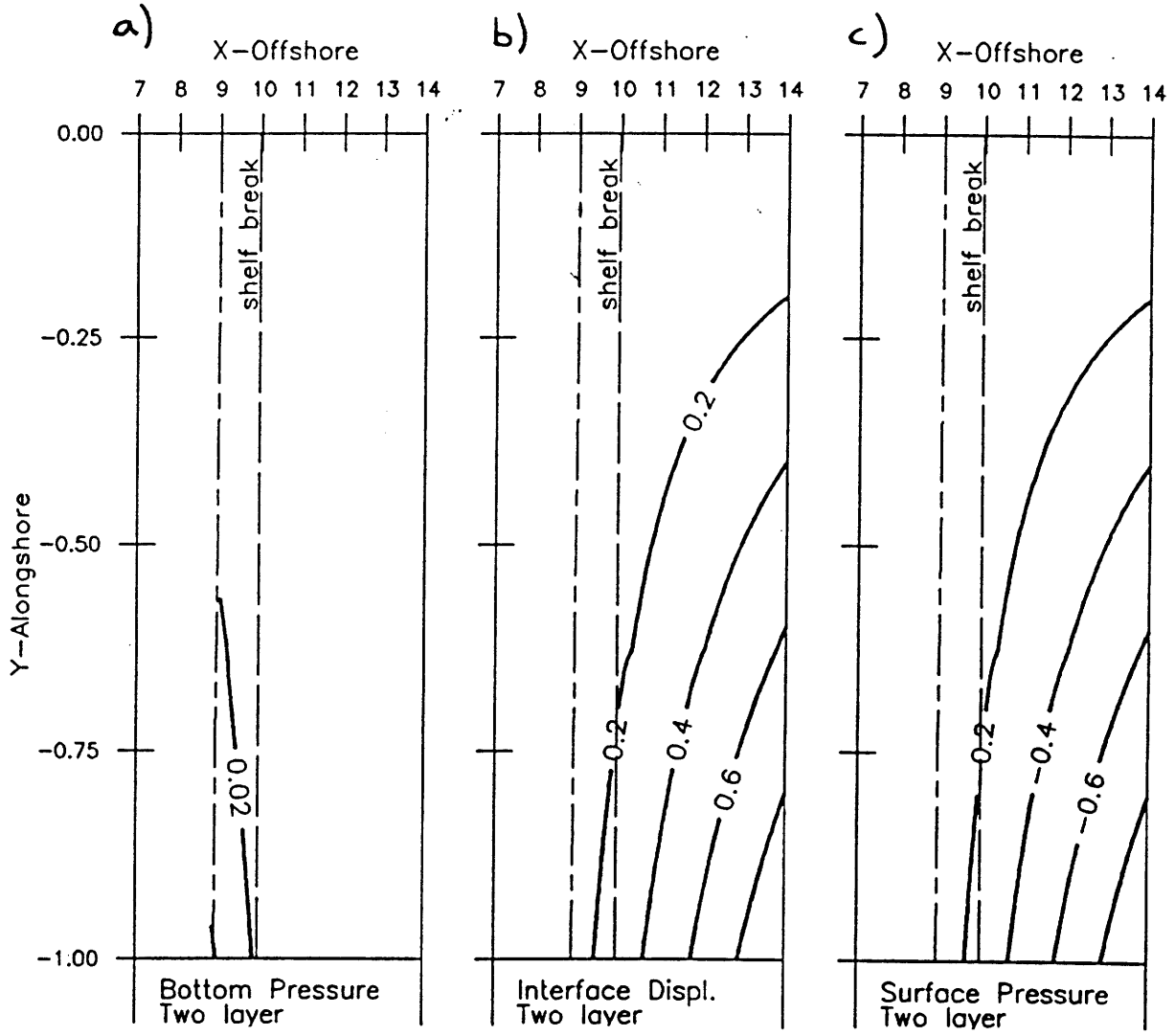


Figure 3-12: Solution when upper layer has a thickness $\frac{9}{10}$ of depth at shelf break so that interface intersects the shelf. a) Isobars of lower layer pressure. b) Interface displacement. c) Isobars of upper layer pressure.

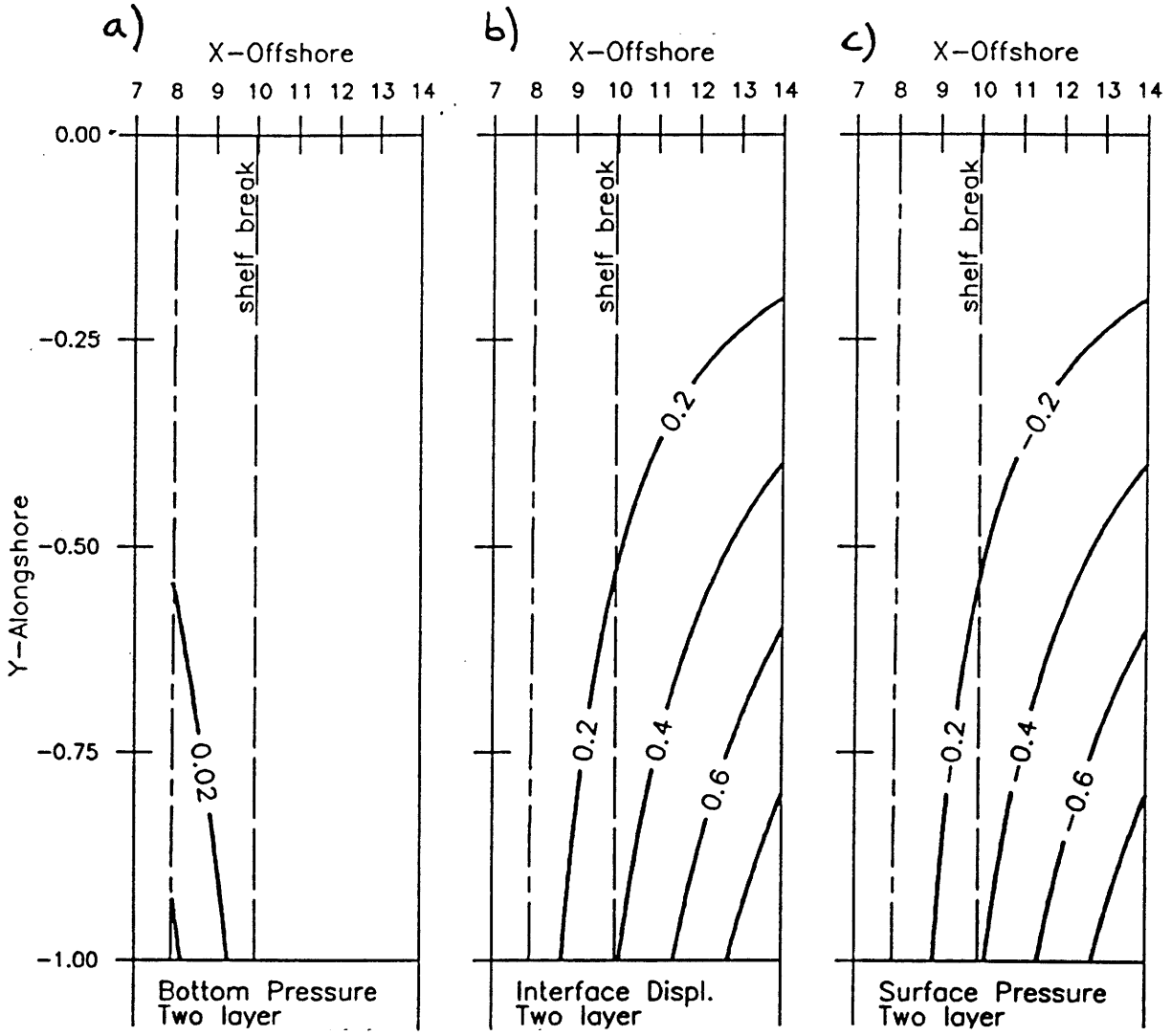


Figure 3-13: Solution when upper layer has a thickness $\frac{8}{10}$ of depth at shelf break so that interface intersects the shelf. a) Isobars of lower layer pressure. b) Interface displacement. c) Isobars of upper layer pressure.

### 3.4h Stratification and Interfacial Friction, $R$

The importance of stratification and interfacial friction in the dynamical balance is determined by the size of the non-dimensional number $R$ in (3.70b). For typical scales $R$ is 1.8 (see Table 3.2). The solution for a motionless deep ocean lower layer where the upper layer thickness is twice the depth at the shelf break for a small $R$ of 0.1 is shown in Figure 3-14.The solution with a large $R$ value of 10, in Figure 3-15. The differences between these two figures are slight. However a large value of $R$ gives a slightly wider cross-slope penetration of upper layer flow due to an enhanced spreading effect (compare the 0.2 contour in Figures 3-14c and 3-15c). Thus a more highly stratified deep ocean or one with stronger interfacial friction will have a slightly wider cross-topography scale than an ocean which is weakly stratified or which has weak interfacial friction. However, significant upper layer flow is still confined to the region between the forcing and the interface/bottom intersection.

A higher value of $R$ enhances the ability of the upper layer to drag the lower layer. The resultant enhanced interfacial Ekman transport which is blocked by the interface/bottom intersection will in turn mean a larger geostrophic flow induced at the intersection (see Figures 3-14 and 3-15).

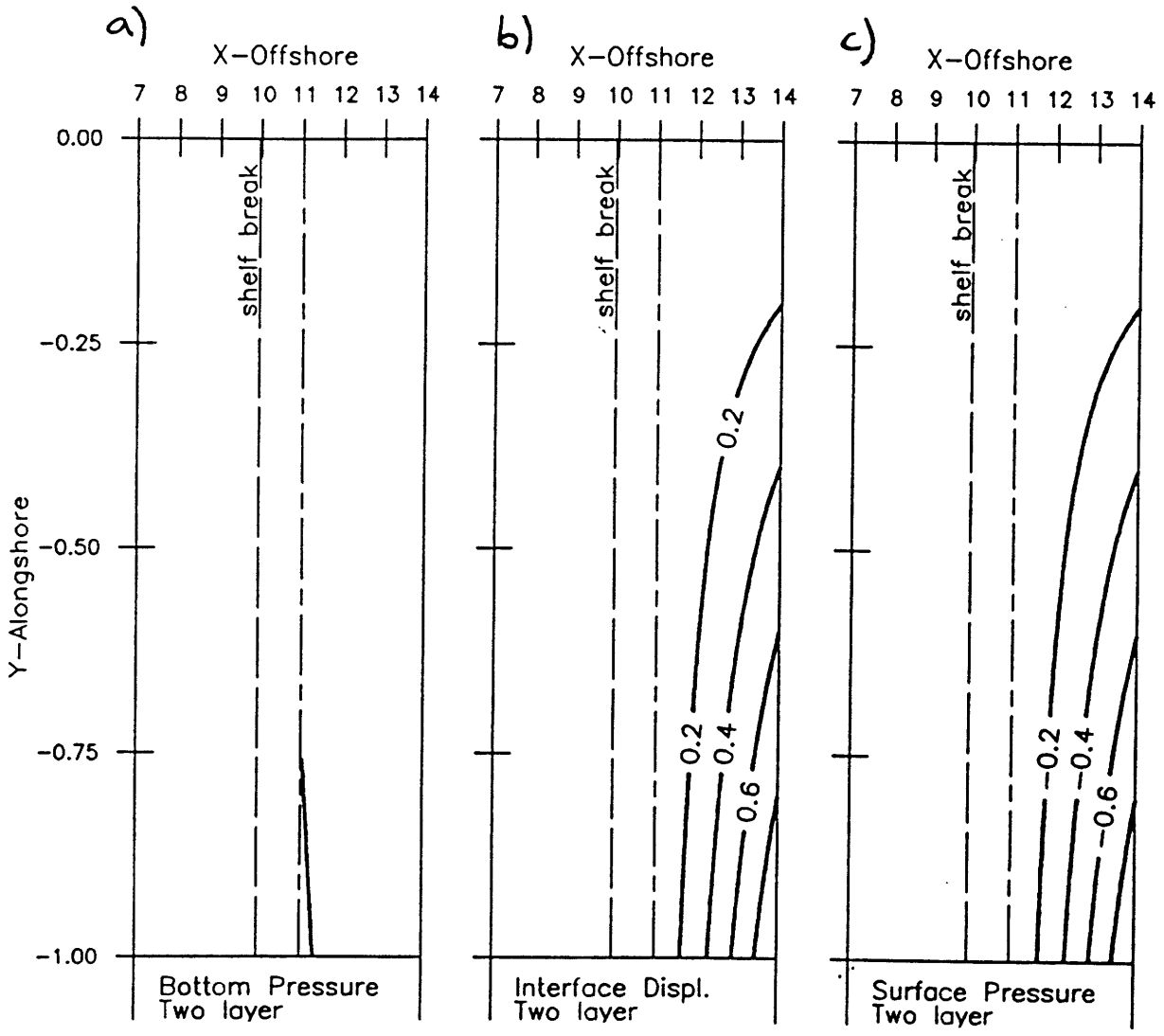


Figure 3-14: Solution for deep ocean forcing for a small value of $R$. ($R = 0.1, \delta_{rel} = 0.3, \Delta_s = 0, s_{rel} = 0.1, \Gamma' = 0$). The interface intersects the continental slope. a) Very weak bottom flow, only contour is 0.02. b) Interface displacement. c) Isobars of upper layer pressure.

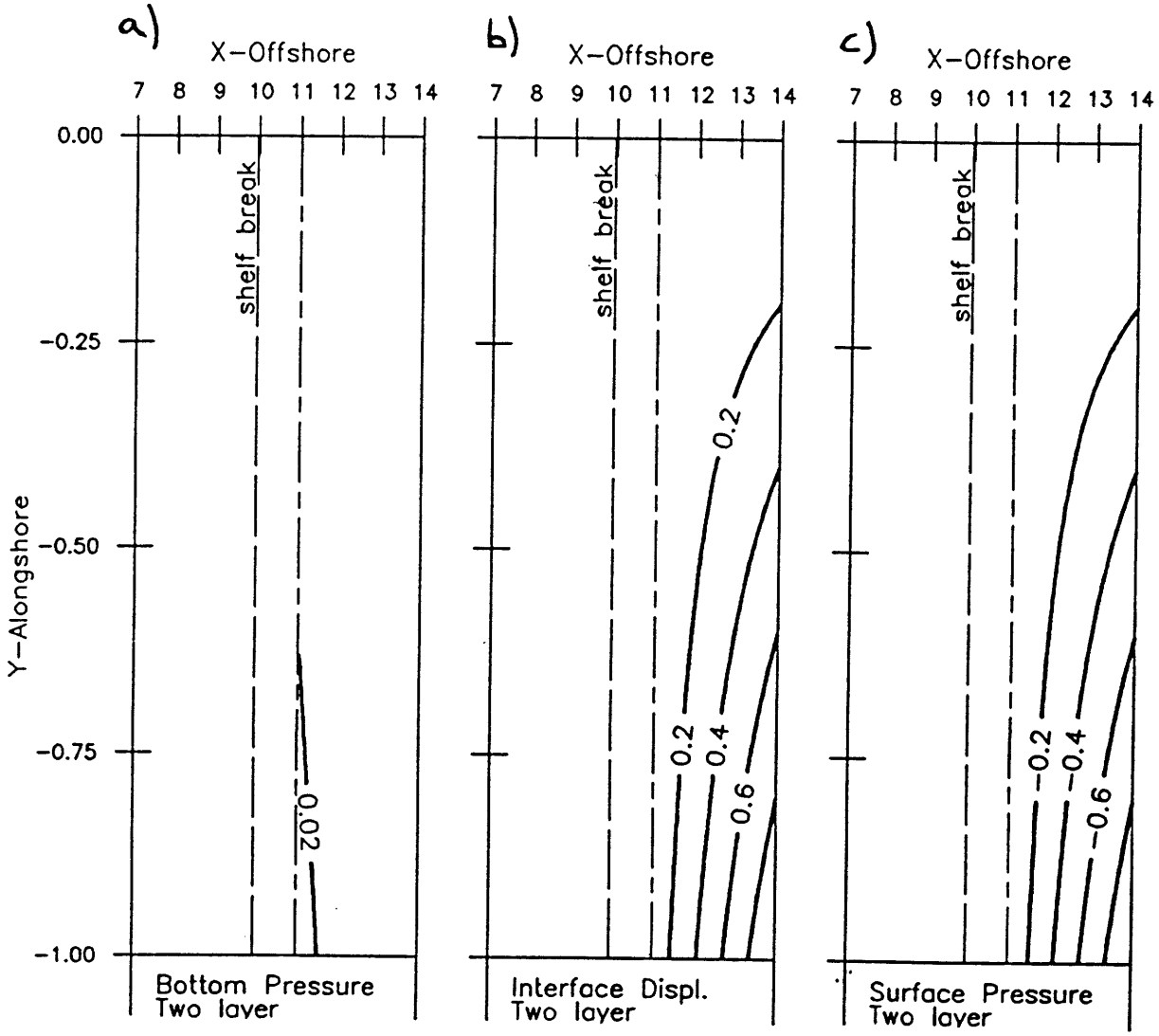


Figure 3-15: Solution for deep ocean forcing for a large value of $R$. ($R = 10, \delta_{rel} = 0.3, \Delta_s = 0, s_{rel} = 0.1, \Gamma' = 0$). The interface intersects the continental slope. a) Very weak bottom flow, only contour is 0.02. b) Interface displacement. c) Isobars of upper layer pressure.

### 3.4i Relative Ekman Layer Thickness, $\delta_E^{rel}$

The last of the non-dimensional numbers which will be varied is the relative Ekman layer thickness, $\delta_E^{rel}$. Though $R$ is also dependent on the interfacial Ekman layer thickness it will be kept constant by compensating changes in stratification. This will isolate the effects of Ekman layer thicknesses due to the boundary condition (3.76) and the matching condition(3.79). The two $f$-plane solutions shown both have a motionless deep ocean bottom layer and an upper layer thickness $\frac{9}{10}$ the depth at the shelf break. Consequently the interface intersects the shelf.

When the interfacial Ekman layer is thin, $\delta_E^{rel} = 0.1$, flow is confined offshore of the interface/bottom intersection (Figure 3-16b), and the induced lower layer flow

is very weak (less than 0.01). The flow pattern when the interfacial Ekman layer has a thickness equal to the bottom Ekman layer is shown in Figure 3-17 and is significantly different from any previous solution to this model. The lower layer flow (Figure 3-17a) which is induced by the blocking of interfacial Ekman transport is five times stronger than in any previous case. There is a significant upward movement of the interface at the interface/bottom intersection in Figure 3-17b which results in an observable shoreward movement of the intersection, and there is also a small but significant upper layer flow which crosses the intersection (note the 0.2 contour in Figure 3-17c).

The confinement of significant upper layer flow to offshore of the interface/bottom intersection is due to two mechanisms. The first mechanism can be seen in the matching condition (3.79) which ensures that upper layer bottom and interfacial Ekman transports are equal at the intersection. Both the upper layer interfacial and bottom Ekman transports are proportional to geostrophic velocities within the layers (see (3.57) and (3.58a)). In order to match interfacial and bottom Ekman transports across the intersection the strength of the geostrophic flow shoreward of the intersection must be of order $\delta_E^{rel}$ times the strength of the flow offshore of the intersection. Thus if the interfacial Ekman layer is thinner than the bottom Ekman layer, then flow shoreward of the intersection must be weaker than flow offshore. This is a partial explanation

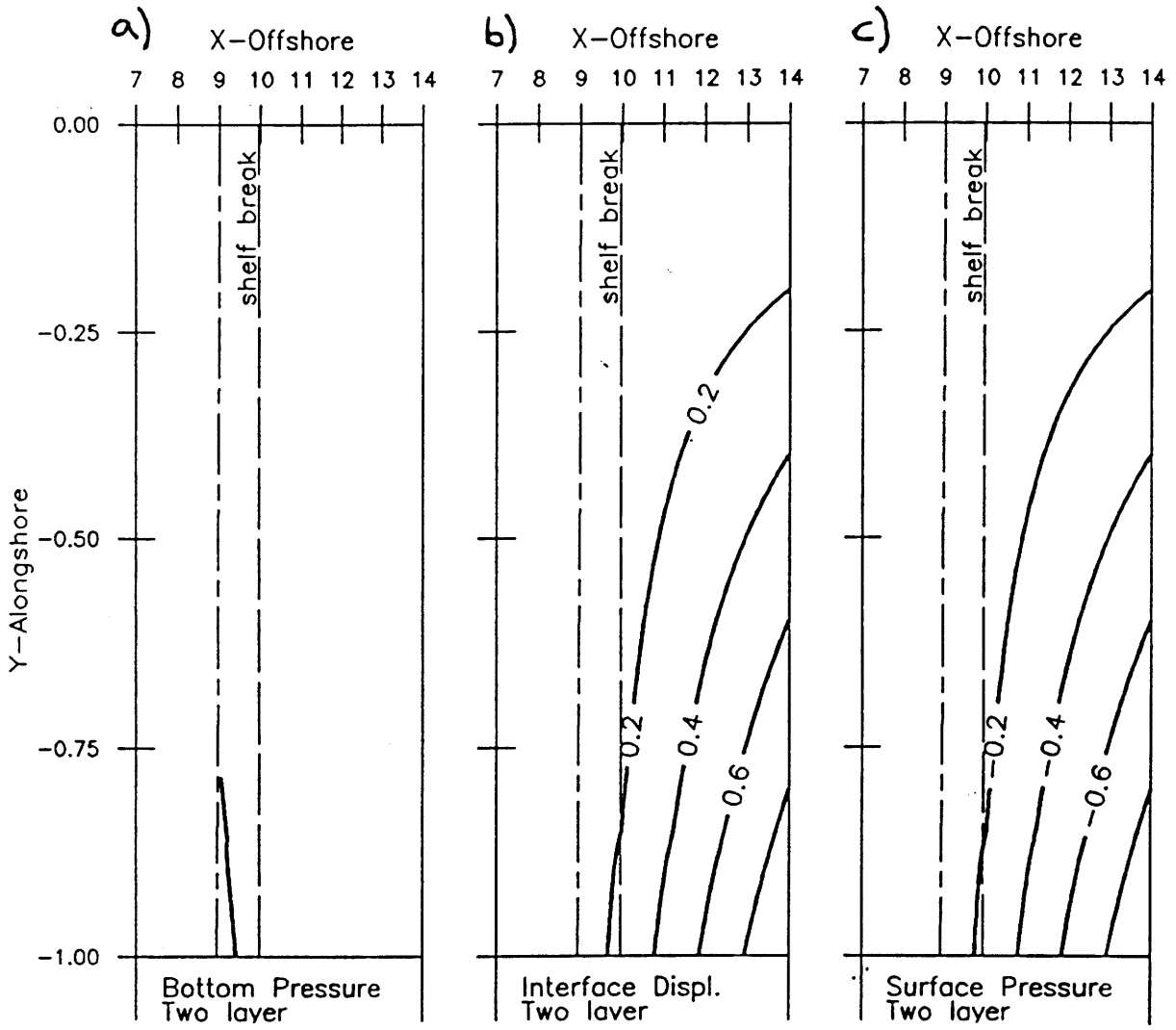


Figure 3-16: Solution for thin interfacial Ekman layer, $\delta_E^{rel} = 0.1$. $(R = 0.6, \Delta_s = 0.1, s_{rel} = 0.1, \Gamma' = 0)$. Interface intersects the shelf. a) Isobars of bottom pressure, flow is weak, shown is the .02 contour. b) Interface displacement. c) Isobars of upper layer pressure.

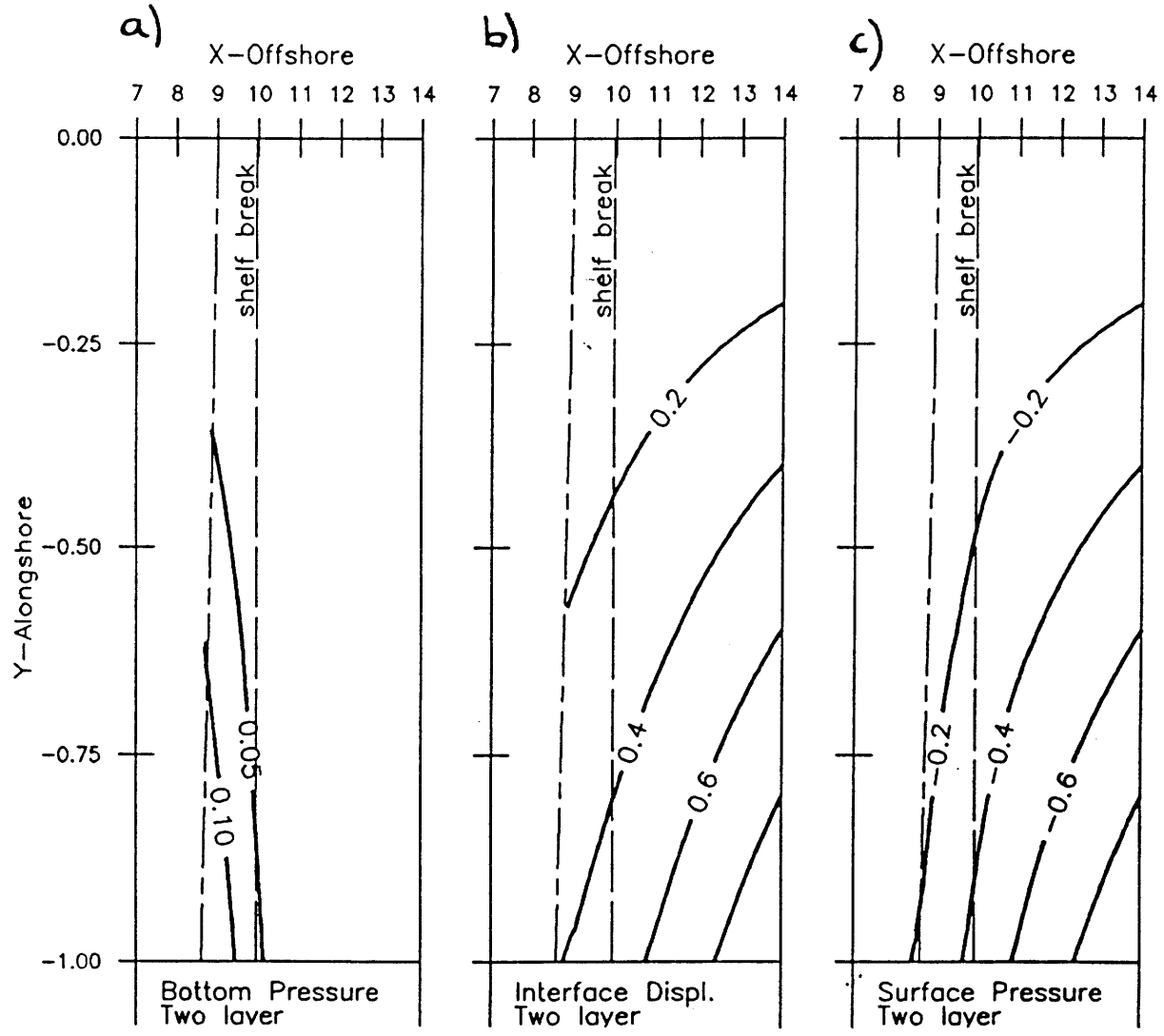


Figure 3-17: Solution for interfacial Ekman layer with a thickness equal to that of the bottom Ekman layer, $\delta_E^{rel} = 1$. $(R = 3, \Delta_s = 0.1, s_{rel} = 0.1, \Gamma' = 0)$. Interface intersects the bottom and exhibits a small but noticeable cross-shelf movement. a) Isobars of bottom pressure. Induced bottom layer flow is much stronger than in any previous case. b) Interface displacement is upward and significant when the interface intersects the bottom.

for the negligible amount of flow shoreward of the intersection in Figure 3-16c when $\delta^{rel} = 0.1$, whereas in Figure 3-17c, when $\delta_E^{rel} = 1$, the flow strength is similar on both sides.

The above explanation of mismatched Ekman layer thicknesses does not explain why only part of the flow crosses the intersection in Figure 3-17c where $\delta_E^{rel} = 1$. The second mechanism involved is that steering by the induced lower layer flow (Figure 3-17a) will tend to turn the upper layer flow parallel to the intersection before it reaches it. The lower layer flow is induced by the upper layer flow through the boundary condition (3.76) so that the importance of this steering mechanism is coupled to the strength of the upper layer flow at the intersection. If the induced bottom layer flow were stronger, then steering would turn more upper layer flow parallel to the intersection, reducing the amount of upper layer flow reaching the intersection, which in turn would reduce the induced bottom layer flow. Figure 3-17 represents the equilibrium point of this negative feed-back loop.

Both mechanisms, the steering and the mismatching of Ekman layer thicknesses, act to inhibit flow from crossing the interface/bottom intersection and thus restrict the region of significant deep ocean influence to be offshore of the intersection.

### 3.4j Planetary $\beta$

Previous solutions to both the two- and three-layer models have been for $f$ plane flow. In this section the influence of planetary $\beta$ on the interfacial friction model will be considered. For typical values in Table 3.2 $\beta'$ is 0.1 and hence the effects of planetary $\beta$ are of order 1 in the governing equations (3.70a), (3.70b) and (3.70c).

Figure 3-18 shows the flow pattern for a high latitude $\beta$-plane (i.e. weak $\beta' = 0.01$), Figure 3-19 show that for mid latitudes (typical $\beta' = 0.1$) and Figure 3-20, that for lower latitudes (large $\beta' = 0.25$). In all these Figures the deep ocean lower layer has a flow one quarter as strong as that in the upper layer ($\Gamma' = \frac{1}{4}$).

The high latitude weak $\beta'$ solution is very similar to that for an $f$ plane in Figure 3-6. The flow direction in the two layers is strongly coupled and cross-topography penetration is limited by the steep continental slope. The solution for a typical mid latitude $\beta'$ in Figure 3-19 is similar to that at a lower latitude and shows that the coupling between the layers is much weaker. Near the forcing upper layer flow tends to follow lower layer flow but, once beyond the region of significant lower layer flow, it travels easily across the topography until encountering the interface/bottom intersection. When planetary $\beta$ is significant (Figures 3-19c and 3-20c) the upper layer exhibits a much larger cross-topography scale than in the $f$ plane or weak $\beta'$ cases (Figure 3-18c). The cross-topography scale in the lower layer slightly increases with $\beta'$ (cf. Figures 3-18a and 3-20a). The increase of cross-topography scale in both layers is due to the tendency of $\beta-$plane flow to follow lines of latitude.

The flow patterns for a high, mid and lower latitude $\beta$-plane when the deep ocean's lower layer is motionless are shown in Figures 3-21, 3-22 and 3-23 ($\Gamma' = 0$). The flow when $\beta'$ is weak is very similar to that on an $f$ plane in Figure 3-8 and shows an even distribution of upper layer flow between the forcing and the interface/bottom intersection. For a typical value of $\beta'$ in Figure 3-22 upper layer flow is almost zonal near the forcing and turns to parallel the intersection with a concentration of alongshore flow adjacent to the intersection.

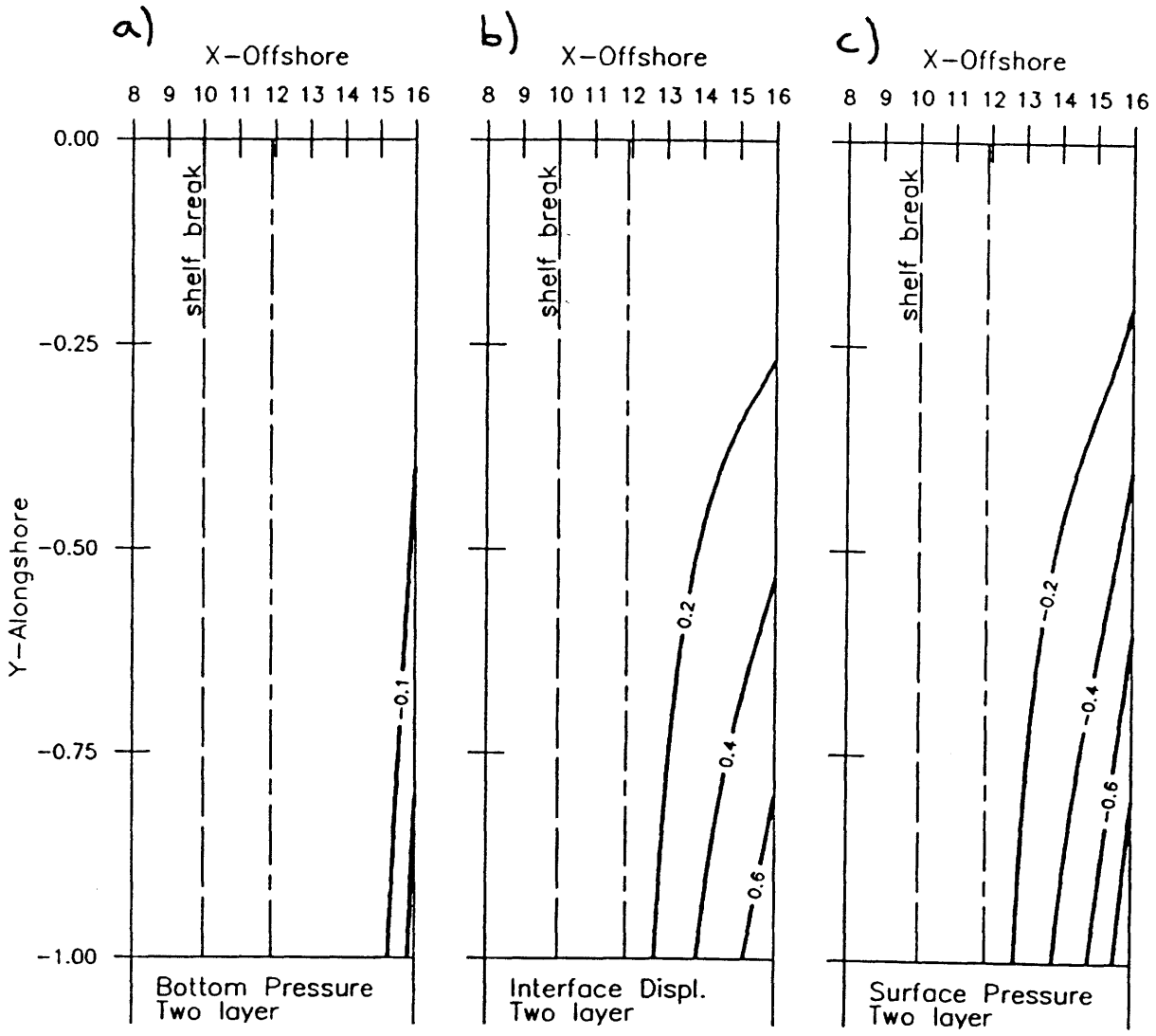


Figure 3-18: Solution for high latitude $\beta$-plane for baroclinic deep ocean forcing. ($\delta_E^{rel} = 0.3, R = 0.8, \Delta_s = 0.2, s_{rel} = 0.02, \Gamma' = 0.25, \beta' = 0.01$). a) Lower layer pressure, minimum $-0.25$. b) Interface displacement. c) Upper layer pressure, minimum $-1.0$.

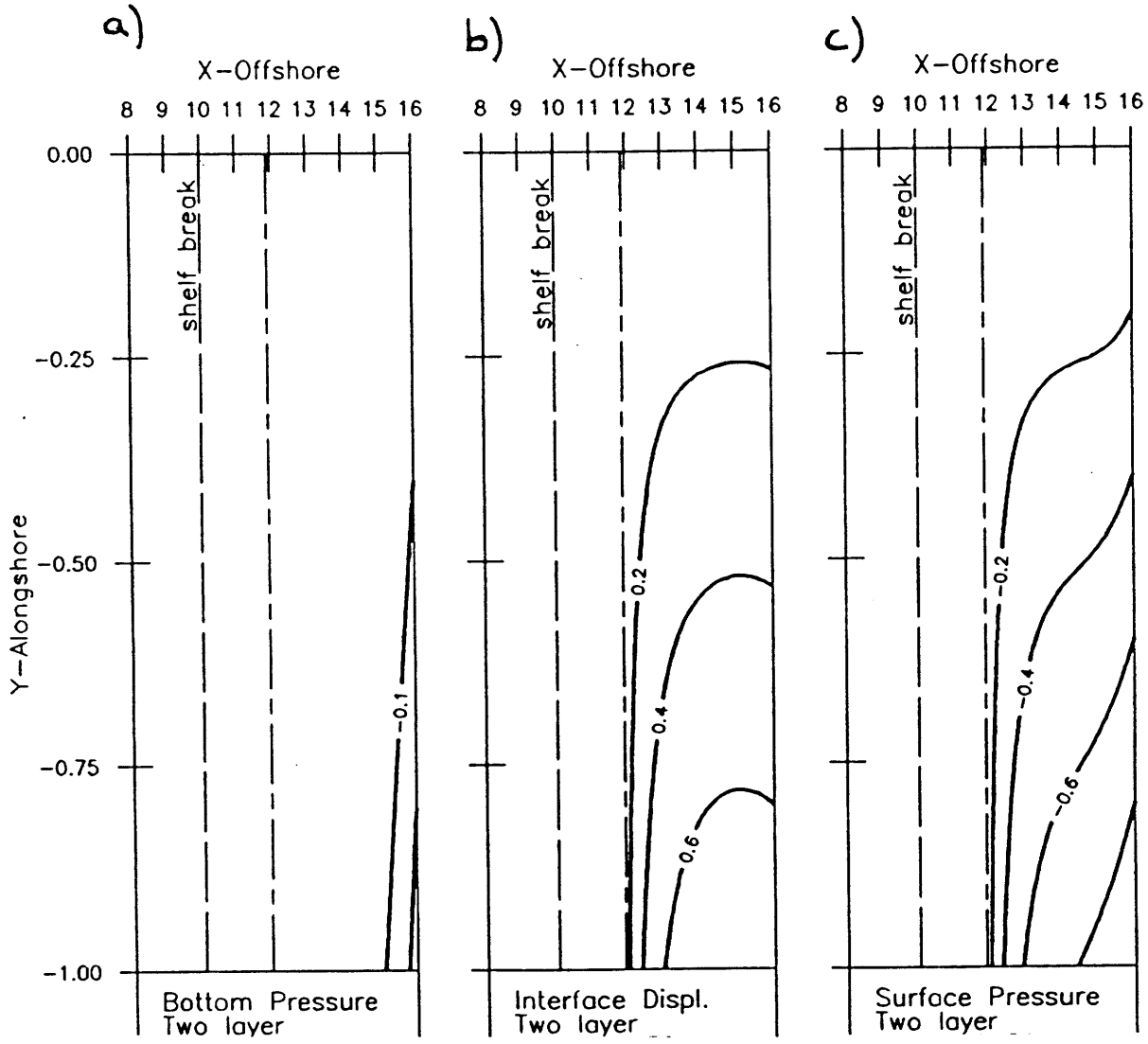


Figure 3-19: Solution for mid latitude $\beta$-plane. ($\delta_E^{rel} = 0.3$, $R = 0.8, \Delta_s = 0.2, s_{rel} = 0.02, \Gamma' = 0.25, \beta' = 0.1$). a) Lower layer pressure, minimum $-0.25$. b) Interface displacement. c) Upper layer pressure, minimum $-1.0$.

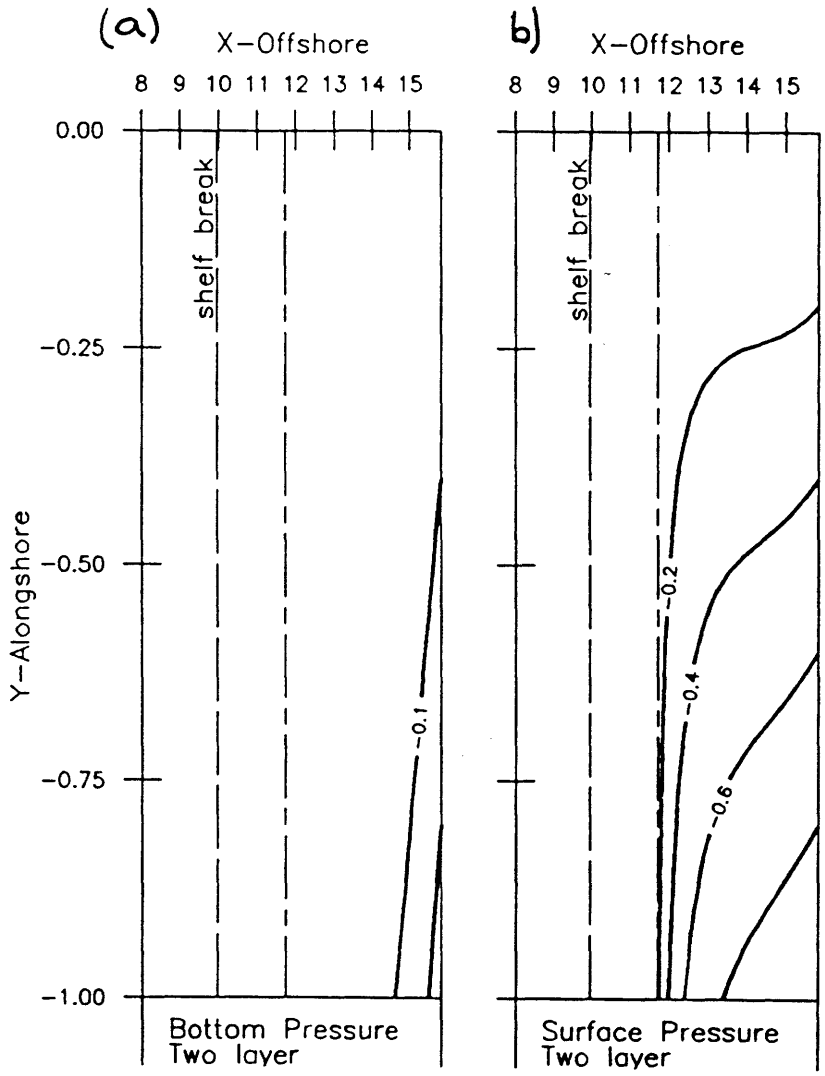


Figure 3-20: Solution for lower latitude $\beta$-plane. ($\delta_E^{rel} = 0.3$, $R = 0.8, \Delta_s = 0.2, s_{rel} = 0.02, \Gamma' = 0.25, \beta' = 0.25$). a) Lower layer pressure, minimum $-0.25$. b) Upper layer pressure, minimum $-1.0$. Interface displacement not shown

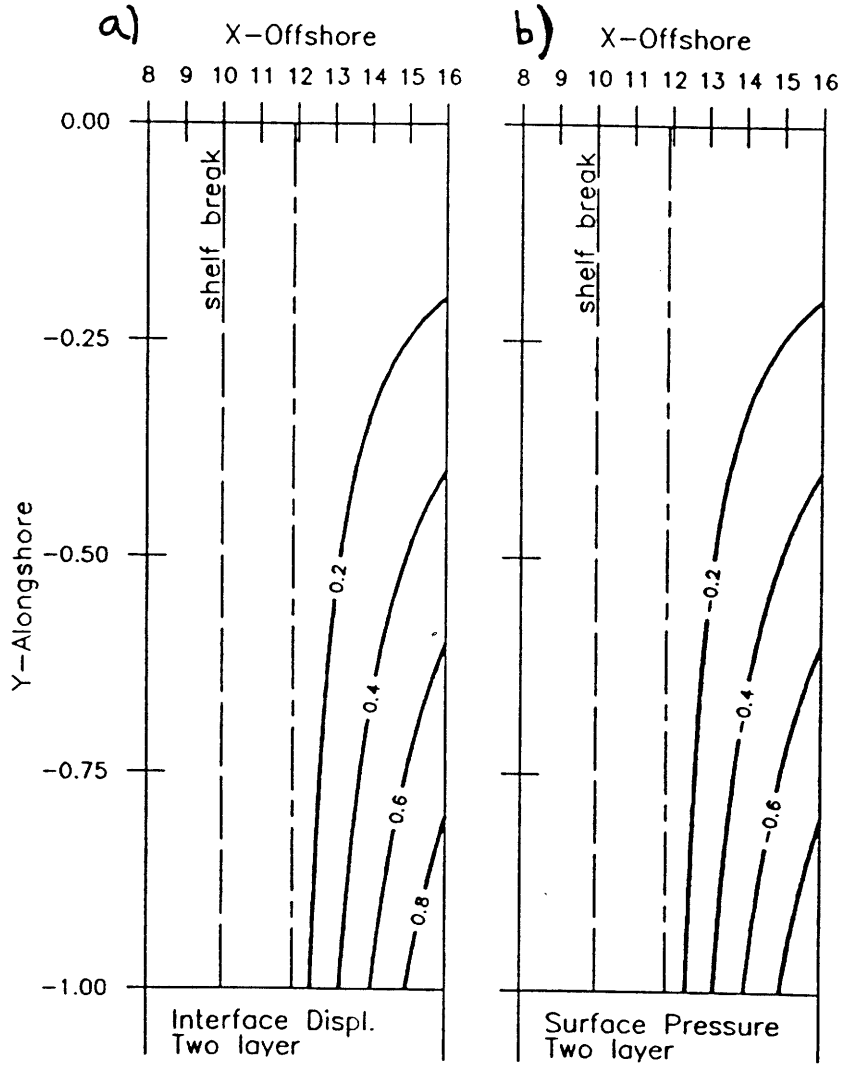


Figure 3-21: Solution for high latitude $\beta$-plane when deep ocean lower layer is motionless. ($\delta_E^{rel} = 0.3$, $R = 0.8, \Delta_s = 0.2, s_{rel} = 0.02, \Gamma' = 0, \beta' = 0.01$). a) Interface displacement. b) Upper layer pressure, minimum $-1.0$. Weak lower layer pressure not shown.

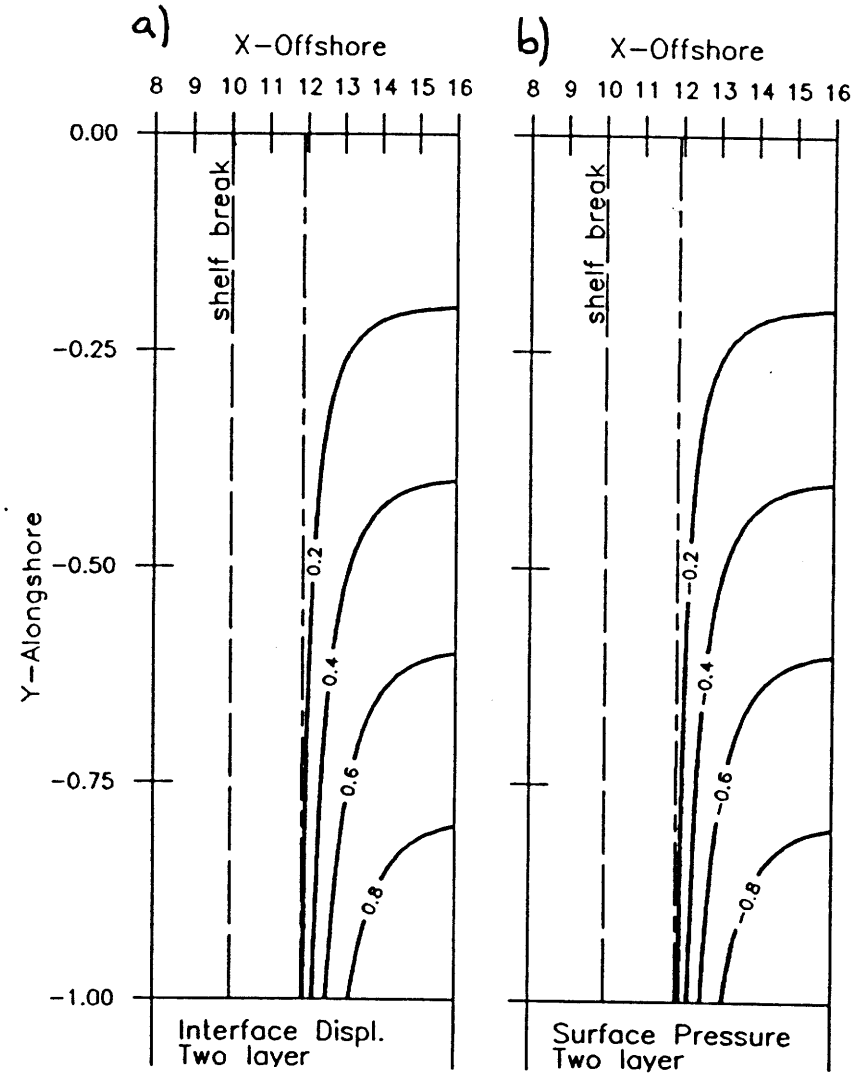


Figure 3-22: Solution for mid latitude $\beta$-plane when deep ocean lower layer is motionless. ($\delta_E^{rel} = 0.3$, $R = 0.8, \Delta_s = 0.2, s_{rel} = 0.02, \Gamma' = 0, \beta' = 0.1$). a) Interface displacement. b) Upper layer pressure, minimum $-1.0$. Weak lower layer pressure not shown.

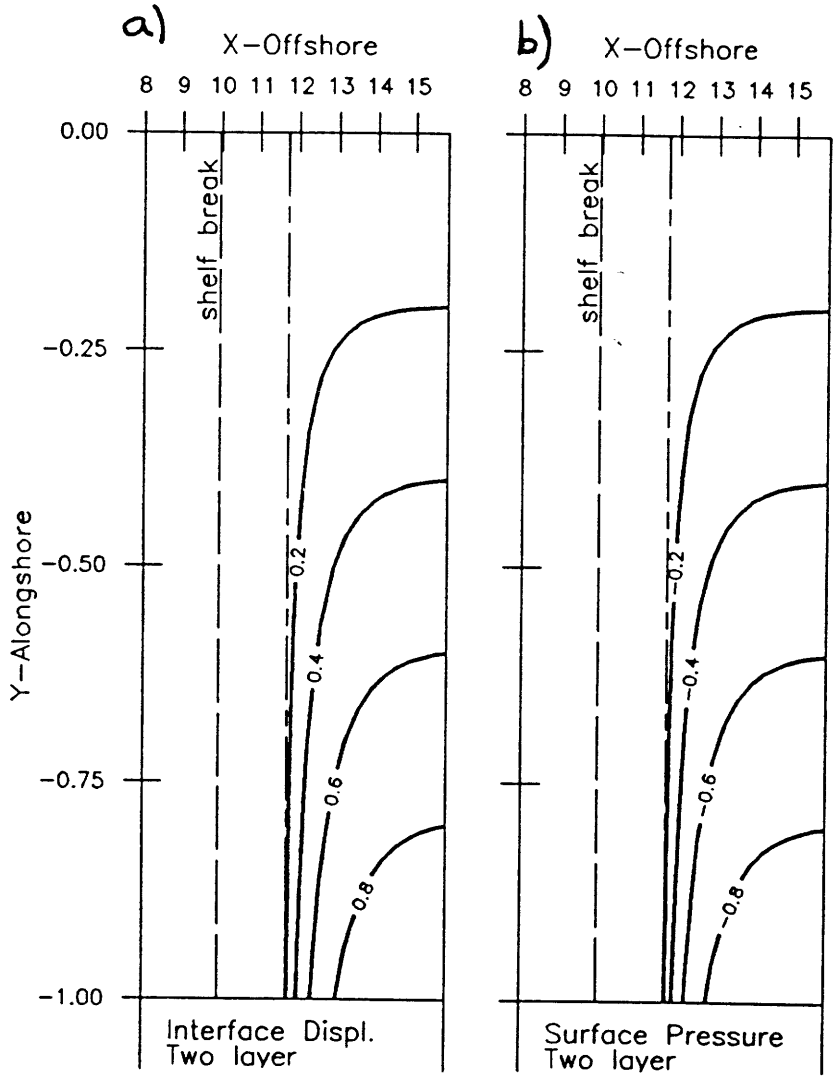


Figure 3-23: Solution for lower latitude $\beta$-plane when deep ocean lower layer is motionless. ($\delta_E^{rel} = 0.3$, $R = 0.8, \Delta_s = 0.2, s_{rel} = 0.02, \Gamma' = 0, \beta' = 0.25$). a) Interface displacement. b) Upper layer pressure, minimum $-1.0$. Weak lower layer pressure not shown.

As the upper layer thins the importance of planetary $\beta$ in the upper layer as measured by (3.11) declines. When the upper layer thickness is comparable to the depth at the shelf break and the lower layer is motionless, then planetary $\beta$ has little effect on the flow pattern. Such cases are covered by the $f$-plane results in section 3.4g.

The interfacial friction model cannot be used to determine the effects of planetary $\beta$ on a deep ocean flow impinging on a west coast (the ocean's eastern boundary) for the following reason. In the absence of interfacial and bottom friction fluid columns of the deep ocean inflow must conserve the potential vorticity and therefore follow contours of $\frac{f_0+\beta y}{t_i}$, where $t_i$ is the thickness of the $i$th layer. As columns move into shallower water they will be compressed and thus must turn equatorward in order to conserve their potential vorticity. If $\beta$ were negligible the two-layer model with interfacial and bottom friction would show the deep ocean inflow impinging on the west coast to turn poleward. The solution scheme used here exploits the parabolic nature of the governing equations by integrating them in the "time-like" direction. This direction is the direction in which a Kelvin wave would propagate along the coast. For a west coast this direction is poleward. The numerical scheme assumes that there is no flow at some initial latitude and, when applied to a west coast, integrates poleward. However, at least in the deep water near the forcing, the tendacy for flow to follow lines of $f$ divided by layer thickness will cause the flow to turn equatorward across the initial latitude. Consequently it is not possible to assume that there is a latitude of no flow when planetary $\beta$ is included into the interfacial friction model for a west coast. This difficulty could be resolved if the assumption that $\frac{L_x}{L_y} << 1$ is relaxed. However in this case the governing equations are no longer parabolic and would require a considerably more complex numerical solution scheme than that used here.

### 3.4k Alongshore Forcing

In the Mid-Atlantic Bight mean currents oppose the mean winds (see Figure 1-3 from SEEP for summer and winter means). The calculations of Chapman et al. (1986) using oxygen isotope data show that water over the mixed and outer shelf of the Mid-Atlantic

Bight originates on or north of the Scotian Shelf. Chapman and Beardsley (1988) show that the Scotain shelf flow originates along the southern coast of Greenland. This Scotian Shelf water flows south along the Mid-Atlantic Bight , slowly mixing with water from over the continental slope, but is still clearly discernible off the Virginian coast. Chapman et al. (1986) show that the observed mean shelf flow could be driven by an alongshore pressure gradient due to a pressure head over the Scotian Shelf. By using a model with realistic bottom topography they also show that a barotropic deep ocean cannot force significant shelf flow, but acts to prevent shelf water from flowing off the shelf into deeper water.

In this section the two-layer model will be used to extend the results of the model of Chapman et al. to a baroclinic deep ocean. The shelf flow is forced by prescribing a uniform band of inflow across $y = 0$ adjacent to the coast. Two different widths for this inflow will be considered as well as various vertical structures for the deep ocean inflow which enters across the deepest isobath. The results given in this section will be for an $f$-plane in order to isolate the effects of the alongshore forcing from those due to planetary $\beta$. To force a uniform alongshore flow in the upper layer across the northern boundary of the two layer model a linear gradient in pressure is used as an "initial" condition

$$\chi_1' = \begin{cases} \frac{x'}{w'} & x' < w' \\ 1 & x' \geq w' \end{cases} \quad on \quad y' = 0 \tag{3.85}$$

where $w'$ is the width of the alongshore inflow. Two cases are considered, firstly that when the inflow is half the shelf width and, secondly, that when the inflow is as wide as the shelf. It is assumed that the alongshore inflow is confined to the upper layer and therefore the lower layer pressure must be constant on $y = 0$, i.e.

$$\chi_2 = C \quad on \quad y' = 0 \quad . \tag{3.86}$$

This constant will be chosen so that the interface displacement where the interface intersects the bottom on $y = 0$ is zero (i.e. $\varsigma(x_I(0), 0) = 0$). The constant has a

different value depending on whether the interface intersects the bottom offshore or shoreward of the outer edge of the alongshore forcing

$$C = \begin{cases} 1 & x_I'(0) \geq w' \\ \frac{x_I'(0)}{w'} & x_I'(0) < w \end{cases} \quad . \tag{3.87}$$

The boundary conditions for the deep ocean inflow (3.73) need to be slightly revised

$$\begin{aligned} \chi_1' &= -y' + 1 \\ \chi_2' &= -\Gamma y' + C \end{aligned} \qquad on \quad x' = x'_{max} \quad . \tag{3.88}$$

The extra constants assure that pressure is continuous around the model's perimeter, but do not change the relative flow strength between layers of the deep ocean. The upper layer flow pattern for an alongshore forcing when the deep ocean is motionless and the upper layer thickness is thicker than the depth at the shelf break is shown in Figure 3-24. In Figure 3-24a the alongshore inflow is half the shelf width and in Figure 3-24b the inflow is as wide as the shelf. In both cases the offshore boundary condition is that the pressure in both layers is constant along the deepest isobath. Such a boundary condition prevents flow from crossing the deepest isobath and therefore the offshore edge is not "open" to the deep ocean. However these solutions show that there is no significant flow offshore of the shelf break and consequently neither flow pattern is sensitive to the choice of offshore boundary condition.

For a narrow alongshore inflow (Figure 3-24a) motion is significant between the coast and mid shelf. Even for an alongshore inflow as wide as the shelf (Figure 3-24b) significant flow is confined to shoreward of the shelf break. In equation (3.70a) which governs upper layer flow shoreward of the interface/bottom intersection along and cross-shore scales are related by (3.35) which depends on the bottom slope. Over the shelf the slope is mild so that the flow's cross-shore scale is of order the shelf width. Over the continental slope the topography is much steeper and consequently the cross-topography scale is much smaller. Therefore any shelf flow which does cross the shelf

break does not penetrate far beyond it. These two examples demonstrate that for this layer geometry, shelf flow is trapped on the shelf by the steep continental slope.

The solution shown in Figure 3-25 is the same as that in Figure 3-24 except that the upper layer is thinner than the depth at the shelf break. In this case flow is significant at the deepest isobath and therefore an "open" boundary condition should be used. In Figure 3-25 the pressure is assumed to be constant in both layers along the deepest isobath and therefore no flow can cross the deepest isobath. For this closed open boundary condition it is found that the -0.6 and -0.8 contours move farther offshore as the offshore boundary is moved offshore in such manner that flow is evenly distributed between the interface/bottom intersection and the offshore boundary. This indicates that a truly open boundary would allow Scotian shelf water to penetrate far offshore. Thus Figure 3-25 gives a lower bound for the cross-topography scale of an alongshore inflow acting alone. For the purposes of this work such a lower bound is sufficient because a moving deep ocean either does not change or reduces the cross-topography scale of the flow due to an alongshore inflow relative to this lower bound. It is the further reduction of this cross-topography scale below this lower bound by a deep ocean inflow which is significant. In reality Figure 3-25 should be viewed not as an approximation to a open boundary solution but as the solution when the deep ocean flow impinging on the offshore edge is very weak.

Figure 3-25a shows the upper layer flow due to an alongshore inflow half the shelf width when the deep ocean is motionless. Note how significant flow can cross the interface/bottom intersection but is still confined over the shelf (see $-0.8$ contour). Figure 3-25b gives the upper layer flow for an inflow as wide as the shelf. Since the upper layer is relatively thin the inflow directly forces flow in the upper layer where it overlies the lower layer. In this case upper layer flow can be significant beyond the shelf break ( note the $-0.8$ contour). The interface tends to isolate the upper layer from the effects of the topography and consequently the steep continental slope does not prevent water from the inflow from moving offshore beyond the shelf break.

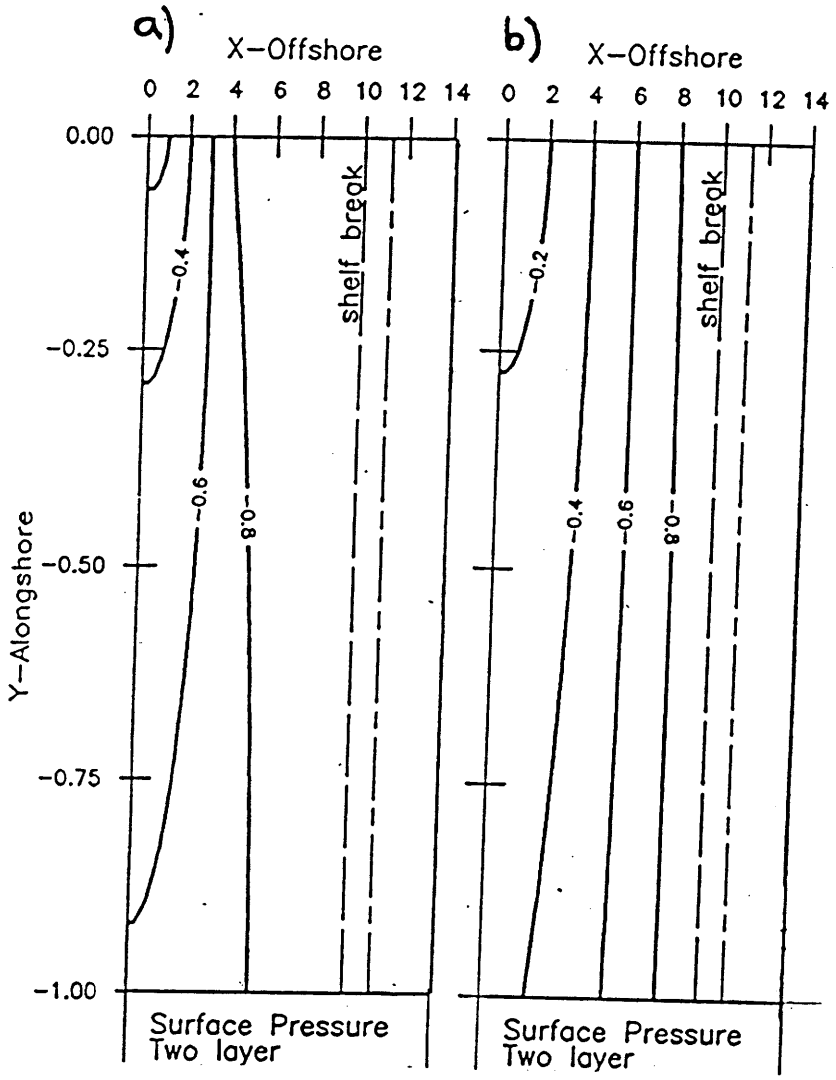


Figure 3-24: Upper layer pressure for alongshore inflow when deep ocean is motionless and upper layer is thicker than the depth at the shelf break. ($\delta_E^{rel} = 0.3$, $R = 1.8, \Delta_s = 0.1, s_{rel} = 0.1$). a) Narrow inflow, $w' = 5$. b) Wide inflow, $w' = 10$.

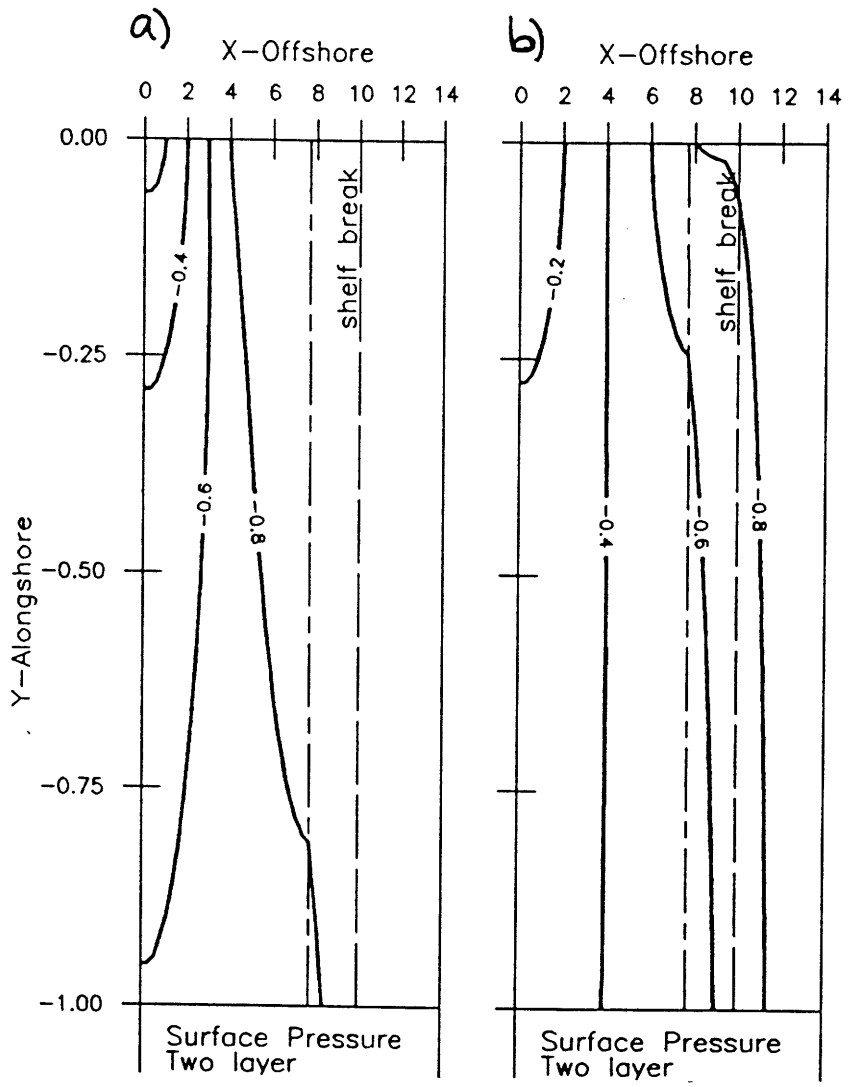


Figure 3-25: Solution for alongshore inflow and motionless deep ocean when the upper layer is thinner than the depth at the shelf break. ($\delta_E^{rel} = 0.3$, $R = 1.8, \Delta_s = 0.1, s_{rel} = 0.1$). a) Narrow inflow, $w' = 5$. b) Wide inflow, $w' = 10$.

The following figures show the flow patterns due to combined forcing by a deep ocean inflow and an alongshore inflow. The solution for a barotropic deep ocean and an alongshore inflow which is half the shelf width is given in Figure 3-26. This case reproduces one of the results of Chapman et al. (1986) for the idealized topography used here and shows that deep ocean inflow is confined to a band adjacent to the deep ocean forcing and that the alongshore flow is confined over the shelf adjacent to the coast. These two distinct regions of flow can be thought of as distinct water masses, one of deep ocean origin and another originating at higher latitudes over the shelf (i.e. slope water and Scotian shelf water, respectively, using the terminology of Chapman et al. (1986) for the Mid-Atlantic Bight ).

Figure 3-27 shows the solution for a barotropic deep ocean inflow and an alongshore inflow which is as wide as the shelf. Upper layer flow in Figure 3-27 also occurs in two distinct regions, in that over the slope near the oceanic forcing and in that over the shelf.

The solutions for a baroclinic deep ocean where the deep ocean's lower layer is motionless and the upper layer is thicker than the depth at the shelf break are given in Figure 3-28 for a narrow alongshore inflow and in Figure 3-29 for a wide alongshore inflow. The deep ocean is still confined offshore of the interface/bottom intersection. Its flow pattern is the same as that in Figure 3-8. The flow pattern over the shelf is unaltered by the change in the deep ocean's vertical structure. The solutions for a barotropic and baroclinic deep ocean show that, when the upper layer is significantly thicker than the depth at the shelf break, deep ocean flow and shelf flow form distinct water masses separated from each other by the steep topography of the upper continental slope. The deep ocean flow has no dynamical influence on the shelf and consequently does not affect any flow which may occur there due to the alongshore inflow, i.e. essentially the two flows are dynamically independent for this geometry.

Figure 3-30 shows the solution for a combined deep ocean and a narrow alongshore inflow where the upper layer thickness is $\frac{8}{10}$ the depth at the shelf break and the deep ocean's lower layer is motionless. The deep ocean upper layer flow in Figure 3-30b has a

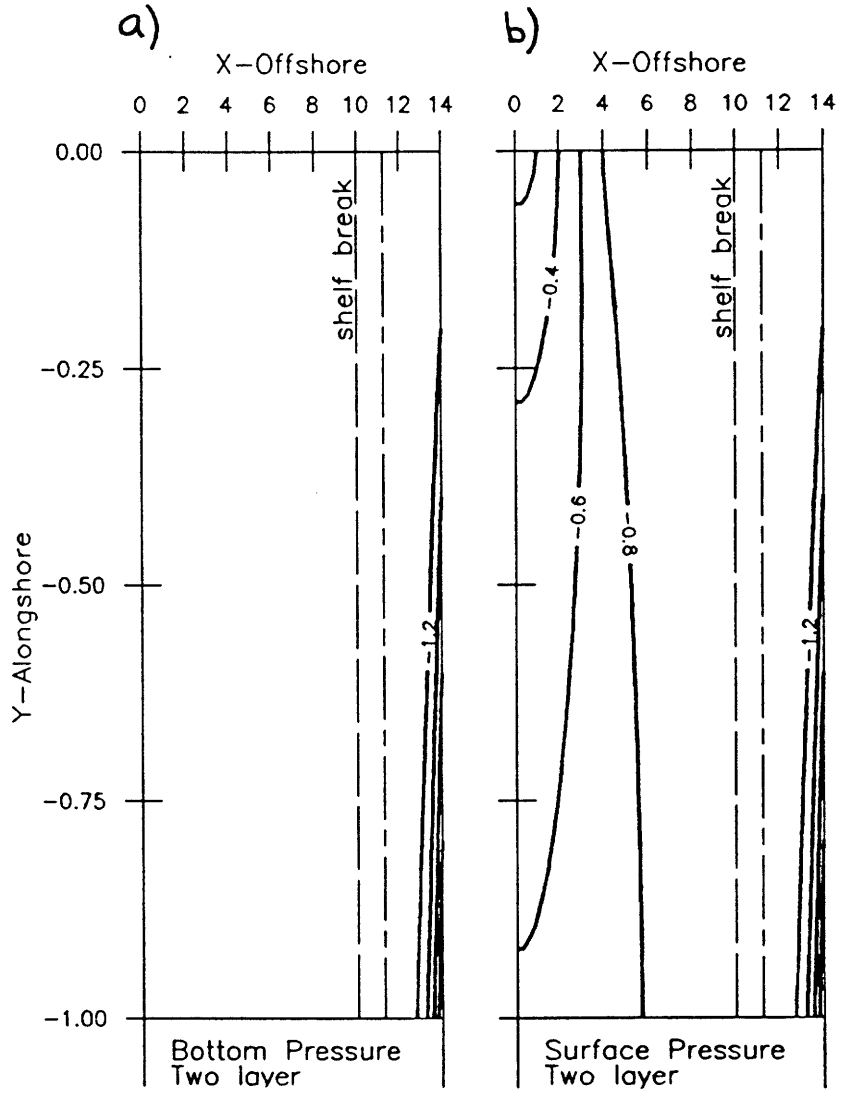


Figure 3-26: Solution for narrow alongshore inflow and barotropic deep ocean forcing. ($w' = 5$, $\Gamma' = 1$)). a) Lower layer pressure. b) Upper layer pressure.

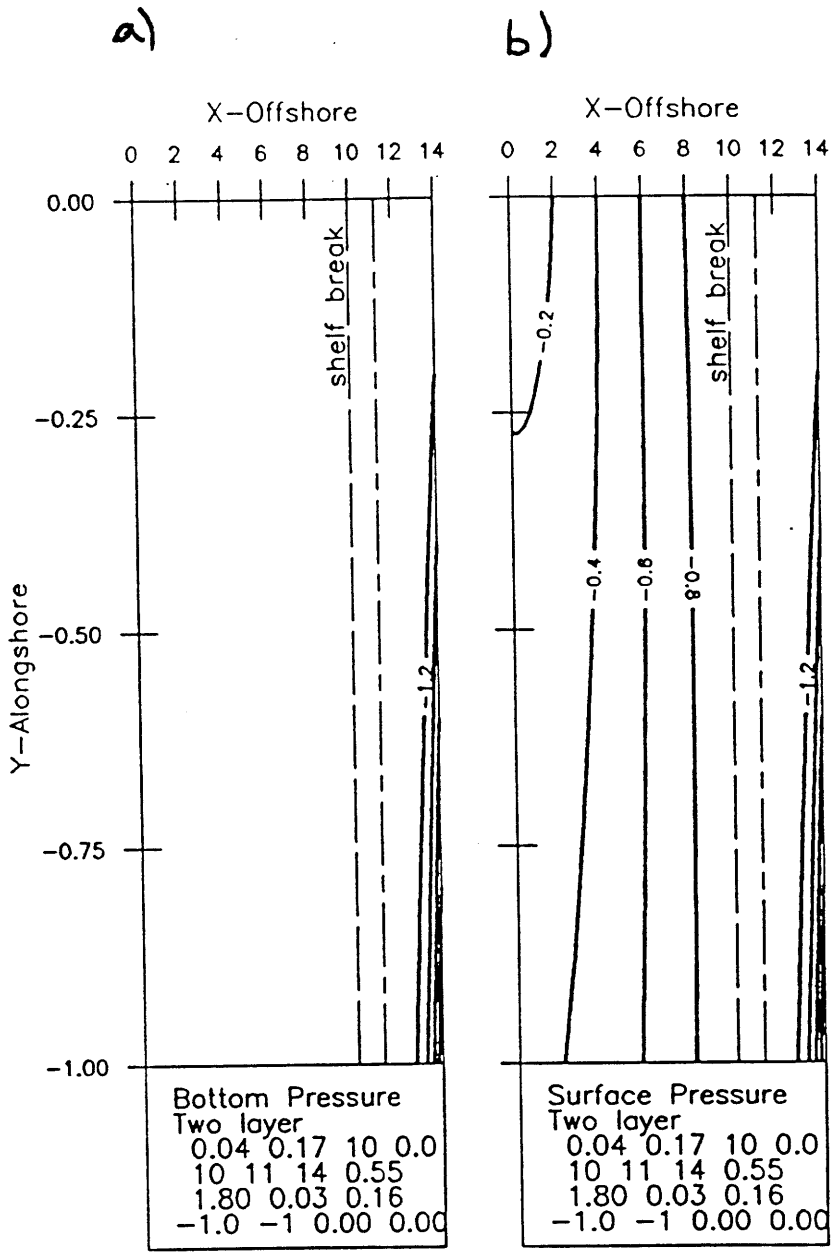


Figure 3-27: Solution for wide alongshore inflow and barotropic deep ocean forcing. ($w' = 10, \Gamma' = 1$)). a) Lower layer pressure. b) Upper layer pressure.

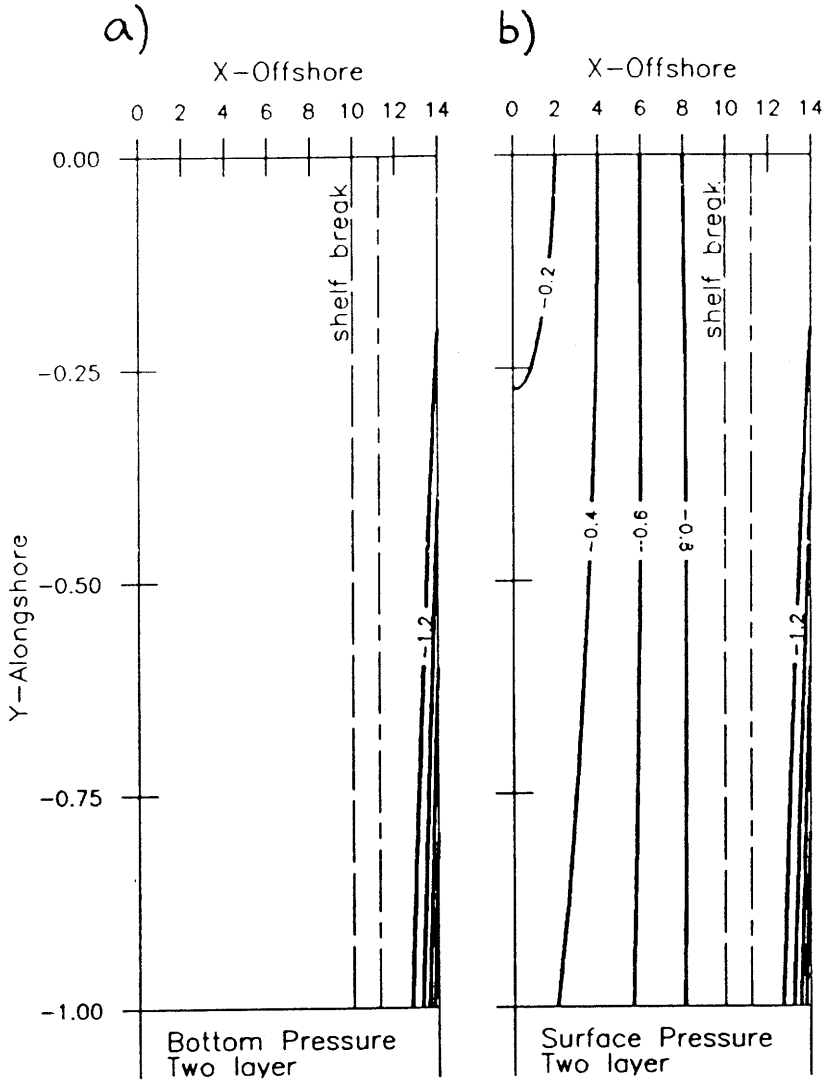


Figure 3-28: Solution for a Baroclinic Deep Ocean and a narrow alongshore inflow where the upper layer is thicker than the depth at the shelf break. ($w' = 5$, $\Gamma' = 0$)). a) Interface displacement. b) Upper layer pressure.

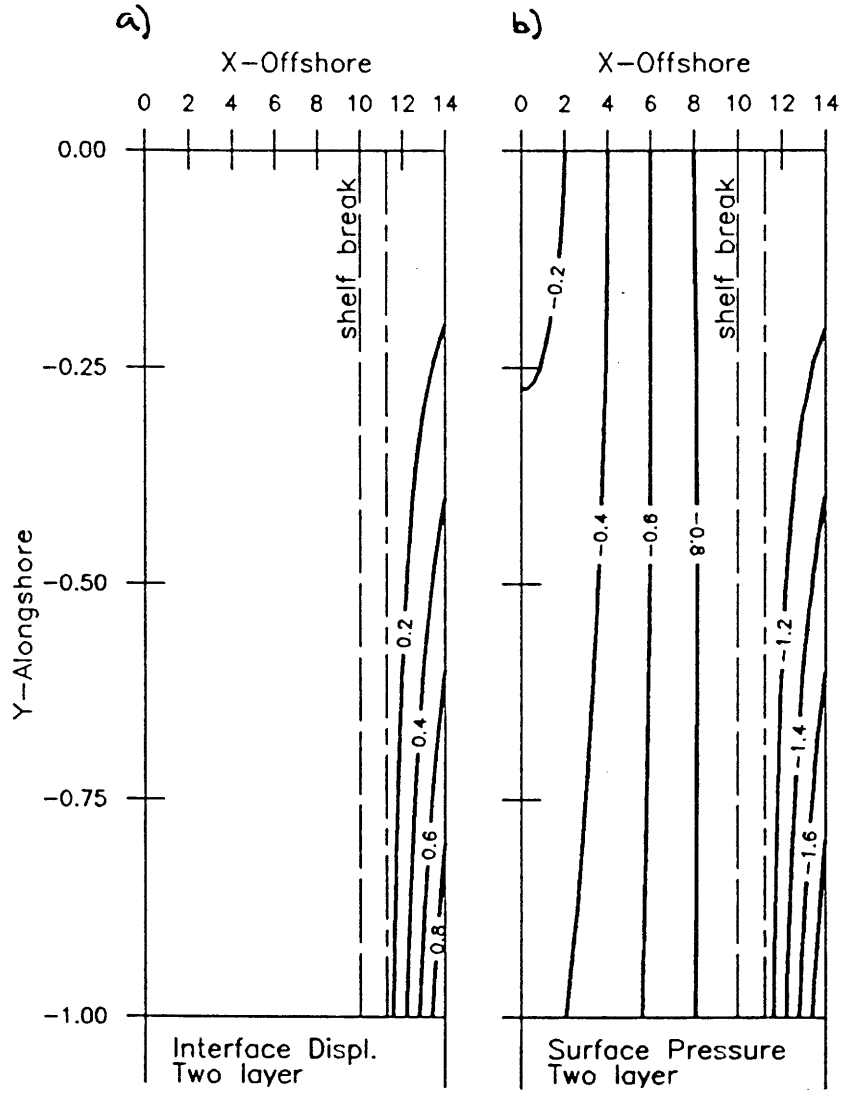


Figure 3-29: Solution for a Baroclinic Deep Ocean and a wide alongshore inflow where the upper layer is thicker than the depth at the shelf break. ($w' = 10$, $\Gamma' = 0$)). a) Interface displacement. b) Upper layer pressure.

wider cross-topography scale than 3-28b but is confined offshore of the interface/bottom intersection which is consistent with the results of section 3.4g. The flow pattern due to the alongshore forcing is similar to that when the upper layer is thicker (see Figure 3-28b). The solution in Figure 3-31 is the same as that in Figure 3-30 except that the alongshore forcing has the same width as the shelf break. This case shows the mutual effects of alongshore and deep ocean inflow. The water from alongshore inflow can cross the interface/bottom intersection just as in Figure 3-25 but is displaced shoreward by the deep ocean inflow (compare the $-1.2$ contour in these figures), while the deep ocean inflow is displaced offshore compared to Figure 3-13c .

As demonstrated, under certain circumstances, namely a thin upper layer, deep ocean and Scotian shelf inflow of approximately the same strength and a wide Scotian inflow, the two inflows interact with each other. Changes in the relative strength of the inflows warrants further discussion. The two extreme cases are Figure 3-8, where there is a unit deep ocean inflow and no Scotian inflow, and Figure 3-25, where there is a unit Scotian inflow and a very weak deep ocean inflow. Figure 3-29 gives the intermediate case where the inflows are of equal strength. When the conditions for interaction are met an increase in the strength of the deep ocean inflow moves the boundary between the two inflows shoreward. As noted earlier little deep ocean flow can cross the interface/bottom intersection, the boundary between the two flows will not move shoreward of this intersection even for a very weak Scotian inflow. Thus any Scotian inflow is able to expand to fill the region between either the interface/bottom intersection or the shelf break, depending on which is closer to the coast.

It was shown earlier that one reason why the deep ocean could not cross the interface/bottom intersection was the difference between the interfacial and bottom Ekman layer thicknesses. This mismatch enhances the ability of shelf flow to cross the interface/bottom intersection and is responsible for the tendency for shelf flow to cross the intersection at right angles (see for example Figure 3-25a).

The second reason that deep ocean flow did not cross the interface/bottom intersection is due to steering by induced lower layer flow. When the shelf flow crosses the

intersection it also induces a lower layer flow with the same pattern as that in Figure 3-8a, a narrow band of alongshore flow 1 unit wide adjacent to the intersection. The direction for lower layer flow induced by deep ocean or shelf flow is in the same direction, i.e. southward, because the upper layer flow in both is southward. The strength of this flow varies directly with the intensity of the alongshore in the vicinity of the intersection. For the case in Figure 3-25 the induced flow is weak (less than 0.01 ) and thus the tendency for the induced flow to steer the upper layer flow parallel to the intersection will be weaker than the case given in Figure 3-8a where the induced flow is of order 0.02 . Thus even if a true open boundary were applied in Figure 3-25 the induced flow would not cause significant trapping of upper layer flow near the intersection. When the deep ocean inflow is significant (Figure 3-29) the induced flow is of the same order (0.02) as that when there is no shelf flow.

This section demonstrates that the deep ocean and the flow over the shelf are isolated from each other by the steep continental slope except when the deep ocean's upper layer is sufficiently thin and the shelf flow is sufficiently wide. In these circumstances the two flows remain as distinct water masses ( outside of frictional layers) and the deep ocean prevents shelf flow from escaping into the deep ocean's upper layer.

It is only in particular circumstances that the deep ocean and shelf flow interact. These conditions are, most importantly a thin upper layer and inflows of sufficient strength ( i.e. of approximately similar strength) . Under these conditions the boundary between the two inflows moves shoreward as the relative of the deep ocean inflow increases but does not move shoreward of the interface/bottom intersection.

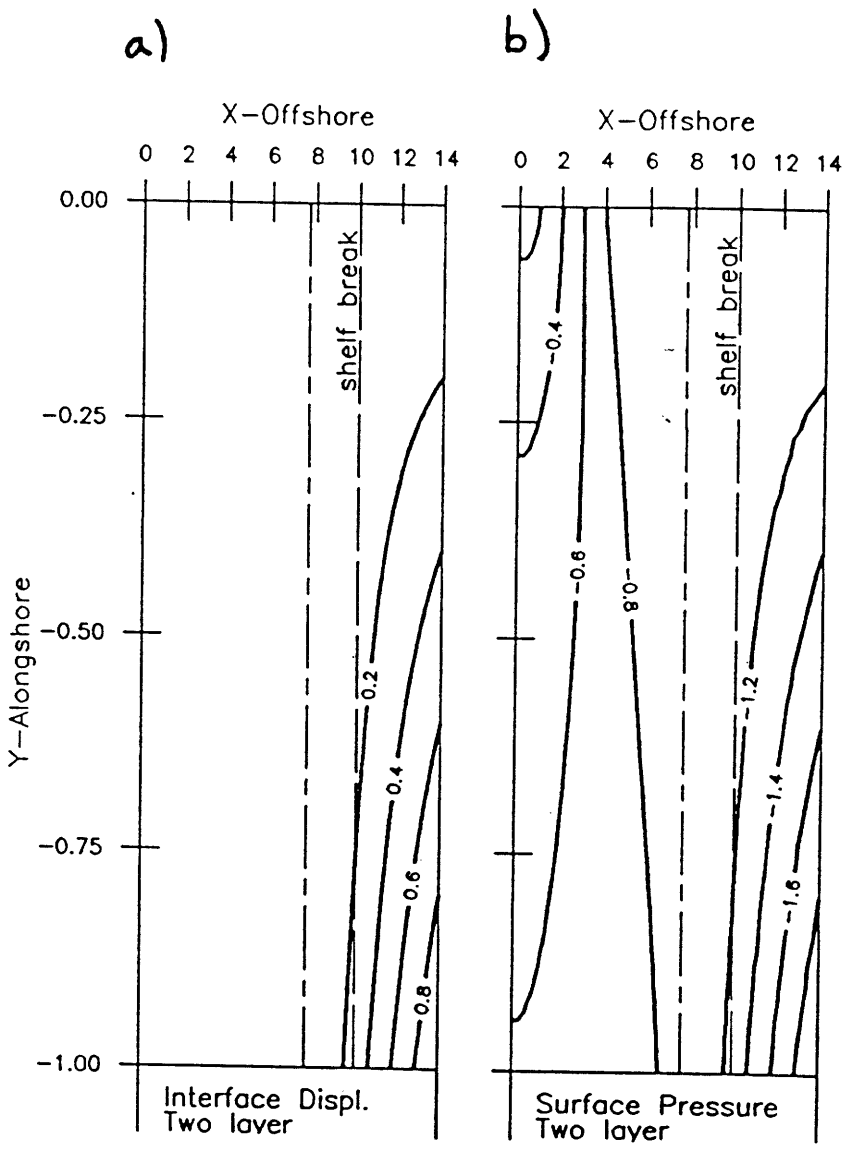


Figure 3-30: Solution for a combined deep ocean inflow and a narrow alongshore inflow when the upper layer thickness is $\frac{8}{10}$ the depth at the shelf break ($w' = 5$, $\Gamma' = 0$). The deep ocean lower layer is motionless. a) Interface displacement. b) Upper layer pressure.

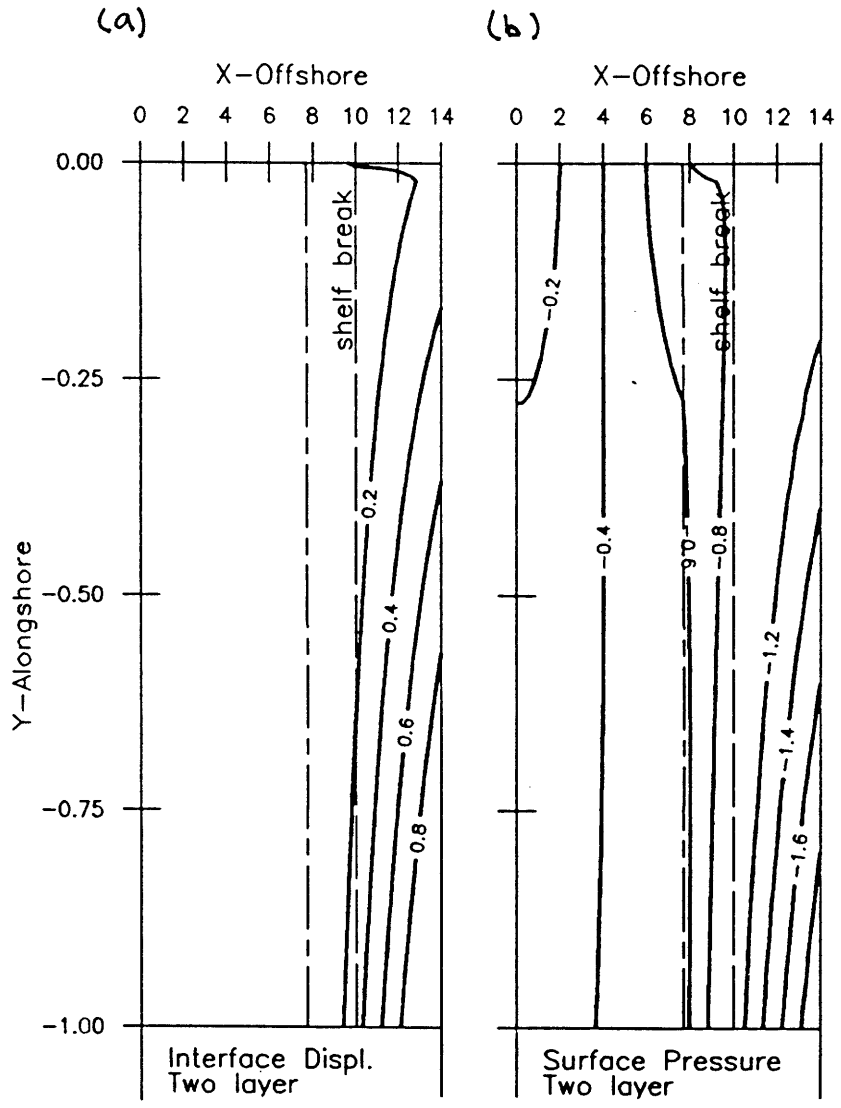


Figure 3-31: Solution for a combined deep ocean inflow and a wide alongshore inflow when the upper layer thickness is $\frac{8}{10}$ the depth at the shelf break ($w' = 10$, $\Gamma' = 0$). The deep ocean lower layer is motionless. a) Interface displacement. b) Upper layer pressure.

## 3.5 Conclusions For Layered Models

The two- and three-layer models presented here have a number of common features and several differences. For $f$-plane flow the equations governing flow in layers which are in contact with the bottom have exactly the same form in both layered models (see (3.70a), (3.70c) and (3.53)). The point source solution (3.32) demonstrates that, even if the "longwave approximation" were relaxed in these equations, provided the forcing is large compared to $\frac{\delta_E}{2s}$, solutions would still exhibit a short cross-topography scale compared to their along-topography scale. The length scale $\frac{\delta_E}{2s}$ is of order $5km$ over the shelf and only $500m$ over the slope. The narrowest deep ocean forcing used in the layered models has a length scale of order $250km$ which is much larger than $\frac{\delta_E}{2s}$. From this it is inferred that solutions to the deep ocean forcing problem will exhibit short cross-topography scales compared to their along-topography scale and this property is not an artifact of having assumed such a scale relationship (i.e. that $\frac{L_x}{L_y} << 1$) in order to produce a tractable set of equations. Planetary $\beta$ increases the cross-topography scale, but not to such an extent that $L_x$ becomes comparable to $L_y$.

In both models where layers on an $f$-plane are in direct contact with the bottom there is a balance between the vertical velocity due to Ekman pumping and that due to cross-isobath geostrophic motion. The equations governing these regions have the same form as the ATW equation but bottom pressure replaces the barotropic pressure. Physically, geostrophic flow in those layers in direct contact with the bottom can move shoreward only if Ekman pumping absorbs fluid into the Ekman layer at exactly the right rate so that fluid columns in the geostrophic core of the layer are neither stretched nor compressed. Conversely, geostrophic flow may move offshore only if Ekman pumping draws fluid from the Ekman layer into the geostrophic core at a rate which neither stretches nor compresses the fluid columns (see Figure 3-2). In these models Ekman pumping is the mechanism which allows geostrophic flow to cross topography; in its absence flow would be parallel to the isobaths. For typical scales the along-isobath velocity is much stronger than the cross-isobath velocity. Therefore the tendency for topography to steer geostrophic flow along isobaths is much stronger than the ten-

dency for Ekman pumping to diffuse or spread it across isobaths. This accounts for the ATW horizontal scale relationship (3.35). Cross-isobath motions are strongest for a highly turbulent bottom boundary layer, low latitude and a weak bottom slope. In both models, for typical scales, the cross-isobath influence of the deep ocean's lower layer is severely limited by the steep continental slope to a narrow band adjacent to the forcing.

The dynamics governing the density layers above the bottom layer differ in the two models. In the three-layer model motion in each of the upper two layers is governed by conservation of potential vorticity. Assuming that relative vorticity is small this may be stated as

$$\frac{\mathrm{d}}{\mathrm{d}t}\left(\frac{f}{h_i}\right) = 0 \qquad i = 1,2 \tag{3.89}$$

where $h_i$ is the thickness of the $i$th layer and $\frac{\mathrm{d}}{\mathrm{d}t}$ is the advective derivative, $u_i\frac{\partial}{\partial x}+v_i\frac{\partial}{\partial y}$. A consequence of (3.89) is that the value of $\frac{f}{t_i}$ will be the same along any given streamline (see Pedlosky (1979)). On an $f$-plane with a rigid lid, expanding (3.89) for the upper layer where $h_i = d_1 - \zeta$ yields $u_1\frac{\partial \zeta}{\partial x} + v_1\frac{\partial \zeta}{\partial y} = 0$ which is identical to (3.20). Similarly for the second layer (3.89) can be shown to be the same as (3.24). In order for potential vorticity to be conserved in the upper two layers fluid columns on an $f$-plane must maintain a constant thickness as they move within these layers. In other words they must behave as Taylor Proudman columns and motion is parallel to contours of layer thickness. Because both pressures are prescribed on $x = 0$ the interface displacement, and hence layer thickness, is known at $x = 0$. The value of $\frac{f}{t_i}$ on any given streamline is determined by the layer thickness where the streamline crosses $x = 0$.

In the three-layer model when two adjacent layers are in motion the flow in one must be parallel or anti-parallel to the flow in the other. This coupling can be envisaged as a steering of the upper layer by the lower layer of the pair. An intervening motionless layer decouples the motion in the layers on either side of it. The flow pattern in the lowest density layer is determined by (3.30), and because of coupling the cross-isobath influence of the deep ocean in all layers between a moving bottom layer and

the first motionless layer is limited by the topography and has a cross-slope scale given by (3.35). Layers coupled to the bottom density layer can be thought of as being in indirect contact with the topography.

The results of this three-layer model can be generalized to any larger number of geostrophic layers which would sensibly fit within the maximum water depth permitted by the approximations used (i.e. neglect of relative vorticity and planetary $\beta$). The generalized result would state that motionless layers separate moving layers into groups. Flow in any member of a group must be parallel or anti-parallel to flow in any other member of the group. A group which contains the lowest layer has very limited cross-slope motions. The flow pattern in groups not containing the moving bottom layer cannot be determined from this model because of geostrophic degeneracy.

In the two-layer interfacial friction model flow in the upper layer where it overlies the lower layer is governed by (3.70b) and is not degenerate when the bottom layer is motionless. The physical interpretation of this equation for $f$-plane flow is essentially the same as that for those governing layers in contact with the bottom. Vertical velocity is zero in the upper layer, and therefore fluid columns in the geostrophic core of this layer may cross the isobaths created by the warping of the interface only if upper layer interfacial Ekman pumping absorbs or exports fluid from or to the geostrophic core at a rate such that fluid columns of the core are neither stretched nor compressed (see (3.49)). This mechanism also operates at the interface in the lower layer ensuring that fluid columns in the core of that layer are also neither stretched nor compressed. The main differences between the interfacial and bottom layer dynamics are that interfacial "topography" varies in both $x$ and $y$, and that Ekman pumping results from a velocity difference between layers, i.e. shear, rather than from absolute velocity. The dynamics in (3.49) (or its equivalent (3.51)) can be envisaged as a balance between steering of the upper layer by the lower layer and interfacial drag. The former causes flow to follow the "isobaths" of the interfacial "topography", and the latter tends to spread geostrophic flow across "isobaths". For typical scales (see Table 3.2) steering and drag effects are of approximately equal importance in determining the upper layer flow pattern.

The influence of $\beta$ will be discussed later. The spreading, which was not present in the previous three-layer model, is enhanced by strong stratification and high values of internal turbulent eddy viscosity.

Figure 3-8 shows that, except near the line where the interface intersects the bottom, upper layer flow does not induce motion in the geostrophic core of the lower layer. This apparently contradicts the notion that upper layer motion forces lower layer motion through interfacial drag. It can be shown that a motionless lower layer core is not inconsistent with a moving upper layer and, by analogy to motion forced by surface winds, that such a situation is physically reasonable. The core of the lower layer is motionless when $\chi_2 = 0$. In this case the interface displacement is related to the upper layer pressure by

$$\varsigma = -\frac{1}{\epsilon}\,\chi_1 \tag{3.90}$$

which implies that geostrophic flow in the upper layer is along contours of interface displacement. On an $f$-plane the governing equation (3.51) for $\chi_2 = 0$ becomes

$$\nabla^2\,\chi_1 = 0 \quad . \tag{3.91}$$

The dimensional curl of the interfacial stress from (B.15) and (B.16) is

$$\frac{\partial \tau^y_{int}}{\partial x} - \frac{\partial \tau^x_{int}}{\partial y} = -\frac{g}{f_0}\nabla^2\,\chi_1 \quad . \tag{3.92}$$

The right hand side is zero because of (3.91) and consequently the interfacial stress is non-divergent when the core of the lower layer is motionless. For barotropic motions forced by surface winds a non-divergent wind stress implies that Ekman transports are also non-divergent and that Ekman pumping is zero (see Gill (1982)). In the absence of Ekman pumping the fluid in geostrophic balance below the Ekman layer is not set in horizontal motion except near coastal boundaries where the surface Ekman transport is blocked. Thus when the wind stress is non-divergent, motion is confined to a thin surface Ekman layer. The lower layer of the interfacial friction model is analogous

to a wind-forced barotropic model in that it experiences a stress on its upper surface due to motion in the upper layer. This stress produces Ekman transport in the lower interfacial Ekman layer. By analogy a non-divergent interfacial stress is consistent with there being no motion in the core of the lower layer except near the interface/bottom intersection where interfacial Ekman transport is blocked. Consequently a motionless lower layer core is not inconsistent with a moving upper layer. The above reasoning applies only to a motionless lower layer on an $f$-plane.

A motionless upper layer is inconsistent with a moving lower layer (see Figure 3-10). Irrespective of motion in the upper layer (3.70b) shows that in general a moving lower layer implies that $\nabla^2 \chi_2 \neq 0$. Thus even if the upper layer is motionless the interfacial stress is divergent. Consequently when the lower layer is in motion there must be a compensating upper layer motion across the "topography" to balance the divergence of Ekman transport in the upper interfacial Ekman layer. In Figure 3-10 the deep ocean upper layer is motionless, i.e. $\chi_1|_{x=x_{max}} = 0$, however the moving lower layer establishes a cell of upper layer motion between the deep ocean and the topography/bottom intersection.

It is found that the cross-topography scale of the upper layer is dependent on the degree of baroclinicity, $\Gamma'$, the upper layer thickness, $d_1$, the relative Ekman layer thickness, $\delta_E^{rel}$, and planetary $\beta$. When deep ocean flow is near to barotropic, ($\Gamma' \geq 0.5$), the velocity difference between layers is small, interfacial drag is weak and steering of the upper layer by the lower layer dominates. When planetary $\beta$ is not important the upper layer will have almost the same cross-topography scale as the lower layer given by (3.35), and therefore will also be confined to a narrow band near the deep ocean forcing.

When the deep ocean flow is weak in the lower layer, ($\Gamma' \leq 0.1$), the cross-topography extent of significant upper layer flow is limited to offshore of the interface/bottom intersection. Figure 3-32 shows that in the two-layer model the cross topography scale is linearly related to both the baroclinicity and the upper layer thickness.

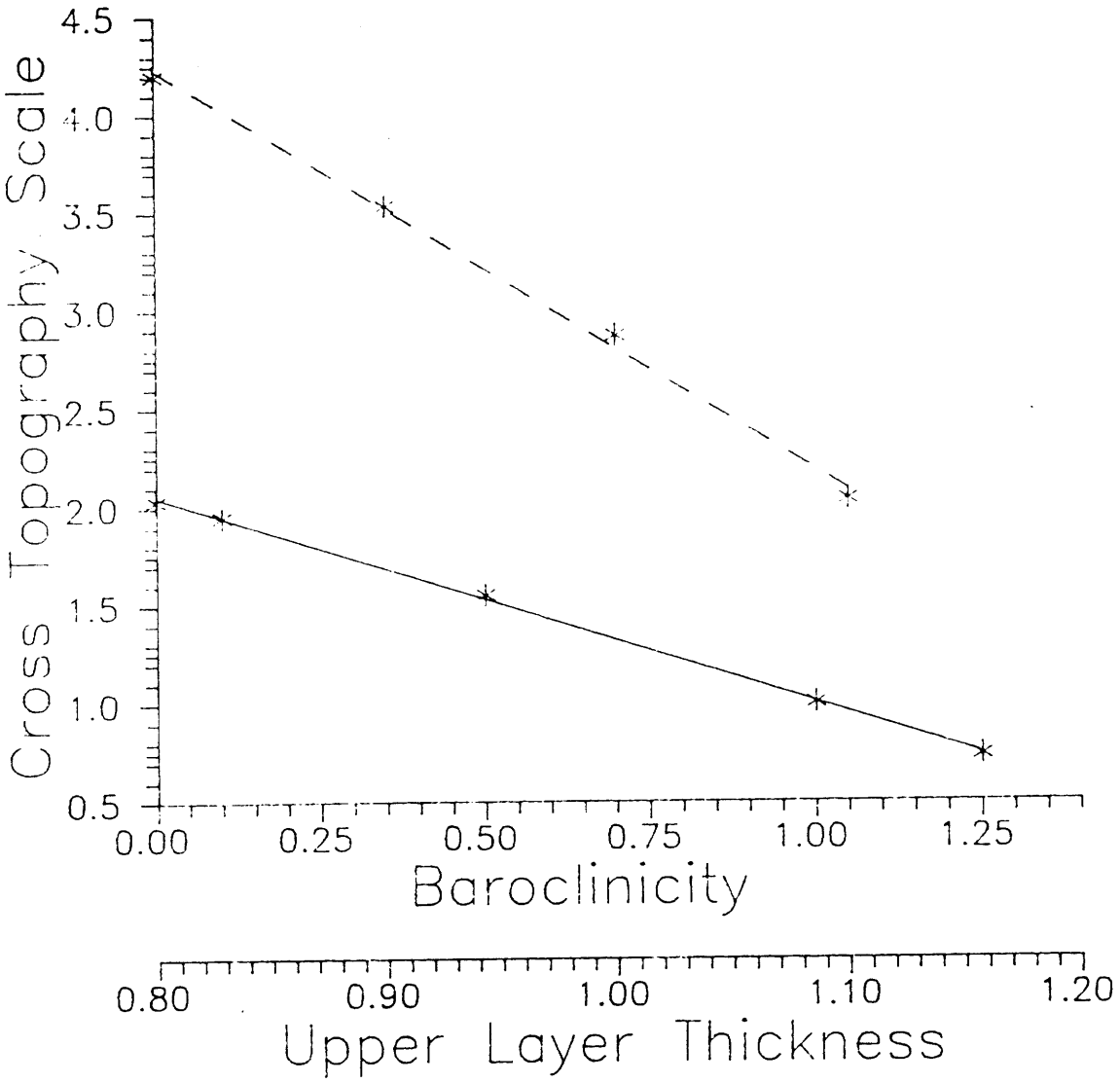


Figure 3-32: Cross topography scale relative to that of a barotropic flow as a function of baroclinicity (solid line ) and as a function of upper layer thickness (dashed line ) when the deep oceans lower layer is motionless. Baroclinicity is the ratio of the strength of the deep oceans upper layer flow to that in the lower layer. Upper layer thickness is relative to the depth at the shelf break. The lines are linear fits to the width of the flow as measured by the 0.2 contour at $y' = -1$.

Planetary $\beta$ increases the cross-topography penetration in both layers of a deep ocean flow impinging on an east coast. However the maximum penetration is confined to offshore of the interface/bottom intersection. A thin upper layer and surface intensification enhance penetration for both $f$- and $\beta$-plane flows. The effect of planetary $\beta$ on the deep ocean inflow can be explained by comparing the governing equations to those governing two-dimensional heat diffusion. The $\beta$ term acts to "advect" the pressure field westward. Consequently planetary $\beta$ enhances cross-topography penetration on an east coast. This explanation suggests that the effect of planetary $\beta$ on a west coast deep ocean inflow (i.e. impinging on the ocean's eastern boundary) would be to reduce its cross-topography penetration. However such a hypothesis cannot be tested with the model presented here because if $\beta$ is important the numerical scheme cannot be used for a deep ocean flow impinging on a west coast.

Significant upper layer flow is confined between the deep ocean and the interface/bottom intersection for two reasons. Firstly, to match Ekman transports across the intersection, the ratio of the flow strength in the upper layer just shoreward of the intersection to that just offshore of the intersection must be equal to the ratio of the interfacial Ekman layer thickness to the bottom Ekman layer thickness, i.e. $\delta_E^{rel}$. For the scales used this ratio is less than unity and therefore upper layer flow shoreward of the intersection must be weaker than the flow offshore of it. Secondly, interfacial Ekman transport results from the relative motion of the two layers. When lower layer flow is weak interfacial Ekman transport is mainly due to motion in the upper layer. Blocking of lower layer interfacial Ekman transport at the interface/bottom intersection induces a narrow band of weak geostrophic flow in that layer adjacent to the intersection. In summary, little deep ocean upper layer flow reaches the line where the interface intersects the bottom and only a small proportion of this flow is able to cross the line. Consequently the cross-slope influence of the deep ocean is limited to offshore of the interface/bottom intersection. This conclusion is independent of the dynamic significance of planetary $\beta$.

The internal mass balance of the layer models warrants a more detailed discussion. In the three-layer model deep ocean fluid enters the slope region as geostrophic flow across the offshore edge. Only in the bottom Ekman layer is there a return flow across the offshore edge to the deep ocean. The mass balance is not however two dimensional in the $x - z$ plane, most of the deep ocean inflow leaves the domain of interest across the southern boundary and only a small proportion flows back to the deep ocean in the bottom Ekman layer. The global mass balance of the two-layer interfacial model is similar to that of the three-layer model. Deep ocean fluid enters the shelf slope region across the offshore edge as geostrophic transport, most of this flow leaves the region across the southern boundary and if the core of the deep ocean's lower layer is moving then there is a leakage of fluid back to the deep ocean in the bottom Ekman layer. As shown earlier the upper and lower interfacial Ekman transports are equal in magnitude but in opposite directions and therefore there is no net transport across the offshore edge due to interfacial friction. To examine the interfacial transports in more detail consider the case where the deep ocean's lower layer core is motionless (Figure 3-8). There is a weak return flow to the deep ocean in the upper interfacial Ekman layer and consequently an influx of fluid from the deep ocean into the lower interfacial Ekman layer. This weak lower interfacial Ekman transport caused by interfacial drag flows southward and shoreward. Eventually this transport will hit the line where the interface intersects the bottom. At this point it is converted into bottom Ekman transport and is responsible for the interior flow adjacent to the intersection seen in Figure 3-8a.

The diagnostic two-layer model of Csanady (1985) has a similar geometry to the models presented here. His model also predicts shoreward and southward flow and that deep ocean flow does not penetrate far shoreward of the interface/bottom intersection. It assumes apriori that the interface has a linear alongshore gradient everywhere. Implicit in this assumption is that all upper layer flow must cross the interface/bottom intersection. In the more realistic model presented here little flow is able to cross the intersection and this shows that Csanady's model overestimates the deep ocean's

cross-isobath influence. In his model pressure is continuous across the line where the interface intersects the bottom and this ensures that geostrophic transport normal to the intersection is continuous across it. Just shoreward of the intersection there is an Ekman transport normal to it, however just offshore of the intersection there is no matching transport in the upper layer. Thus Ekman transport, and therefore total mass, is not conserved across the line of intersection. In Csanady's model mass can be conserved only if no flow is permitted to cross the intersection. The two-layer model presented here approaches Csanady's model when interfacial friction is weak. In this case it is found that almost no flow crosses the intersection.

The results for the combined alongshore inflow and deep ocean inflow show that when the upper layer is significantly thicker than the depth at the shelf break the deep ocean flow is confined over the continental slope and the alongshore inflow is confined over the shelf. For this geometry the two regions of flow do not dynamically influence each other. The steep slope acts as an insulating barrier between the shelf and slope water masses. When the upper layer is thinner than the depth at the shelf break the flows due to deep ocean and alongshore forcing can influence each other. For a sufficiently thin upper layer and a sufficiently wide alongshore inflow shelf water can escape from the shelf into the deep ocean's upper layer. A deep ocean inflow acts to prevent shelf flow from moving far offshore, trapping it on or near the shelf. Thus one conclusion of Chapman et al. (1986), namely that a barotropic deep ocean acts to hold water on the shelf, can be extended to the baroclinic flows used here.

As the number of layers get larger the three layer model will tend towards a continuously stratified model with a geostrophic interior and a bottom Ekman layer. However the interfacial friction model assumes that the density difference between layers is strong enough that mixing between layers is prevented. Thus this model cannot be considered as a discretization of a continuously stratified ocean because as the number of layers increases the density difference between layers will decrease to the point that the assumption of no inter-layer mixing will no longer be valid. Thus the interfacial

friction model is more appropriate as a mathematical model of a layered laboratory model.

## 3.6 Summary of Layered Models

The layered models show that:

1. the cross-topography scale of the deep ocean's lower water column is severely limited by the steep continental slope;

2. the cross-topography scale of the deep ocean's upper water column depends primarily on the vertical profile of the deep ocean flow;

    - In near barotropic flows the upper water column is coupled to the lower water column and therefore has a small cross-topography scale.
    - In surface intensified flows the upper water column is decoupled by the stratification from the lower water column and can flow shoreward until encountering the bottom.

3. planetary $\beta$ increases the cross-topography scale of the entire water column and in surface intensified flow acts to further decouple the upper and lower water columns.

# Chapter 4

# Conclusion

The sequence of models developed here can be linked in the following way. The first model in the series is that of Vennell and Malanotte-Rizzoli (1987). It assumes that the horizontal density field of the vertical well mixed flow is known everywhere a priori and that it does not change. This diagnostic approach is useful in determining the flow induced by an alongshore density gradient. Such an approach unrealistically ignores the advection of density by the induced flow but does avoid the difficulty of solving the non-linear advective density equation, and thus it yields a tractable model.

The second model in the series is the vertically well mixed model of chapter 2. This model incorporates horizontal advection of density. The governing equation (2.29) is in general non-linear. However for particular boundary conditions, i.e. when the density and streamfunction are linearly related on the boundaries, the equation is linear and relatively easily solved. Such a model is a significant improvement over that of Vennell and Malanotte-Rizzoli (1987) but can only determine the influence of the deep ocean once it impinges on the shelf because it is limited to situations where the flow is vertically well mixed, i.e. to depths of order $100m$. Thus it assumes that the deep ocean is able to cross the steep continental slope. The solutions of Wang (1982) and others show that the continental slope has a significant influence on barotropic flow. The well mixed model is limited to depths significantly less than oceanic depths and thus cannot include the topography of the continental slope.

The third model in the series is the three-layer model of section 3.3. Due to the latitudinal and depth restrictions on the $f$-plane model ( see (3.11) and (3.12)) it is

applicable to the upper continental slope, i.e. depths of $500m$ or less, a significant advance over the vertically well mixed model. Its limitation is that it does not determine the flow pattern in layers above the first motionless layer because the model is geostrophically degenerate. Consequently it cannot give a solution for the potentially most interesting case where the lower water column of the deep ocean inflow is motionless. This case is interesting because intuitively it is expected that such a deep ocean flow will not be influenced by the steep topography of the continental slope until it flows into water shallow enough to encounter the bottom.

The fourth model is the two-layer interfacial friction model on an $f$-plane of chapter 3.4 in sections 3.4f through 3.4i. This model resolves the geostrophic degeneracy of the previous three-layer model and verifies the intuitive result for a deep ocean where the lower layer is motionless. Neglect of planetary $\beta$ restricts both the three-layer model and two-layer $f-$plane model to a $250km$ wide deep ocean inflow and to depths $500m$ or less which are scales appropriate for the upper continental slope. Thus it is assumed that a deep ocean flow has already crossed the lower continental slope before impinging on the upper continental slope. This is a valid assumption only if the deep ocean's lower layer is motionless. If the deep ocean's lower layer is moving, then the topography of the lower slope should be included in the model.

The fifth and final model in the series is the extension of the two-layer interfacial friction model to a $\beta$-plane in section 3.4j. This model is applicable to deep ocean inflows $1000km$ wide, comparable to the scale of the general oceanic circulation, and to depths of order $3000m$ or more. The evolution of this series of models has expanded the depth range of applicability while retaining vertical structure in the deep ocean and while keeping the models simple enough that physical mechanisms which influence the flow pattern can be determined. The final model in the series, the two-layer $\beta$-plane model, is valid over the full depth range of the continental slope and to horizontal scales representative of the deep ocean, and thus can properly address the question of deep ocean influence on the shallow continental shelf.

The vertically well mixed and layered models have a number of common features and differences. In both flow is in geostrophic balance outside the Ekman layers. Flow in the well mixed model, in the lowest layer of the three-layer model, in the two-layer model shoreward of the interface/bottom intersection and in the bottom lower layer of the two-layer model is in the same direction at all depths above the bottom Ekman layer. Therefore the influence of the topography on the near bottom flow permeates the entire depth of these flow regions and they can be considered to be in direct contact with the bottom. Since flow in direct contact with the bottom is determined by topography and bottom friction the cross-topography scale of flow in these regions on an $f$-plane is primarily given by the ATW scale relationship (3.35).

In the vertically well mixed model vertical shear causes a variation in the cross-topography scale, however this variation is of secondary importance. Shear affects the strength of the near bottom velocities and hence the strength of bottom friction. For the layered models layers in direct contact with the bottom have horizontal velocities which are depth independent within the layers and this secondary variation is not present. For typical values the ATW scale relationship predicts a small cross-topography scale for all flow in direct contact with the bottom. Although planetary $\beta$ can significantly increase the cross-topography scale of these flows in deep water this increase is insufficient to permit such flows to cross the steep continental slope.

The vertically well mixed model shows that geostrophic flow requires bottom friction to cross isobaths thus flows with weak bottom velocities should not cross the topography very well as bottom stresses are weak. The layered interfacial friction model shows that the upper water column flow should have little knowledge of the topography if bottom velocities are weak and therefore should not be strongly influenced by it. Thus the vertically well mixed and two-layer models are apparently contradictory in that the well mixed model shows that surface intensification reduces the cross-topography scale whereas the two-layer model shows that it increases the cross-topography scale. In the well mixed model the cross-topography scale is primarily determined by the ATW scaling while vertical shear is of secondary importance. In the two-layer model vertical

shear is of primary importance. Stratification combined with surface intensification can significantly increase the cross-topography scale beyond that predicted by the ATW scaling because it decouples upper level flow from the topography below. Essentially the well mixed model only considers the secondary effect of the near bottom shear on the spatial variation of bottom stress, whereas the two-layer model considers the primary effect of vertical shear on the much deeper stratified water column.

In the two- and three-layer models the influence of topography on the layers overlying the lowest layer depends on the vertical profile of the flow. Motion in the three-layer model in layers above a moving layer but below the first motionless layer must be parallel or anti-parallel to motion in the lowest layer. These layers can be considered to be in indirect contact with the topography below them through the effects of interfacial displacements. Consequently flow in these layers will also exhibit a very short cross-topography scale given by the ATW scaling. Flow in layers above the lowest motionless layer is completely decoupled from the topography below and cannot be determined by the three-layer model. In fact the behavior of flows in the upper layers of the three-layer model is singular depending on whether the flow in the layer immediately below is zero or non-zero.

This singular behavior is bridged by the two-layer interfacial friction model. The coupling of the flow in the two layers is a continuous function of the flow's vertical profile. For near barotropic flows coupling of the upper layer to the lower layer is strong and the upper layer's cross-topography scale is given approximately by the ATW scaling. When flow is surface intensified upper layer flow is decoupled from lower layer flow and has a much wider cross-topography scale than that given by the ATW scaling. Planetary $\beta$ acts to reduce the coupling in surface intensified flows.

The models presented here are dynamically similar to the model given in Kelly and Chapman (1987) (hereafter KC). KC showed that diffusion due to mixing had little effect on the cross-topography penetration of the deep ocean. This suggests, despite the mixing of momentum, that their model is close to geostrophic balance outside of the thin bottom frictional layer. KC assume that the bottom stress is proportional to

the velocity just above the bottom boundary layer. This leads to a bottom boundary condition which is very similar to those used in this work, where the vertical velocity just above the frictional layer is the sum of the vertical velocities due to topography and Ekman pumping.

Despite the similar dynamics and boundary conditions the model of KC and those presented here are very different in the manner in which density is included. The density equation for steady flow can be stated

$$\underset{A}{u\frac{\partial \rho}{\partial x}} \quad \underset{B}{+v\frac{\partial \rho}{\partial y}} \quad \underset{C}{+w\frac{\partial \rho}{\partial z}} \quad = \underset{D}{K_H \nabla_H^2 \rho} \quad \underset{E}{+K_V \frac{\partial^2 \rho}{\partial z^2}} \tag{4.1}$$

where $K_H$ and $K_V$ are the horizontal and vertical eddy diffusivities. KC assumes that density can be written as a mean background stratification and a perturbation density, i.e. $\rho = \rho_0(1 + \rho_b(z) + \rho'(x, y, z))$. They ignore horizontal advection of density and balance terms C,D and E in (4.1). Such an assumption leads to a linear model. Horizontal advection of density can be ignored by KC provided horizontal velocities are not too strong. The vertically well mixed model presented here balances terms A and B in (4.1), exactly those terms neglected by KC, yet they both demonstrate the strong influence topography has on the flow. Unlike KC the layered models presented here neglect the mixing of density. Thus a fluid parcel does not change its density as it is advected around within layer. In this sense the layered models are purely advective. Consequently both the well mixed and layered models treat density in the opposite manner to KC.

KC's results show that the cross-topography influence is primarily determined by the deep ocean's velocity profile, near bottom flow has a limited cross-topography penetration, stratification decouples the upper and lower water column and surface intensified flows are able to move shoreward until they encounter the bottom. The similarity of the results to those found here is interesting in the light of the opposing treatments of density. This suggests that it is not the form of the density equation which determines the nature of the flow pattern but the common dynamics. Essentially all

the models show that, despite bottom friction, steady geostrophic flow does not cross isobaths very rapidly unless stratification isolates if from the topography below.

Different dynamics are used by Chapman and Brink (1987) in considering the influence of an unsteady deep ocean on the shelf. Their linear $f-$plane model includes bottom friction and ignores the mixing of density and momentum. The density equation balances the time rate of change of perturbation density against vertical advection of the background stratification. Despite the differences their conclusions for low frequencies are similar to those obtained here. They find that if the deep ocean flow encounters the bottom within the forcing's horizontal decay scale then the flow turns to follow isobaths ( although in their model such a flow forms a bottom trapped wave mode with a velocity maximum offshore of the shelf break) and that the shelf response is always weak and barotropic. The results common to this work, KC and Chapman and Brink (1987) are that stratification decouples the upper and lower water column and that deep ocean flow is not strongly influenced by the topography until it encounters the bottom. Once the bottom is encountered further cross topography motion is severely limited by the continental slope.

The mean currents observed over the shelf and slope during both NSFE79 and SEEP were closely aligned with the isobaths. All the models presented here show this alignment. Aikman et al.(1986) noted that the mean velocities had a minimum at the shelf break. The oxygen isotope data of Chapman et al. (1986) show that Scotian shelf water remains on the shelf during its southwestward passage down the Mid-Atlantic Bight . The combined deep ocean and alongshore forcing of section 3.4k suggests that Scotian shelf water and deep ocean water should remain distinct water masses confined over the shelf and slope respectively. The two water masses can dynamically influence each other only when the upper layer is thinner than the depth at the shelf break. For such a thin upper layer Scotian shelf water can escape the shelf into the deep ocean unless there is a deep ocean inflow. Consequently the deep ocean acts to hold Scotian shelf water on the shelf. When combined with the oxygen isotope and mean flow observations the results of this model suggest that the observed mean flow over

the shelf is of Scotian shelf origin, the mean flow over the slope is of deep ocean origin and the mean flow minimum marks the boundary between the two water types.

Although KC found that mixing had little effect on the penetration of the deep ocean the oxygen isotope data shows that horizontal mixing does occur between the shelf and slope. The neglect of horizontal mixing in the vertically well mixed model and the neglect of all mixing in the layered models is clearly a limitation.

The well mixed model is of limited use in addressing the question of deep ocean influence on the shelf because it does not include the steep topography of the continental slope. This question, which is central to this work, is best addressed by the layered models since they include the continental slope. The two-layer model demonstrates that the deep ocean can influence the shelf if the the depth scale of both density and velocity is less than the depth at the shelf break. Consequently a large proportion of a steep shelf could be influenced by the deep ocean. A wide gently sloping shelf could only be influenced by deep ocean flows with a very small depth scale. The main thermocline at mid-latitudes is at about $1000m$ depth which is too deep to permit deep ocean influence on the shelf. Gulf Stream Rings have a considerably smaller depth scale ($O(500m)$ Joyce (1984)) and therefore could influence the shelf if the shelf break were deep enough. In the Mid-Atlantic Bight this is not the case since the shelf is both wide ($O(100km)$) and shallow at the shelf break ($O(100 - 200m)$). Consequently features with such depth scales could not be responsible for the observed mean shelf flow.

In conclusion the degree of cross-topography influence of any given deep ocean flow depends on its vertical structure. Near-bottom deep ocean flow has a very short cross-topography scale due to the steep continental slope and consequently never reaches the shallow shelf. The effect of the continental slope on the upper water column of the deep ocean depends on the vertical structure of the deep ocean flow. For a barotropic or near barotropic deep ocean the upper water column tends to follow the near bottom flow and thus does not cause significant flow over the shelf. In a surface-intensified deep ocean the upper water column is decoupled from the lower water column and consequently is not influenced by the topography below it until it encounters the bottom. Therefore

a surface-intensified deep ocean may have a much larger cross-topography scale than a barotropic or near barotropic deep ocean. A surface-intensified deep ocean can cause significant shelf flow but only if flow is confined to a layer thinner than the depth at the shelf break and if the flow in this layer is at least an order of magnitude stronger than the flow below the surface layer. In the deep ocean the depth scale for both the density and velocity is generally larger than the depth at the shelf break . Consequently the steep continental slope insulates the shelf from deep ocean influence.

## Appendix A

## Near Field Solution for a Vertically Well Mixed Shelf

By deriving an approximate form of the density equation valid in the "near field" and by solving the transport equations for surface pressure and density, it is possible to obtain an analytical solution which greatly aids physical understanding of the manner in which topography influences flow. The near field solution can be used to analytically obtain the flow induced over the shelf by the edge of a Gulf Stream Ring.

### A.1 Near Field Advective Density Equation

The transport equations (2.12a) and (2.12b) suggest a partition of the total cross-shelf transport into geostrophic and ageostrophic transport. The latter is due to frictional effects at the lower boundary. The cross-shelf geostrophic transport is defined as

$$fU^g = -gh(\frac{\partial \eta}{\partial y} + \frac{h}{2}\frac{\partial \epsilon}{\partial y}) \tag{A.1}$$

and the cross-shelf ageostrophic transport is

$$fU^{ag} = -\frac{r}{f}v_b \quad . \tag{A.2}$$

The total cross-shelf transport, $U$, is equal to $U^g + U^{ag}$. Under the assumption that cross-shelf scales are small compared to alongshore scales, alongshore frictional transports can be neglected and alongshore flow is in approximate geostrophic balance.

The ratio of cross-shelf ageostrophic transport to geostrophic transport, using the definitions of bottom velocities (A.2) and assuming that surface pressure and density

make approximately equal contributions to total pressure, is of order

$$\left|\frac{U^{ag}}{U^g}\right| = \frac{r}{fh_0}\frac{L_y}{L_x} \quad . \tag{A.3}$$

$\frac{r}{fh_0}$ is equal to $E_v^{\frac{1}{2}}$ which is small, however under the long wave assumption $\frac{L_y}{L_x}$ is large. The product of these two ratios can be shown to be small in a particular region, and thus the transport of density by cross-shelf Ekman transport can be neglected.

Noting that the ATW relationship between horizontal scales (2.34) can be rewritten as $\frac{L_y}{L_x} = \frac{fsL_x}{r}$,

$$\frac{r}{fh_0}\frac{L_y}{L_x} = \frac{sL_x}{h_0} \quad . \tag{A.4}$$

The near field is where the above non-dimensional number is small and this occurs when the depth change over the flow's cross-shelf scale is small compared to the water depth, i.e. where

$$\frac{sL_x}{h_0} << 1 \quad . \tag{A.5}$$

$h_0$ is approximately $s\ell$, ( $\ell$ is the shelf width), if the depth at the coast is small, and therefore the near field is the region where

$$\frac{L_x}{\ell} << 1 \tag{A.6}$$

i.e. where the inflow from the deep ocean has not expanded too far across the shelf. A flow which enters the shelf across $x = \ell$ follows the topography while expanding slowly across it due to friction. This is a consequence of the ATW scaling (2.34). In the near field region this expansion across the shelf is still small implying that the flow has not moved too far along the shelf. Therefore the near field is the region of the shelf confined to the shelf edge within a few $L_y's$ of the point where flow first enters the shelf. Dimensionally the advective density equation (2.26) in the near field where total

transport may be approximated by geostrophic transport is

$$\frac{\partial \eta}{\partial y}\frac{\partial \epsilon}{\partial x} - \frac{\partial \eta}{\partial x}\frac{\partial \epsilon}{\partial y} = 0 \quad . \tag{A.7}$$

This may be written in terms of a Jacobian

$$J(\epsilon, \eta) = 0 \quad . \tag{A.8}$$

Therefore density is conserved along surface displacement contours in the near field. Neglecting the ageostrophic advection of density allows an approximation of the Jacobian (2.27) by (A.8) in the near field. This is a good approximation only as long as surface displacement contours are almost the same as transport streamlines - a condition that is true only for a finite distance along the shelf.

From (A.8) the density is a function of the free surface displacement, $\eta$, i.e.

$$\epsilon = \mathcal{G}(\eta) \quad . \tag{A.9}$$

If $\eta$ and $\epsilon$ are prescribed along the outer edge of the shelf then $\mathcal{G}(\eta)$ will be known there and, because of density conservation (A.8), this functional relation will hold in the near field in regions which contain flow which crossed the outer edge.

## A.2 Surface Pressure Flow Equation

An alternative form of the flow equation (2.16) can be obtained by solving the transport equations (2.12a), (2.12b) and (2.12c) for the free surface displacement yielding

$$\frac{r}{f}\frac{\partial^2 \eta}{\partial x^2} + h_x \frac{\partial \eta}{\partial y} = -\frac{\partial h}{\partial x} h \frac{\partial \epsilon}{\partial y} - \frac{r}{f}\frac{\partial}{\partial x}\left(h\frac{\partial \epsilon}{\partial x}\right) \quad . \tag{A.10}$$

This is the same as the equation derived by Csanady (1979) but for a vertically well mixed shelf.

Combining (A.9) and (A.10) yields an equation in a single variable

$$\frac{r}{f}\frac{\partial}{\partial x}\left((1 + h\frac{\mathrm{d}\mathcal{G}}{\mathrm{d}\eta})\frac{\partial \eta}{\partial x}\right) + h_x(1 + h\frac{\mathrm{d}\mathcal{G}}{\mathrm{d}\eta})\frac{\partial \eta}{\partial y} = 0 \tag{A.11}$$

which can be solved for $\eta$. Given the solution for $\eta$ the density $\epsilon$ can be calculated using (A.9).

An example of a case when (A.11) has an analytical solution is when the boundary conditions are such that $\eta$ and the density $\epsilon$ are proportional to each other, i.e.

$$\epsilon = K\eta \quad . \tag{A.12}$$

In this case $\frac{d\varrho}{d\eta}$ is the constant, $K$, and (A.11) becomes

$$\frac{r}{f}\frac{\partial}{\partial x}\left((1+Kh)\frac{\partial \eta}{\partial x}\right) \quad + \quad h_x(1+Kh)\frac{\partial \eta}{\partial y} = 0 \quad . \tag{A.13}$$

From the hydrostatic relation (2.4c) and (A.12) the flow's geostrophic velocities for a well mixed shelf can be written

$$-fv^g = -g(1+Kz)\tfrac{\partial \eta}{\partial x} \tag{A.14}$$

$$fu^g = -g(1+Kz)\tfrac{\partial \eta}{\partial y} \tag{A.15}$$

showing that $K$ can be physically interpreted as a measure of the vertical shear in geostrophic velocity. These equations also show that the geostrophic velocity is parallel to the surface displacement contours at all depths.

The relative size of the cross-shelf transport of density by geostrophic flow to that by ageostrophic flow in this special case of parallel density and surface displacement contours is given by the ratio

$$\frac{U^{ag}}{U^g_{barotropic}} = \frac{\frac{r}{f}(1+Kh)\frac{\partial \eta}{\partial x}}{h\frac{\partial \eta}{\partial y}} \quad . \tag{A.16}$$

This ratio will be calculated from the final solution to ensure it remains small in the near field, in which case (A.7) will be valid. This ratio shows that the near field will be longer for bottom intensified flows ( $K < 0$ ) than for surface intensified flows ($K > 0$).

## A.3 Near Field Boundary Conditions

Equation (A.13) is parabolic. Its boundary conditions are:

(i) $\frac{\partial \eta}{\partial x} = 0$ where h =0, no flow through coast.

(ii) $\eta = 0$ at y = 0, "initial condition" no inflow from higher latitudes.

These conditions are the same as those used by Csanady in his ATW model. At the shelf edge the jet will be driven by a linear ramp in the free surface.

(iii)

$$\eta = \begin{cases} 0 & 0 < y \\ Ay, & y \leq 0 \end{cases} \quad at \quad x = \ell \quad . \tag{A.17}$$

The boundary condition for density, $\epsilon$, at the shelf edge will be also taken as a linear ramp,

$$\epsilon = \begin{cases} 0 & 0 < y \\ By & y \leq 0 \end{cases} \quad at \quad x = \ell \tag{A.18}$$

so that the functional relation, $K$, is $\frac{A}{B}$.

## A.4 Near Field Solution

Equation A.13 can be solved for linear topography, i.e. $h = sx$, by noting its analogy to that governing heat diffusion in a cylinder. (A.13) becomes

$$\frac{r}{fs}\frac{\partial}{\partial x}\left((1+Ksx)\frac{\partial \eta}{\partial x}\right) \quad + \quad (1+Ksx)\frac{\partial \eta}{\partial y} = 0 \quad . \tag{A.19}$$

which can be rewritten

$$\frac{rsK^2}{f}\frac{\partial}{\partial R}\left(R\frac{\partial \eta}{\partial R}\right) + R\frac{\partial \eta}{\partial y} = 0 \tag{A.20}$$

where $R = 1 + Ksx$. The boundary conditions for surface displacement are:

(i) $\frac{\partial \eta}{\partial R} = 0$ at R= 1, no flow through coast

(ii) $\eta = 0$ at y = 0

(iii)

$$\eta = \begin{cases} 0 & 0 < y \\ \beta y, & y \leq 0 \quad \text{at R} = 1 + \text{Ks}\ell \end{cases} \quad . \tag{A.21}$$

The analogous cylindrical heat conduction problem for K positive is an infinitely long annulus with an insulated core, zero initial temperature, and a prescribed temperature at the outer surface which grows linearly with time $(-y)$. A solution to this heat flow problem can be obtained using Carslaw and Jaeger (1959) (Section 13.4, p322) to obtain the solution for a fixed temperature at the outer boundary and extending this to a time variable outer boundary temperature using Duhamels Theorem (Carslaw and Jaeger (1959), Section 1.14, p30). For negative $K$ it is the outer surface which is insulated and the inner one which has the prescribed temperature. Manipulation of the solution obtained from Carslaw and Jaeger (1959) for this heat flow problem shows it to be the same as the solution for positive $K$. The solution is

$$\eta = \begin{cases} 0 & 0 < y \\ \beta \eta_l(x, y), & y \leq 0 \end{cases} \tag{A.22}$$

where

$$\begin{aligned} \eta_l(x, y) \qquad &= y + \frac{\pi f}{K^2 sr} \sum_{n=1}^{\infty} \frac{J_0(b\alpha_n) J_1(\alpha_n)}{\alpha_n^2 (J_1^2(\alpha_n) - J_0^2(b\alpha_n))} \\ &\quad \times (J_0(R\alpha_n) Y_1(\alpha_n) - Y_0(R\alpha_n) J_1(\alpha_n)) \\ &\quad \times \left( \exp\left( \frac{K^2 sr \alpha_n^2 y}{f} \right) - 1 \right) \quad . \end{aligned} \tag{A.23}$$

$b = 1 + Ks\ell$ and $J_0, J_1, Y_0$ and $Y_1$ are Bessel functions of the first and second kind. In order to satisfy the outer and inner boundary conditions the transcendental equation for $\alpha_n$

$$J_0(b\alpha_n) Y_1(\alpha_n) - Y_0(b\alpha_n) J_1(\alpha_n) = 0 \tag{A.24}$$

must be solved. For $Ks\ell < -1$ the radius of the cylinder becomes negative for some range of $x$. This is physically impossible and hence there is no solution for this range of shear. It should be noted that restricting the solution to $Ks\ell > -1$ is the same as requiring that there is no level of no motion in the geostrophic flow.

Scaling the surface displacement by its maximum value i.e. assuming that $\eta_0 = \mathcal{A}L_y$, the non-dimensional form of the solution is

$$\eta' = \begin{cases} 0 & 0 < y' \\ \eta'_l(x', y') & y' \leq 0 \end{cases} \tag{A.25}$$

where

$$\eta'_l(x', y') = y' + \frac{\pi}{(Kh_0a)^2} \sum_{n=1}^{\infty} \frac{J_0(b\alpha_n)J_1(\alpha_n)}{\alpha_n^2(J_1^2(\alpha_n) - J_0^2(b\alpha_n))} \times (J_0(R\alpha_n)Y_1(\alpha_n) - (Y_0(R\alpha_n)J_1(\alpha_n)) \times (\exp((Kh_0a)^2\alpha_n^2 y) - 1) \tag{A.26}$$

$R = 1 + (Kh_0)ax'$, $b = 1 + (Kh_0)$, and $h_0 = s\ell$ is the water depth at the shelf edge.

## A.5 Results and Discussion of Near Field Solution

The solution depends on only two dimensionless numbers. The first, $Kh_0$, gives the importance of density effects within the flow. It is large for high shear and because density forces increase with water depth it is also large for a deep shelf.

In the heat conduction analogy $(Kh_0a)^2$ is the thermal diffusivity. High diffusivity implies rapid conduction of heat and hence rapid heating of the cylinder. This translates into a shorter alongshore distance for the boundary layer to grow to a given width or more effective flow penetration of the shelf. From this analogy it can be seen that the flow penetration is enhanced by the following : high shear, a deep shelf, strong bottom friction, low latitude, a wide flow or a narrow shelf.

For this near field solution the free surface displacement over $100km$ is $0.2cm$ and the maximum density anomaly was chosen for three cases to be $+0.018$, $+0.01$, $-0.005$ parts per thousand over $100km$.

A small extension of this model is to use it to illustrate the effect on the shelf of the outer edge of a Gulf Stream Ring. This gives an analytical solution to the case considered in section 2.3b. The forcing of the shelf by the ring is idealized as a linear peak in surface displacement and density along the models offshore edge. In non-dimensional form these conditions can be stated

$$\eta = \begin{cases} 0 & 0 < y' \\ a'y' & -1 < y \leq 0 \\ -a'(y'+2) & -2 < y' \leq -1 \\ 0 & y' \leq -2 \end{cases} \quad \text{at } x' = 1 \quad . \tag{A.27}$$

$a' < 0$ represents a cyclonic ring and $a' > 0$, a anti-cyclonic ring.

$$\epsilon = \begin{cases} 0 & 0 < y \\ aKy' & -1 < y' \leq 0 \\ -aK(y'+2) & -2 < y' \leq -L_y \\ 0 & y' \leq -2 \end{cases} \quad \text{at x} = \ell \quad . \tag{A.28}$$

For both Warm and Cold Core Gulf Stream Rings the density structure is such that the flow is surface intensified (in our model $K < 0$).

The solution is

$$\eta = \begin{cases} 0 & 0 < y \\ a'\eta_l(x',y') & -1 < y' \leq 0 \\ a'(\eta_l(x',y') - 2\eta_l(x',y'+1) & \\ & -2 < y' \leq -1 \\ a'(\eta_l(x',y') - 2\eta_l(x',y'+1) + \eta_l(x',y'+2) & y' \leq -2 \end{cases} \tag{A.29}$$

where $\eta_l$ is given by (A-3). The solutions for $Kh_0 = -0.9$, $-0.5$ and $+.25$ for $a = 0.167$ are shown in Figure A-3. These contours are also density contours of the interior layer when scaled by $K$. The relative error in neglecting ageostrophic transport calculated for (A.16) is 5% or less in each case. The near field density equation is valid over a larger alongshore distance than the previous inflow example because an outflow is adjacent to the inflow, which reduces the flow's cross-shelf scale making (A.6) a good

approximation. For typical scales the plotted domain corresponds to $150km$ of a $100km$ wide shelf. The contours in Figure A-3 give the flow direction at the free surface and because the geostrophic flow is in the same direction at all depths they are flow lines for the geostrophic flow. In using the approximated density Jacobian (A.8) it is assumed that $\eta$ contours are approximate transport streamlines in the nearfield. Therefore these Figures may be viewed in four ways; as barotropic pressure contours, as density contours, as geostrophic flow direction or transport streamlines.

The ring does not penetrate the shelf very well. The steering of the flow by the topography is evident by the skewed flow pattern. The length of shelf influenced by the ring is quite short, about three times $L_y$. The density structure on shelf penetration is such that both Warm and Cold Core Rings are able to influence the shelf less than a barotropic ring because the flow is surface intensified ($K < 0$).

Figure A-3 shows how increased shear, $Kh_0$, causes the flow to penetrate less along the shore and more across the topography. A simplistic reason for this is that shear increases the bottom velocities and therefore increases the frictional drag on the flow enhancing the ability of the geostrophic flow to cross isobaths. That this is incorrect is shown by considering a barotropic flow ( $Kh_0 = 0$ ). In this case doubling the bottom velocities does not alter the flow's pattern because the amount of fluid to be absorbed into the Ekman layer, as measured by the flow's transport, is also doubled. The more subtle reason for enhanced shelf penetration by sheared flows lies in the rate of absorption into the Ekman layer relative to the volume being transported by the flow.

Equation A.20 can be thought of as the equation governing heat diffusion in a thin tapered bar of thickness $1+Ksx$. The boundary conditions are that the bar is insulated at $x = 0$ and that the temperature is prescribed at $x = \ell$ and varies with time. The rate at which the bar heats is governed by the cross-sectional area at the heated end and the volume of the bar. For the same prescribed temperature, the heat flux into the bar is proportional to the area of the end, $1 + Kh_0$. The volume to be heated is proportional to $\ell(1 + \frac{Kh_0}{2})$. Hence, since the flux increases faster than the volume with

increasing taper, i.e. larger $K$, a more highly tapered bar will heat more quickly. The heating rate of the bar is therefore governed by the ratio

$$\frac{1+Kh_0}{\ell(1+\frac{Kh_0}{2})} \quad . \tag{A.30}$$

In oceanographic terms the greater the shear, (taper), the shorter the alongshore distance traveled (time) required by the barotropic pressure, $\eta$, (heat) to penetrate the shelf.

This ratio (A.30) is in fact proportional to the inflow's near bottom cross-shelf velocity at the shelf edge divided by the inflow's transport. Ekman pumping, which determines the rate of absorption into the Ekman layer, is

$$w^E = h_x u_b = -h_x \frac{g}{f}(1+Kh)\frac{\partial \eta}{\partial y} \quad . \tag{A.31}$$

The total transport onto the shelf as measured by the flow's depth averaged cross-shelf geostrophic velocity at the shelf edge is

$$\overline{u^g} = \frac{U^g}{h} = -\frac{g}{f}(1+Kh)\frac{\partial \eta}{\partial y} \qquad at \qquad x=\ell \tag{A.32}$$

which is the cross-shelf velocity of a barotropic flow with the same transport as the sheared flow. Using the above definitions evaluated at the shelf edge the ratio becomes

$$\begin{aligned} \text{Cross-shelf flow penetration} \quad &\propto \frac{\text{Cross-shelf bottom velocity}}{\text{Depth averaged cross-shelf vel.}} \\ &\propto \frac{\text{Ekman pumping ( absorption rate)}}{\text{Geostrophic inflow transport}} \\ &= \frac{1+Kh_0}{(1+\frac{Kh_0}{2})} \quad . \end{aligned} \tag{A.33}$$

Therefore, as alluded to earlier, cross-shelf penetration of the inflow is determined by the ratio of absorption rate ( Ekman pumping ) to volume to be absorbed ( geostrophic transport on to the shelf). The ratio, plotted in Figure A-2, gives a measure of how well the inflow is able to penetrate the shelf compared to the penetration of a a barotropic inflow. High ratios indicate more effective penetration of the shelf. From Figure A-2

it is clear that a bottom intensified flow ($K > 0$) crosses the topography more easily than a surface intensified flow ($K < 0$).

In chapter 2 it was determined that the vertical well mixed model is not valid when the bottom velocity is too small because effects such as inertia become too large to be neglected. This near field solution can be used to examine cases where the inflow has a level of no motion. The range $Kh_0 < -1$ was eliminated from the near field solution because it corresponded to a cylinder with negative radius, the thin tapered bar analogy will be used to explore this range. Using the tapered bar analogy, when $Kh_{crit} = -1$ the bar has zero thickness at at the cross-shelf point $x_{crit}$. Oceanographically, from (A.12), (A.14) and (A.15) this is the line where the depth of no motion in the geostrophic flow equals the water depth. Expanding the cross-shore derivative in the flow equation (A.19) and setting $h = h_{crit}$ yields

$$\frac{\partial \eta}{\partial x} = 0 \tag{A.34}$$

at this line. Hence no heat may cross the line $x_{crit}$ (and geostrophic flow must cross normal to it) and there will be no heat (and no flow) for $x$ less than $x_{crit}$ because the bar has no thickness there. Thus flow must make a sharp right angle turn at $x_{crit}$. Inertial effects will become large enough to violate the scaling (2.6) and therefore the range $Kh_0 < -1$ cannot be covered by this model.

The near field solution yields a useful analogy with heat diffusion in a thin tapered bar. This analogy leads to the conclusion that it is not absolute magnitude of the bottom velocity which determines the rate at which topography is crossed but rather the ratio of near bottom cross-shelf velocity to the geostrophic transport. This ratio is the same as the ratio of Ekman pumping to flow transport, showing that it is the rate of absorption into the Ekman layer relative to the volume of fluid to be absorbed that determines the ability of a geostrophic flow to cross topography.

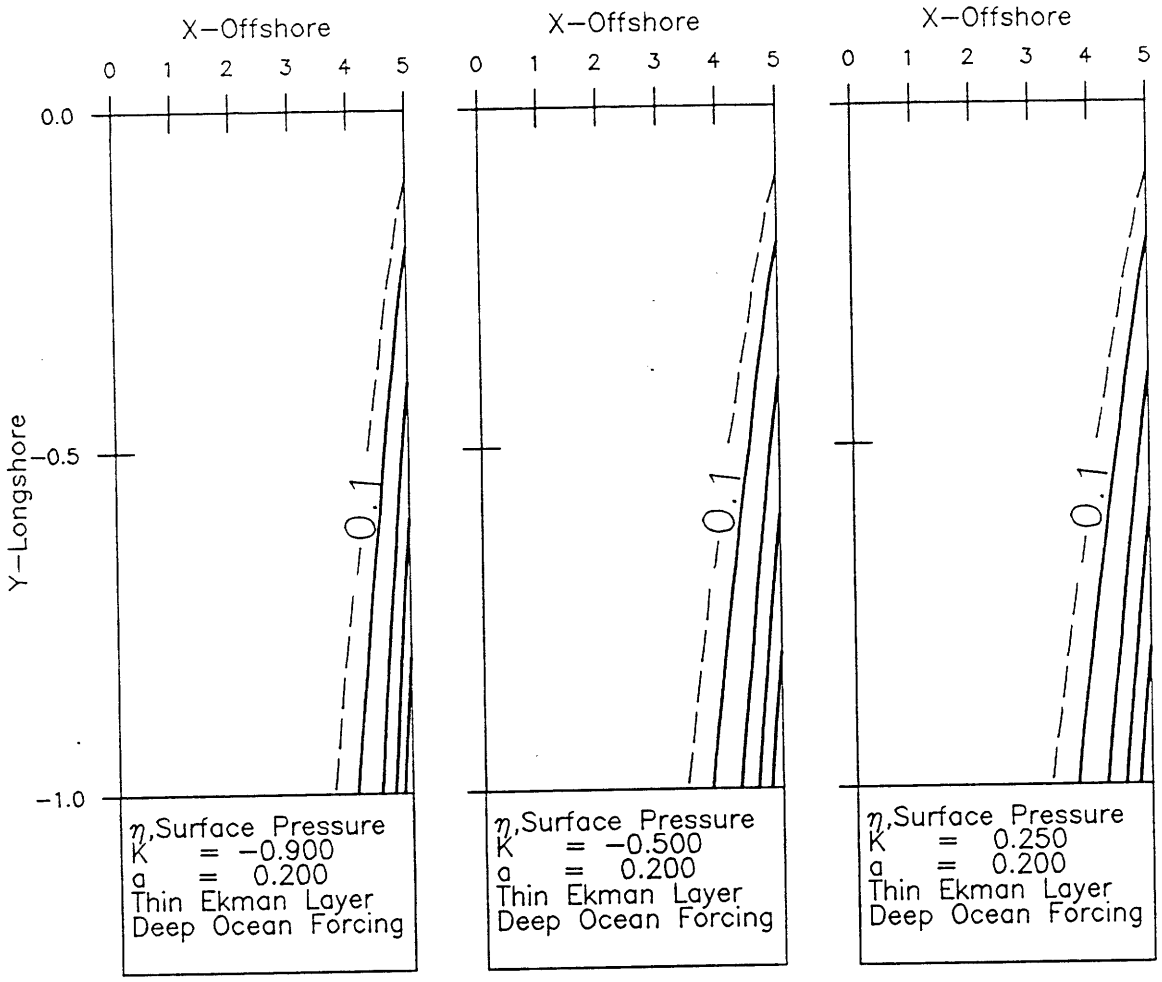


Figure A-1: Free surface displacement contours for varying degrees of vertical shear in the flow which enters the shelf between y' = -1 and y'= 0. The contours also give the density, the flow direction in the geostrophic layer and approximate transport streamlines. The alongshore extent of these Figures is 100km for typical scales and the solid contour spacing is 0.2. a) $Kh_0 = -0.9$, a surface intensified flow penetrates the shelf poorly. b) $Kh_0 = -0.5$. c) $Kh_0 = 0.25$. The barotropic flow pattern lies between the shapes give in b) and c). The relative size of the ageostrophic transport, which was ignored in calculating these near field solutions is 5%, 11%, 20% respectively.

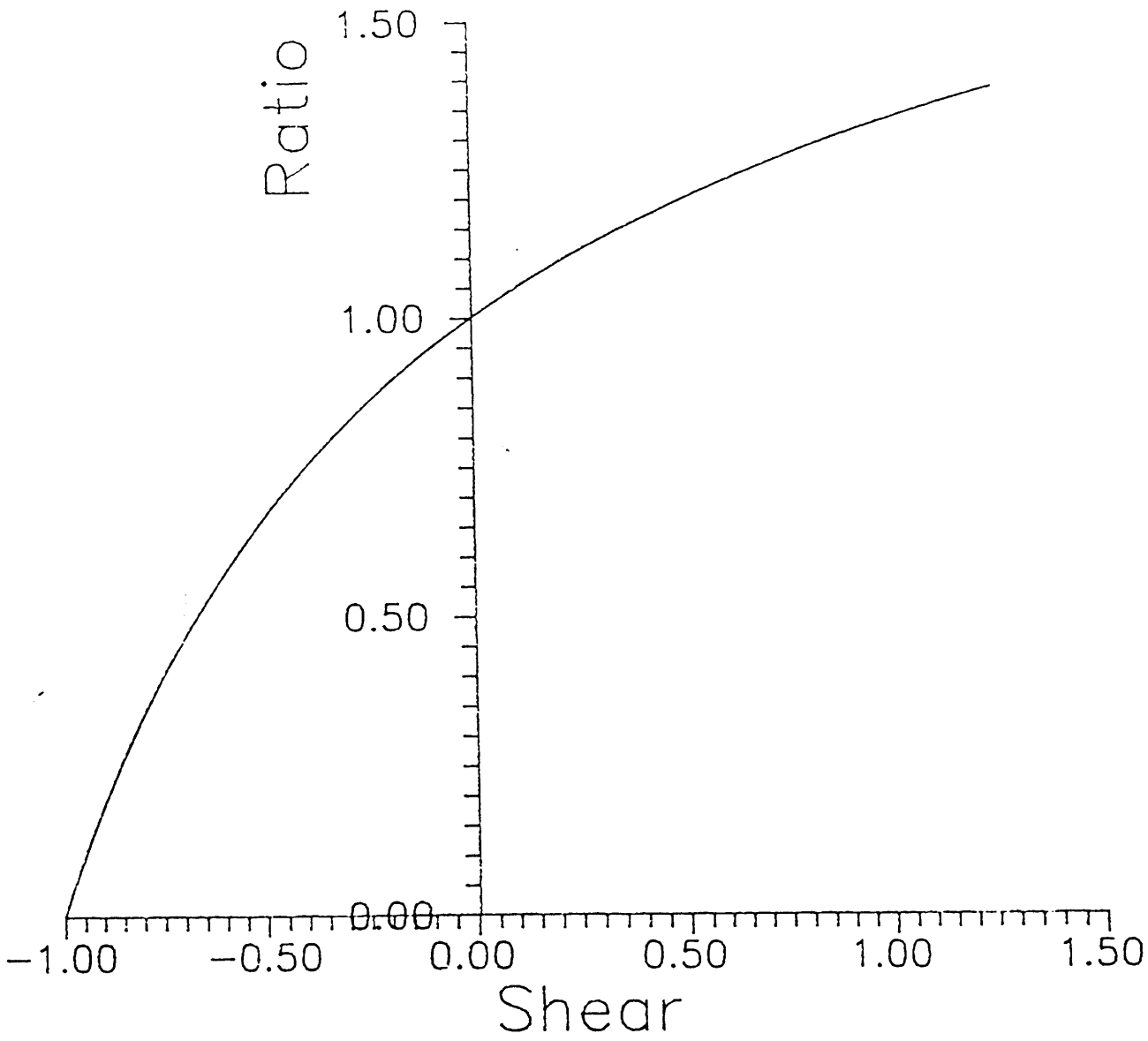


Figure A-2: Ratio which determines the degree of shelf penetration of the flow flow, plotted against the degree of shear in the flow's horizontal velocity ( $Kh_0$ ). The penetration of a barotropic flow is assumed to be unity. High ratios indicate more effective penetration of the shelf. If $Kh_0 > 0$, the flow is more effective than a barotropic flow and if $Kh_0 < 0$, it is less effective. The geostrophic velocity profile for different ranges of shear is shown schematically. The degree of flow penetration is zero when $Kh_0 = -1$, corresponding to flow with zero near bottom velocities.

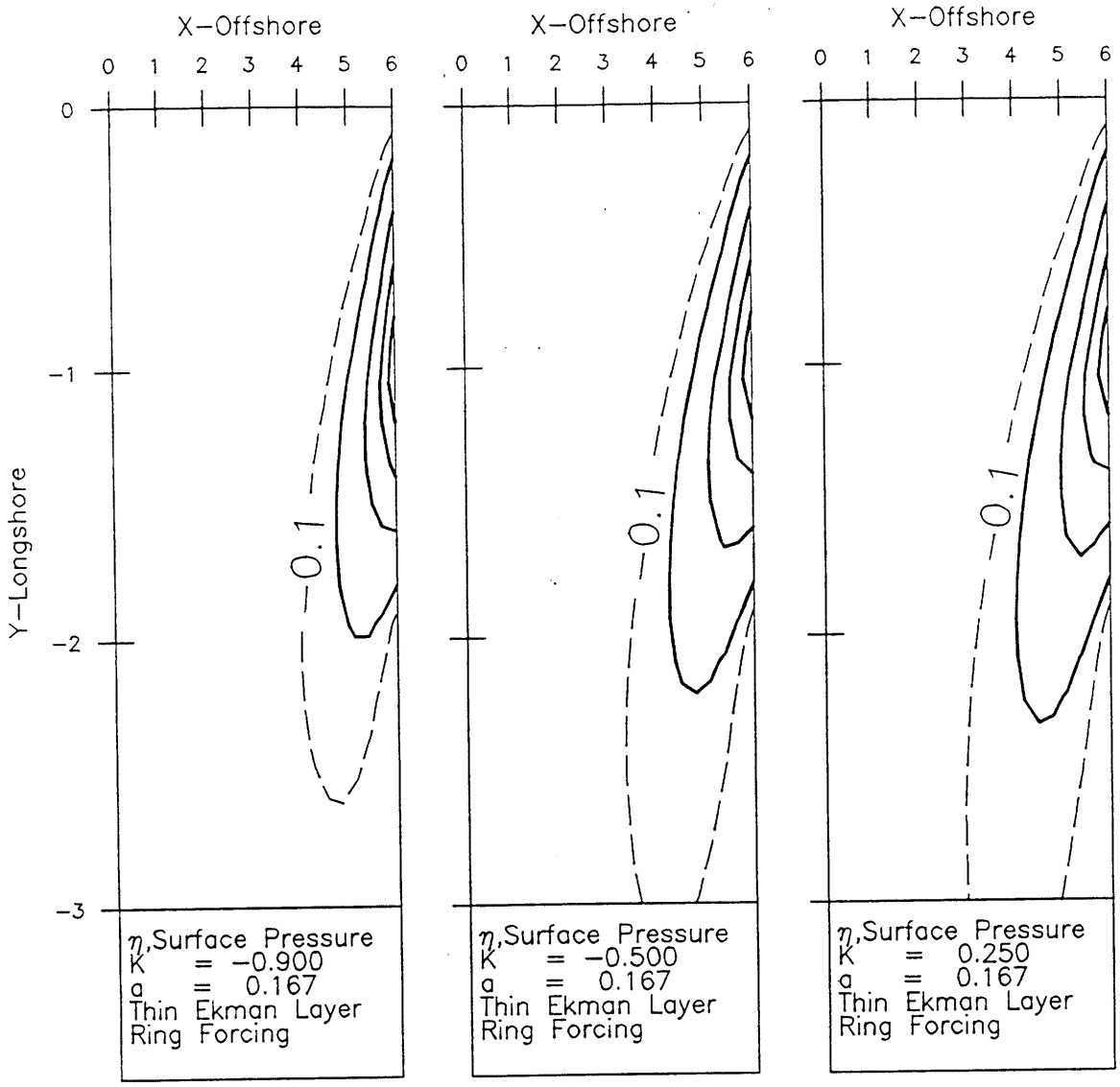


Figure A-3: Free surface displacement contours for varying degrees of vertical shear in the flow which enters the shelf between $y' = -1$ and $y' = 0$ and which leaves the shelf between $y' = -2$ and $y' = -1$. This example is intended to show the effect on the shelf of the outer edge of a $100km$ diameter Gulf Stream Ring. The contours also give the density, the flow direction in the geostrophic layer and approximate transport streamlines. The alongshore extent of these Figures is 150km for typical scales. The solid contour spacing is 0.2. a) $Kh_0 = -0.9$, a surface intensified flow penetrates the shelf poorly. b) $Kh_0 = -0.5$. c) $Kh_0 = 0.25$. The barotropic flow pattern lies between the shapes given in b) and c). The skewed flow pattern is due to the tendency for flow to follow isobaths.

## Appendix B

### Ekman Layers at an Interface

When two layers are in relative motion some frictional stress will result from the shear in horizontal velocity. One way to include the effects of internal friction is to allow each homogeneous density layer to contain an Ekman layer adjacent to the interface. Solutions will be developed for flow within the interfacial Ekman layers assuming that the Ekman layers are thin compared to the thickness of the density layer. The aim of this appendix is to determine the vertical velocity induced by Ekman layers adjacent to an interface in the geostrophic interior of the density layers, and to evaluate the frictional transports within the interfacial Ekman layers.

The equations governing flow in an Ekman layer on a sloping interface are essentially the same as those derived by Pedlosky (1979) for an Ekman layer on a rigid sloping bottom. Pedlosky's derivation assumes that while bottom slope may be as large as the vertical aspect ratio, changes in slope occur on scales which are large compared to the horizontal scale of the motion. Changes in the "topography" of an interface must occur over the motion's horizontal scale. However Pedlosky's derivation may be used and is simplified for a sloping interface because interface slopes must be small compared to the vertical aspect ratio.

Following Pedlosky (1979) the "natural" coordinate system for a sloping boundary is one rotated to be normal to the boundary. Assuming that $y$ is locally parallel to contours of interface displacement, then the horizontal and vertical $(x, y, z)$ coordinate system can be rotated into the $(x', y, z')$ coordinate system, where $z'$ is normal to the interface, by a non-dimensional rotation $\theta$ in the $x$,$z$ plane. This angle is related to the

dimensional slope $\frac{\partial \zeta^*}{\partial x^*}$ by

$$\frac{\partial \zeta^*}{\partial x^*} = \frac{d}{L}\theta \quad .$$

$d$ is a representative layer thickness and $L$, the horizontal scale of the motion. Variables in the rotated and unrotated frames are related for small angles to order $\theta_0^2$, where $\theta_0$ is the magnitude of $\theta$, by

$$\begin{aligned} x &= x' \\ z &= \theta x' + z' \\ u &= u' \\ w &= \theta u' + w' \quad . \end{aligned} \tag{B.1}$$

Note that both horizontal distances and velocities are the approximately the same in both frames. Horizontal derivatives are related to $O(\theta_0^2)$ by

$$\frac{\partial}{\partial x'} = \frac{\partial}{\partial x} + \theta \frac{\partial}{\partial z} \quad . \tag{B.2}$$

From Pedlosky (1979), equations (4.9.8a), (4.9.11), (4.9.12) and (4.9.14), the steady non-dimensional equations governing motion in frictional boundary layers in the rotated frame when the rotation is small are

$$-v = -\frac{\partial p}{\partial x'} + \frac{1}{2}\frac{\partial^2 u}{\partial \sigma^2} \tag{B.3}$$

$$u = -\frac{\partial p}{\partial y} + \frac{1}{2}\frac{\partial^2 v}{\partial \sigma^2} \tag{B.4}$$

$$\frac{\partial u}{\partial x'} + \frac{\partial v}{\partial y} + \frac{1}{\sqrt{2E_V^I}}\frac{\partial w'}{\partial \sigma} = 0 \tag{B.5}$$

$$\frac{\partial p}{\partial \sigma} = 0 \tag{B.6}$$

where $\sigma$ is the stretched boundary layer coordinate

$$\sigma = \frac{z'}{\sqrt{2E_V^I}} \quad . \tag{B.7}$$

$E_V^I$ is the vertical Ekman number in the unrotated frame equal to $\frac{A_V^I}{fd^2}$. $A_V^I$ is the vertical turbulent eddy viscosity appropriate to the interface.

Dynamically significant pressure does not vary with depth in the geostrophic core of the layer (see Section 3.2) and , by (B.6), also does not change across the thickness of any boundary layers. Therefore the horizontal gradient of pressure from (B.2) is approximately the same in both forms, i.e. $\frac{\partial p}{\partial x'} = \frac{\partial p}{\partial x}$. Consequently (B.3) is also approximately the same in both frames and the boundary conditions that velocity is geostrophic outside the boundary layers may be stated

$$u = \begin{cases} u_1 = -\frac{\partial p_1}{\partial y} & \sigma \to \infty \\ u_2 = -\frac{\partial p_2}{\partial y} & \sigma \to -\infty \end{cases} \tag{B.8}$$

$$v = \begin{cases} v_1 = \frac{\partial p_1}{\partial x} & \sigma \to \infty \\ v_2 = \frac{\partial p_2}{\partial x} & \sigma \to -\infty \end{cases} \tag{B.9}$$

where $u_1$ and $v_1$ are the components of geostrophic velocity just above the upper interfacial Ekman layer and $u_2$ and $v_2$ are the components of geostrophic velocity just below the lower interfacial Ekman layer.

Pressure and therefore the geostrophic velocities defined by (B.8) and (B.9) are depth-independent within a density layer. Thus if the geostrophic velocity in adjacent layers is different, then the horizontal pressure gradient must be discontinuous across the interface.

Matching conditions at the interface, $\sigma = 0$, are that $u$ and $v$ are continuous across the interface and that the shear stresses $\frac{\partial u}{\partial \sigma}$ and $\frac{\partial v}{\partial \sigma}$ are also continuous. Combining (B.3) and (B.4) into a single equation and using (B.8) yields for the upper interfacial

Ekman layer

$$\frac{1}{4}\frac{\partial^4 u}{\partial \sigma^4} + (u - u_1) = 0 \qquad \sigma > 0 \tag{B.10}$$

and for the lower interfacial Ekman layer

$$\frac{1}{4}\frac{\partial^4 u}{\partial \sigma^4} + (u - u_2) = 0 \qquad \sigma < 0 \quad . \tag{B.11}$$

Solutions satisfying the boundary and matching conditions for flow in the upper interfacial Ekman layer are

$$\left.\begin{aligned} u - u_1 &= -\tfrac{1}{2}(v_1 - v_2)e^{-\sigma}sin\sigma - \tfrac{1}{2}(u_1 - u_2)e^{-\sigma}cos\sigma \\ v - v_1 &= -\tfrac{1}{2}(v_1 - v_2)e^{-\sigma}cos\sigma - \tfrac{1}{2}(u_1 - u_2)e^{-\sigma}sin\sigma \end{aligned}\right\} \quad \sigma > 0 \tag{B.12}$$

and in the lower interfacial Ekman layer are

$$\left.\begin{aligned} u - u_2 &= -\tfrac{1}{2}(v_1 - v_2)e^{\sigma}sin\sigma + \tfrac{1}{2}(u_1 - u_2)e^{\sigma}cos\sigma \\ v - v_2 &= \tfrac{1}{2}(v_1 - v_2)e^{\sigma}cos\sigma + \tfrac{1}{2}(u_1 - u_2)e^{\sigma}sin\sigma \end{aligned}\right\} \quad \sigma < 0 \quad . \tag{B.13}$$

The horizontal velocity components at the interface are

$$\begin{aligned} u_{int} &= \frac{1}{2}(u_1 + u_2) \\ v_{int} &= \frac{1}{2}(v_1 + v_2) \quad . \end{aligned} \tag{B.14}$$

Note that the interfacial velocities are the average of the geostrophic velocities in the layers either side of the interface. The components of interfacial stress are

$$\tau^x_{int} = -\frac{1}{2}(u_1 - u_2) + \frac{1}{2}(v_1 - v_2) \tag{B.15}$$

$$\tau^y_{int} = -\frac{1}{2}(u_1 - u_2) - \frac{1}{2}(v_1 - v_2) \quad . \tag{B.16}$$

Integrating the right hand sides of (B.12) between the interface and the interior ($\sigma =$ 0 to $\infty$) yields the interfacial Ekman transports due to frictional effects

$$U_1^I = -\frac{\sqrt{2E_V^I}}{4}((u_1 - u_2) + (v_1 - v_2)) \tag{B.17}$$

$$V_1^I = \frac{\sqrt{2E_V^I}}{4}((u_1 - u_2) - (v_1 - v_2)) \quad . \tag{B.18}$$

Similarly, integrating the right hand sides of (B.13) between $-\infty$ and zero gives the frictional transports in the lower interfacial Ekman layer

$$U_2^I = \frac{\sqrt{2E_V^I}}{4}((u_1 - u_2) + (v_1 - v_2)) \tag{B.19}$$

$$V_2^I = \frac{\sqrt{2E_V^I}}{4}(-(u_1 - u_2) + (v_1 - v_2)) \quad . \tag{B.20}$$

Note that these transports are equal and opposite to those in the upper interfacial Ekman layer, and that even if geostrophic flow in a given density layer is zero, there can be an Ekman transport induced in that layer by motion in the other density layer of the pair.

To determine the vertical velocity just outside the boundary layer the continuity equation (B.5) must be integrated. For the upper density layer in the stretched $\sigma$ coordinate system this can be stated as

$$w|_{z=-(d_1+\delta_E)} - w_I' = -\sqrt{2E_V^I}\int_0^\infty (\frac{\partial u}{\partial x'} + \frac{\partial v}{\partial y})d\sigma \tag{B.21}$$

where $w_I'$ is the vertical velocity at the interface. If there is locally no net flow across the interface, then the vertical velocity in the interior of the upper density layer from (B.21) and (B.12) is

$$w|_{z=-(d_1+\delta_E)} = \frac{\sqrt{2E_V^I}}{4}\left(\frac{\partial}{\partial x'}(v_1 - v_2) - \frac{\partial}{\partial y}(u_1 - u_2)\right) \quad . \tag{B.22}$$

As demonstrated geostrophic velocities are independent of depth within a density layer. Consequently from (B.2) horizontal gradients of geostrophic velocity will be the same in both rotated and unrotated frames e.g. $\frac{\partial v_1}{\partial x'} = \frac{\partial v_1}{\partial x}$. Using this and the relationship between $w'$ and $w$ the vertical velocity in the unrotated frame in the upper density layer just outside the upper interfacial Ekman layer is

$$w|_{z=-(d_1+\delta_E)} = \theta u_1 + \frac{\sqrt{2E_V^I}}{4}\left(\frac{\partial}{\partial x}(v_1 - v_2) - \frac{\partial}{\partial y}(u_1 - u_2)\right) \quad . \tag{B.23}$$

For a $y$ axis which is not aligned to the contours of interface displacement this can be generalized to

$$w|_{z=-(d_1+\delta_E)} = \vec{u_1} \bullet \nabla\zeta + \frac{\sqrt{2E_V^I}}{4}(\frac{\partial}{\partial x}(v_1 - v_2) - \frac{\partial}{\partial y}(u_1 - u_2)) \tag{B.24}$$

where $\vec{u_1}$ is the geostrophic velocity vector in the upper density layer and $\nabla\zeta$ is a vector whose components are non-dimensional interface slopes. Similarly the vertical velocity just outside the lower interfacial Ekman layer in the lower density layer is

$$w|_{z=-(d_1+\delta_E)} = \vec{u_2} \bullet \nabla\zeta + \frac{\sqrt{2E_V^I}}{4}(\frac{\partial}{\partial x}(v_1 - v_2) - \frac{\partial}{\partial y}(u_1 - u_2)) \quad . \tag{B.25}$$

## Appendix C

## Coastal Flows Driven by Alongshore Density Gradients.

The following ,Vennell and Malanotte-Rizzoli (1987), is reproduced from the Journal of Physical Oceanography. The model and calculations are the work of R. Vennell. The text and discussion is the work of R. Vennell and P. Malanotte-Rizzoli.

Reprinted from JOURNAL OF PHYSICAL OCEANOGRAPHY, Vol. 17, No. 6, June 1987
American Meteorological Society

# Coastal Flows Driven by Alongshore Density Gradients

ROSS VENNELL

*Joint Program, MIT/WHOI*

PAOLA MALANOTTE-RIZZOLI

*Massachusetts Institute of Technology, Department of Earth, Atmospheric, and Planetary Sciences, Center for Meteorology and Physical Oceanography, Cambridge, MA 02139*

7 March 1986 and 2 September 1986

ABSTRACT

In this note we study the effect of an alongshore density gradient in driving the near-coastal circulation and determining the direction of the alongshore flow. We revisit and extend the results obtained by Malanotte-Rizzoli and Bergamasco (MRB) using the same simple analytical model but changing the longshore density distribution and examining the full solution, not only its far-field behavior as done by MRB. We find as a new result that the near-coastal flow is profoundly modified when passing from monotonic, northward increasing density profiles, the case studied by MRB, to double-ramp profiles with a density maximum. In particular, the reversal of the density gradient north of its maximum is a necessary condition for the creation of a strong southward flowing coastal cell. This cell does not exist when the density increases monotonically northward. The examples shown, even though idealized, compare well both in flow direction and in order of magnitude with what is observed in winter in the northern Adriatic sea.

## 1. Introduction

In this note we exploit a simple analytical model of Csanady's (1978) "Arrested Topographic Wave" type which was used by Malanotte-Rizzoli and Bergamasco (1983, hereafter referred to as MRB) to explain the dynamical effects of an alongshore (north–south) density gradient in driving the coastal circulation on the shelf.

Csanady's approach (1978) was also exploited by Shaw and Csanady (1983). The starting dynamic equations of Shaw and Csanady (1983) and MRB are the same, which is not surprising in view of the fact that their basic physical assumptions are the same. It should be pointed out, however, that both the Shaw and Csanady (1983) and MRB models can be derived from a model originally proposed by Hendershott and Malanotte-Rizzoli (1976) by neglecting some factors like cross-shelf bottom friction and along-shelf topography variations. This fact was clearly pointed out and discussed in detail in the MRB paper. Furthermore, even though the starting MRB and Shaw and Csanady's models are the same, the equations are manipulated and analyzed in a rather different way to focus upon different aspects of shelf dynamics.

The MRB model refers to the northern Adriatic sea in which the north–south density gradient is determined in winter by the formation in the basin interior of a pool of very dense water thanks to deep convective cooling which mixes the water column to the bottom. In summer, instead, the north–south density gradient is established by the spreading of light river water, the Po River being the major source of fresh water input into the Northern Adriatic. MRB suggests that the nearcoastal circulation is driven by the bottom torque, which dominates the dynamical balance as soon as an alongshore density gradient is present. To this gradient the intensity and direction of the alongshore flow may be ascribed.

In this note we revisit the results obtained by MRB, extending them to more relevant, even though idealized, north–south density distributions and discuss the full solution, not only its far field behavior as done by MRB. Finally, we relate the direction of the alongshore flow and its reversals to the shape of the alongshore density profile and to the sign of its gradient (increasing or decreasing northward), a point on which MRB has given only an incomplete analysis.

## 2. The model

Csanady (1978, 1985) uses a diagnostic model where the density field is assumed frozen to study shelf flows. Such a decoupling of the density and velocity fields greatly reduces the difficulty of obtaining a solution. However, such a diagnostic model should not be expected to give more than the magnitude and sense of that particular flow which is consistent with the as-

sumed density distribution. With this in mind we will proceed to diagnostically examine the flow patterns consistent with an idealization of the observed Adriatic density field.

Following Csanady (1985) we write the steady transport equations for a vertically well-mixed coastal strip as

$$-fV = -gh\eta_x - \frac{gh^2}{2}\epsilon_x \tag{1a}$$

$$fU = -gh\eta_y - \frac{gh^2}{2}\epsilon_y - rv_b \tag{1b}$$

$$U_x + V_y = 0. \tag{1c}$$

No wind stress is present and we use the rigid-lid approximation. Subscripts indicate partial derivatives; ($U$, $V$) are the transport components respectively across shore ($U$) and alongshore ($V$); $\eta(x, y)$ is the free surface elevation; $f$ is the (constant) Coriolis parameter; $\epsilon$ is the density anomaly defined as $\epsilon = (\rho - \rho_0)/\rho_0$ if $\rho_0$ is a reference density; $(u_b, v_b)$ are the bottom geostrophic velocity components; $r$ is the bottom friction coefficient; $h(x, y)$ is the depth.

The flow is envisioned as a geostrophic interior overlying a frictional bottom layer. In the geostrophic interior the flow obeys the thermal wind balance. The bottom stress is taken to be proportional to the bottom geostrophic velocity

$$u_b = -\frac{g}{f}(\eta_y + h\epsilon_y) \tag{2a}$$

$$v_b = \frac{g}{f}(\eta_x + h\epsilon_x). \tag{2b}$$

We also make the long wave assumption, for which the cross-shore scale $L_x$ is assumed to be small compared to the longshore one $L_y$: $L_x/L_y \ll 1$. Thus we are able to neglect the cross-shore bottom stress. As a final assumption, we take the depth to vary only in cross-shore direction: $h = h(x)$. We consider a north–south coastline, with $x$ pointing eastward, $y$ northward and the land corresponding to $x < 0$ (a western boundary).

We can combine the model equations (1a, b, c) and the definitions (2a, b) for $(u_b, v_b)$ as done by Shaw and Csanady (1983) to obtain a single equation for $v_b$:

$$r\left(\frac{v_{bx}}{h_x}\right)_x + fv_{by} = -gh_x\epsilon_y. \tag{3a}$$

If the depth vanishes at $x = 0$ [i.e., $h(0) = 0$], from (1b) with $U = 0$ at the coast, the appropriate boundary condition is

$$v_b = 0 \quad \text{at} \quad x = 0. \tag{3b}$$

Alternatively, a single equation for $u_b$ can be derived:

$$r u_{bxx} + h_x f u_{by} = -gr(h_x\epsilon_y)_x. \tag{4a}$$

The appropriate boundary condition is obtained as follows. Combining (2a, b) one gets $u_{bx} + v_{by} = (-gh_x/f)\epsilon_y$; noting that if $v_b = 0$ at $x = 0$, then $\partial v_b/\partial y = 0$ too, then

$$u_{bx} = \frac{-gh_x}{f}\epsilon_y \quad \text{at} \quad x = 0. \tag{4b}$$

The mathematical difficulty posed by systems (3)–(4) can be reduced if we consider the simplified case of a linear topography, $h = sx$, with $s$ the slope $>0$ as done in MRB, and a linear density variation: $\rho = \rho_0(1 + \alpha x + \beta y)$. In this case (3a, b) reduces to

$$\frac{\partial v_b}{\partial y} + \frac{r}{fs}\frac{\partial^2 v_b}{\partial x^2} = -gs\frac{\beta}{f}$$

$$v_b = 0 \quad \text{at} \quad x = 0, \tag{5}$$

and (4a, b) to

$$\frac{\partial u_b}{\partial y} + \frac{r}{fs}\frac{\partial^2 u_b}{\partial x^2} = 0$$

$$\frac{\partial u_b}{\partial x} = \frac{-gs\beta}{f} \quad \text{at} \quad x = 0. \tag{6}$$

As pointed out by Csanady (1978), Eqs. (5)–(6) are one-dimensional heat diffusion equations with $-y$ the time-like coordinate and $r/fs$ the "thermal diffusivity". The right-hand side (rhs) of (5) is analogous to a constant internal heating of the medium at a rate $gs\beta/f$.

We shall furthermore restrict ourselves to cases in which there is only a longshore density gradient all over the coastal strip, i.e., $\alpha \equiv 0$. Even though this restriction does not change Eqs. (5) and (6), there will no longer be any vertical shear in the longshore velocity $v_b$. Thus, the longshore bottom velocity $v_b$ is the velocity at all depths.

With $\rho = \rho(y)$ only, given the solution for $v_b$, the transport stream function defined by

$$\psi_x = V; \quad \psi_y = -U$$

can be evaluated by direct integration of the first definition:

$$\psi = \int_0^x h v_b\, dx, \tag{7}$$

with $v_b$ the solution of Eq. (5). The constant of integration, an arbitrary $y$-function, can be taken to be zero if the boundary condition is assumed to be $\psi = 0$ at $x = 0$. For a Northern Hemisphere western boundary, the time-like direction of Eqs. (5)–(6) is southward. In general, it is the longshore direction given by the sign of $-r/fs$, and is also the direction of propagation of the coastal Kelvin wave.

Equations (5)–(6) both require an "initial" condition, that is we must specify the bottom geostrophic velocity at some latitude $y = 0$. All we need to assume is that the flow north of the origin has no influence on the

flow to the south, that is $v_b = 0$ at $y = 0$ is the "initial" condition for Eq. (5). The "initial" condition for Eq. (6) can be obtained from a straightforward manipulation of the model equations (1a, b, c). First we derive the equation (as did Shaw and Csanady, 1983):

$$h_x u_b = \frac{r}{f} v_{bx}.$$

Then we note that if $v_b = 0$ at $y = 0$, then $\partial v_b/\partial x = 0$ at $y = 0$, and hence, using the above, $u_b = 0$ at $y = 0$.

MRB took the origin of the time-like coordinate $y = 0$ to be located at the density extremum (density maximum in winter; minimum in summer). They also assumed, rather arbitrarily,

$$v_b = a + bx \quad \text{at} \quad y = 0.$$

As they only study the far-field limit of their solution, the chosen initial condition does not affect the final result. If, however, one wants to examine the behavior of the solution in the near-field region, the history of the flow north of the density extremum is very important in determining the flow south of it. A meridional density distribution including both the positive and negative longshore density gradient is required. We shall locate the density extremum south of the origin $y = 0$, with $v_b = 0$ [Eq. (5)] or $u_b = 0$ [Eq. (6)], thus idealizing a northern coast.

### 3. Direction of the flow and some simple examples

We first rewrite Eq. (5) as:

$$\frac{\partial v_b}{\partial(-y)} - \left(\frac{r}{fs}\right)\frac{\partial^2 v_b}{\partial x^2} = \frac{gs\beta}{f}, \tag{8}$$

with the standard sign convention for the heat diffusion equation (Carslaw and Jaeger, 1956). In this geometry, $-y$ is the time-like direction. If we move southward (forward in time), the velocity (temperature) will change due to diffusive processes and to the heating on the rhs of (8). If the initial "temperature" is $v_b = 0$ at $y = 0$, and the "heating rate" is positive, $\beta > 0$, (density increasing northward), the "temperature", $v_b$, must increase with "time", $-y$, and $v_b$ will always be greater than its "initial" value of zero. This implies that a ramplike longshore density distribution continuously increasing northward will force a positive longshore flow, that is a northward flow everywhere. This can be seen directly from (8) noticing that far away from the coastline at $x = 0$ diffusive effects are small and the prescribed boundary condition at $x = 0$ will not be felt. Thus the longshore velocity is the "time" integral of the "heating rate":

$$v_b(-y) - v_b(0) = \frac{gs}{f}\int_0^{-y} \beta d(-y)$$

$$= \frac{-gs}{f\rho_0}\int_0^{-y} \frac{\partial \rho}{\partial(-y)} d(-y). \tag{9a}$$

Integration of the above relationship gives

$$v_b = \frac{gs}{f\rho_0}[\rho(0) - \rho(-y)] > 0. \tag{9b}$$

The longshore velocity far away from the coastline at a given latitude is proportional to the difference between the density anomaly at the northern coastline and the density anomaly at that latitude. This feature of linear "heating" or "cooling" can clearly be seen in the examples shown in Figs. 1b, 2b and 3b.

Analogous considerations can be made for the

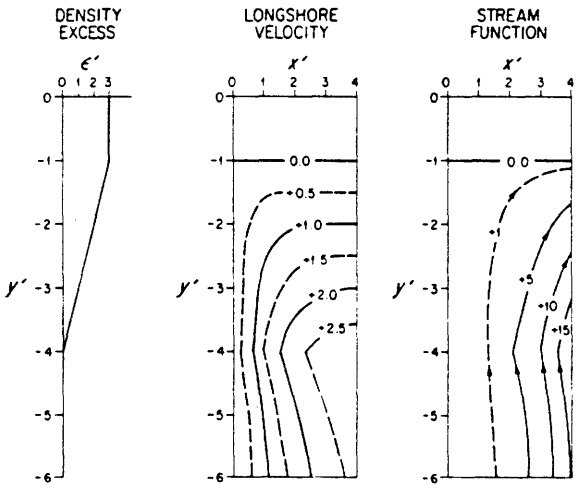


FIG. 1. (a) One-ramp alongshore density distribution, monotonically increasing northward. (b) Pattern of the longshore velocity $v_b$. (c) Pattern of the transport streamfunction $\psi$. Dimensionless units are discussed in Table 1.

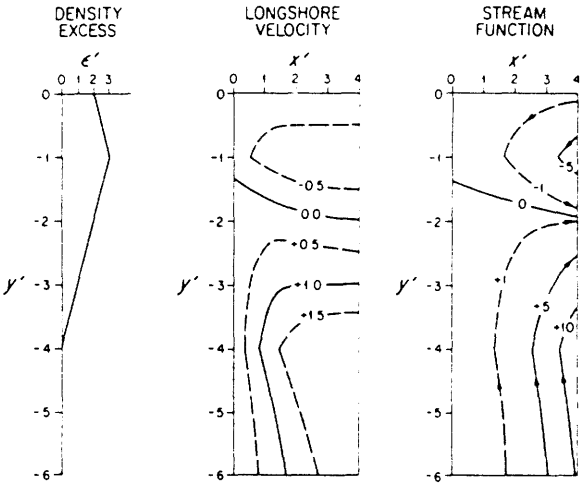


FIG. 2. (a) Two-ramp alongshore densities distribution with $\beta' = -1$ for $-1 \leq y' \leq 0$. (b) Pattern of the longshore velocity $v_b$. (c) Pattern of the transport streamfunction $\psi$. Dimensionless units are discussed in Table 1.

across-shore velocity $u_b$ governed by Eq. (6), which shows the flow to be offshore for a northward positive density gradient ($u_b > 0$ if $\beta > 0$). Thus, with $\beta > 0$, the flow will be northward and offshore. It must, however, be emphasized that these arguments for flow direction based on the longshore density gradient apply only to regions with a monotonic density variation. Any "history" of density forcing at higher latitudes, i.e., any deviation from the monotonic behavior, may alter the flow direction in the region at study.

We now explicitly solve Eq. (5) for $v_b$, under the previous assumption $h = sx$ with $s > 0$ and with a ramp-like, northward increasing longshore density profile:

$$\epsilon = \begin{cases} \epsilon_{max}, & y \geq 0 \\ \epsilon_{max}(1 + \beta y), & y < 0. \end{cases} \tag{10}$$

In the distribution (10) the origin $y = 0$ is located at the position of the density anomaly maximum that is, in a situation like that occurring in the Adriatic sea, at the center of the winter interior dense water mass. The initial condition is assumed to be $v_b = 0$ at $y = 0$.

The solution of (8) is then (Carslaw and Jaeger, 1956):

$$v_b = 0 \quad \text{for} \quad y \geq 0$$

$$v_b = \frac{gs^2\beta}{r}\left\{\frac{r}{fs}(-y)\,\mathrm{erf}\left(\frac{x}{2\left[\frac{r}{fs}(-y)\right]^{1/2}}\right) - \frac{x^2}{2}\left(1 - \mathrm{erf}\frac{x}{2\left[\frac{r}{fs}(-y)\right]^{1/2}}\right) + x\left[\frac{r}{fs}\frac{(-y)}{\pi}\right]^{1/2}\frac{-x^2}{e^{4(fs)(-y)}}\right\} \quad \text{for} \quad y < 0, \tag{11}$$

which is the same solution obtained by MRB. Note, however, that $v_b$ is positive for $\beta > 0$; hence, as previously discussed, a positive longshore density gradient forces a northward flow in the region $y < 0$ and not southward as observed in the Adriatic sea. The crucial point in deriving the solution (11) is the assumed density anomaly profile (10) for which the "initial" condition of zero meridional flow is assigned at the point of maximum density anomaly, $v_b = 0$ for $\epsilon = \epsilon_{max}$. This in effect places an artificial northern wall at the density maximum. We shall see in the following that the flow pattern will change drastically with a double-ramp density distribution, in which the northern wall $v_b = 0$ is located in a region of constant density, near the real northern boundary, and not in the middle of a dense (or light) water mass. Figures 1a, b, c show the above solution. Specifically, Fig. 1a shows the one-ramp density profile; Fig. 1b shows the distribution of the positive longshore velocity $v_b$ given by (11); Fig. 1c the transport streamfunction $\psi$ evaluated through (7). The flow is northward and directed into the basin interior, away from the coastline.

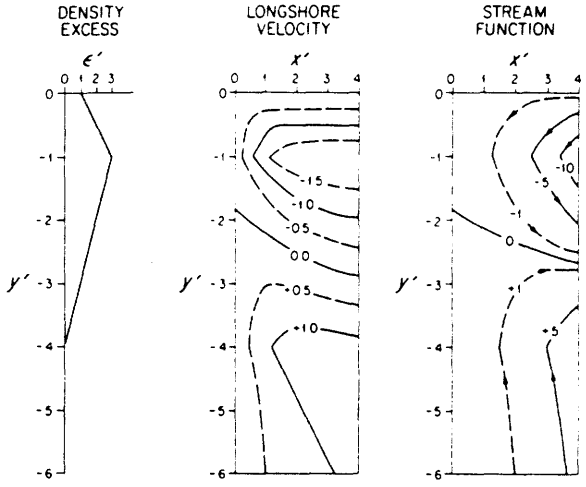


FIG. 3. As in Fig. 2, but with $\beta' = -2$ for $-1 \leq y' \leq 0$. Dimensionless units are discussed in Table 1.

The units in Figs. 1a, b, c are dimensionless. A convenient nondimensional form, used throughout in the following, can be obtained taking

$$x = L_x x' \quad y = L_y y' \quad \beta = \beta_0 \beta' \quad \psi = \psi_0 \psi'$$
$$u_b = u_0 u' \quad v_b = v_0 v' \quad \epsilon = \epsilon_0 \epsilon'$$

in which primed quantities are dimensionless. The various scales may be related by

$$L_x^2 = \frac{r}{fs} L_y \tag{12a}$$

$$u_0 = g\beta_0\left[\frac{rsL_y}{f^3}\right]^{1/2} \tag{12b}$$

$$v_0 = \frac{gs\beta_0}{f} L_y \tag{12c}$$

$$\psi_0 = \frac{gs\beta_0 r L_y^2}{f^2} \tag{12d}$$

$$\epsilon_0 = \frac{1}{3}\epsilon_{max} \tag{12e}$$

$$\beta_0 = \epsilon_{max}/3L_y. \tag{12f}$$

The solutions for the heat Eqs. (5), (6) can then be written quite generally:

$$v_b = \begin{cases} 0 & \text{for} \quad y' \geq 0 \\ \beta' F(x', y') & \text{for} \quad y' < 0. \end{cases} \tag{13}$$

In particular, for the solution (11):

$$F(x', y') = (-y')\,\mathrm{erf}\frac{x'}{2(-y')^{1/2}} - \frac{x'^2}{2}\left[1 - \mathrm{erf}\frac{x'}{2(-y')^{1/2}}\right] + x'\left(\frac{-y'}{\pi}\right)^{1/2} e^{-x'^2/4(-y')}. \quad (14)$$

To evaluate the scales defined by Eq. (13), and to construct the figures, we use typical values observed in winter in the Adriatic sea. In fact, our intent is to show that the southward flow observed in winter in the Italian nearcoastal region is due to the longshore density variations when the longshore density profile and the northern coastline, representing the "initial" condition for $v_b$, are appropriately taken. Thus, we shall assume a profile in which the density anomaly maximum $\epsilon_{max}$ is located 50 km south of the northern coastline $y' = 0$, a value representative of the winter pattern in the Adriatic. The reference density $\rho_0$ is taken to be corresponding to $\sigma_t = 29.0$, the anomaly value observed in winter in the Jabuka pit (see MRB for geographical locations). The pit is taken to be at $y = -200$ km, where therefore $\epsilon = 0$. The density $\epsilon$ at the northern wall $y' = 0$ will be taken in the range $0 \leqslant \epsilon \leqslant \epsilon_{max}$. We have already discussed the solution for $\epsilon = \epsilon_{max}$, shown in Figs. 1a, b, c.

The values used for the scales (12a through f), characteristic of the Adriatic winter situation, are listed in Table 1 with short explanations of the way they were obtained.

Before showing the successive examples, the far-field solution of (14) [or (11) in dimensional form] will be discussed. The far field examined here is "far along the shore", that is $y' \to -\infty$. This far-field solution is the one examined both by Csanady (1978) and MRB, and is obtained when $y' \to -\infty$, or $x'/(-y')^{1/2} \to 0$. From (14) this gives

$$\lim_{y' \to -\infty} v_b = \frac{2}{\sqrt{\pi}}\beta' x'(-y')^{1/2}. \quad (15)$$

Equation (15) again gives $v_b > 0$ in the far field for a northward positive density gradient $\beta'$, but also shows the longshore velocity to grow without bound because the region of forcing is infinite in extent. Actually, the area in which far-field solutions apply is so thin in cross-shore direction to be meaningless in this Adriatic example, as the following considerations show. In order for the argument of the error function to be small, say O(0.05), then $x'/(-y')^{1/2} = O(0.05)$. Thus, to be in a far-field region we must be closer to the western coastline than the limiting curve:

$$x' = 0.05(-y')^{1/2}$$

or

$$x' = 0.05\left[\frac{r}{fs}(-y)\right]^{1/2} \text{ dimensionally.}$$

If $r/fs = 2$ km is a typical value for the chosen scales, at $y = -150$ km we must be closer to the coast than 0.9 km; at $y = -300$ km we must be closer than 1.2 km. It is therefore rather meaningless to examine this type of far-field solution. The solution is better considered in its full form and with finite regions of forcing.

TABLE 1. Values used in the calculations.

| | | |
|---|---|---|
| Independent scales | | |
| Latitude | | 45°N |
| Coriolis parameter | $f$ | $10^{-4}$ rad s$^{-1}$ |
| Bottom slope | $s$ | $2 \times 10^{-3}$ |
| Frictional coefficient | $r$ | $5 \times 10^{-4}$ m s$^{-1}$ |
| Longshore scale (units of $y'$) | $L_y$ | 50 km |
| Thus the southern limit, the Jabuka pit, is at $y' = -4$. | | |
| Density anomaly scale | $\epsilon_0 = \frac{1}{3}\epsilon_{max}$ | $= 0.167 \times 10^{-3}$ |
| with $\epsilon_{max} = 0.5 \times 10^{-3}$ as $\sigma_t$ is observed in winter to change from 29.5 at the interior maximum to 29.0 in the Jabuka pit (from MRB) | | |
| Longshore density gradient | $\beta_0 = \frac{\epsilon_{max}}{150\,\text{km}}$ | $= 3.33 \times 10^{-6}$ km$^{-1}$ |
| Dependent Scales ($r/fs = 2.5$ km) | | |
| Cross-shore scale $L_x$ (units of $x'$) (13a) | | 10 km |
| Longshore velocity $v_0$ (13c) (units of $v'$)* | | 3.2 cm s$^{-1}$ |
| Cross-shore velocity $u_0$ (13b) | | 0.7 cm s$^{-1}$ |
| Streamfunction $\psi_0$ (13d) (units of $\psi'$)** | | $8 \times 10^3$ m$^3$ s$^{-1}$ |

* For Figs. 1b, 2b, 3b, 4b

** For Figs. 1c, 2c, 3c, 4c

Each unit of nondimensional longshore flow is equivalent to 3.2 cm s$^{-1}$. The largest values of $v'$ from Figs. 1b, 2b, 3b, 4b are +3, +2, −2, −3 respectively or, dimensionally, +10, +6, −6, −10 cm s$^{-1}$. The observed longshore flows are of the order of −10 cm s$^{-1}$ in winter.

In all the following examples the density anomaly is taken to vanish at the Jabuka pit, $\epsilon' = 0$ at $y' = -4$; the density gradient is positive south of the density maximum, that is

$$\beta' = +1 \quad \text{for} \quad -4 \leqslant y' \leqslant -1$$

and to be variable and negative north of the maximum for $-1 < y' \leqslant 0$. We consider $0 \leqslant \epsilon' \leqslant \epsilon'_{max}$ in succession. For these examples there is a far-field $y' \to -\infty$ as the band of density variation is finite in its latitudinal extent.

The first example we have already discussed is given by (10), (11) or (14) dimensionless. Equation (10) corresponds to the dimensionless condition on the density gradient:

$$\begin{cases} \beta' = 0 & \text{for} \quad -1 \leqslant y' \leqslant 0 \\ \beta' = +1 & \text{for} \quad -4 \leqslant y' \leqslant -1; \end{cases} \quad (16a)$$

The flow pattern is given in Figs. 1a, b, c and shows the already discussed northward flow all over the coastal strip. The dimensionful solution (11) corresponds in dimensionless quantities to

$$v'_b = \begin{cases} 0 & \text{for} \quad y' \geqslant -1 \\ F(x', y' + 1) & \text{for} \quad -4 \leqslant y' \leqslant -1 \\ F'(x', y' + 1) - F(x', y' + 4) & \text{for} \quad y' < -4, \end{cases} \quad (16b)$$

with $F(x', y')$ given by (14).

In the second example we choose

$$\beta' = \begin{cases} -1 & \text{for } -1 \leq y' \leq 0 \\ +1 & -4 \leq y' \leq -1 \\ 0 & \text{otherwise} \end{cases} \tag{17a}$$

with solution

$$v_b' = \begin{cases} 0 & \text{for } y' \geq 0 \\ -F(x', y') & \text{for } -1 \leq y' \leq 0 \\ -F(x', y') + 2F(x', y'+1) & \text{for } -4 \leq y' \leq -1 \\ -F(x', y') + 2F(x', y'+1) & \\ \quad - F(x', y'+4) & \text{for } y' < -4. \end{cases} \tag{17b}$$

The solution is shown in Figs. 2a, b, c with patterns corresponding to those of Figs. 1a, b, c. Specifically, 2a shows the alongshore density profile; 2b the longshore velocity field; 2c the streamfunction pattern.

In the successive examples we progressively decrease the density anomaly at the northern wall $y' = 0$. Specifically, the gradient:

$$\beta' = \begin{cases} -2 & -1 \leq y' \leq 0 \\ +1 & -4 \leq y' \leq -1 \end{cases} \tag{18}$$

leads to Figs. 3a, b, c, and

$$\beta' = \begin{cases} -3 & -1 \leq y' \leq 0 \\ +1 & -4 \leq y' \leq -1 \end{cases} \tag{19}$$

leads to Figs. 4a, b, c. We do not explicitly give the solutions for $v_b'$, which are straightforward.

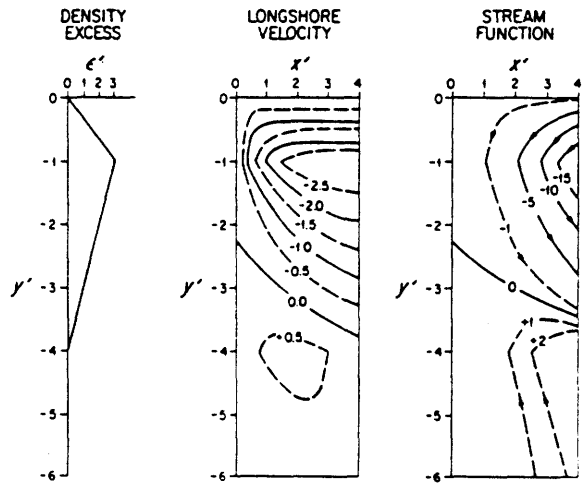


FIG. 4. As in Fig. 2, but with $\beta' = -3$ for $-1 \leq y' \leq 0$. Dimensionless units are discussed in Table 1.

Passing from Fig. 2 to Fig. 4, we notice that the inclusion of a region of negative-density gradient (density anomaly decreasing from the interior maximum to the reference value at the northern coastline) generates a region of southward flow north of the density maximum at $y' = -1$, simultaneously reducing the intensity of the northward flow in the southern cell. For the weak negative gradient of Fig. 2a, the southward flow is weak and mostly confined to the region north of the density maximum. When, however, we increase the negative gradient to $\beta' = -2$, as in Fig. 3a, the northern, southward flowing cell enlarges and becomes much stronger, pushing southward the northflowing current, now much weaker.

Finally, in the patterns of Figs. 4b, c we observe a very intense and broad cell of southward flow. The streamfunction pattern of Fig. 4c shows the current entering the near coastal region north of the density maximum at $y' = -1$, flowing southward for a considerable distance in the nearcoastal strip and finally turning offshore into the interior at the height of the Jabuka pit $y' = -4$. The northward-flowing cell is confined to the southernmost region of the coastal strip and is very weakened (maximum intensity of +2 compared to the negative maximum of −15). Notice that the density anomaly profile of Fig. 4a, even though idealized, is much more representative of the winter conditions in the northern Adriatic than the one-ramp profile of Fig. 1a.

## 4. Conclusions

The examples discussed in section 3 clearly show the profound effect of the reversal in density gradient north of the density maximum in driving the nearcoastal circulation and determining the direction of the alongshore flow. We have examined density profiles which, even though idealized, represent the alongshore density distribution observed in the northern Adriatic in wintertime. Inasmuch as the simple analytical model we have used is meaningful to represent the dynamical balance in the near-coastal strip, the inclusion of the negative northern density gradient, from the interior maximum to the northern coastline, allows the creation of a strong southward-flowing coastal cell. This is exactly the flow pattern observed in wintertime in the western coastal region adjacent to the Italian shoreline, both in numerical simulations (Hendershott and Malanotte-Rizzoli, 1976) and in current records (see MRB for experimental vector diagrams). The alongshore density profile reverses in summertime: the location of the density maximum would be replaced by a density minimum created by the light Po river water spreading in the surface layer throughout the northern basin (MRB). This reversed alongshore density profile would then be responsible for the current reversals observed in summertime in the same nearcoastal region, north-

ward flowing (MRB experimental records). The associated nearcoastal patterns would then be exactly the opposite of those shown in Figs. 4a, b, c.

*Acknowledgments.* This research was carried out with the support of the National Science Foundation, Grant OCE-85-18487.

REFERENCES

Carslaw, A. S., and J. C. Jaeger, 1956: *Conduction of Heat in Solids*, 2nd ed., Oxford University Press, 510 pp.

Csanady, G. T., 1978: The arrested topographic wave. *J. Phys. Oceanogr.*, **8**, 47–62.

Csanady, G. T., 1985: Pycnobatic currents over the upper continental slope. *J. Phys. Oceanogr.*, **15**, 306–315.

Hendershott, M. C., and P. Malanotte-Rizzoli, 1976: The winter circulation of the Adriatic Sea. *Deep-Sea Res.*, **23**, 353–373.

Malanotte-Rizzoli, P., and A. Bergamasco, 1983: The dynamics of the coastal region of the Northern Adriatic Sea. *J. Phys. Oceanogr.*, **13**, 1105–1130.

Shaw, P. T., and G. T. Csanady, 1983: Self-advection of density perturbations on a sloping continental shelf. *J. Phys. Oceanogr.* **13**, 769–782.

## References


Aikman, F, H-W Ou and R.W. Houghton (1986). Current variablity across the New England shelf break and slope. *submitted to J. Cont. Shelf Res.*

Beardsley, R.C., W. Boicourt and D. Hanson (1976). Physical oceanograpy of the Mid-Atlantic Bight. *J. Limnol. Ocean., Spec. Symp.* **2**, 20-24.

Beardsley, R.C., D.C.Chapman, K.H.Brink, S.R.Ramp and R.Schlitz (1979). The Nantucket Shoals Flux Expirement (NSFE79). Part I: A basic description of the current and temperature variablity. *J. Phys. Oceanogr.* **15**, 714-748.

Beardsley, R.C and C.D. Winant (1979). On the mean circulation of the Mid-Atlantic Bight. *J. Phys. Oceanogr.* **9**, 612-618.

Chapman, D.C., J.A. Barth, R.C. Beardsley, R.G. Fairbanks (1986). On the Continuity of Mean Flow between the Scotian Shelf and the Middle Atlantic Bight. *J. Phys. Oceanogr.* **16**, 758-772.

_____, and K.H. Brink (1987) Shelf and slope ciruculation induced by fluctuating offshore forcing. *J. Geophys. Res.* **92**, 11741-11759.

Chapman,D.C. and Beardsley (1988) A Note on the Origin of Shelf Water in the Middle Atlantic Bight. *submitted to J. Phys. Oceanogr.*

Carslaw, H.S. and J.C. Jaeger (1959). *Conduction of Heat in Solids,* 2nd ed., Oxford University Press, 510pp.

Csanady, G.T. (1978). The arrested topographic wave. *J. Phys. Oceanogr.* **8**, 47-62.

_____ (1979). The pressure field along the western margin of the North Atlantic. *J. Geophys. Res.* **84**, 4905 - 4914.

_____ (1981). Shelf circulation cells. *Philos. Trans. Royal Soc. Lond.* ***A302***, 515-530.

_____ (1982). *Circulation in the Coastal Ocean,* D. Reidel Publishing Co., Environmental Fluid Mechanics Monographs, 279pp.

_____ (1984). Circulation induced by river inflow over a well mixed continental shelf. *J. Phys. Oceanogr.* **14**, 1383-1392.

_____ (1985). Pycnobathic currents over the upper continental slope. *J. Phys. Oceanogr.* **15**, 306-315.

_____, and P.T. Shaw (1983). The insulating effect of a steep continental slope. *J. Geophys. Res.* **88**, 7519-7524.

Gill, A.E. (1982). *Atmosphere Ocean Dynamics,* Academic Press, 662pp.

Huang,R.X. (1987) A three-layer model for the Wind Driven Circulation in the Subtropical-Subpolar Basin. Part I:Model Formulation. *J. Phys. Oceanogr.* **17**, 664-678.

Hendershott, M.C. and P. Malanotte-Rizzoli (1976). The winter circulation of the Adriatic Sea. *Deep-Sea Res.* **23**, 353-373.

Huthnance, J.M. (1984). Slope currents and "JEBAR". *J. Phys. Oceanogr.* **14**, 795-810.

Johnson, J.A. and N. Rockliff (1986). Shelf break circulation processes. *Baroclinic Processes on Continental Shelves,* C.N.K. Mooers Edition, American Geophysical Union, 130pp.

Joyce, T.M. (1984) Velocity and hydrographic structure of Gulf Stream warm core rings. *J. Phys. Oceanogr.*, **14**, 936-947.

Kelly, K.A. and D.C. Chapman (1987). The response of a stratified shelf and slope to steady offshore forcing. *Manuscript in preparation.*

Malanotte-Rizzoli, P. and A. Bergamasco (1983). The dynamics of the coastal region of the Northern Adriatic Sea. *J. Phys. Oceanogr.* **13**, 1105-1130.

McCreary, J.P and S-Y Chao (1985). Three dimensional shelf circulation along an eastern boundary. *J. Marine Res.* **43**, 13-36.

Mitchum, G.T. and A.J. Clarke (1986). The frictional nearshore response to forcing by synoptic scale winds. *J. Phys. Oceanogr.* **16**, 934-946.

Pedlosky, J. (1979). *Geophysical Fluid Dynamics,* Springer-Verlag, 617pp.

_____ (1974). Longshore currents, upwelling and bottom topography. *J. Phys. Oceanogr.* **4**, 214-226.

Sarkisyan, P.-T, and V.P. Keonjiyan (1975). Review of numerical ocean circulation models using the observed density field. *Numerical Models of Ocean Circulation*, R. O. Reid, Ed. National Academy of Sciences, Washington D.C., 76-93

Scott, J.T. and G.T. Csanady (1976). Nearshore currents off Long Island. *J. Geophys. Res.* **81**, 5401-5409.

Semtner, A.J. and Y. Mintz (1977). Numerical simulation of the Gulf Stream and mid-ocean eddies. *J. Geophys. Res.* **7**, 208-230.

Vennell, M.R. and P. Malanotte-Rizzoli (1987). Coastal flows driven by alongshore density gradients. *J. Phys. Oceanogr.* **17**, 822-827.

Wang, D.P. (1982). Effects of slope on the mean shelf circulation. *J. Phys. Oceanogr.* **12** , 1524-1526.

Welander, P., (1959). The Atmosphere and the Sea in Motion. B.Bolin, Ed., Oxford University Press, 95-101

Zang, Q.H., G.S. Janowitz and L.J. Pietrafesa (1987). *The interaction of estuarine and shelf waters: a model and applications. J. Phys. Oceanogr.* **17**, 455-469.